AWARD NUMBER: W81XWH-18-1-0082

TITLE: Design of a 3D Mammography System in the Age of Personalized Medicine

PRINCIPAL INVESTIGATOR: Raymond J. Acciavatti, Ph.D.

CONTRACTING ORGANIZATION: University of Pennsylvania
Philadelphia, PA

REPORT DATE: April 2021

TYPE OF REPORT: Annual

PREPARED FOR: U.S. Army Medical Research and Development Command
Fort Detrick, Maryland 21702-5012

DISTRIBUTION STATEMENT: Approved for Public Release;
Distribution Unlimited

REPORT DOCUMENTATION PAGE

Form Approved
OMB No. 0704-0188

1. REPORT DATE April 2021	**2. REPORT TYPE** Annual	**3. DATES COVERED** 15Mar2020 – 14Mar2021

4. TITLE AND SUBTITLE Design of a 3D Mammography System in the Age of Personalized Medicine	**5a. CONTRACT NUMBER**
	5b. GRANT NUMBER W81XWH-18-1-0082
	5c. PROGRAM ELEMENT NUMBER
6. AUTHOR(S) Raymond J. Acciavatti, Ph.D. E-Mail: racci@pennmedicine.upenn.edu	**5d. PROJECT NUMBER**
	5e. TASK NUMBER
	5f. WORK UNIT NUMBER
7. PERFORMING ORGANIZATION NAME(S) AND ADDRESS(ES) University of Pennsylvania Philadelphia, PA 19104	**8. PERFORMING ORGANIZATION REPORT NUMBER**
9. SPONSORING / MONITORING AGENCY NAME(S) AND ADDRESS(ES) U.S. Army Medical Research and Development Command Fort Detrick, Maryland 21702-5012	**10. SPONSOR/MONITOR'S ACRONYM(S)**
	11. SPONSOR/MONITOR'S REPORT NUMBER(S)

12. DISTRIBUTION / AVAILABILITY STATEMENT

Approved for Public Release; Distribution Unlimited

13. SUPPLEMENTARY NOTES

14. ABSTRACT

Digital breast tomosynthesis (DBT) or "3D mammography" has been shown to offer higher sensitivity and specificity for breast cancer detection relative to 2D digital mammography. However, studies have demonstrated that the benefits of DBT are limited to non-calcification findings. We have developed new tomosynthesis system designs to enhance the visibility of calcifications based on the principle of super-resolution (SR). We published a manuscript describing a Fourier-based image-quality metric for high-frequency star-pattern phantoms for investigating SR [IEEE TMI 2021 40(3):1055-64]. Using this phantom, we showed that there are anisotropies in SR in current clinical systems. Additionally, we investigated how the magnification call-back exam can be optimized for 3D imaging with SR, and analyzed how the anisotropies in SR vary with the use of magnification. More specifically, a system design was analyzed with a secondary component of scanning motion in the posteroanterior (PA) direction; this motion eliminates the anisotropies in SR. We also explored how the use of PA source motion improves the accuracy of the separation between fibroglandular (dense) and adipose tissue, as well as the segmentation of the 3D breast outline, in voxel breast phantoms. This new design offers additional advantages in terms of Fourier-space sampling and signal-to-noise ratio (SNR).

15. SUBJECT TERMS

Digital breast tomosynthesis (DBT), mammography, super-resolution, personalized medicine, Defrise phantom, image reconstruction, calcification, virtual clinical trial, magnification mammography

16. SECURITY CLASSIFICATION OF:			**17. LIMITATION OF ABSTRACT**	**18. NUMBER OF PAGES**	**19a. NAME OF RESPONSIBLE PERSON** USAMRMC
a. REPORT Unclassified	**b. ABSTRACT** Unclassified	**c. THIS PAGE** Unclassified	Unclassified	130	**19b. TELEPHONE NUMBER** *(include area code)*

Table of Contents

1. INTRODUCTION

In clinical digital breast tomosynthesis (DBT) systems, every patient is currently imaged the same way. The x-ray tube scans in the left-to-right direction and there is no motion in the perpendicular direction; i.e., the posteroanterior (PA) direction (orthogonal to the chest wall).[1-4] In this project, we have demonstrated the benefits of introducing source motion in both the lateral (left-to-right) and PA directions, and personalizing the shape of the motion around the breast's dimensions.[5] We have successfully used virtual clinical trials (VCTs) with computational breast phantoms to demonstrate that this new design offers better portrayal of calcifications[6], as well as dense fibroglandular tissue (the tissue that is radiographically brightest and can potentially hide a cancer[7-9]). VCTs allow optimum system designs to be identified rapidly without requiring human subject recruitment.[10] In the last year, we also analyzed how the magnification call-back exam can be re-designed with the latest 3D imaging techniques. With the use of 3D magnification imaging, there is far superior spatial resolution compared with current clinical systems that use 2D magnification imaging techniques for diagnostic mammography. The new design also allows for isotropic resolution (high image quality in all directions) in both screening and magnification DBT, unlike current clinical systems which have anisotropic spatial resolution.

2. KEYWORDS

Digital breast tomosynthesis (DBT), mammography, super-resolution, personalized medicine, Defrise phantom, image reconstruction, calcification, virtual clinical trial, magnification mammography.

3. ACCOMPLISHMENTS

3.A. What were the major goals of the project?

The Statement of Work is shown below. Milestones achieved in the past 12 months are summarized for each of the major tasks. More detail about these milestones is given in Section 3.B.

3.A.1. Specific Aim 1: Design a personalized image acquisition technique for screening mammography.

Specific Aim 1: Design a personalized image acquisition technique for screening mammography.	**Timeline (Months)**
Major Task 1: Optimize super-resolution (SR) with simulations of high-frequency, sinusoidal test objects and calculations of the *r*-factor.	
Subtask 1: Develop a design for optimizing SR. Through our prototype system, we learned that SR can be optimized by introducing detector motion that varies the source-to-image distance (SID) during the scan. However, to minimize the need for a thick detector housing, we will investigate more complex combinations of x-ray tube and detector motion that can be used to optimize SR.	1-12
Subtask 2: Make refinements to the motions of the x-ray tube and detector based on the on-going results of the virtual clinical trial (VCT) in specific aim 3.	13-30
Milestones Achieved In the Past 12 Months: Theoretical model of SR for high-frequency imaging tasks (documents 2 and 6 of Section 9); Voxel phantom model of SR (document 5 of Section 9); Development of a Fourier-based image-quality metric for SR (document 1 of Section 9); Analysis of Fourier-space sampling to identify acquisition geometries with the highest resolution in all three directions (document 9 of Section 9).	
Major Task 2: Simulate the reconstruction of glandular and adipose tissue with Defrise phantoms.	
Subtask 1: Prepare Defrise phantoms modeled in the shape of breasts.	1-3
Subtask 2: Simulate the image acquisition. First, a 2D scout image is acquired at low radiation dose. Second, the 3D scan parameters are determined based on estimates of the breast size, shape, and internal composition.	4-9
Subtask 3: Prepare reconstructions, and calculate the relative contrast at the septa between glandular and adipose tissue.	10-15

Subtask 4: Determine the effect of the reconstruction filter on the relative contrast. To optimize the image quality, the filter will be personalized to the phantom.	16-21
Subtask 5: Update the reconstructions and calculations of contrast as new acquisition geometries are identified based on the on-going results of the virtual clinical trial in specific aim 3.	22-30
<u>Milestone Achieved in the Past 12 Months:</u> Voxel phantom model consisting of equidistant tubes of dense tissue in a background of adipose tissue, forming a lattice of two tissue types used for signal-to-noise ratio optimization (document 10 of Section 9).	
Major Task 3: Develop a personalized acquisition geometry yielding a more accurate segmentation of the breast outline.	
Subtask 1: Prepare database of binary phantom masks (uniform phantoms with no internal composition). These will be used to calculate the breast outline (convex hull) in the reconstruction.	4-6
Subtask 2: Determine the motions of the x-ray tube and detector that yield the most accurate breast outline segmentation. These motions will be personalized to the breast size and shape based on a 2D scout image.	7-21
<u>Milestone Achieved in the Past 12 Months:</u> Development of new scanning motions for optimizing the breast outline segmentation (document 8 of Section 9).	

3.A.2. Specific Aim 2: Design a 3D Magnification Mammography Call-Back Exam.

Specific Aim 2: Design a 3D Magnification Mammography Call-Back Exam.	**Timelines (Months)**
Major Task 4: Optimize super-resolution (SR).	
Subtask 1: Develop designs for the source and detector motion that optimize SR in magnification imaging. This will ensure the highest image quality in imaging calcifications (small, closely-spaced structures).	1-12
Subtask 2: Make refinements to the motion of the x-ray tube and detector based on the on-going results of the virtual clinical trial in specific aim 3.	13-30
<u>Milestones Achieved in the Past 12 Months:</u> Theoretical model of SR used to optimize the design of magnification tomosynthesis systems (document 7 of Section 9).	
Major Task 5: Perform a contrast-detail reader study.	
Subtask 1: Simulate a contrast-detail (C-D) array in a uniform background at different positions. The scan parameters for the 3D acquisition will be customized around the region containing the C-D array.	7-12
Subtask 2: Perform a reader study. Prepare plots of the smallest thickness visible as a function of the cross-sectional area of the lesion. Determine how a personalized 3D acquisition compares against: (1) a non-personalized 3D acquisition, and (2) 2D magnification imaging (the current gold standard).	13-18
Subtask 3: Repeat subtasks 1 and 2 with the C-D array in structured (anatomical) backgrounds. Determine how the breast background (density and texture) impacts the reader performance.	19-24
Subtask 4: Update the results of subtasks 2-3 based on the new reconstruction filters and the new acquisition geometries developed in specific aims 1 and 3.	25-30
<u>Milestone Achieved in the Past 12 Months:</u> Database of calcification polycubes with varying size (detail) and varying contrast (percentage of hydroxyapatite, or weighting fraction), as described in document 4 of Section 9.	

3.A.3. Specific Aim 3: Evaluate the new designs for screening and call-back imaging with a virtual clinical trial.

Specific Aim 3: Evaluate the new designs for screening and call-back imaging with a virtual clinical trial.	**Timeline (Months)**
Major Task 6: Quantify breast density in anatomical phantoms.	
Subtask 1: Prepare anatomical phantoms with variable size, shape, and internal composition.	1-3
Subtask 2: Simulate x-ray images in personalized and non-personalized acquisition geometries.	4-6
Subtask 3: Calculate reconstructions. Model the differentiation between adipose and glandular tissue as a binary classification task with a receiver operating characteristic (ROC) curve.	7-12
Subtask 4: Optimize the reconstruction filter; it will be personalized to the phantom. The filter should maximize the area under the ROC curve.	13-18
Subtask 5: Repeat subtasks 2-4 as on-going refinements are made to the motion paths of the x-ray tube and detector, as well as the reconstruction filter. We are working to maximize the area under the ROC curve.	19-30
Milestone Achieved in the Past 12 Months: Model of classification accuracy of segmenting fibroglandular and adipose tissue compartments in virtual breast phantoms, illustrating the benefits of new scanning motions in DBT (document 8 of Section 9).	
Major Task 7: Perform a virtual clinical trial (VCT) with simulated lesions.	
Subtask 1: Prepare computational breast phantoms with lesions (masses and calcifications) of variable size, shape, and contrast.	1-6
Subtask 2: Design the VCT. Numerical observers will be trained on the statistics of images. Channelized Hotelling Observer parameters will be determined to match the performance of the observer on real and breast model images.	7-12
Subtask 3: Conduct the VCT. The sensitivity index (*d*′) and call-back rate will be estimated for the detection and characterization of lesions in different system designs. These calculations will be used to compare new acquisition geometries against conventional acquisition geometries.	13-30
Subtask 4: The results of the VCT will be used to rule out poor design choices and identify the best possible system designs for a human clinical trial. We will perform statistical power calculations to design the future clinical trial.	31-36
Milestone Achieved in the Past 12 Months: Virtual clinical trials of breast phantom models with simulated lesions (document 4 of Section 9); Validation of anthropomorphic phantom model (document 3 of Section 9).	

3.B. What was accomplished under these goals?

3.B.1. Specific Aim 1: Design a personalized image acquisition technique for screening mammography.

Optimizing Calcification Imaging:

In breast imaging, calcifications can act as early signs of cancer.[11,12] Studies have shown that the benefits of current DBT systems over conventional 2D mammography are limited to non-calcification findings.[13] We have proposed the idea of using super-resolution (SR) to improve calcification visualization;[14-20] this requires a reconstruction grid with smaller pixelation than the detector.

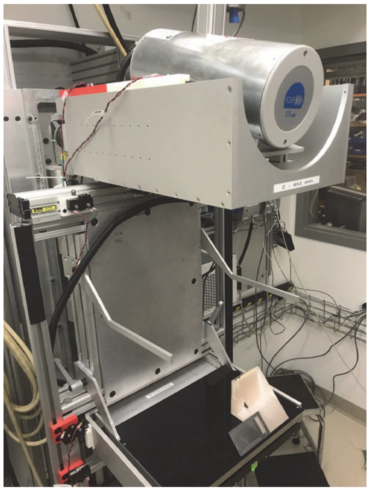

Fig. 1. Photograph of next-generation tomosynthesis (NGT) prototype system in our lab and bar pattern phantom at 45° angle.

Although clinical DBT offers the potential for SR, current system designs do not maximize this effect.[15] In the last year, we published a paper [IEEE TMI 2021 40(3):1055-64] to illustrate the anisotropies in SR using the "Fourier spectral distortion metric" (**document 1 of Section 9**), a metric that analyzes the Fourier transform of high-frequency star-pattern images.[20] This metric is an important computational tool for investigating anisotropies in SR, and demonstrating the advantages of our next-generation tomosynthesis (NGT) system[21] - a prototype system in our lab designed specifically to suppress these anisotropies.

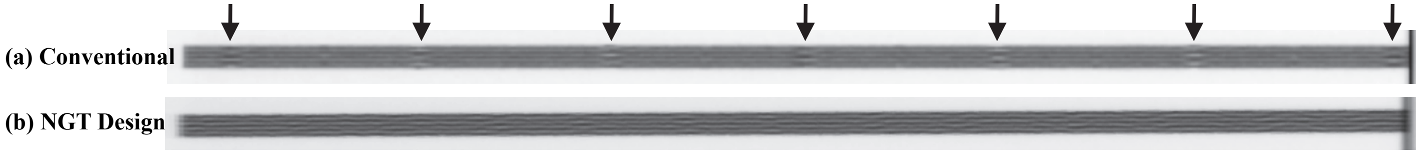

Fig. 2. (a) Reconstruction showing anisotropies in super-resolution (SR) at the arrows. (b) SR is achieved everywhere in the NGT design with detector motion in the *z* direction.

In Figs. 1-2, we illustrate anisotropies in SR with a bar pattern phantom (SuperTech, Model 07-525) oriented at a 45° angle relative to the breast support. The frequency (8.0 mm^{-1}) was chosen to be higher than the alias frequency of the detector used in the NGT system (5.9 mm^{-1} for 0.085 mm detector pixelation). Angling the phantom allowed for visualization of anisotropies in the *z* direction (perpendicular to the breast support). In the reconstruction plane[22] (Real Time Tomography, Villanova, PA) matched to the oblique plane of the phantom, there are anisotropies in regularly-spaced increments in the *z* direction [Fig. 2(a), arrows].[19] These anisotropies can be understood from the projection images of a point-like object (Fig. 3). Since the x-ray tube moves laterally (left-to-right), there are shifts in the *x* direction between projections [Fig. 3(b)]. The shifts vary by a constant increment, which is depicted as a subpixel fraction of the detector element (del) size allowing for SR. As the elevation of the object changes, this increment varies in proportion with the magnification. At some elevations, it is possible for the increment to be an integer multiple of the del size, creating an anisotropy in SR.

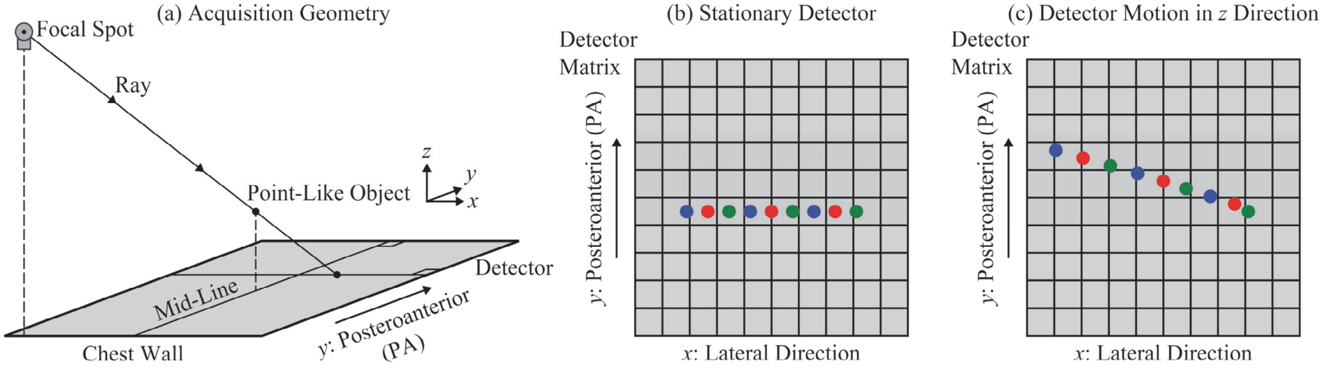

Fig. 3: In this example, nine projection images of a point-like object are acquired as the x-ray tube moves laterally (left-to-right).

Through this DoD grant, we have developed two technical innovations to tomosynthesis system design that eliminate the anisotropies in SR in 3D mammography.

- *Clustering of focal spot positions.* In current clinical systems, the spacing between the x-ray source positions is constant; there is a fixed angular increment between all the source positions. We proposed the idea of re-arranging the source positions in clusters[23,24], where there is submillimeter spacing between the source positions within each cluster and broader spacing between clusters. This design has been shown to eliminate the anisotropies in SR in the *z* direction (**document 2 of Section 9**).
- *Detector motion in the z direction (perpendicular to the breast support).* Unlike clinical systems, the NGT system is capable of detector motion in the *z* direction (specifically, 45 mm of descending motion).[19] Fig. 3(c) illustrates how the projections of a point-like object are impacted by this motion. The shifts no longer vary by a constant increment. This guarantees that even if the increment between some projections is an integer multiple of the del size, there will be other projections having subpixel sampling differences. The NGT design with detector motion ensures that SR is achieved everywhere in the image [Fig. 2(b)]. Our progress is summarized in the manuscript draft being prepared for journal submission (**document 6 of Section 9**) as well as our 2020 Proceedings manuscript of the 15th International Workshop on Breast Imaging (**document 5 of Section 9**).

Optimizing Dense Tissue Visualization:

In our previous progress reports, we described how Defrise phantoms were used to quantify the improvements in image quality in the NGT system.[5] Defrise phantoms consist of alternating bands of fibroglandular (dense) and adipose tissue. It is difficult to see the separation between these two tissue types in the conventional system design, but the separations are portrayed much more clearly in the NGT system. To expand on our prior work modeling alternating patterns of fibroglandular and adipose tissue, we created computational phantoms consisting of equidistant tubes of fibroglandular tissue in a background of adipose tissue. These phantoms were used to measure the signal-to-noise ratio (SNR) throughout the image. The tubes run in two directions (*x* and *y*), forming a lattice. Each tube has dimensions 4.4 × 240 × 4.4 (in mm). We determined SNR in a region-of-interest (15 × 15 pixels) using the ratio of mean signal to the standard deviation in signal. The regions-of-interest were shifted in each direction, at intervals halfway between tube intersections, to generate a surface plot of SNR at all positions. We demonstrated that the NGT system offers higher SNR than the conventional system design (**document 10 of Section 9**).[25] In a related work, we calculated the Fourier-sampling planes of various scanning motions, and showed that the NGT system offers better Fourier-space sampling (better resolution in all three directions) than the conventional system design (**document 9 of Section 9**).[26]

Optimizing Breast Outline Segmentation:

An additional drawback of the conventional system design is that the reconstruction of the 3D breast outline is overestimated in the PA direction.[27] We have calculated the breast outline volume for various scanning motions, and showed that the NGT system design offers a more accurate breast outline segmentation than the conventional system design (**document 8 of Section 9**).[28]

3.B.2. Specific Aim 2: Design a 3D Magnification Mammography Call-Back Exam.

In mammography, microcalcifications are often less than 1.0 mm in diameter and require additional diagnostic imaging, such as magnification mammography, for more detailed characterization. To date, all medical centers acquire a 2D magnification image. We are proposing a new design for magnification mammography based on the principles of 3D imaging (tomosynthesis). We are also designing the magnification exam to achieve SR and hence the sharpest possible image quality. These design advances are unique to our lab's prototype NGT system (Fig. 4).

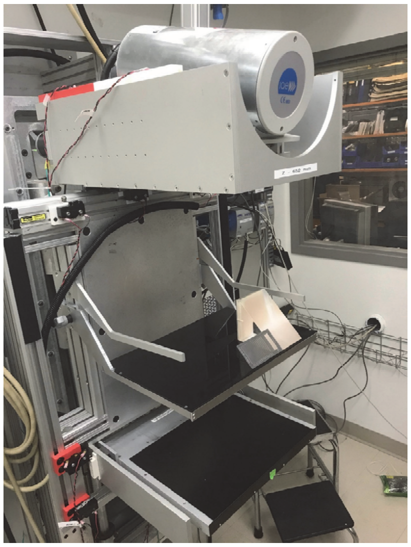

Fig. 4. Photograph of our lab's prototype NGT system with the bar pattern positioned on a stand for magnification tomosynthesis imaging.

In magnification mammography, the breast is elevated closer to the x-ray source. This setup magnifies small findings in the breast. Based on our experience with modeling 3D screening mammography, we have determined that there are anisotropies in SR throughout the image volume. Anisotropies in magnification tomosynthesis were analyzed with our theoretical model of SR.[15,24] To summarize the model briefly, the reconstruction of a sinusoidal test object was calculated, and analyzed with the Fourier transform. We measured the ratio of the amplitudes of two peaks in Fourier space: the peak below the input frequency (A_1) relative to the peak at the input frequency (A_2); *i.e.*, a ratio known as the *r*-factor (Fig. 5). The *r*-factor should be as small as possible (approaching zero) to achieve SR with high image quality; a threshold of 1/3 is shown in Fig. 6.

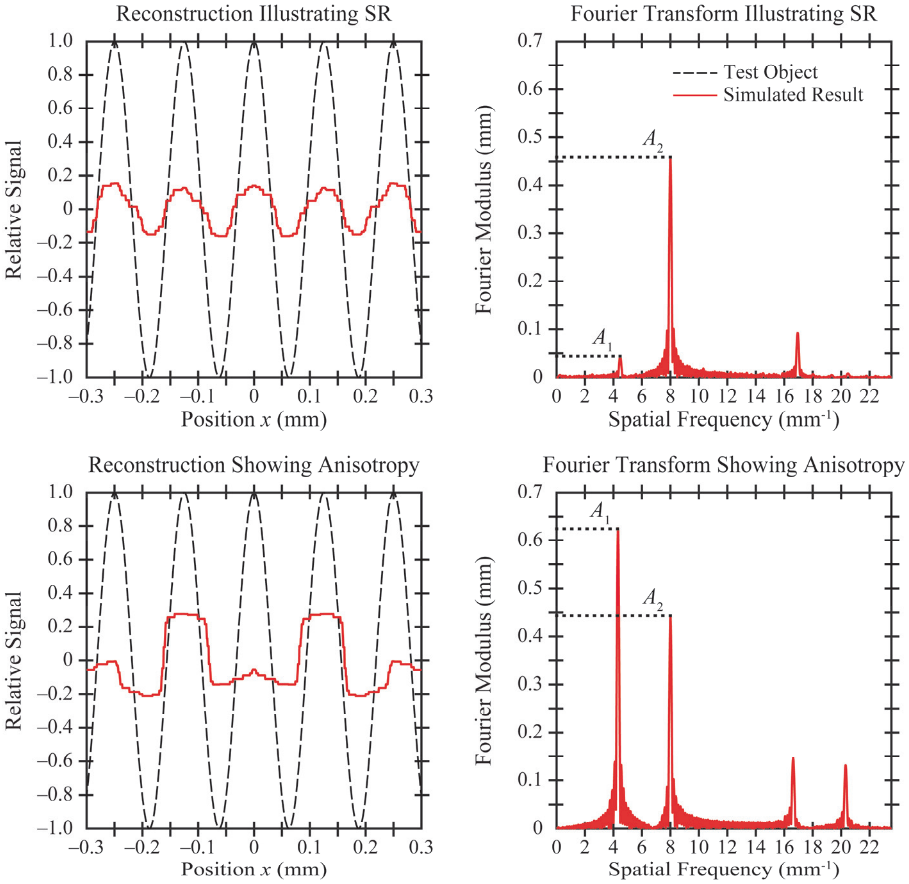

Reconstruction Illustrating SR

Fourier Transform Illustrating SR

Reconstruction Showing Anisotropy

Fourier Transform Showing Anisotropy

Fig. 5. The Fourier transform of the reconstruction is analyzed in terms of two peaks: one at the input frequency (A_2) and one at a lower frequency (A_1). This figure is adapted from our 2020 SPIE proceedings manuscript.[23]

We applied this model to analyze a 9.5 mm^{-1} input frequency in a scanning motion with 15 projections, 0.085 mm detector pixelation, and 180 mm of source motion (scanning left-to-right). We simulated the object being elevated from z = 0 (plane of breast support) to z = 200 mm. There are sharp peaks in the *r*-factor at various z coordinates; SR is not achieved at these positions (Fig. 6). We found that the spacing between peaks (anisotropies) gets narrower with increasing magnification; however, the relative amplitude of low-frequency (aliasing) signal is not as pronounced as in screening mode.

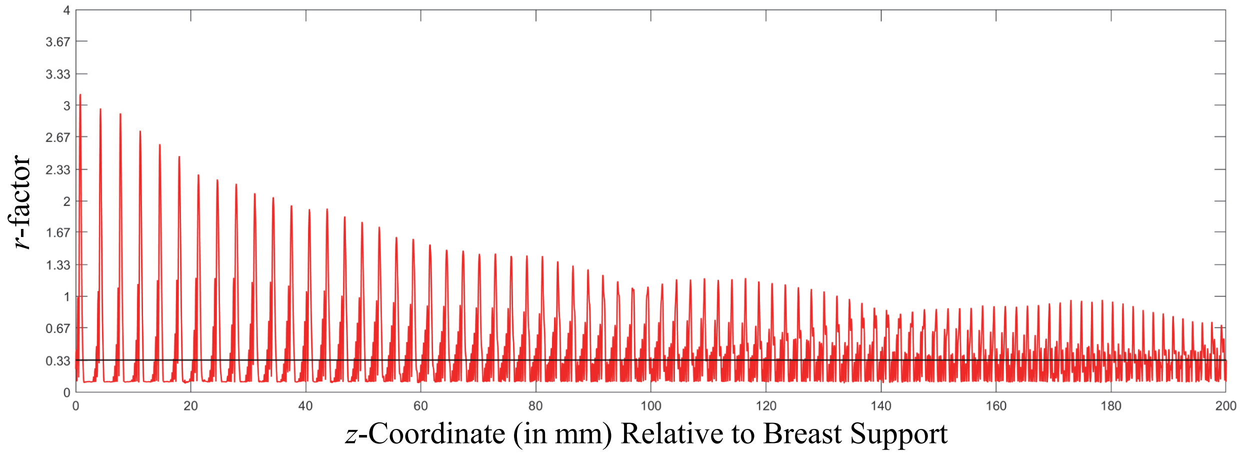

Fig. 6. A high-frequency test object was analyzed with theoretical modeling. The *r*-factor should be as small as possible to achieve SR with high quality. With the use of magnification, the overall amplitude of the *r*-factor decreases.

To validate the model experimentally, we imaged a bar pattern phantom (SuperTech, Model 07-525) with the NGT system. The phantom was canted at an angle, as shown in Fig. 4. The reconstruction plane (Real Time Tomography software, Villanova, PA) was matched to the oblique plane of the phantom, allowing for visualization of anisotropies in the z direction (the direction perpendicular to the breast support). Reconstructions with the bar pattern phantom validated the theoretical model. There are seven anisotropies, denoted by the arrows, in screening mode [Fig. 7(a)]. However, if the phantom is elevated by 80 mm above the breast support, there are nine anisotropies [Fig. 7(b)]. According to the theoretical model, the peaks in the *r*-factor decrease in amplitude with increasing magnification (Fig. 6). This indicates that the anisotropies do not include as much low-frequency (aliasing) content with increasing magnification.

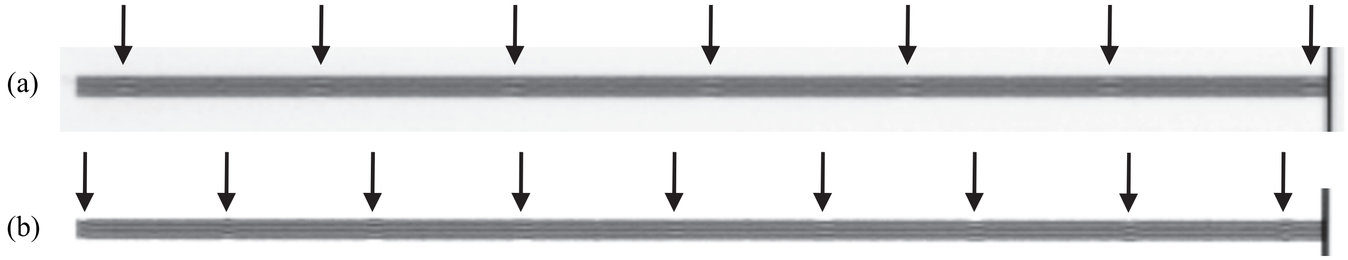

Fig. 7. (a) Reconstruction in screening mode showing anisotropies in SR at the arrows. (b) Magnification stand elevated 80 mm above breast support.

We presented our work on magnification tomosynthesis at the virtual 2021 SPIE Medical Imaging conference (**document 7 of Section 9**). In that work, we also demonstrated how PA source motion (a technical innovation in the NGT system) is an important tool to suppress anisotropies in super-resolution. We modeled the system with a secondary component of scanning motion in the PA direction.

3.B.3. Specific Aim 3: Evaluate the New Designs for Screening and Call-Back Imaging with a Virtual Clinical Trial

Calcification Imaging:

Virtual clinical trials (VCTs) with breast phantoms are computational tools for demonstrating the advantages of new system designs. VCTs were conducted with highly-attenuating polycubes used to simulate small calcific lesions:

- We validated super-resolution (SR) as a mechanism for improving calcification detection in DBT (**document 4 of Section 9**).[6]
- We used VCTs to demonstrate anisotropies in SR; these anisotropies impact the portrayal of calcifications in the reconstruction (**document 2 of Section 9**).[24]

Dense Tissue Visualization:

In specific aim 1, we used Defrise phantoms to illustrate how the separation between fibroglandular and adipose tissue is portrayed more clearly with the NGT system design. Complementing this work, we analyzed reconstructions of fibroglandular and adipose tissue in anthropomorphic phantoms.

- We calculated the detectability index (d') associated with the fibroglandular-adipose segmentation task and showed that the NGT system has higher d' than the conventional system design (**document 8 of Section 9**).[28]
- We validated the anthropomorphic phantom as having realistic parenchymal texture (**document 3 of Section 9**).

3.C. What opportunities for training and professional development has the project provided?

- The PI (Raymond Acciavatti) became a Research Assistant Professor in the Radiology Department at Penn on 7/1/2020. Previously the PI was a Research Associate in the Radiology Department at Penn.

3.D. How were the results disseminated to communities of interest?

- Our work on VCTs was presented in the "Computer-Aided Diagnosis Live Demonstrations" session on 2/17/2021 at the SPIE Medical Imaging conference, which was held virtually due to the COVID-19 Pandemic. The presentation was titled "PhysicsVCTs: A Framework to Evaluate Spectral Distortion in the Fourier Domain" (authors: Trevor Vent, Bruno Barufaldi, Raymond Acciavatti, and Andrew Maidment). The presenting author for this Live Demonstration was Trevor Vent.

- As described in Section 9, **documents 2 and 3** were presented by the PI (Raymond Acciavatti) at the 15th International Workshop on Breast Imaging in May of 2020, and **document 7** was presented by the PI at the SPIE Medical Imaging conference in February of 2021. These were all virtual conference presentations due to the COVID-19 Pandemic.

3.E. What do you plan to do during the next reporting period to accomplish the goals?

We have the following goals for the next 12 months; this is the “No Cost Extension” (NCE) period. Our goals for the NCE were detailed in the document submitted to the DoD on 2/12/2021, and are summarized below.

- Expand conference proceedings manuscripts on SR (documents 2 and 5 of Section 9) to journal papers. Two strategies for optimizing SR were described previously in this report: (1) clustering of focal spot positions; (2) detector motion in the *z* direction (perpendicular to the breast support). We will also perform the NGT x-ray experiments necessary to complete these works using high-frequency phantoms.

- Expand conference proceedings manuscripts demonstrating the advantages of PA source motion (documents 8 and 10 of Section 9), as described previously in this report; namely, higher SNR, more accurate breast outline segmentation, and higher d' in the task of segmenting fibroglandular and adipose tissue in VCTs.

- Expand the SPIE proceedings manuscript on magnification tomosynthesis (document 7 of Section 9) to a journal paper using physical experiments with the star-pattern phantom and the FSD metric described in document 1 of Section 9.

4. IMPACT

4.A. What was the impact on the development of the principal discipline(s) of the project?

Our work has an impact on both screening DBT and magnification call-back imaging:

- With the use of SR, small calcific findings can be detected more readily with higher d', as shown by VCTs (document 4 of Section 9).

- The use of x-ray source motion in the PA direction, as described in document 8 of Section 9, allows the separation between fibroglandular and adipose tissue to be portrayed more sharply in anthropomorphic phantoms.

- There is far superior spatial resolution with the use of 3D magnification imaging than with the use of 2D magnification imaging (the current standard for clinical diagnostic magnification imaging), as shown in document 7 of Section 9.

- Re-arranging the x-ray source positions in clusters (document 2 of Section 9) allows the anisotropies in SR to be suppressed, so SR can be achieved reliably everywhere in the image. This offers the best possible resolution for calcification imaging.

4.B. What was the impact on other disciplines?

Nothing to report.

4.C. What was the impact on technology transfer?

Nothing to report.

4.D. What was the impact on society beyond science and technology?

Nothing to report.

5. CHANGES / PROBLEMS

5.A. Changes in approach and reasons for change

Nothing to report.

5.B. Actual or anticipated problems or delays and actions or plans to resolve them

Nothing to report.

5.C. Changes that had a significant impact on expenditures

Nothing to report.

5.D. Significant changes in use or care of human subjects, vertebrate animals, biohazards, and/or select agents

Nothing to report.

5.E. Significant changes in use or care of human subjects

Nothing to report.

5.F. Significant changes in use or care of vertebrate animals

Nothing to report.

5.G. Significant changes in use of biohazards and/or select agents

Nothing to report.

6. PRODUCTS.

6.A. Publications, conference papers, and presentations

- **Journal publications**
    - Vent TL, Acciavatti RJ, Maidment ADA. Development and Evaluation of the Fourier Spectral Distortion Metric. IEEE Transactions on Medical Imaging 2021, vol. 40, no. 3, pp. 1055-1064. *This paper was published in March of 2021.*
    - Acciavatti RJ, Vent TL, Barufaldi B, Wileyto EP, Noël PB, Maidment ADA. Super-Resolution in Digital Breast Tomosynthesis: Limitations of the Conventional System Design and Strategies for Optimization. In: Bosmans H, Marshall N, Van Ongeval C, editors; 15th International Workshop on Breast Imaging; 2020; Virtual Conference (held during COVID-19 Pandemic): SPIE; 2020. p. 115130V-1 - 115130V-9. *This paper was published in May of 2020. The PI (Raymond Acciavatti) gave a "virtual" presentation at this conference.*
    - Acciavatti RJ, Cohen EA, Maghsoudi OH, Gastounioti A, Pantalone L, Hsieh M-K, Barufaldi B, Bakic PR, Chen J, Conant EF, Kontos D, Maidment ADA. Calculation of Radiomic Features to Validate the Textural Realism of Physical Anthropomorphic Phantoms for Digital Mammography. In: Bosmans H, Marshall N, Van Ongeval C, editors; 15th International Workshop on Breast Imaging; 2020; Virtual Conference (held during COVID-19 Pandemic): SPIE; 2020. p. 1151309-1 - 1151309-7. *This paper was published in May of 2020. The PI (Raymond Acciavatti) gave a "virtual" presentation at this conference.*
    - Vent TL, Barufaldi B, Acciavatti RJ, Maidment ADA. Simulation of high-resolution test objects using non isocentric acquisition geometries in next-generation digital tomosynthesis. In: Bosmans H, Marshall N, Van Ongeval C, editors; 15th International Workshop on Breast Imaging; 2020; Virtual Conference (held during COVID-19 Pandemic): SPIE; 2020. p. 1151317-1 - 1151317-8. *This paper was published in May of 2020. The first author (Trevor Vent) gave a "virtual" presentation at this conference.*

    - Barufaldi B, Vent TL, Acciavatti RJ, Bakic PR, Noël PB, Maidment ADA. MRMC ROC Analysis of Calcification Detection in Tomosynthesis Using Computed Super Resolution and Virtual Clinical Trials. In: Bosmans H, Marshall N, Van Ongeval C, editors; 15th International Workshop on Breast Imaging; 2020; Virtual Conference (held during COVID-19 Pandemic): SPIE; 2020. p. 1151313-1 - 1151313-7. *This paper was published in May of 2020. The first author (Bruno Barufaldi) gave a "virtual" presentation at this conference.*

- **Books or other non-periodical, one-time publications**
    - Nothing to report.

- **Other publications, conference papers, and presentations**
    - Martin DA, Vent TL, Choi CJ, Barufaldi B, Acciavatti RJ, Maidment ADA. Signal-to-Noise Ratio and Contrast-to-Noise Ratio Measurements for Next Generation Tomosynthesis. In: Bosmans H, Zhao W, Yu L, editors; Physics of Medical Imaging; 2021 (virtual conference held during COVID-19 Pandemic): SPIE; 2021. p. 115951L-1 - 115951L-9. *This conference paper was published in February 2021. The first author (David Martin) gave a "virtual" presentation.*
    - Choi CJ, Vent TL, Acciavatti RJ, Maidment ADA. Analysis of Digital Breast Tomosynthesis Acquisition Geometries in Sampling Fourier Space. In: Bosmans H, Zhao W, Yu L, editors; Physics of Medical Imaging; 2021 (virtual conference held during COVID-19 Pandemic): SPIE; 2021. p. 115954W-1 - 115954W-10. *This conference paper was published in February 2021. The first author (Chloe Choi) gave a "virtual" poster presentation.*
    - Vent TL, Barufaldi B, Acciavatti RJ, Krishnamoorthy S, Surti S, Maidment ADA. Next generation tomosynthesis image acquisition optimization for dedicated PET-DBT attenuation corrections. In: Bosmans H, Zhao W, Yu L, editors; Physics of Medical Imaging; 2021 (virtual conference held during COVID-19 Pandemic): SPIE; 2021. p. 115954V-1 - 115954V-7. *This conference paper was published in February 2021. The first author (Trevor Vent) gave a "virtual" poster presentation.*
    - Acciavatti RJ, Vent TL, Choi CJ, Wileyto EP, Noël PB, Maidment ADA. Development of Magnification Tomosynthesis for Superior Resolution in Diagnostic Mammography. In: Bosmans H, Zhao W, Yu L, editors; Physics of Medical Imaging; 2021 (virtual conference held during COVID-19 Pandemic): SPIE; 2021. p. 115951J 1 - 115951J-7. *This conference paper was published in February 2021. The PI (Raymond Acciavatti) gave a "virtual" presentation.*

6.B. Website(s) or other Internet site(s)

The VCT software developed by the X-Ray Physics Lab at the University of Pennsylvania can be accessed through the website https://sourceforge.net/projects/openvct/.

6.C. Technologies or techniques

Nothing to report.

6.D. Inventions, patent applications, and/or licenses

Nothing to report.

6.E. Other products

Nothing to report.

7. PARTICIPANTS AND OTHER COLLABORATING ORGANIZATIONS.

7.A. What individuals have worked on the project?

Name:	Raymond J. Acciavatti, Ph.D.
Project Role:	Principal Investigator (Research Assistant Professor)
Research Identifier:	ORCiD ID: 0000-0003-4822-3353
Nearest person month worked:	7
Contribution to project:	Lead investigator for all specific aims of the project; author on documents detailed in Section 9.
Funding Support:	

Name:	David Higginbotham
Project Role:	Software Developer
Research Identifier:	
Nearest person month worked:	6
Contribution to project:	VCT software development for x-ray projection simulation and breast phantom creation.
Funding Support:	

7.B. Has there been a change in the active other support of the PD/PI(s) or senior / key personnel since the last reporting period?

The most <u>current</u> description of <u>active</u> grant support for all key personnel is included in the pages that follow.

Raymond J. Acciavatti, Ph.D. – Active Grant Support:

W81XWH-18-1-0082 Acciavatti, Raymond 3/15/2018-3/14/2022 (NCE) 7.2 calendar
Department of Defense Breast Cancer Research Program Breakthrough Award (Level 1)
Science Officer: Laurie Shuman-Moss
Design of a 3D Mammography System in the Age of Personalized Medicine.
This grant proposes a personalized acquisition geometry for 3D mammography, as well as additional design changes that offer improvements in super-resolution.

R01CA161749 Kontos, Despina 4/1/2017-3/31/2022 3.0 calendar
NIH
Program Official: Kimery Griffin
Digital breast tomosynthesis imaging biomarkers for breast cancer risk estimation
No overlap. The improved clinical performance achieved with digital breast tomosynthesis is currently fueling a broad adaptation of tomosynthesis for general population breast cancer screening. Our study will be the first to evaluate tomosynthesis imaging measures in breast cancer risk assessment and will develop the necessary technology to enable larger multi-center studies. Ultimately, these novel imaging biomarkers may lead to more accurate individualized risk stratification, improving personalized breast cancer screening and prevention.

IRSA 1016451 Maidment, Andrew 9/1/2016-8/31/2021 1.2 calendar
Burroughs Wellcome Fund
Contact: Rusty Kelley
ViCTRE – Virtual Clinical Trials in the Regulatory Environment.
No overlap. We propose ViCTRE as a cost-effective and timely alternative to the current regulatory process. This vision is not fanciful; the elements of our proposed VCT pipeline are mature. VCTs are already commonly used in the design and development of imaging devices by academia and industry.

OVERLAP: There is no scientific or budgetary overlap between active research grants and DoD grant W81XWH-18-1-0082.

<u>Emily Conant, M.D. – Active Grant Support:</u>

W81XWH-18-1-0082 Acciavatti, Raymond 3/15/2018-3/14/2022 (NCE) 0.12 calendar
Department of Defense Breast Cancer Research Program Breakthrough Award (Level 1)
Science Officer: Laurie Shuman-Moss
Design of a 3D Mammography System in the Age of Personalized Medicine.
This grant proposes a personalized acquisition geometry for 3D mammography, as well as additional design changes that offer improvements in super-resolution.

R01CA161749 Kontos, Despina 4/1/2017-3/31/2022 1.20 calendar
NIH
Program Official: Kimery Griffin
Digital breast tomosynthesis imaging biomarkers for breast cancer risk estimation
No overlap. The improved clinical performance achieved with digital breast tomosynthesis is currently fueling a broad adaptation of tomosynthesis for general population breast cancer screening. Our study will be the first to evaluate tomosynthesis imaging measures in breast cancer risk assessment and will develop the necessary technology to enable larger multi-center studies. Ultimately, these novel imaging biomarkers may lead to more accurate individualized risk stratification, improving personalized breast cancer screening and prevention.

1R01CA207084 (NIH) Vachon, Celine 4/1/2017-3/31/2022 0.48 calendar
Mayo Clinic (Subcontract)
Program Official: Tawana McKeither
Radiomic phenotypes of breast parenchyma and association with breast cancer risk and detection
No overlap. The main goals of this study are to characterize ‘intrinsic’ parenchymal complexity features reflecting the heterogeneity of breast tissue, to examine the association of ‘intrinsic’ parenchymal complexity features with breast cancer risk and to examine the contribution of parenchymal complexity features to masking cancers.

<u>OVERLAP:</u> There is no scientific or budgetary overlap between active research grants and DoD grant W81XWH-18-1-0082.

Despina Kontos, Ph.D. – Active Grant Support:

R33CA225310	Mankoff, David	9/1/17-8/31/21 (NCE)	0.0 calendar
NIH		DC (over 3 years)	

Program Official: Justin Birken
Area B: Multi-Tracer Volumetric PET (MTV-PET) to Measure Tumor Glutamine and Glucose Metabolic Rates in a Single Imaging Session
No overlap. We will take advantage of recent developments in volumetric positron emission tomography (PET) scanners, fast reconstruction, and 4D image analysis to develop methods for multi-tracer PET with the goal of generating quantitative, multi-parametric whole-body images of specific aspects of cancer biology, including cancer metabolism as the focus of our proposed technology development projects. Successful completion of our proposed technology development will yield a clinically practical method for multi-tracer PET that would provide multi-valent, whole-body molecular parametric images that would change the landscape for cancer imaging diagnostic biomarkers and precision oncology.

U24CA189523	Davatzikos/Kontos	9/1/2015-8/31/2021	0.0 calendar
NIH		(NCE)	

Program Official: Mutema Nyankale
Cancer imaging phenomics software suite: application to brain and breast cancer
No overlap. This project will develop advanced computer analysis methodology for interpretation of radiologic images of cancer, emphasizing brain and breast cancer. The functionality of the software will substantially transcend limitations of current analysis of cancer images, and will open the way for more precise and effective surgical planning as well as for more specific diagnosis of cancer based on its imaging characteristics, eventually leading to individualized medicine.

W81XWH-18-1-0082	Acciavatti, Raymond	3/15/2018-3/14/2022	0.12 calendar
Department of Defense Breast Cancer Research Program Breakthrough Award (Level 1)		(NCE)	

Science Officer: Laurie Shuman-Moss
Design of a 3D Mammography System in the Age of Personalized Medicine.
This grant proposes a personalized acquisition geometry for 3D mammography, as well as additional design changes that offer improvements in super-resolution.

R01-CA161749	Kontos, Despina	4/1/2017-3/31/2022	2.16 calendar
NIH			

Program Official: Kimery Griffin
Digital breast tomosynthesis imaging biomarkers for breast cancer risk estimation
No overlap. The improved clinical performance achieved with digital breast tomosynthesis is currently fueling a broad adaptation of tomosynthesis for general population breast cancer screening. Our study will be the first to evaluate tomosynthesis imaging measures in breast cancer risk assessment and will develop the necessary technology to enable larger multi-center studies. Ultimately, these novel imaging biomarkers may lead to more accurate individualized risk stratification, improving personalized breast cancer screening and prevention.

R01CA197000 Kontos, Despina 4/19/2016-3/31/2022 1.32 calendar
NIH (NCE)
Program Official: Kimery Griffin
Multi-parametric 4-D Imaging Biomarkers for Neoadjuvant Treatment Response
No overlap. Pattern analysis and machine learning methods are powerful knowledge discovery tools that can be very effective in identifying complex multi-parametric patterns from a diverse set of imaging and non-imaging biomarkers that can best predict treatment response and outcome. Our method will leverage the richness of available data to point to new imaging biomarkers that are better early predictors of response, enabling personalized treatment decisions for women undergoing neoadjuvant chemotherapy for breast cancer.

1R01CA207084 Vachon, Celine 4/1/2017-3/31/2022 2.76 calendar
Mayo Clinic (Subcontract)
Program Official: Tawana McKeither
Radiomic phenotypes of breast parenchyma and association with breast cancer risk and detection
No overlap. The main goals of this study are to characterize ‘intrinsic’ parenchymal complexity features reflecting the heterogeneity of breast tissue, to examine the association of ‘intrinsic’ parenchymal complexity features with breast cancer risk and to examine the contribution of parenchymal complexity features to masking cancers.

1R01CA223816 Kontos/Chodosh 4/1/2018-3/31/2023 1.5 calendar
NIH
Program Official: Kimery Griffin
Radiogenomic Biomarkers of Breast Cancer Recurrence
No overlap. We propose to analyze imaging features of phenotypic tumor heterogeneity that will provide information to complement histopathologic and molecular markers, enhancing our prognostic ability for breast cancer. Ultimately, integrating imaging with novel molecular tumor markers could enable more informed, precision-medicine, treatment decisions to reduce unnecessary side-effects while improving long-term outcomes for women diagnosed with breast cancer.

UM1CA221939 Ritzwoller/Doubeni 4/15/2018-3/31/2023 0.84 calendar
NCI
Program Official: Priyanga Tuovinen
Center for Research to Optimize Precision Lung Cancer Screening in Diverse Populations
No overlap. The goal of this Center is to build a comprehensive data ecosystem of the entire lung cancer screening process and to assess associated multilevel factors to conduct high impact multilevel studies including interventions to address gaps in care that may lead to lung cancer health disparities in the PROSPR initiative.
Role: Project leader.

R01CA237129 Kontos 9/1/2019-8/31/2024 cal 0.6
UNC subcontract
Program Official: Kimery Griffin
Understanding the biological basis for the association between parenchymal texture features and breast cancer risk
No overlap. The goals of this study are to identify parenchymal texture features associated with breast cancer risk in general population of women participating in screening mammography and, for those features associated with breast cancer risk, to evaluate (1) associations with endogenous estrogens and (2) associations with benign breast histologic features.

R01CA236468 NIH	Chen, Jinbo	9/15/2019-6/30/2023 total direct costs (over three years)	0.96 cal

Program Official: Huann-Sheng Chen
Data and Information Integration for Risk Prediction in the Era of Big Data
No overlap. Toward precision medicine and precision disease prevention, the over-arching goal of this proposal is to develop innovative statistical methods for accurate risk prediction. We address three challenges that plague studies on the value of new predictors that adds to standard predictors for improving predictive accuracy: lack of independent validation data, lack of statistical methods for developing risk prediction models using individually-matched case-control data, and lack of statistical methods to guide study design beyond standard power calculation for testing predictor-outcome association.
Role: Co-Investigator

OVERLAP: There is no scientific or budgetary overlap between active research grants and DoD grant W81XWH-18-1-0082.

Andrew Maidment, Ph.D. – Active Grant Support:

W81XWH-18-1-0082 Acciavatti, Raymond 3/15/2018-3/14/2022 (NCE) 0.24 calendar
Department of Defense Breast Cancer Research Program Breakthrough Award (Level 1)
Science Officer: Laurie Shuman-Moss
Design of a 3D Mammography System in the Age of Personalized Medicine.
This grant proposes a personalized acquisition geometry for 3D mammography, as well as additional design changes that offer improvements in super-resolution.

R01CA227142 Cormode, David 5/1/2018-4/30/2023 1.0 calendar
NIH
Program Official: Peter Ogunbiyi
Nanoparticle contrast agents for earlier breast cancer detection.
No overlap. The objective of this project is to develop polyphosphazene nanoparticles containing silver alloy contrast agents to enhance the efficacy of dual energy mammography for tumor detection.

R01CA161749 Kontos, Despina 4/1/2017-3/31/2022 0.24 calendar
NIH
Program Official: Houston Baker
Digital breast tomosynthesis imaging biomarkers for breast cancer risk estimation
No overlap. The improved clinical performance achieved with digital breast tomosynthesis is currently fueling a broad adaptation of tomosynthesis for general population breast cancer screening. Our study will be the first to evaluate tomosynthesis imaging measures in breast cancer risk assessment and will develop the necessary technology to enable larger multi-center studies. Ultimately, these novel imaging biomarkers may lead to more accurate individualized risk stratification, improving personalized breast cancer screening and prevention.

IRSA 1016451 Maidment, Andrew 9/1/2016-8/31/2021 1.2 calendar
Burroughs Wellcome Fund
Contact: Rusty Kelley
ViCTRE – Virtual Clinical Trials in the Regulatory Environment.
No overlap. We propose ViCTRE as a cost-effective and timely alternative to the current regulatory process. This vision is not fanciful; the elements of our proposed VCT pipeline are mature. VCTs are already commonly used in the design and development of imaging devices by academia and industry.

R01CA196528 Surti, Suleman 4/1/2016-3/31/2022 0.84 calendar
NIH
Program Official: Houston Baker
High Performance, Quantitative Breast PET Scanner Integrated with Tomosynthesis
No overlap. A dedicated breast PET-DBT scanner provides higher resolution and sensitivity compared to a wholebody PET/CT scanner, and hence quantitative images from such a device can play a significant role in providing personalized therapy for patients diagnosed with breast cancer. In this project we develop such a device in an integrated multi-modality design, and subsequently evaluate its clinical performance in patients for ER+ tumor characterization and diagnostic imaging of patients with dense breasts.

R01CA207084 (NIH) Vachon, Celine 4/1/2017-3/31/2022 0.36 calendar
Mayo Clinic (Subcontract)
Program Official: Tawana McKeither
Radiomic phenotypes of breast parenchyma and association with breast cancer risk and detection
No overlap. The main goals of this study are to characterize 'intrinsic' parenchymal complexity features reflecting the heterogeneity of breast tissue, to examine the association of 'intrinsic' parenchymal complexity features with breast cancer risk and to examine the contribution of parenchymal complexity features to masking cancers.

T32EB009384 Gee, Maidment, Ives 8/1/2009-7/31/2024 0.0 calendar
NIH
Training Program in Biomedical Imaging and Informational Sciences
No overlap. A PhD training program with a focus on medical imaging.

<u>OVERLAP:</u> There is no scientific or budgetary overlap between active research grants and DoD grant W81XWH-18-1-0082.

7.C. What other organizations were involved as partners?

Nothing to report.

8. SPECIAL REPORTING REQUIREMENTS.

8.A. Collaborative Awards

Nothing to report.

8.B. Quad Charts

Nothing to report.

REFERENCES

1. Sechopoulos I. A review of breast tomosynthesis. Part I. The image acquisition process. *Medical Physics.* 2013;40(1):014301-014301 to 014301-014312.

2. Sechopoulos I. A review of breast tomosynthesis. Part II. Image reconstruction, processing and analysis, and advanced applications. *Medical Physics.* 2013;40(1):014302-014301 to 014302-014317.

3. Conant EF, Zuckerman SP, McDonald ES, et al. Five Consecutive Years of Screening with Digital Breast Tomosynthesis: Outcomes by Screening Year and Round. *Radiology.* 2020;295(2):285-293.

4. Friedewald SM, Rafferty EA, Rose SL, et al. Breast Cancer Screening Using Tomosynthesis in Combination With Digital Mammography. *Journal of the American Medical Association.* 2014;311(24):2499-2507.

5. Acciavatti RJ, Barufaldi B, Vent TL, Wileyto EP, Maidment ADA. Personalization of X-Ray Tube Motion in Digital Breast Tomosynthesis Using Virtual Defrise Phantoms. Paper presented at: SPIE Medical Imaging2019; San Diego, CA.

6. Barufaldi B, Vent TL, Acciavatti RJ, Bakic PR, Noel PB, Maidment ADA. MRMC ROC Analysis of Calcification Detection in Tomosynthesis Using Computed Super Resolution and Virtual Clinical Trials. Paper presented at: 15th International Workshop on Breast Imaging2020.

7. Wanders JOP, Holland K, Veldhuis WB, et al. Volumetric breast density affects performance of digital screening mammography. *Breast Cancer Res Treat.* 2017;162:95-103.

8. Wanders JOP, Holland K, Karssemeijer N, et al. The effect of volumetric breast density on the risk of screen-detected and interval breast cancers: a cohort study. *Breast Cancer Research.* 2017;19(67):1-13.

9. Boyd NF, Guo H, Martin LJ, et al. Mammographic Density and the Risk and Detection of Breast Cancer. *New England Journal of Medicine.* 2007;356(3):227-236.

10. Maidment ADA. Virtual Clinical Trials for the Assessment of Novel Breast Screening Modalities. *Lecture Notes in Computer Science.* 2014;8539:1-8.

11. Lanyi M. Chapter 7: Differential Diagnosis of Microcalcifications. *Diagnosis and Differential Diagnosis of Breast Calcifications*. Berlin: Springer-Verlag; 1988:193-231.

12. Lanyi M. Chapter 4: Calcifications Within the Lobular and Ductal System of the Breast. *Diagnosis and Differential Diagnosis of Breast Calcifications*. Berlin: Springer-Verlag; 1988:29-143.

13. Rafferty EA, Park JM, Philpotts LE, et al. Assessing Radiologist Performance Using Combined Digital Mammography and Breast Tomosynthesis Compared with Digital Mammography Alone: Results of a Multicenter, Multireader Trial. *Radiology.* 2013;266(1):104-113.

14. Acciavatti RJ, Maidment ADA. Investigating the Potential for Super-Resolution in Digital Breast Tomosynthesis. Paper presented at: SPIE Medical Imaging2011; Lake Buena Vista, FL.

15. Acciavatti RJ, Maidment ADA. Observation of super-resolution in digital breast tomosynthesis. *Medical Physics.* 2012;39(12):7518-7539.

16. Acciavatti RJ, Maidment ADA. Proposing an Acquisition Geometry That Optimizes Super-Resolution in Digital Breast Tomosynthesis. *Lecture Notes in Computer Science.* 2012;7361:386-393.

17. Acciavatti RJ, Mein SB, Maidment ADA. Investigating Oblique Reconstructions with Super-Resolution in Digital Breast Tomosynthesis. *Lecture Notes in Computer Science.* 2012;7361:737-744.

18. Acciavatti RJ, Maidment ADA. Oblique reconstructions in tomosynthesis: II. Super-resolution. *Medical Physics.* 2013;40(11):111912-111911 to 111912-111919.

19. Acciavatti RJ, Wileyto EP, Maidment ADA. Modeling Acquisition Geometries with Improved Super-Resolution in Digital Breast Tomosynthesis. Paper presented at: SPIE Medical Imaging2016; San Diego, CA.

20. Vent TL, Acciavatti RJ, Maidment ADA. Development and Evaluation of the Fourier Spectral Distortion Metric. *IEEE Transactions on Medical Imaging.* 2021;40(3):1055-1064.

21. Eben JE, Vent TL, Choi CJ, et al. Development of a Next Generation Tomosynthesis System. Paper presented at: SPIE Medical Imaging2018; Houston, TX.

22. Kuo J, Ringer PA, Fallows SG, Bakic PR, Maidment ADA, Ng S. Dynamic Reconstruction and Rendering of 3D Tomosynthesis Images. Paper presented at: SPIE Medical Imaging2011; Lake Buena Vista, FL.

23. Acciavatti RJ, Vent TL, Barufaldi B, Wileyto EP, Noel PB, Maidment ADA. Proposing Rapid Source Pulsing for Improved Super-Resolution in Digital Breast Tomosynthesis. Paper presented at: Medical Imaging 2020: Physics of Medical Imaging2020; Houston, TX.

24. Acciavatti RJ, Vent TL, Barufaldi B, Wileyto EP, Noel PB, Maidment ADA. Super-Resolution in Digital Breast Tomosynthesis: Limitations of the Conventional System Design and Strategies for Optimization. Paper presented at: 15th International Workshop on Breast Imaging2020.

25. Martin DA, Vent TL, Choi CJ, Barufaldi B, Acciavatti RJ, Maidment ADA. Signal-to-Noise Ratio and Contrast-to-Noise Ratio Measurements for Next Generation Tomosynthesis. Paper presented at: SPIE Medical Imaging2021; Conference Held Virtually Due to COVID-19 Pandemic.

26. Choi CJ, Vent TL, Acciavatti RJ, Maidment ADA. Analysis of Digital Breast Tomosynthesis Acquisition Geometries in Sampling Fourier Space. Paper presented at: SPIE Medical Imaging2021; Conference Held Virtually Due to COVID-19 Pandemic.

27. Acciavatti RJ, Rodriguez-Ruiz A, Vent TL, et al. Analysis of Volume Overestimation Artifacts in the Breast Outline Segmentation in Tomosynthesis. Paper presented at: SPIE Medical Imaging2018; Houston, TX.

28. Vent TL, Barufaldi B, Acciavatti RJ, Krishnamoorthy S, Surti S, Maidment ADA. Next generation tomosynthesis image acquisition optimization for dedicated PET-DBT attenuation corrections. Paper presented at: SPIE Medical Imaging2021; Conference Held Virtually Due to COVID-19 Pandemic.

9. APPENDICES

1. Vent TL, Acciavatti RJ, Maidment ADA. Development and Evaluation of the Fourier Spectral Distortion Metric. IEEE Transactions on Medical Imaging, vol. 40, no. 3, pp. 1055-1064. *This paper was published in March of 2021.*
2. Acciavatti RJ, Vent TL, Barufaldi B, Wileyto EP, Noël PB, Maidment ADA. Super-Resolution in Digital Breast Tomosynthesis: Limitations of the Conventional System Design and Strategies for Optimization. In: Bosmans H, Marshall N, Van Ongeval C, editors; 15th International Workshop on Breast Imaging; 2020; Virtual Conference (held during COVID-19 Pandemic): SPIE; 2020. p. 115130V-1 - 115130V-9. *This paper was published in May of 2020. The PI (Raymond Acciavatti) gave a "virtual" presentation at this conference.*
3. Acciavatti RJ, Cohen EA, Maghsoudi OH, Gastounioti A, Pantalone L, Hsieh M-K, Barufaldi B, Bakic PR, Chen J, Conant EF, Kontos D, Maidment ADA. Calculation of Radiomic Features to Validate the Textural Realism of Physical Anthropomorphic Phantoms for Digital Mammography. In: Bosmans H, Marshall N, Van Ongeval C, editors; 15th International Workshop on Breast Imaging; 2020; Virtual Conference (held during COVID-19 Pandemic): SPIE; 2020. p. 1151309-1 - 1151309-7. *This paper was published in May of 2020. The PI (Raymond Acciavatti) gave a "virtual" presentation at this conference.*
4. Barufaldi B, Vent TL, Acciavatti RJ, Bakic PR, Noël PB, Maidment ADA. MRMC ROC Analysis of Calcification Detection in Tomosynthesis Using Computed Super Resolution and Virtual Clinical Trials. In: Bosmans H, Marshall N, Van Ongeval C, editors; 15th International Workshop on Breast Imaging; 2020; Virtual Conference (held during COVID-19 Pandemic): SPIE; 2020. p. 1151313-1 - 1151313-7. *This paper was published in May of 2020. The first author (Bruno Barufaldi) gave a "virtual" presentation at this conference.*
5. Vent TL, Barufaldi B, Acciavatti RJ, Maidment ADA. Simulation of high-resolution test objects using non isocentric acquisition geometries in next-generation digital tomosynthesis. In: Bosmans H, Marshall N, Van Ongeval C, editors; 15th International Workshop on Breast Imaging; 2020; Virtual Conference (held during COVID-19 Pandemic): SPIE; 2020. p. 1151317-1 - 1151317-8. *This paper was published in May of 2020. The first author (Trevor Vent) gave a "virtual" presentation at this conference.*
6. Acciavatti *et al*. Detector Motion Design for Next-Generation Digital Breast Tomosynthesis. This paper is being prepared for submission to a journal.
7. Acciavatti RJ, Vent TL, Choi CJ, Wileyto EP, Noël PB, Maidment ADA. Development of Magnification Tomosynthesis for Superior Resolution in Diagnostic Mammography. In: Bosmans H, Zhao W, Yu L, editors; Physics of Medical Imaging; 2021 (virtual conference held during COVID-19 Pandemic): SPIE; 2021. p. 115951J 1 - 115951J-7. *This conference paper was published in February 2021. The PI (Raymond Acciavatti) gave a "virtual" presentation.*
8. Vent TL, Barufaldi B, Acciavatti RJ, Krishnamoorthy S, Surti S, Maidment ADA. Next generation tomosynthesis image acquisition optimization for dedicated PET-DBT attenuation corrections. In: Bosmans H, Zhao W, Yu L, editors; Physics of Medical Imaging; 2021 (virtual conference held during COVID-19 Pandemic): SPIE; 2021. p. 115954V-1 - 115954V-7. *This conference paper was published in February 2021. The first author (Trevor Vent) gave a "virtual" poster presentation.*
9. Choi CJ, Vent TL, Acciavatti RJ, Maidment ADA. Analysis of Digital Breast Tomosynthesis Acquisition Geometries in Sampling Fourier Space. In: Bosmans H, Zhao W, Yu L, editors; Physics of Medical Imaging; 2021 (virtual conference held during COVID-19 Pandemic): SPIE; 2021. p. 115954W-1 - 115954W-10. *This conference paper was published in February 2021. The first author (Chloe Choi) gave a "virtual" poster presentation.*

10. Martin DA, Vent TL, Choi CJ, Barufaldi B, Acciavatti RJ, Maidment ADA. Signal-to-Noise Ratio and Contrast-to-Noise Ratio Measurements for Next Generation Tomosynthesis. In: Bosmans H, Zhao W, Yu L, editors; Physics of Medical Imaging; 2021 (virtual conference held during COVID-19 Pandemic): SPIE; 2021. p. 115951L-1 - 115951L-9. *This conference paper was published in February 2021. The first author (David Martin) gave a "virtual" presentation.*
11. Award Chart summarizing progress made in Years 1-3 of the grant.

Development and Evaluation of the Fourier Spectral Distortion Metric

Trevor Lewis Vent, *Graduate Student Member, IEEE*, Raymond Joseph Acciavatti,
and Andrew D. A. Maidment, *Senior Member, IEEE*

***Abstract*— A spatial resolution metric is presented for tomosynthesis. The Fourier spectral distortion metric (FSD) was developed to evaluate specific resolution properties of different imaging techniques for digital tomosynthesis using a star pattern image to plot modulation in the frequency domain. The FSD samples the spatial resolution of a star-pattern image tangentially over an acute angle and for a range of spatial frequencies in a 2D image or 3D image reconstruction slice. The FSD graph portrays all frequencies present in a star pattern quadrant. In addition to the fundamental input frequency of the star pattern, the FSD graph shows spectral leakage, square wave harmonics, and residual noise. The contrast transfer function (CTF) is obtained using the FSD graph. The CTF is analogous to the modulation transfer function (MTF), but it is not normalized to unity at zero spatial frequency. Unlike the MTF, this metric separates the fundamental input-frequency from the other signals in the Fourier domain. This metric helps determine optimal image reconstruction parameters, the in-plane limit of spatial resolution with respect to aliased signals, and a threshold criterion for an image to support super resolution and reduce aliasing artifacts. Various sampling parameters were evaluated to optimize this metric and ascertain measurement accuracy. The FSD adequately compares resolution properties of 2D images and 3D image reconstruction slices for various x ray imaging modes without suppressing aliased signals.**

***Index Terms*— Aliasing, contrast transfer function, digital breast tomosynthesis, Fourier spectral distortion metric, modulation transfer function, spectral leakage, super resolution.**

I. INTRODUCTION

DIGITAL breast tomosynthesis (DBT) systems acquire multiple two-dimensional (2D) x-ray projections over a range of angles. The collected projections are used to reconstruct a three-dimensional (3D) image. Various DBT systems are available for screening mammography, and each system is constructed with different x-ray components and a distinct mechanical design and geometric configuration. These systems vary in terms of the number of projections and angular range. In-plane spatial-resolving capabilities of digital tomosynthesis systems are limited most commonly by the detector element spacing (d_{el}) or by the sampling aperture (λ) used for 3D image reconstruction. The variation in the mechanical design and acquisition techniques of these systems necessitates a spatial resolution metric that is specific to differences in tomosynthesis design and implementation.

The preferred method for evaluating spatial resolution of x-ray imaging devices is the pre-sampled modulation transfer function (MTF). The importance of measuring both the 3D MTF and the in-plane MTF for tomosynthesis was presented by Zhao *et al* [1]. IEC 62220-1 outlines a method to measure the MTF of x-ray systems using the slanted edge [2], and AAPM TG-245 proposes an alternative approach by using a tilted tungsten wire. Both of these methods suppress aliasing through super-sampling. We sought a resolution metric that would reveal evidence of aliasing.

The MTF has proven reliable for 2D imaging modalities such as conventional radiography and mammography, but the spatial resolution properties of tomosynthesis image reconstruction slices exhibit behavior atypical of 2D x-ray images. Spatial resolution is generally isotropic for 2D projection images and anisotropic for tomosynthesis reconstruction slices (Fig. 1). For tomosynthesis image reconstructions, the frequencies aligned parallel with x-ray source motion ($\sigma_{\parallel}$) are favored by super-resolution, whereas the frequencies aligned perpendicular to x-ray source motion ($\sigma_{\perp}$) are prone to aliasing (manifest as Moiré patterns in Fig. 1) [3]–[6]. The pre-sampled MTF will typically show modulation up to the sampling frequency and will be in close agreement for both frequency orientations (as shown in Fig. 14 of this work) [7]; ostensibly however, this behavior is not reflected in the tomosynthesis image reconstruction slice due to aliasing.

Although the spatial-resolving capabilities of digital x-ray detectors are limited by the aliasing frequency (ξ), the pre-sampled MTF measures modulation up to f_N for detectors that have an active area of 100%. ξ is given by one half of the first zero of the Fourier transform of the system's d_{el}. The Fourier transform of an aperture is a sinc function, where f_N is the first zero of the sinc function ($f_N = 1/d_{el}$) and the alias frequency relates to d_{el} by:

$$\xi(d_{el}) = \frac{0.5}{d_{el}} \tag{1}$$

Manuscript received October 30, 2020; revised December 10, 2020; accepted December 13, 2020. Date of publication December 16, 2020; date of current version March 2, 2021. This work was supported in part by the Department of Defense Breast Cancer Research Program under Grant W81XWH-18-1-0082, in part by the Burroughs Welcome Fund under Grant IRSA 1016451, in part by the National Institute of Health under Grant 1R01CA196528, and in part by Susan G. Komen under Grant IIR13264610. *(Corresponding author: Trevor L. Vent.)*

Trevor Lewis Vent is with the Department of Bioengineering, University of Pennsylvania, Philadelphia, PA 19104 USA (e-mail: tvent@seas.upenn.edu).

Raymond Joseph Acciavatti and Andrew D. A. Maidment are with the Department of Radiology, University of Pennsylvania, Philadelphia, PA 19104 USA (e-mail: racci@pennmedicine.upenn.edu; andrew.maidment@pennmedicine.upenn.edu).

Digital Object Identifier 10.1109/TMI.2020.3045325

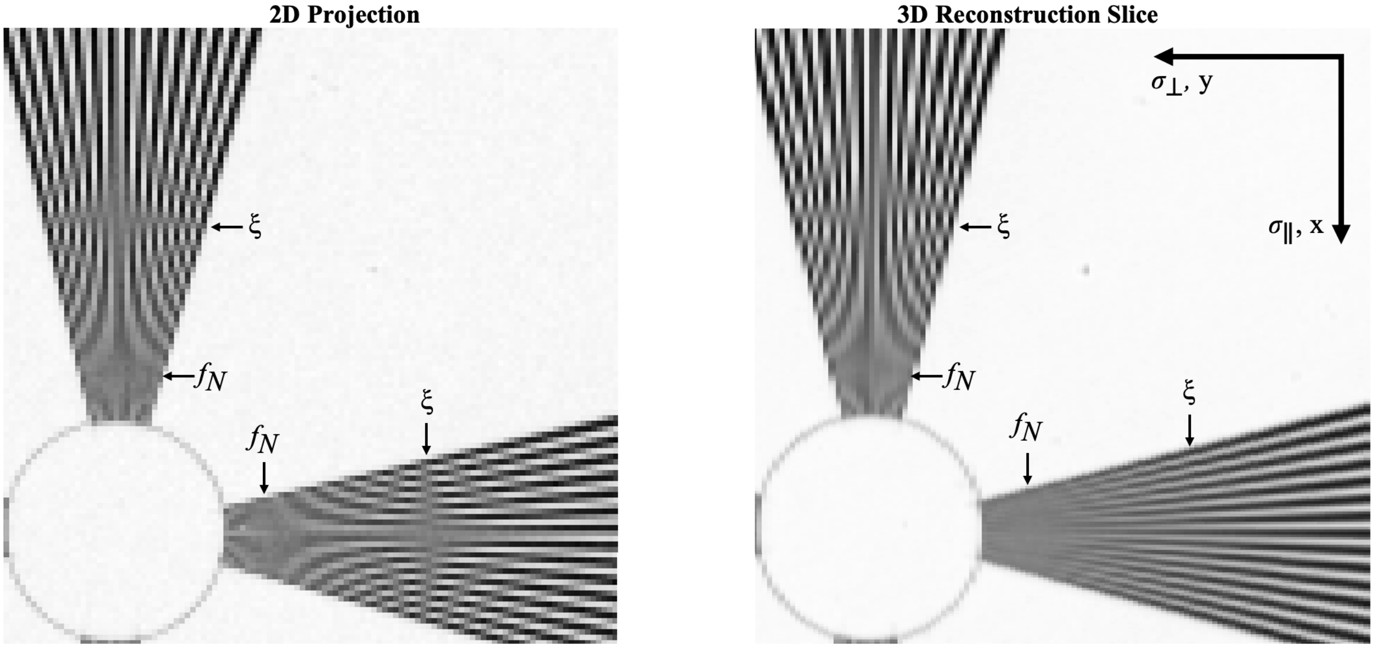

Fig. 1. The 2D projection image shows isotropic resolution and aliasing in both directions, whereas the 3D reconstruction slice shows anisotropic resolution with aliasing for $\sigma_\perp$ and super resolution for $\sigma_\parallel$.

Aliasing is predominant in 2D images for both frequency orientations, $\sigma_\parallel$ and $\sigma_\perp$, at any spatial frequency above ξ. It is important to consider the impact of aliasing on image quality to ensure that erroneous information for clinical readings is mitigated.

The prominence of aliasing in 3D image reconstructions is more nuanced, when compared with 2D images, and depends on sampling techniques, the orientation of the input object, and the acquisition geometry [8]. Two factors can give rise to aliasing in 3D image reconstructions; d_{el} and λ. The alias frequency of λ in 3D reconstruction slices can be determined by substituting λ for d_{el} in (1). In the Fourier domain, aliasing takes the form of *spectral leakage*, which is the misrepresentation of the input-frequency modulation at an incorrect, lower or higher response-frequency (the shaded regions in Fig. 2c). Aliasing dominates the input signal of these reconstructions because the magnitude of the spectral-leakage modulation is greater than the magnitude of the input-frequency modulation in the Fourier domain. A pre-sampled MTF calculation for any x-ray imaging device shows modulation for frequencies higher than ξ. This is evidence that super-resolution is achievable with proper sampling and reconstruction techniques [10]. However, the pre-sampled MTF will not show that the frequencies above ξ are dominated by aliasing.

In this work, we propose the Fourier spectral distortion metric (FSD) and the contrast transfer function (CTF) that evaluate spatial resolution for digital images without suppressing relevant information, such as aliasing. This metric can be applied to 2D digital images and 3D image reconstruction slices (for in-plane evaluation), where it is particularly useful for comparing differences in tomosynthesis acquisition. The FSD discerns aliasing by identifying signals of spectral leakage separate from fundamental input frequencies in the Fourier domain. Another goal of this study is to optimize the FSD for various sampling factors and imaging characteristics.

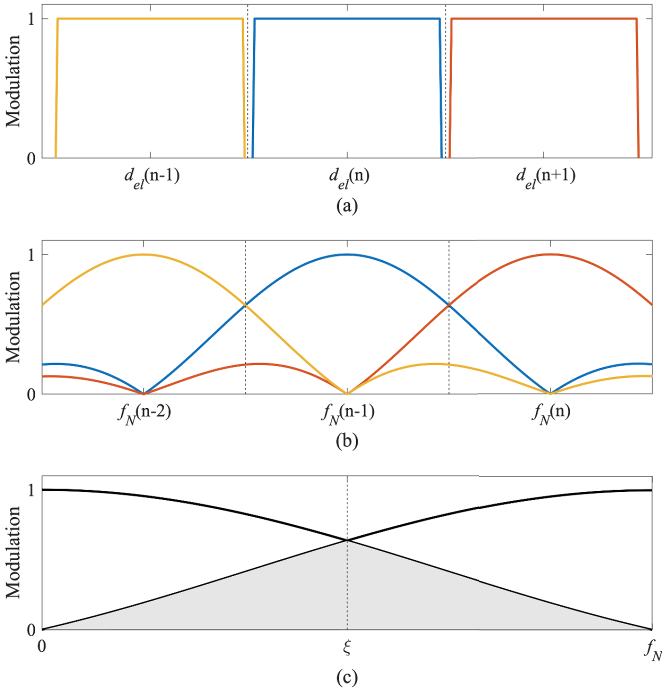

Fig. 2. A one-dimensional diagram of a digital detector aperture function for three detector aperture samples (a), the impulse responses of the three apertures (b), and an example of the aliased signals from d_{el}(n+1) reflected back into the impulse response function for half of one detector aperture, d_{el}(n) (c)

This metric is better suited to evaluating tomosynthesis image reconstructions by presenting data in a more useful format, capturing modulation contrast, and revealing aliased signals.

II. Materials & Method

A. Next Generation Tomosynthesis Prototype

The FSD was developed for characterizing our next generation tomosynthesis (NGT) prototype system. The NGT

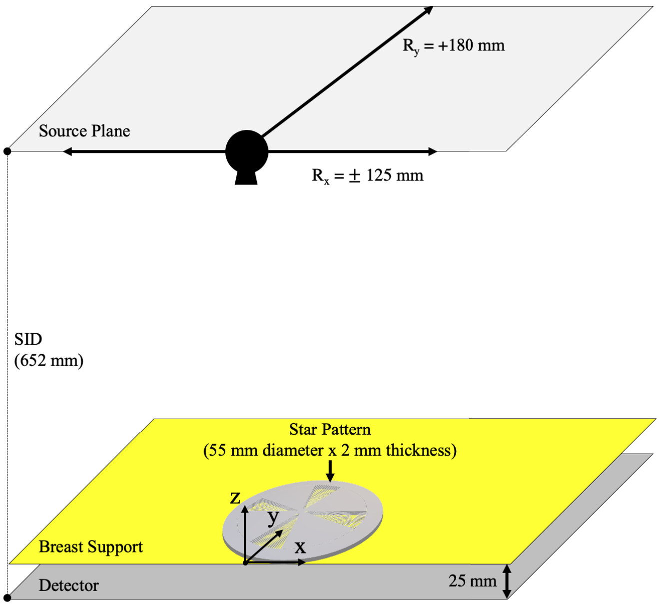

Fig. 3. The coordinate axes and the design geometry are defined for the NGT prototype. The Cartesian coordinate system defines the origin of the NGT system. It is located at the center of the of the detector along the chest-wall edge relative to the patient. The **x**-axis is parallel to the chest wall and is also parallel with $\sigma_{\parallel}$ for NGT-X.

system configuration is shown in Fig. 3. This prototype was developed to investigate novel acquisition geometries for DBT. Whereas a conventional DBT system scans linearly in one dimension, the NGT prototype positions the x-ray source at various locations within the source plane for a 3D acquisition, introducing x-ray source motion in the posteroanterior direction. This sampling technique enhances the sampled frequencies in the Fourier domain [8], [9]. The source-to-image distance (SID) for the NGT system is 652 mm. The range of motion for the x-ray tube is ±125 mm in **x** (R_x) and +180 mm in **y** (R_y). Given these ranges, the NGT prototype is capable of investigating myriad acquisition geometries [10]. For this work, we use a DBT acquisition geometry with source motion in the x-direction only (NGT-X) to introduce this metric.

B. Star Pattern Test Object

To obtain the CTF, we use the frequencies contained in one quadrant of a star-pattern test object as the fundamental input frequency (ν). The star pattern consists of four quadrants of 29 alternating lead and acrylic sectors at 1° spacings. Thus, the angular range of each quadrant is 29° (model 07-542). The sharpness of the edge on the lead foil is a square-wave input similar to a bar-pattern test object. The Fourier transform of a square-wave of input frequency, ω, and period of the star pattern quadrant, L, is a series of sinusoidal waves:

$$\mathrm{F}(\omega) = \frac{4}{\pi}\sum_{m=1}^{\infty} \sin\left(\frac{2\pi(2m-1)\omega \mathrm{L}}{2m-1}\right) \tag{2}$$

The fundamental frequency ($m = 1$) is the dominant frequency in an image reconstruction without aliasing. The finite size of the focal spot and the detector blur the signal of the angle at which thehigh frequencies, producing a sinusoidal response function (Fig. 4). As predicted by Coltman [11], square-wave harmonics are also present in image reconstructions at lower spatial frequencies of the star pattern.

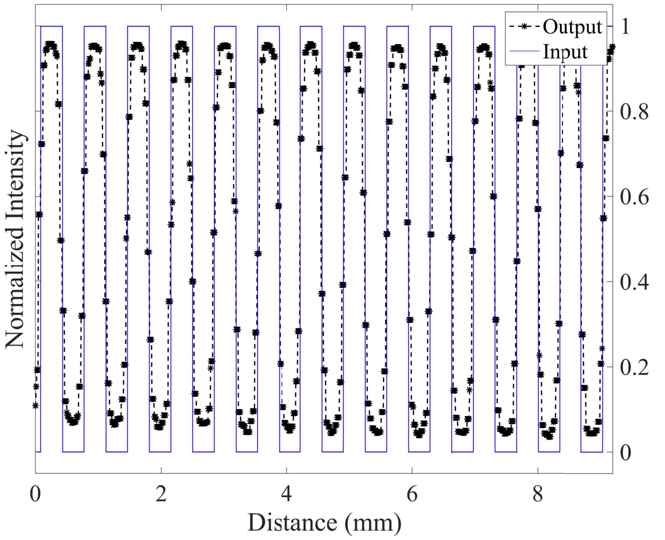

Fig. 4. The sine-wave response (Output) of the square wave (Input) at a resolution of 1.4 lp/mm in the image reconstruction of the star pattern [11].

C. Image Acquisition

Images of the star pattern were acquired on the NGT prototype using various techniques. We use the term, ϕ, to describe the angle of ν relative to the detector grid. The star pattern was positioned at the origin with a ϕ of 0° for all image acquisitions. NGT-X supports an angular range (15°) and projection-to-projection angular spacing (1°) that are similar to a commercial DBT system (Selenia Dimensions, Hologic, Marlborough, MA), but utilizes a step-and-shoot acquisition technique. Projection images from NGT-X were used in image reconstructions. NGT-X was repeated ten times by removing and repositioning the star pattern at the origin, with the same ϕ, between each acquisition. The central projection from each of the ten tomosynthesis acquisitions was used to obtain 2D data. Each projection image was acquired using 28 kV, 1.5 mAs, and 0.5 mm Aluminum filtration. The anode for this system is a tungsten alloy with a nominal focal spot size of 0.3 mm.

The projection images were reconstructed using commercial reconstruction software (Piccolo™; version 4.0.5; Real Time Tomography; Villanova, PA). This software can produce super-sampled reconstructed volumes with a λ of up to 10 times smaller than the detector aperture. The 3D images were reconstructed at 5 different λ values: 85.0 μm (1.0x), 56.7 μm (1.5x), 42.5 μm (2.0x), 37.0 μm (2.3x), and 28.3 μm (3.0x). The 3D images are reconstructed conventionally, with slices parallel to the **x-y** plane using simple back-projection. The exact depth of the reconstruction is arbitrary. Images were reconstructed with a slice spacing of 0.1 mm initially; but to achieve greater accuracy, we used 0.01 mm slice spacing compared with the 0.03 mm lead foil thickness of the star pattern. Either the slice of the in-focus star pattern (in-plane 3D) or individual projections (2D) are used as the 3D and 2D inputs to the FSD. A summary of the acquisitions and reconstruction techniques performed for this study is shown in Table I.

TABLE I
IMAGE ACQUISITION

Acquisition	Acquisition Geometry	Star Pattern Alignment (ϕ)	λ (µm)	Technique
a	NGT-X	0°	85.0 (1.0x)	28 kV 1.5 mAs 0.5 mm Al Filter
b			56.7 (1.5x)	
c			42.5 (2.0x)	
d			37.0 (2.3x)	
e			28.3 (3.0x)	

Images were obtained using the NGT prototype. The same technique was used for all acquisitions. The NGT-X acquisition geometry was repeated ten times and reconstructed at a λ of 42.5 µm for each acquisition to obtain average spectra. The ten 2D images were obtained from the central projection of each tomosynthesis acquisition.

D. Fourier Spectral Distortion Metric

The FSD is calculated using one quadrant of a star pattern image as an input to create a graph of modulation in the frequency domain. This graph is referred to as the Fourier spectral distortion (FSD) graph. The FSD graph is the normalized modulation of all frequencies contained within a quadrant of the star pattern.

The center of the star pattern is determined using an image of the star pattern. The center is calculated using the perpendicular bisectors of two secant lines created by choosing two intersections arbitrarily between the three points located along the profile of the outer circle of the star pattern image (Fig. 5), requiring user input. Then, starting at the radius (r) from the center of the star pattern to the inner ring ($r_{\min} \mathrel{\hat{=}}$ 16 lp/mm), the plot profile, $\psi_r(\delta\omega)$, is extracted tangentially along an arc for the quadrant of interest. The quadrants are named by the angle in radians relative to the center (0, $\pi/2$, π, and $3\pi/2$).

The 1D fast Fourier transform (FFT) is computed for this profile. The 1D FFT of $\psi_r(\delta\omega)$ computes the modulation of each frequency – aliased or not – within the quadrant. The radius is then incremented by one pixel and the process is repeated to the outer ring of the star pattern ($r_{\max} \mathrel{\hat{=}}$1.27 lp/mm). An example of one FFT calculation at a radius of 8 lp/mm is shown in Fig. 6 for $\sigma_{\parallel}$ and $\sigma_{\perp}$.

The waveform of each quadrant is sampled using Fourier interpolation with four increments at each r: 512, 1024, 1536, and 2048. These four conditions and oversampling factors, $\Gamma(r)$, for the range of frequencies of the star pattern are summarized in Table II. The value of Γ is determined by the number of samples (N) over the number of pixels per $\psi_r(\delta\omega)$ at $r_{\min}$ and $r_{\max}$ and a 37 μm λ by (3).

$$\Gamma(r) = \frac{N}{\text{pixels}/\psi_r(\omega)} \tag{3}$$

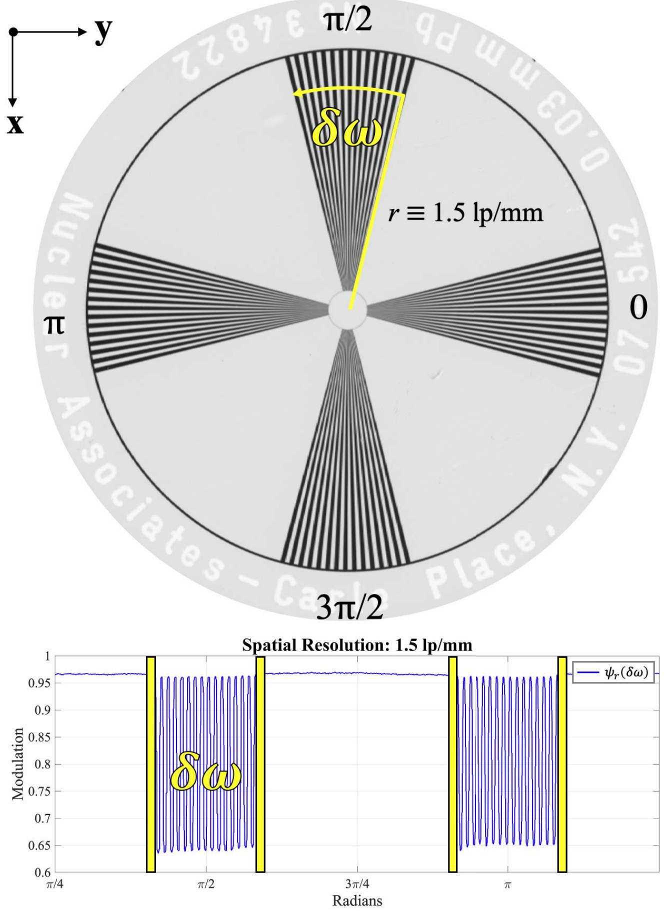

Fig. 5. The profile extraction of the 0-radian quadrant for f_y at a resolution of 1.5 lp/mm. $\delta\omega$ represents the range of the quadrant at all radii. The plot profile, $\psi_r(\delta\omega)$, is shown in blue and the quadrant is named by the angle of the unit circle in radians.

TABLE II
FSD SAMPLING FOR $\delta\omega$

Condition	SAMPLES (N)	Oversampling Factors, Γ(1.27 – 16 lp/mm)
A	512	1.6 – 22.3
B	1024	3.2 – 44.5
C	1536	4.8 – 89.0
D	2048	6.4 – 178.1

The four conditions of sampling used to determine optimal sampling rate for FSD calculations. The values of Γ correspond to a reconstructed pixel pitch of 37 µm. The oversampling factor increases with resolution, and the N is the same for each $\delta\omega$.

The angle at which the star pattern input frequencies are oriented across the reconstruction grid varies from one edge of the quadrant to the other. When $\phi = 0$, the largest angle of orientation for the frequencies is approximately 15° relative to the reconstruction grid (Fig. 7). For comparison, the MTF should be computed using an edge that is aligned between 2-3° (relative to the detector grid) with an ROI of at least 10 cm to achieve sufficient sampling [12]–[14]. The tangential sampling of the star pattern samples various orientations across the detector grid. This is shown by the various different vertical positions of the star points in Fig. 4.

The maximum modulation of ν is normalized to the value of the pre-sampled MTF at 1.27 lp/mm. The 1D FFT profiles are plotted as a function of star pattern frequency (lp/mm) and normalized frequency response (cycles/$\delta\omega$) to create the FSD graph (Fig. 8). The most prominent spine in the graph is the signal of the input frequency, located at 15 cycles per quadrant (cycles/$\delta\omega$), corresponding to the period of the star

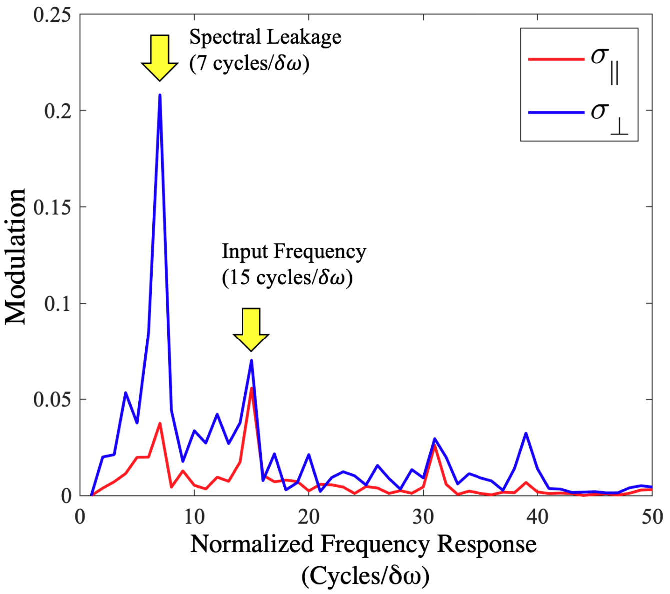

Fig. 6. Example of the 1D FFT at a radius which corresponds to a star pattern frequency of 8 lp/mm. The modulation of spectral leakage, occurring at a frequency response of 7 Cycles/$\delta\omega$, is well above that of the input frequency occurring at a frequency response of 15 Cycles/$\delta\omega$ for $\sigma_{\perp}$. This indicates aliasing at this star pattern frequency in the image. In contrast, the modulation of the input frequency for $\sigma_{||}$ is greater than that of spectral leakage, demonstrating super resolution.

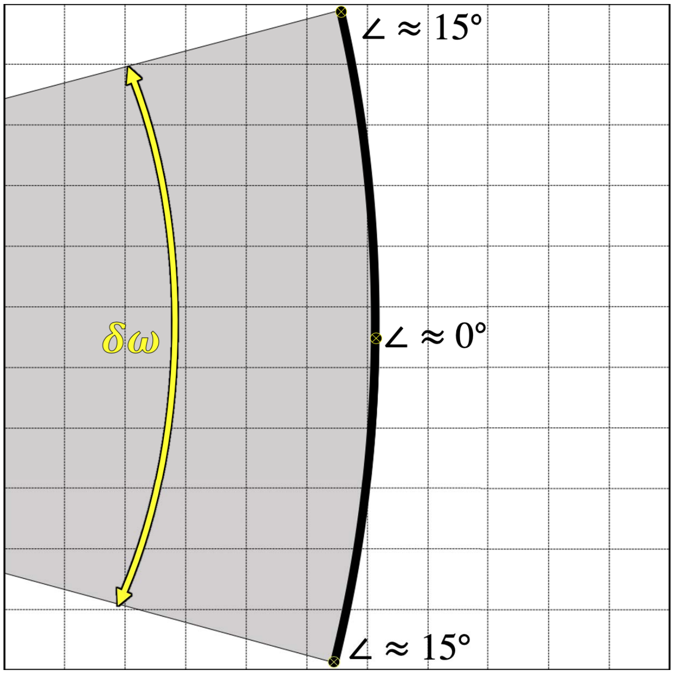

Fig. 7. Angular variation of the plot profile, with respect to the detector grid, over the range, $\delta\omega$.

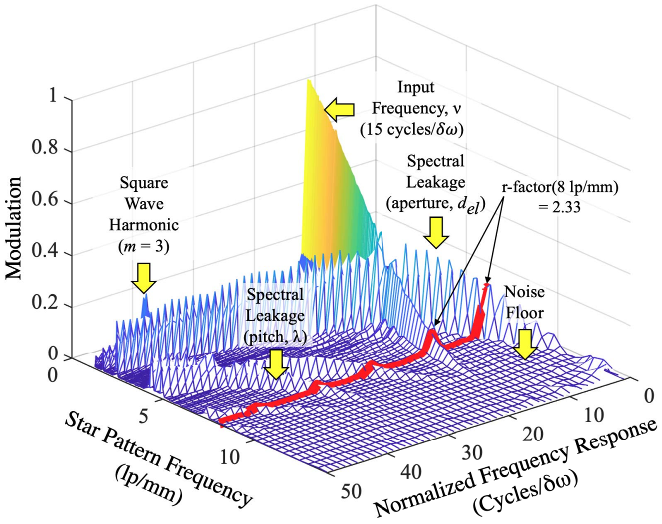

Fig. 8. An example of the FSD graph for $\sigma_{\perp}$ of a star pattern. The spine of ν occurs at a period of 15 Cycles/$\delta\omega$. This spine is the expected response signal from a single quadrant of the star pattern. The spine of spectral leakage intersects the fundamental frequency at a resolution of 5.88 lp/mm (ξ). The spine of the square wave harmonic for m = 3 occurs at 45 cycles/$\delta\omega$.

pattern input (e.g. reference the plot profile in Fig. 5). This arises because the angular spacing is independent of radius, and, hence, input frequency. Spectral leakage that arises from the sampling aperture is also prominent at various other cycles, creating a spine of frequencies that intersects ν at ξ. Spectral leakage that arises from λ creates a spine that intersects ν at $1/\lambda$. When present with a greater magnitude than the input frequencies, aliased signals dominate the input signals in image reconstructions. The least prominent spine in the plot occurs at 45 Cycles/$\delta\omega$ and represents the modulation for a square wave harmonic of the star pattern ($m = 3$). The input of the star pattern would produce an exact square wave response function if there were no intrinsic blurring of the system. The waveform is sinusoidal in the plot profile but maintains square-wave characteristics for resolutions lower than 2.5 lp/mm. This follows the findings of Coltman for the sine-wave response function given a square-wave input [11]. Image noise contributes to the rough texture observed in the other areas of the graph. The FSD graph produces a super-sampled Fourier transform of a quadrant in the star pattern. In contrast to the pre-sampled MTF, the FSD identifies aliasing as spectral leakage in digital x-ray images.

The r-factor described by Acciavatti [15] is used as the criterion for distinguishing super resolution from aliasing-dominated image reconstructions. It is important to note that the r-factor is typically computed for a sine-wave input. Although we start with a square-wave input, the FFT is performed, producing a sinewave decomposition of the frequencies in the image. This suggests that the r-factor can be determined using the frequency response computed by the FSD without performing the Coltman transform. If the peak of ν is greater than the value of the peak of spectral leakage at any resolution greater than ξ, the r-factor will be below a value of 1, indicating super resolution; otherwise, aliasing is predominant and super resolution is not achieved.

E. Contrast Transfer Function

The contrast transfer function (CTF) graph is the normalized modulation of ν, obtained from the FSD graph, as a function of resolution. The CTF corresponds to a square-wave response function calculated from the sine-wave response of the star pattern input [11]. The CTF can be used to discern the aliasing-dependent limit of spatial resolution (LSR) and is plotted against the pre-sampled MTF (Fig. 9).

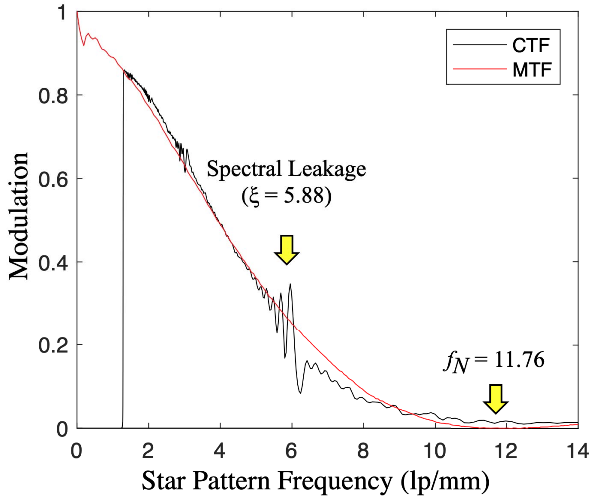

Fig. 9. The normalized modulation of the CTF and MTF are plotted as a function of spatial resolution. The distinction between the MTF and CTF is the characteristic oscillatory behavior of the CTF plot. These oscillations are a manifestation of spectral leakage.

The MTF calculation for this system was measured using the slanted edge method [8]. The slanted-edge method enforces a fixed phase shift of one line relative to another which suppresses spectral leakage through super-sampling and thus renders the MTF unable to discern aliasing. An example is the oscillatory behavior of the CTF graph in Fig. 9. The CTF is analogous to the MTF but is not normalized to unity at zero spatial frequency.

III. RESULTS

A. Evaluation of Sampling Rate for FSD

The FSD is computed at the four different sampling rates using the $\pi/2$-radian quadrant (f_y) for one image reconstruction slice from acquisition **a**. The differences in the FSD graph are indiscernible via visual inspection; thus, only the two spectra that show the greatest absolute differences are used as examples ($N = 512$ and 2048) in Fig. 10a-b. Also presented in Fig. 10c is a graph that shows the differences between the two examples. The maximum absolute difference at any point of the conditions tested is 0.018 (shown in Fig. 10). The average absolute difference is 0.001 (for all conditions tested, not shown in Fig. 10) compared with the 0.0017 average measurement error (95% confidence, assuming normality) across the entire spectrogram.

B. 2D FSD for NGT System

The FSD was computed for the ten 2D projection images using the central projection obtained from acquisition **c**. The range of Γ at this pixel size (85 μm) is approximately 6.4-178.1. Fig. 11 shows a single sample of the FSD graph for the 0-radian quadrant (f_x) as an example. The average spectra of the ten 2D projection images is shown for f_x (Fig. 12a) and for f_y (Fig. 12b). The spectral leakage of d_{el} intersects ν at ξ, and λ intersects at the sampling rate of the detector.

C. Evaluation of Reconstruction Sampling Pitch for FSD

The FSD is computed using images that are obtained from the five λ values of NGT-X described in Table I using acquisitions **a**-**e**. The five FSD and CTF graphs are summarized in Fig. 13 for each respective λ. The spectral leakage due to λ intersects ν at the resolution corresponding to the $1/\lambda$ for each graph. Similarly, residual spectral leakage is seen at the resolution corresponding to d_{el}.

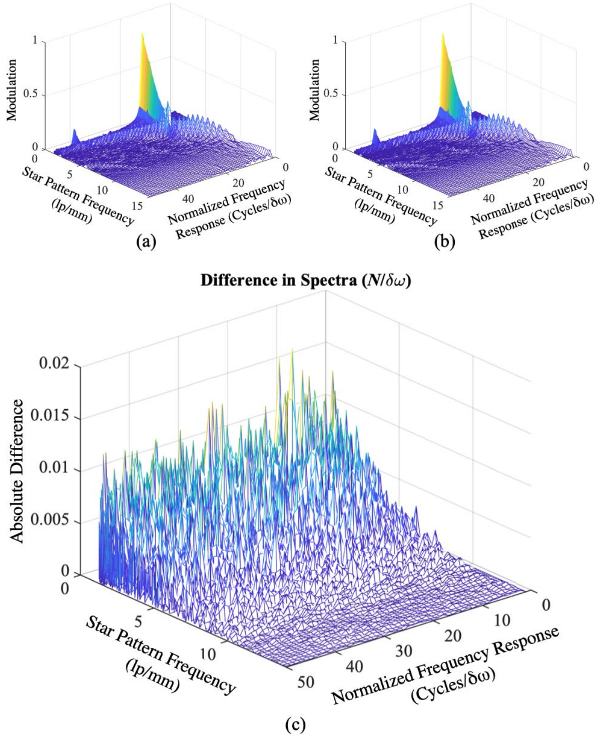

Fig. 10. Sampling rates: (a) 512, (b) 2048, and their difference (c) used to determine optimal sampling for the FSD.

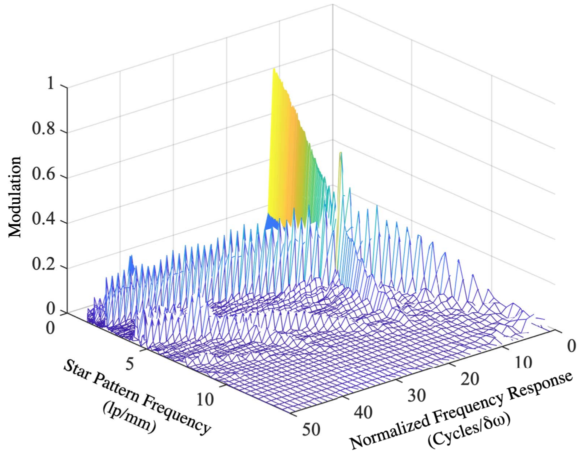

Fig. 11. FSD graph of a single 2D projection image.

D. Comparing f_x With f_y for NGT-X

The results for NGT-X are represented in Fig. 14a and Fig. 14b for the 0- and $\pi/2$-radian quadrants of the star pattern, respectively. Images for NGT-X are obtained from acquisition **c**; these graphs represent the average of the ten spectra. The average spectra are less noisy than the individual spectra realizations above, and the details within the FSD and CTF graphs are accentuated. For Fig. 14 (a and b): top left is the FSD graph, top right is a plot of the CTF and corresponding pre-sampled MTF, and the bottom are cropped images of the

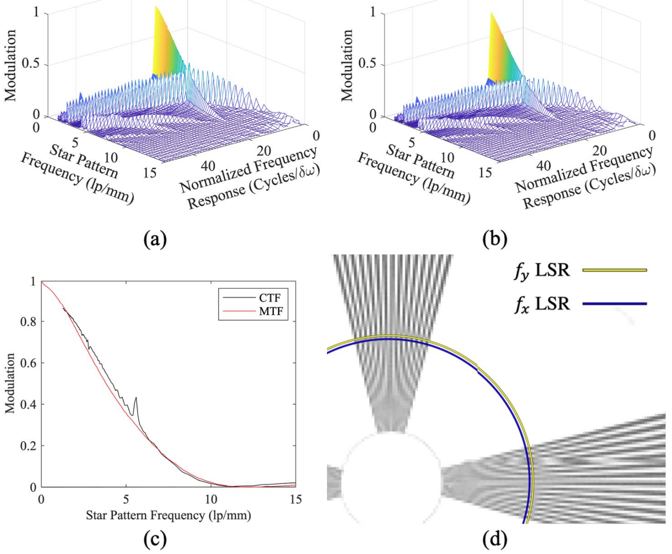

(a) (b) (c) (d)

Fig. 12. The results for the average 2D spectra include the FSD graphs for f_y (a), f_x (b), the CTF graph for f_y (c), and the image indicating the LSR for f_y and f_x (d) .

in-plane reconstructions for the quadrants being analyzed. The blue arcs in the images indicate the LSR, measured at 5% modulation in the presence of super resolution or near ξ if aliasing is predominant.

The 0-radian quadrant, f_x, of NGT-X shows evidence of super-resolution and residual aliasing artifacts. It is important to note that f_x is $\sigma_\parallel$ for NGT-X. The FSD graph (Fig. 14a, top left) shows the spine of ν, the spine of the square-wave harmonic, and spines of residual spectral leakage arising from ξ and d_{el}. The prominence of spectral leakage is diminished, and super-resolution is observed in the image reconstruction. The fundamental frequency is essentially the only frequency with significant modulation. As a result, the image reconstruction accurately portrays ν for modulation above ξ. The CTF (Fig. 14a, top right) is normalized at 1.27 lp/mm using the modulation of the MTF at the same star pattern frequency. Like the pre-sampled MTF, the CTF shows modulation up to the sampling frequency of the detector. The image in Fig. 14a shows the 0-radian quadrant of the reconstructed star pattern, and the blue line indicates the LSR measured at 5% modulation.

The $\pi/2$-radian quadrant contains f_y, which is $\sigma_\perp$ for NGT-X. The results for this orientation are represented in Fig. 14b. The FSD graph shows the same spines of ν and the square-wave harmonic as before; however, in contrast to f_x, spectral leakage is prominent for f_y. The spine of spectral leakage has higher modulation for frequencies above and below ξ (the intersection at ν). The CTF for f_y (Fig. 14b, top right) shows characteristic oscillatory behavior at the same location and is determined as the LSR, due to aliasing. The image for f_y shows Moiré patterns for frequencies above and below ξ. The oscillatory behavior in the CTF and the Moiré patterns in the image reconstructions repeat according to the detector's pixels (n), described by (4):

$$M(n) = \frac{\xi}{n} \tag{4}$$

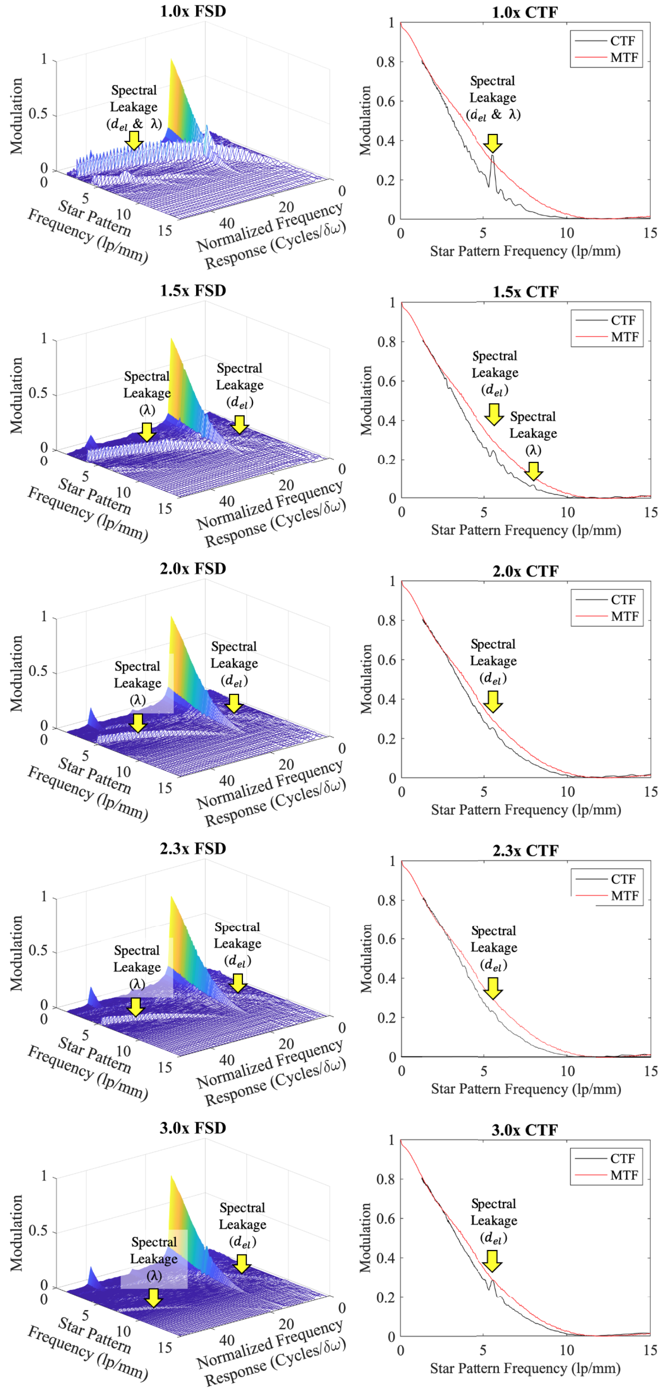

Fig. 13. Results for different reconstruction pitch values, λ. These graphs were created using f_x of NGT-X. The FSD (left column) and CTF vs. pre-sampled MTF (right column) graphs for the five λ values from Table I are shown. The two forms of spectral leakage, aperture (d_{el}) and pitch (λ) are indicated. Note that the aperture spectral leakage is only residual for f_x.

The repetition of the Moiré patterns and how they correspond to the FSD graph are depicted in Fig. 15 by viewing the FSD graph from an aerial perspective next to its corresponding quadrant in the image reconstruction. This figure portrays ν vertically from top to bottom. The spectral leakage appears as the diagonal ripples that intersect the fundamental frequency at three locations. This first occurs near 6 lp/mm, which is 1/2 cycles per pixel ($n = 1$). Residual peaks of spectral

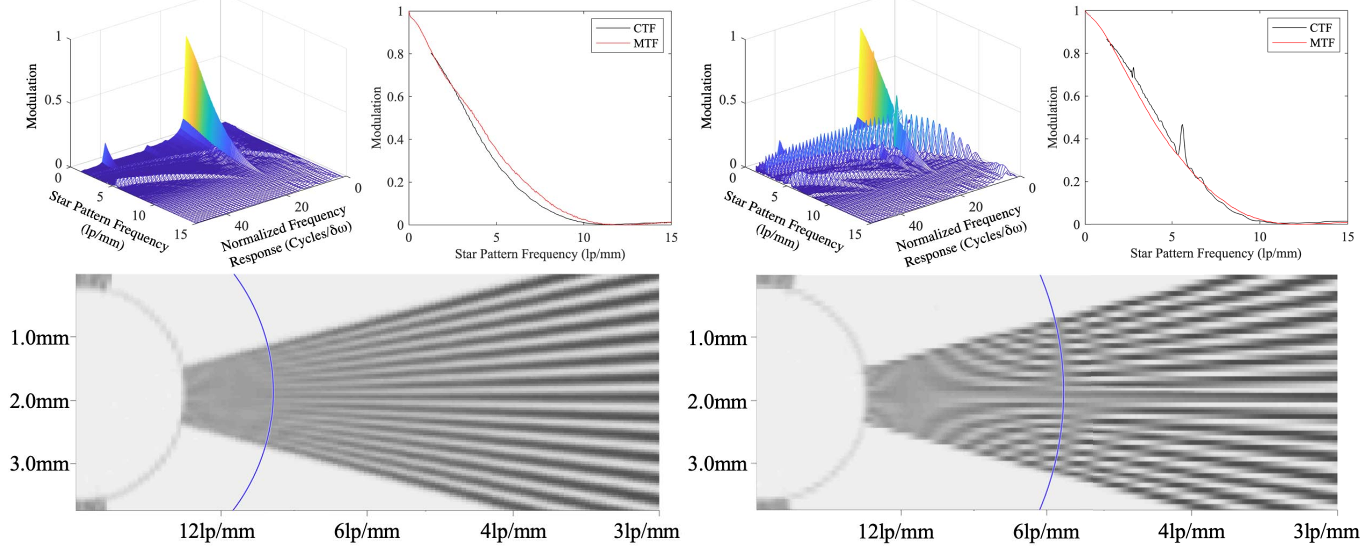

(a) (b)

Fig. 14. Results for NGT-X f_x (a) and f_y (b) for the 0-radian and $\pi/2$-radian quadrants, respectively. The FSD graph (top left graph), CTF plot (top right graph), and image with the LSR (bottom image) are shown. The input frequency, ν, and square wave harmonic are the only dominant signals in (a). The LSR is evident in the CTF plot near 9 lp/mm where modulation is 5%. The FSD graph of (b) is similar to that of (a), but shows significant spectral leakage. The spectral leakage intersects ν at ξ in the FSD graph and the LSR is reduced to ξ.

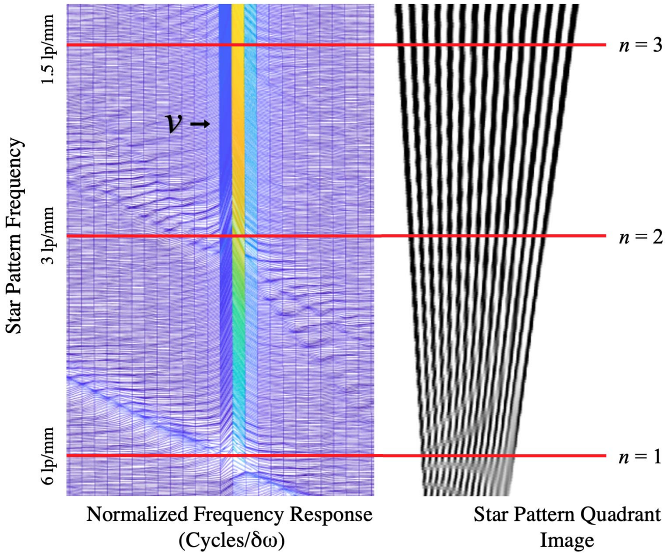

Fig. 15. Depiction of the FSD graph from an aerial perspective alongside the corresponding star pattern quadrant with repeating Moiré patterns. The integer value n corresponds to (4). The repeating oscillations are observed in Fig. 14b.

leakage then repeat at integer values of n: 3 lp/mm (1/4 cycles per pixel, $n = 2$) and at 1.5 lp/mm (1/6 cycles per pixel, $n = 3$).

IV. DISCUSSION

By presenting the imaging system with spatially separated stimuli of various known spatial frequencies, the FSD is able to separate the frequency response into the fundamental frequency, harmonics, spectral leakage, and aliasing. By contrast, conventional measures of MTF confound these factors. For these reasons, it is particularly useful for tomosynthesis and other modalities supporting super resolution. Studies suggest that the FSD can also distinguish differences between tomosynthesis acquisition geometries [5], [6], [8], [16], which makes it a useful tool for evaluating the myriad acquisition geometries of the NGT prototype.

In this work, the FSD is demonstrated using one acquisition geometry of the NGT prototype. The FSD graphs show full visualization of the spectral leakage, which can change significantly with even minor changes in acquisition geometry. The CTF graphs do show evidence of spectral leakage, but not spectral leakage itself. The FSD graphs show *all* frequency responses (including spectral leakage) for every input frequency, whereas the CTF graphs show the response at the specific period of the fundamental input frequency only. Furthermore, the r-factor which is the criterion for determining super resolution, cannot be computed using the CTF alone. Optimization of tomosynthesis acquisition geometries and other factors requires a full account of all the response signals of the star pattern input, suggesting a preference for visualizing FSD graphs over CTF graphs.

The results suggest this method can motivate the design of novel test objects with different resolution properties to separate the response frequencies from fundamental input frequencies. The FSD evaluates the in-plane spatial resolution of a DBT image reconstruction in the conventional reconstruction plane successfully. Similar to the tilted tungsten wire for MTF calculations, the star pattern can be oriented arbitrarily to evaluate spatial resolution for any frequency orientation – including frequencies aligned in the z-axis – to evaluate multiplanar image reconstruction slices for f_z [4].

The sample size (N) used in the FSD calculation is sufficient for the images that we analyzed. If λ were to increase, it is possible that N would also need to increase to achieve sufficient oversampling. For example, in Fig. 10, the absolute difference between conditions A and D decreases as the resolution increases. Condition A is below f_N at the lowest resolution of the star pattern. The absolute difference between any of the conditions with Γ values above 2.0 has no measurable error. This supports the notion that the FSD should not be computed at any Γ below f_N.

Averaging the spectra of individual 2D projections improves the visualization of the spectral features (spectral leakage, square-wave harmonics, etc.). Aliasing is evident in the form of spectral leakage that arises from the detector aperture, and the spectral leakage that arises from the sampling pitch intersects the fundamental input frequency at the sampling rate of the detector, as expected. The aperture spectral leakage is greater for f_y than for f_x. This difference may arise if the focal spot is non-isometric or when the measurement is not proximal to the central ray of the x-ray beam.

The various reconstruction sizes provide insight into proper sampling techniques for tomosynthesis image reconstructions. To achieve super-resolution, $1/\lambda$ needs to be equal to or greater than f_N. A λ of 37μm appears to have the least prominent residual spectral leakage in Fig. 13. This suggests it is advantageous to sample a tomosynthesis reconstruction at a λ that is not an integer multiple of d_{el}, such as 42.5 μm (2.0x) or 28.3μm (3.0x). While we have experimental evidence strictly for our planar-source system, we have seen similar results using a rotational-source system. We posit that the benefit of incorporating non-integer multiples of d_{el} for the reconstruction pitch has more to do with the detector aperture than differences in acquisition geometry (e.g. planar x-ray source sampling vs. rotational x-ray source sampling).

For an NGT-X reconstruction, aliasing is present and manifested as Moiré patterns for f_x and f_y in digital images if $1/\lambda$ is below f_N for the given d_{el}, regardless of the object orientation or acquisition geometry. However, if we consider a conventional DBT acquisition geometry where $1/\lambda$ is at or above f_N for an image reconstruction, aliasing is only present for $\sigma_\perp$.

These results represent a specific image reconstruction method that supports computed super resolution; however, the FSD is agnostic to reconstruction technique. This study focuses on a simple back projection technique to evaluate the underlying physics of conventional tomosynthesis without complicating the analysis with various parameters such as non-linear reconstruction methods or image processing. The FSD has the potential to provide a means of comparing different reconstruction and image processing methods, especially for analyzing spectral leakage and aliasing.

Although the initial application for developing this metric is tomosynthesis, the FSD can be extended to other x-ray imaging modalities and optical imaging devices that utilize digital detectors. Furthermore, it has the potential to be used to evaluate digital monitors. We have already applied the metric to evaluate spatial resolution in the presence of spectral leakage for various systems and a variety of star pattern images, including: virtual clinical trials of a simulated star pattern [16], [17], proton and electron radiation therapy beams on direct conversion detectors [18], and a specimen tomosynthesis system [19] (Mozart 3D, Kubtec, Milford, CT).

V. CONCLUSION

In this work, we demonstrate the FSD using two frequency orientations for a 2D image and a 3D image reconstruction slice. The FSD successfully compares resolution properties of all conditions. It separates the frequencies of spectral leakage (arising from d_{el} and λ) from fundamental input frequencies in 2D images and 3D image reconstructions. The FSD produces the CTF of an in-plane image reconstruction without suppressing spectral leakage through super-sampling. The FSD is a more detailed representation of in-plane resolution properties and imaging artifacts for tomosynthesis than the corresponding pre-sampled MTF. The conceptual change in viewpoint, from a single spectrogram in which the contributions of multiple input frequencies are superimposed, to a 2D spectrogram, in which the detailed response of each input frequency is separated provides additional details of imaging performance: aliasing, square-wave response, and limiting spatial resolution. We have already begun to use the FSD to evaluate resolution properties for all acquisition geometries of our NGT prototype. The tools and instructions for this metric were created using MATLAB and are available online at: https://github.com/trevorvent/FSD.

ACKNOWLEDGMENT

The authors would like to thank Johnny Kuo, Susan Ng, and Peter Ringer of Real Time Tomography for technical assistance with Piccolo. Andrew D. A. Maidment is a shareholder of Real Time Tomography and is a member of the scientific advisory board.

In addition, equipment support was provided by Analogic Inc., Barco NV, and Real Time Tomography. The content is solely the responsibility of the authors and does not necessarily represent the official views of the funding agencies.

REFERENCES

[1] B. Zhao, J. Zhou, Y.-H. Hu, T. Mertelmeier, J. Ludwig, and W. Zhao, "Experimental validation of a three-dimensional linear system model for breast tomosynthesis," *Med. Phys.*, vol. 36, no. 1, pp. 240–251, 2009.

[2] *Medical Electrical Equipment—Characteristics of Digital X-ray Imaging Devices—Part 1–2: Determination of the Detective Quantum Efficiency—Detectors Used in Mammography*, Standard IEC 62220-1-2:2007, IEC. Accessed: Feb. 12, 2019. [Online]. Available: https://webstore.iec.ch/publication/6598

[3] R. J. Acciavatti and A. D. A. Maidment, "Observation of super-resolution in digital breast tomosynthesis," *Med. Phys.*, vol. 39, no. 12, pp. 7518–7539, Nov. 2012.

[4] T. L. Vent, R. J. Acciavatti, Y. J. Kwon, and A. D. A. Maidment, "Quantification of resolution in multiplanar reconstructions for digital breast tomosynthesis," *Proc. SPIE*, vol. 9783, Mar. 2016, Art. no. 978303.

[5] C. J. Choi, T. L. Vent, A. D. A. Maidment, and R. J. Acciavatti, "Geometric calibration for a next-generation digital breast tomosynthesis system using virtual line segments," *Proc. SPIE*, vol. 10573, Mar. 2018, Art. no. 105730D.

[6] T. D. Maidment, T. L. Vent, W. S. Ferris, D. E. Wurtele, R. J. Acciavatti, and A. D. A. Maidment, "Comparing the imaging performance of computed super resolution and magnification tomosynthesis," *Proc. SPIE*, vol. 10132, Mar. 2017, Art. no. 1013222.

[7] A. Kuhls-Gilcrist, A. Jain, D. R. Bednarek, K. R. Hoffmann, and S. Rudin, "Accurate MTF measurement in digital radiography using noise response," *Med. Phys.*, vol. 37, no. 2, pp. 724–735, Jan. 2010.

[8] R. J. Acciavatti and A. D. A. Maidment, "Oblique reconstructions in tomosynthesis. II. Super-resolution," *Med. Phys.*, vol. 40, no. 11, pp. 1–19, 2013.

[9] T. L. Vent, B. L. Lepore, and A. D. A. Maidment, "Evaluating the imaging performance of a next-generation digital breast tomosynthesis prototype," *Proc. SPIE*, vol. 10948, Mar. 2019, Art. no. 109480K.

[10] R. J. Acciavatti *et al.*, “Analysis of volume overestimation artifacts in the breast outline segmentation in tomosynthesis,” *Proc. SPIE*, vol. 10573, Mar. 2018, Art. no. 1057359.

[11] R. J. Acciavatti, B. Barufaldi, T. L. Vent, E. P. Wileyto, and A. D. A. Maidment, “Personalization of X-ray tube motion in digital breast tomosynthesis using virtual defrise phantoms,” *Proc. SPIE*, vol. 10948, Mar. 2019, Art. no. 109480B.

[12] J. W. Coltman, “The specification of imaging properties by response to a sine wave input,” *J. Opt. Soc. Amer.*, vol. 44, no. 6, p. 468, Jun. 1954.

[13] E. Samei, M. J. Flynn, and D. A. Reimann, “A method for measuring the presampled MTF of digital radiographic systems using an edge test device,” *Med. Phys.*, vol. 25, no. 1, pp. 102–113, Jan. 1998.

[14] H. Fujita, K. Ueda, J. Morishita, T. Fujikawa, A. Ohtsuka, and T. Sai, “Basic imaging properties of a computed radiographic system with photostimulable phosphors,” *Med. Phys.*, vol. 16, no. 1, pp. 52–59, Jan. 1989.

[15] S. N. Friedman and I. A. Cunningham, “Normalization of the modulation transfer function: The open-field approach,” *Med. Phys.*, vol. 35, no. 10, pp. 4443–4449, Sep. 2008.

[16] T. L. Vent, B. Barufaldi, R. J. Acciavatti, and A. Maidment, “Simulation of high-resolution test objects using non-isocentric acquisition geometries in next-generation digital tomosynthesis,” *Proc. SPIE*, vol. 11513, May 2020, Art. no. 1151317.

[17] T. L. Vent, B. Barufaldi, and A. D. A. Maidment, “Simulation and experimental validation of high-resolution test objects for evaluating a next-generation digital breast tomosynthesis prototype,” *Proc. SPIE*, vol. 10948, Mar. 2019, Art. no. 109480M.

[18] D. L. Lee *et al.*, “Novel direct conversion imaging detector without selenium or semiconductor conversion layer,” *Proc. SPIE*, vol. 10948, Mar. 2019, Art. no. 1094818.

[19] N. Partain *et al.*, “Differences in re-excision rates for breast-conserving surgery using intraoperative 2D versus 3D tomosynthesis specimen radiograph,” *Ann. Surgical Oncol.*, vol. 27, no. 12, pp. 4767–4776, Nov. 2020.

Super-Resolution in Digital Breast Tomosynthesis: Limitations of the Conventional System Design and Strategies for Optimization

Raymond J. Acciavatti[1], Trevor L. Vent[1], Bruno Barufaldi[1], E. Paul Wileyto[2],
Peter B. Noël[1], Andrew D. A. Maidment[1]
[1]University of Pennsylvania, Department of Radiology, 3400 Spruce Street, Philadelphia PA 19104
[2]University of Pennsylvania, Department of Epidemiology, Biostatistics, & Informatics,
423 Guardian Drive, Philadelphia, PA 19104
E-mail: {Raymond.Acciavatti | Trevor.Vent | Bruno.Barufaldi | epw |
Peter.Noel | Andrew.Maidment}@pennmedicine.upenn.edu

ABSTRACT

Our previous work explored the use of super-resolution as a way to improve the visibility of calcifications in digital breast tomosynthesis. This paper demonstrates that there are anisotropies in super-resolution throughout the reconstruction, and investigates new motion paths for the x-ray tube to suppress these anisotropies. We used a theoretical model of a sinusoidal test object to demonstrate the existence of the anisotropies. In addition, high-frequency test objects were simulated with virtual clinical trial (VCT) software developed for breast imaging. The simulated objects include a lead bar pattern phantom as well as punctate calcifications in a breast-like background. In a conventional acquisition geometry in which the source motion is directed laterally, we found that super-resolution is not achievable if the frequency is oriented in the perpendicular direction (posteroanteriorly). Also, there are positions, corresponding to various slices above the breast support, at which super-resolution is inherently not achievable. The existence of these anisotropies was validated with VCT simulations. At locations predicted by theoretical modeling, the bar pattern phantom showed aliasing, and the spacing between individual calcifications was not properly resolved. To show that super-resolution can be optimized by re-designing the acquisition geometry, we applied our theoretical model to the analysis of new motion paths for the x-ray tube; specifically, motions with more degrees of freedom and with more rapid pulsing (submillimeter spacing) between source positions. These two strategies can be used in combination to suppress the anisotropies in super-resolution.

Keywords: Digital Breast Tomosynthesis, Virtual Clinical Trials, Super-Resolution, Calcifications, Anthropomorphic Phantom, Fourier Transform, Image Quality, Image Reconstruction.

1. INTRODUCTION

1.1 Overview of Super-Resolution in Tomosynthesis

Many medical centers now use digital breast tomosynthesis (DBT) for breast cancer screening.[1-3] In DBT, the x-ray tube rotates in the plane of the chest wall, and a reconstruction is created from a small number of projection views (Figure 1). Since the image of an object is translated in subpixel increments between each projection, a reconstruction created with smaller pixelation than the detector is capable of super-resolution, or resolution of frequencies exceeding the alias frequency of the detector.[4,5] Super-resolution allows fine details to be visualized more clearly, including calcifications. These benefits can be achieved with either backprojection filtering[4] or iterative reconstructions[6].

With theoretical modeling, we have shown that there are some *z*-coordinates at which super-resolution cannot be achieved, corresponding to regularly-spaced slices in the reconstruction.[7] One of the aims of this paper is to understand how these anisotropies could impact virtual clinical trials (VCTs). A VCT is a software tool that allows for simulation of anatomical phantoms under different imaging conditions using model observers to quantify the detection of lesions (*e.g.*, calcifications) with receiver operating characteristic curves.[8] Our recent work showed that a VCT of DBT and 2D digital mammography (DM) performed extremely well in comparison with clinical data.[9] In this paper, we demonstrate that the visualization of calcifications in a VCT is impacted by the presence of the anisotropies in super-resolution. We use theoretical modeling to guide the positioning of these lesions based on the known locations of the anisotropies.

15th International Workshop on Breast Imaging (IWBI2020), edited by Hilde Bosmans,
Nicholas Marshall, Chantal Van Ongeval, Proc. of SPIE Vol. 11513, 115130V
· doi: 10.1117/12.2563839

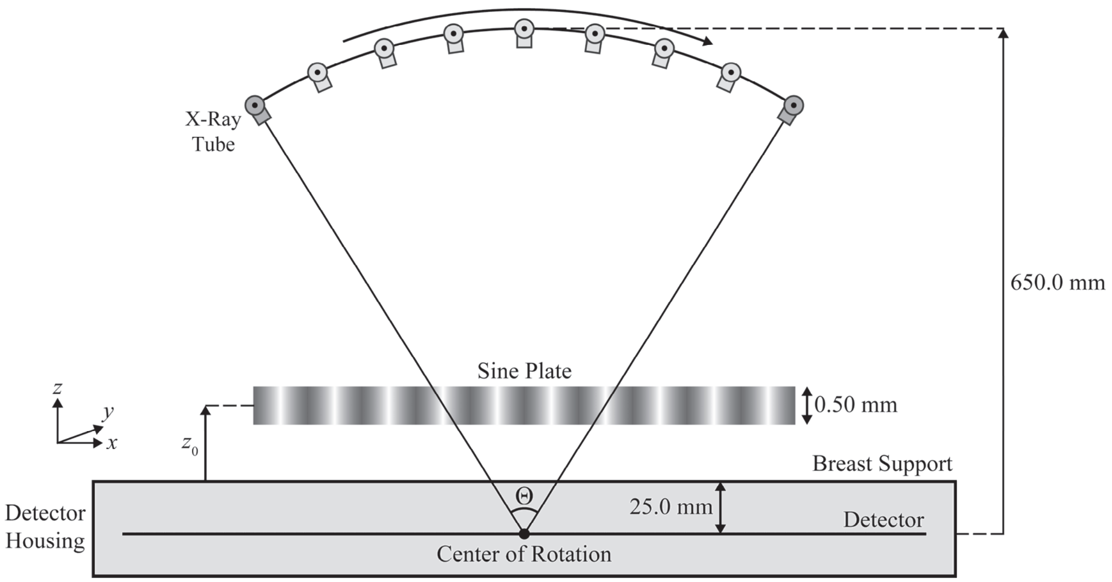

Figure 1. The sine plate is a test object for investigating the existence of super-resolution with theoretical modeling. In a conventional DBT scan, there is source motion in a circular arc in the *xz* plane; *i.e.*, the plane of the chest wall.

1.2 Design of a Next-Generation Tomosynthesis System

In our previous work, we showed that there are fewer anisotropies in a DBT system with narrowly-spaced source positions, but that it is not possible to eliminate the anisotropies entirely. Recently, we proposed a "next-generation" DBT system design in which additional source positions are clustered around the conventional positions in submillimeter increments.[10] This design can be implemented by rapidly pulsing the source during continuous motion of the x-ray tube. For frequencies oriented in the *x* direction (laterally or left-to-right in Figure 1), the anisotropies can be eliminated with the use of rapid source pulsing.

A limitation of our previous work[10] on rapid source pulsing is that the perpendicular orientation of the test frequency was not considered; *i.e.*, the posteroanterior (PA) orientation (into the plane of the page in Figure 1). In a conventional DBT system, super-resolution is not achievable in the PA direction. This idea can be illustrated with projection images of a point-like object (Figure 2). Because there is x-ray tube motion in the *x* direction (laterally), there are noticeable shifts in the image of the object between projections, and hence super-resolution is achieved in this direction. However, the shifts in the *y* direction are too small to achieve super-resolution; there is no x-ray tube motion in this direction. In this paper, we show that super-resolution can indeed be achieved in the PA direction with the use of source motion in this direction. This motion can be applied in combination with the use of rapid source pulsing to ensure that super-resolution is achieved with high quality, regardless of the orientation of the input frequency.

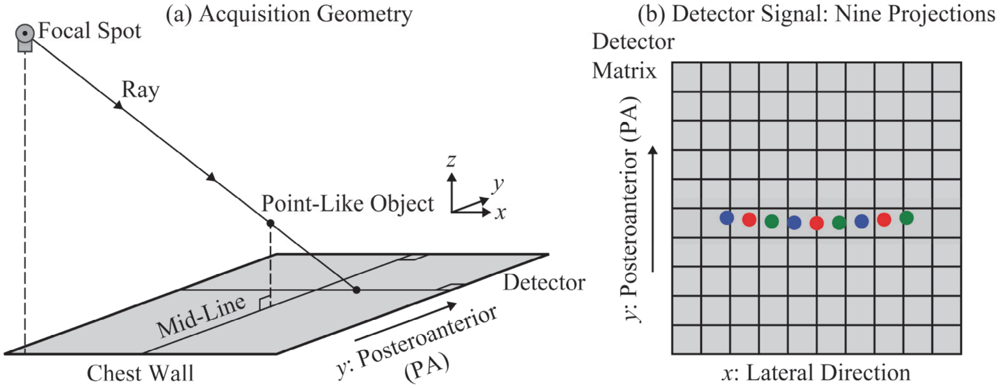
(a) Acquisition Geometry

(b) Detector Signal: Nine Projections

Figure 2. In clinical DBT systems, super-resolution is achieved in the *x* direction, since there is x-ray tube motion in this direction. However, super-resolution is not achieved in the *y* direction; the shifts in the object positions in this direction are minimal.

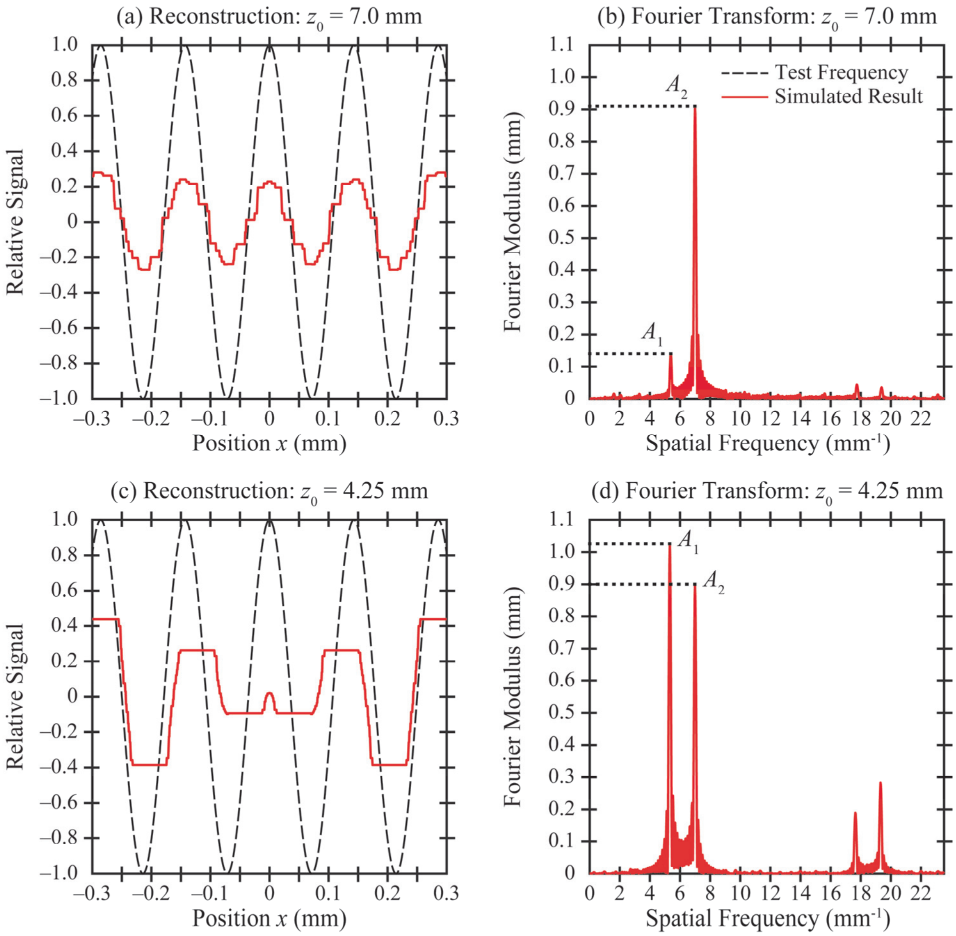

Figure 3. The Fourier transform of the reconstruction is analyzed in terms of two peaks: one at the input frequency (A_2) and one at a lower frequency (A_1). In order for super-resolution to be achieved with high quality, the ratio A_1/A_2 should be as small as possible.

2. METHODS

2.1 Identification of Anisotropies in the Conventional Design

As the first aim of this paper, we demonstrate the existence of anisotropies in the conventional system design. We apply the theoretical model of super-resolution developed in our previous work.[7] In that work, the reconstruction of a sinusoidal test object was calculated from first principles.

The input frequency is modeled separately in two directions: lateral and PA. Anisotropies are identified using the Fourier transform of the reconstruction; this is calculated over 50 cycles with 20 points sampled per cycle. To illustrate how the Fourier transform can be used to assess super-resolution, a 7.0 mm^{-1} test frequency is considered with sampling by a detector with 0.085 mm × 0.085 mm detector elements (Figure 3). The Fourier transform has a major peak at the input frequency if the object is resolved [Figure 3(b)], but has a major peak at a lower frequency if the object is aliased [Figure 3(d)]. Our previous work defined the r-factor as a metric to summarize the results in Fourier space.[4,7]

$$r\text{-Factor} = \frac{A_1}{A_2} \tag{1}$$

In order for super-resolution to be achieved with high quality, the r-factor should be as small as possible. That is, the amplitude of the low-frequency peak (A_1) should be smaller than the amplitude at the input frequency (A_2). For the purpose of this paper, the threshold for high-quality super-resolution is: r-factor < 1/3.

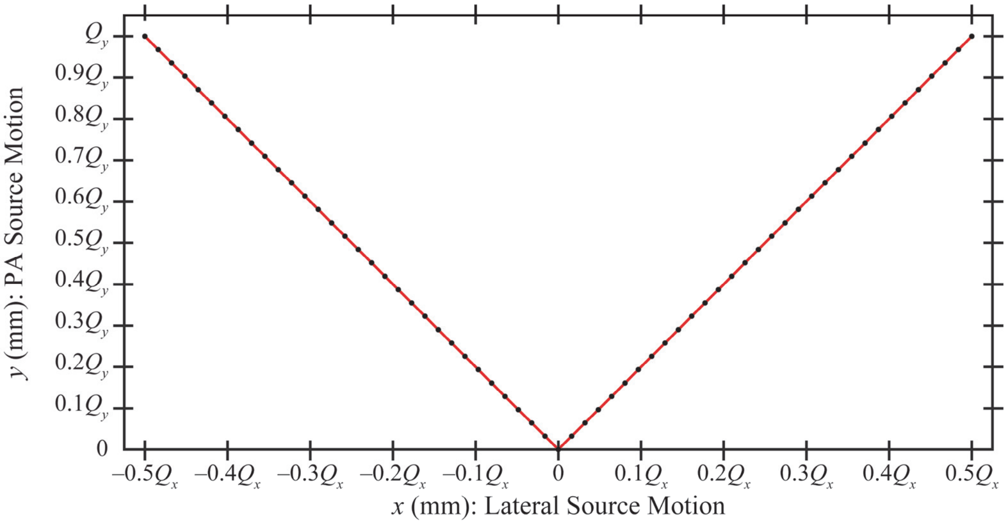

(a) Uniformly-Spaced Projections

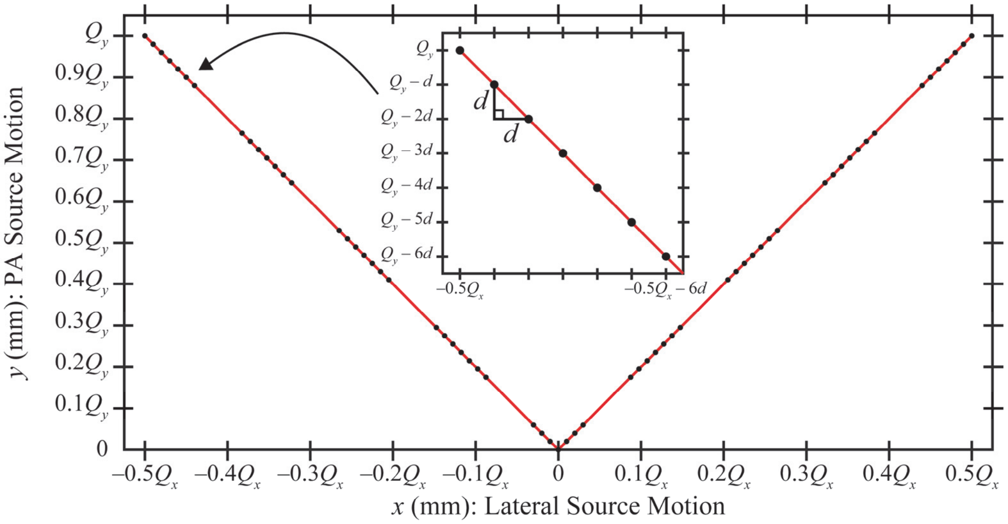

(b) Clustered Projections

Figure 4. (a) There are 63 source positions spaced uniformly along a V-shaped trajectory. (b) The source positions are re-arranged in nine clusters in the same V-shaped trajectory. There is submillimeter spacing between the seven source positions in each cluster ($d = 0.5$ mm).

To identify all the coordinates of the anisotropies in the range between $z_0 = 0$ and $z_0 = 50.0$ mm, we generated a plot of r-factor as a function of z_0. For this simulation, the sine wave was centered at the position 25.0 mm anterior to the chest wall along the mid-line defined in Figure 2. The acquisition parameters for this simulation are summarized in Table 1.

2.2 VCT Simulations of Bar Pattern Phantom and Calcifications

VCT software was then used to validate the position of the anisotropies expected from theoretical modeling. The acquisition parameters in this simulation are detailed in Table 1. First, we simulated a bar pattern phantom with 0.070 mm cubic voxels, a thickness of 0.070 mm, and a frequency of 7.0 mm^{-1} oriented laterally (parallel with the source motion); *i.e.*, the same orientation as Figure 1. Since the input frequency is higher than the alias frequency of the detector (5.9 mm^{-1} in a 0.085 mm detector), this object can be used to investigate super-resolution.

Table 1. The acquisition parameters for theoretical modeling and VCT simulations are summarized below.

Acquisition Parameter	Theoretical Modeling: Conventional DBT	VCT Simulation: Conventional DBT	Theoretical Modeling: Next-Generation DBT
Source Motion	Circular Arc (*xz* Plane)	Linear (*x*): Constant *z*	V-Shaped: Constant *z*
Source-to-Image Distance	650.0 mm (Central Projection)	621.0 mm	650.0 mm
Number of Projections	15	15	63
Range of Source Motion	$\Theta = 17.7°$ (200.0 mm in *x*)	182.7 mm (in *x*)	200.0 mm (*x*), 100.0 mm (*y*)

Secondly, punctate calcifications[11] were simulated in an anthropomorphic voxel phantom.[12] The phantom was positioned in such a way that the inferior surface was in contact with the detector. Each calcification was modeled by a single voxel with dimensions of 0.070 mm in each direction. There were 25 calcifications arranged linearly in the direction of the source motion. Reconstructions for both the bar pattern and calcifications were prepared with Piccolo™ (Real Time Tomography, LLC, Villanova, PA).[13]

The calcification size and composition were chosen with care. The linear dimension (0.070 mm) was chosen to ensure that the frequency of the array of calcifications was greater than the alias frequency of the detector (5.9 mm^{-1}). This linear dimension is smaller than the smallest calcification (0.16 mm) within the Gammex 156 American College of Radiology (ACR) Mammography Accreditation Phantom; however, the shape of the calcifications in the ACR phantom is unspecified and the volume is less than a cube of that size. In our other work[14], we typically use cubic calcifications with dimensions 0.001 mm^3, 0.002 mm^3, and 0.003 mm^3, with weighting factors (fraction by mass) between 10% and 100% hydroxyapatite. These calcifications are equivalent in volume to spherical calcifications of diameters 0.124, 0.156, and 0.180 mm. In this paper, we use a (0.070 mm)^3 calcification with a weighting factor of 100%, which has the same attenuation as a 0.124 mm diameter calcification with a weighting factor of 0.34, consistent with our other VCTs.

2.3 Modeling A New System Design

Next, we investigated a "next-generation" system design. The number of projections (63) is well above the number used clinically (Table 1); this is known from our previous work to improve the quality of super-resolution.[10] The design modeled in this paper differs from our previous work in that we model PA source motion; *i.e.*, an additional degree of freedom in the y direction. The motion follows a V-shape (Figure 4). The ranges of source motion in the lateral and PA directions (Q_x and Q_y) are 200.0 mm and 100.0 mm, respectively. The range of 200.0 mm in the x direction is similar to the conventional system described in Section 2.1.

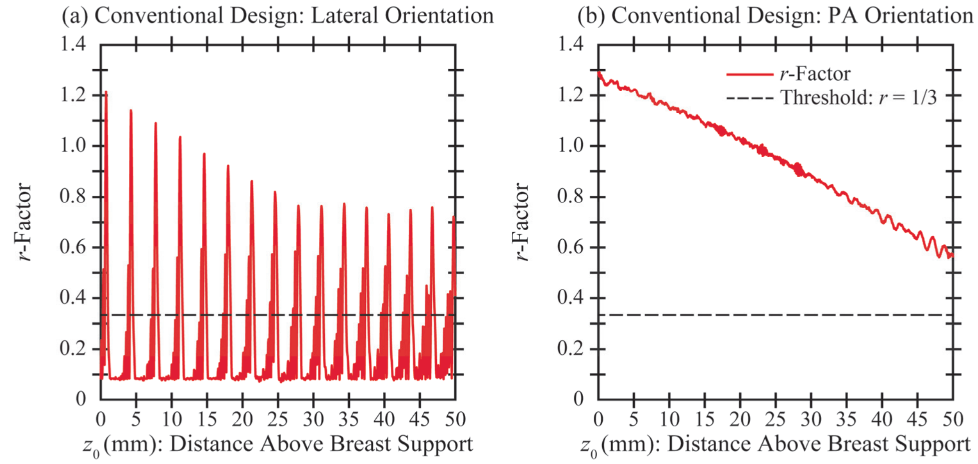

Figure 5. To achieve super-resolution with high quality, the r-factor should be as small as possible (below the threshold of 1/3 for the purpose of this paper). The coordinates of the anisotropies differ based on the orientation of the input frequency.

Figure 6. VCT simulations of a 7.0 mm^{-1} bar pattern phantom illustrate the z-dependency of super-resolution in the reconstruction.

For the same V-shaped motion, we investigated two acquisition geometries, each differing in terms of the choice of source positions. In one scan, we applied the principle of rapid source pulsing [Figure 4(b)], which was proposed in our previous work.[10] The source positions were arranged in nine sets of clusters with seven source positions per cluster (63 source positions in total). Within each cluster, the spacing (d) between the source positions was 0.50 mm in each direction. By contrast, in a second scan, there was equal spacing between all 63 source positions [Figure 4(a)]. We investigated whether the use of clustering offers a benefit over the use of uniform spacing. Like the simulations described in Section 2.1, we calculated the r-factor to determine which of these two acquisition geometries offers the best image quality over the broadest range of positions (z_0).

3. RESULTS

3.1 Modeling the Conventional System Design

First, image quality in a conventional DBT system was modeled by the r-factor (Figure 5). Anisotropies are present in both orientations of the input frequency. In the lateral orientation, super-resolution is not achieved at the z-coordinates at which the r-factor peaks sharply. In the PA orientation, super-resolution is not achieved with high quality anywhere; the r-factor is above the threshold of 1/3. In summary, these results illustrate the limitations of current clinical systems.

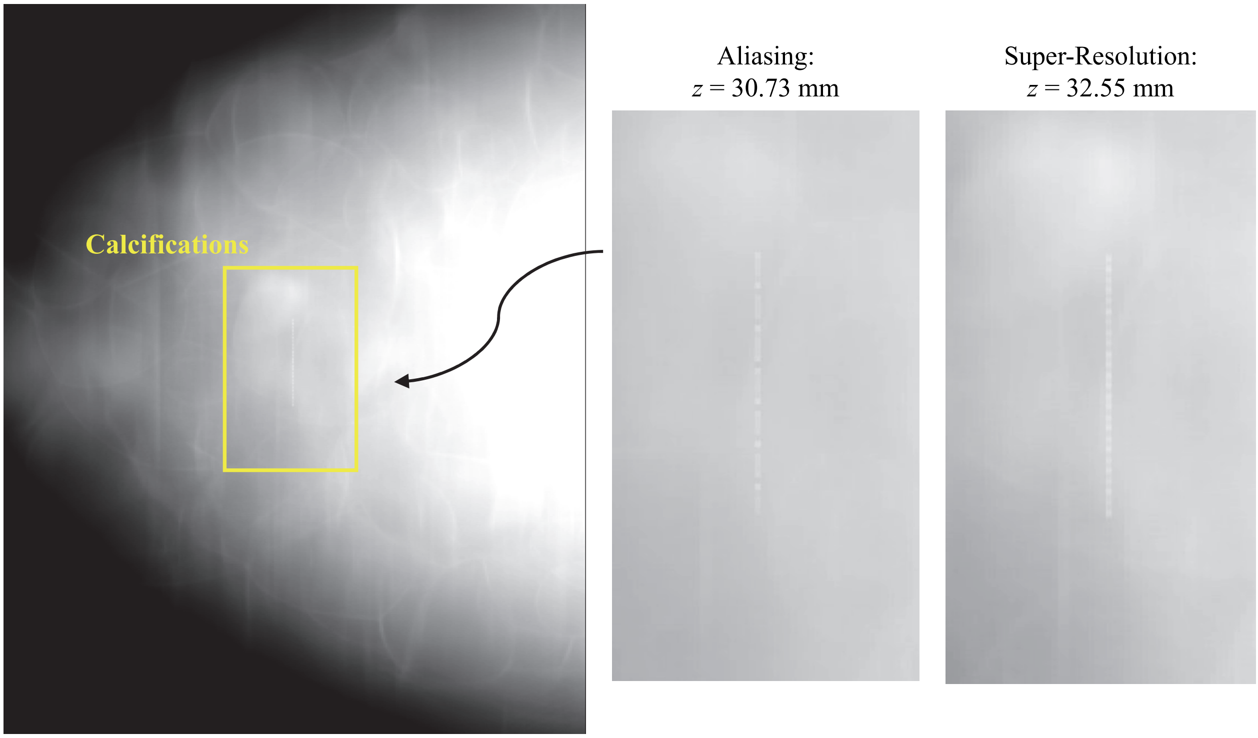

Figure 7. The ability to resolve individual punctate calcifications in a linear array is dependent on the positioning of the cluster.

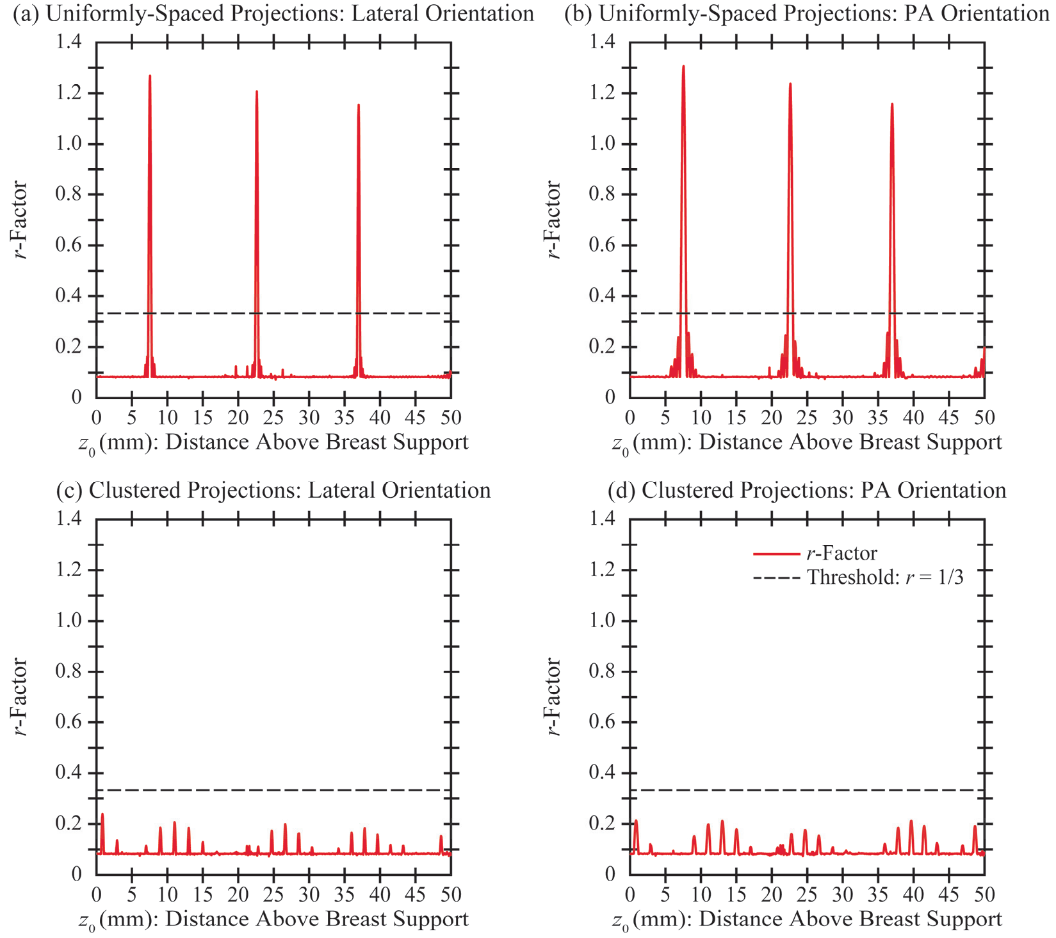

Figure 8. A DBT system is modeled with V-shaped source motion and 63 projections (well above the number of projections used clinically). To eliminate the anisotropies, the source positions should be arranged in clusters; this ensures that the *r*-factor is below 1/3 (the threshold for high-quality super-resolution).

3.2 VCT Simulations of Bar Pattern Phantom and Calcifications

Next, the bar pattern phantom and calcifications were simulated with VCT software in a conventional acquisition geometry (Table 1). This geometry differs slightly from the one analyzed with theoretical modeling (Section 3.1) in that the orbit of the x-ray tube does not follow an arc in the *xz* plane. Instead, the source is translated in only one direction (x) at constant z. This motion is consistent with the next-generation tomosynthesis (NGT) system, which we built for research use to investigate different acquisitions geometries for DBT.[15]

With theoretical modeling of the *r*-factor, a plot similar to Figure 5(a) can be created to identify anisotropies in this acquisition geometry. It can be shown, for example, that there is an anisotropy at the position 30.73 mm above the detector. At this position, the bar pattern phantom shows aliasing (Figure 6), and it is not possible to resolve each individual calcification in the reconstruction (Figure 7). However, super-resolution is supported at other positions in the reconstruction; for example, at the coordinate 32.55 mm above the detector. Here, the bar pattern phantom is resolved and each individual calcification is discernable.

3.3 Modeling A New System Design

Finally, the two V-shaped acquisition geometries were analyzed with theoretical modeling (Figure 8). Unlike the conventional acquisition geometry, super-resolution can indeed be achieved in the PA orientation; this is due to the use of PA source motion, which introduces subpixel sampling gain in that direction. The disadvantage of having uniform spacing between projections is that there are anisotropies; *i.e.*, three peaks in the *r*-factor [Figure 8(a)-(b)]. In order for the anisotropies to be eliminated, the source positions should be re-arranged in clusters [Figure 8(c)-(d)]; this design ensures that the *r*-factor is below 1/3 at all positions in the reconstruction.

4. DISCUSSION AND CONCLUSION

In our previous work, we showed that DBT is capable of super-resolution, but that clinical systems are not yet designed to optimize this effect.[4,7] There are regularly-spaced positions in the *z* direction at which super-resolution is not achievable. This paper validates the VCT software as a tool to simulate the anisotropies. We also show that the appearance of calcifications can be distorted by the presence of anisotropies; this could potentially impact the way calcifications are characterized by a radiologist.

A design for optimizing super-resolution was proposed in our previous work.[10] We modeled a system with additional source positions clustered around the conventional positions in submillimeter increments, and found that super-resolution is achieved everywhere in the reconstruction. A limitation of our previous work is that we only considered frequencies oriented laterally (Figure 1). In this paper, the PA orientation is also analyzed. Anisotropies in both orientations can be eliminated by applying the use of clustering in combination with PA motion; *i.e.*, an additional degree of freedom in the source motion.

Our previous work demonstrated that the use of PA source motion is also beneficial in other imaging tasks. In clinical DBT systems, there is a cone-beam artifact in the PA direction.[16] With Defrise phantoms, we showed that this artifact can be suppressed with the use of PA source motion.[15,17] Another advantage of PA source motion is that the accuracy of the breast outline segmentation in the reconstruction is improved.[18] The air gap between the breast support and the anterior aspect of the breast is visualized more clearly with the PA projection views.

In our previous work, we investigated a new design for the detector (motion in the *z* direction) as an alternative strategy for optimizing super-resolution.[7] In order for this strategy to be implemented clinically, it may be necessary to increase the thickness of the detector housing, which could be cumbersome for patient positioning. The advantage of the design proposed in this paper is that the detector can remain stationary during the scan. This design will require a detector capable of a high frame rate, since the number of projection views (63) exceeds the number that is typically used clinically. Also, the radiation dose per projection will need to be reduced so that the total dose of the scan is unchanged.

5. ACKNOWLEDGEMENT

We thank Johnny Kuo, Susan Ng, and Peter Ringer of Real Time Tomography (RTT) for technical assistance with Piccolo™. Andrew D. A. Maidment is a shareholder of RTT, and is a member of the scientific advisory board. Support was provided by the following grants: W81XWH-18-1-0082 from the Department of Defense Breast Cancer Research Program, IRSA 1016451 from the Burroughs Wellcome Fund, 1R01CA196528 from the National Institute of Health, and IIR13264610 from Susan G. Komen®. In addition, equipment support was provided by Analogic Inc., Barco NV, and RTT. The content is solely the responsibility of the authors and does not necessarily represent the official views of the funding agencies.

6. REFERENCES

1. Friedewald SM, Rafferty EA, Rose SL, et al. Breast Cancer Screening Using Tomosynthesis in Combination With Digital Mammography. *Journal of the American Medical Association.* 2014;311(24):2499-2507.
2. Sechopoulos I. A review of breast tomosynthesis. Part I. The image acquisition process. *Medical Physics.* 2013;40(1):014301-014301 to 014301-014312.
3. Sechopoulos I. A review of breast tomosynthesis. Part II. Image reconstruction, processing and analysis, and advanced applications. *Medical Physics.* 2013;40(1):014302-014301 to 014302-014317.
4. Acciavatti RJ, Maidment ADA. Observation of super-resolution in digital breast tomosynthesis. *Medical Physics.* 2012;39(12):7518-7539.
5. Acciavatti RJ, Maidment ADA. Investigating the Potential for Super-Resolution in Digital Breast Tomosynthesis. Paper presented at: SPIE Medical Imaging2011; Lake Buena Vista, FL.
6. Lu Y, Chan H-P, Wei J, Hadjiiski L, Samala R. Study of Image Quality in Digital Breast Tomosynthesis by Subpixel Reconstruction. Paper presented at: SPIE Medical Imaging2013; Lake Buena Vista, FL.
7. Acciavatti RJ, Wileyto EP, Maidment ADA. Modeling Acquisition Geometries with Improved Super-Resolution in Digital Breast Tomosynthesis. Paper presented at: SPIE Medical Imaging2016; San Diego, CA.

8. Barufaldi B, Higginbotham D, Bakic PR, Maidment ADA. OpenVCT: A GPU-Accelerated Virtual Clinical Trial Pipeline for Mammography and Digital Breast Tomosynthesis. Paper presented at: SPIE Medical Imaging2018; Houston, TX.
9. Bakic PR, Barufaldi B, Higginbotham D, et al. Virtual Clinical Trial of Lesion Detection in Digital Mammography and Digital Breast Tomosynthesis. Paper presented at: SPIE Medical Imaging2018; Houston, TX.
10. Acciavatti RJ, Noël PB, Maidment ADA. Proposing Rapid Source Pulsing for Improved Super-Resolution in Digital Breast Tomosynthesis. Paper presented at: SPIE Medical Imaging2020 (accepted); Houston, TX.
11. Lanyi M. Chapter 4: Calcifications Within the Lobular and Ductal System of the Breast. *Diagnosis and Differential Diagnosis of Breast Calcifications*. Berlin: Springer-Verlag; 1988:29-143.
12. Pokrajac DD, Maidment ADA, Bakic PR. Optimized generation of high resolution breast anthropomorphic software phantoms. *Medical Physics.* 2012;39(4):2290-2302.
13. Kuo J, Ringer PA, Fallows SG, Bakic PR, Maidment ADA, Ng S. Dynamic Reconstruction and Rendering of 3D Tomosynthesis Images. Paper presented at: SPIE Medical Imaging2011; Lake Buena Vista, FL.
14. Barufaldi B, Vent TL, Acciavatti RJ, et al. Determining the Optimal Angular Range of the X-Ray Source Motion in Tomosynthesis Using Virtual Clinical Trials. Paper presented at: SPIE Medical Imaging2020 (accepted); Houston, TX.
15. Eben JE, Vent TL, Choi CJ, et al. Development of a Next Generation Tomosynthesis System. Paper presented at: SPIE Medical Imaging2018; Houston, TX.
16. Acciavatti RJ, Mannherz W, Nolan M, Maidment ADA. An Alternate Design for the Defrise Phantom To Quantify Resolution in Digital Breast Tomosynthesis. Paper presented at: SPIE Medical Imaging2017; Orlando, FL.
17. Acciavatti RJ, Barufaldi B, Vent TL, Wileyto EP, Maidment ADA. Personalization of X-Ray Tube Motion in Digital Breast Tomosynthesis Using Virtual Defrise Phantoms. Paper presented at: SPIE Medical Imaging2019; San Diego, CA.
18. Acciavatti RJ, Rodriguez-Ruiz A, Vent TL, et al. Analysis of Volume Overestimation Artifacts in the Breast Outline Segmentation in Tomosynthesis. Paper presented at: SPIE Medical Imaging2018; Houston, TX.

Calculation of Radiomic Features to Validate the Textural Realism of Physical Anthropomorphic Phantoms for Digital Mammography

Raymond J. Acciavatti[1], Eric A. Cohen[1], Omid Haji Maghsoudi[1], Aimilia Gastounioti[1],
Lauren Pantalone[1], Meng-Kang Hsieh[1], Bruno Barufaldi[1], Predrag R. Bakic[1], Jinbo Chen[2],
Emily F. Conant[1], Despina Kontos[1], Andrew D. A. Maidment[1]
[1]University of Pennsylvania, Department of Radiology, 3400 Spruce Street, Philadelphia PA 19104
[2]University of Pennsylvania, Department of Epidemiology, Biostatistics, & Informatics,
423 Guardian Drive, Philadelphia, PA 19104
E-mail: {Raymond.Acciavatti | Andrew.Maidment}@pennmedicine.upenn.edu

ABSTRACT

In this paper, radiomic features are used to validate the textural realism of two anthropomorphic phantoms for digital mammography. One phantom was based off a computational breast model; it was 3D printed by CIRS (Computerized Imaging Reference Systems, Inc., Norfolk, VA) under license from the University of Pennsylvania. We investigate how the textural realism of this phantom compares against a phantom derived from an actual patient's mammogram ("Rachel", Gammex 169, Madison, WI). Images of each phantom were acquired at three kV in 1 kV increments using auto-time technique settings. Acquisitions at each technique setting were repeated twice, resulting in six images per phantom. In the raw ("FOR PROCESSING") images, 341 features were calculated; *i.e.*, gray-level histogram, co-occurrence, run length, fractal dimension, Gabor Wavelet, local binary pattern, Laws, and co-occurrence Laws features. Features were also calculated in a negative screening population. For each feature, the middle 95% of the clinical distribution was used to evaluate the textural realism of each phantom. A feature was considered realistic if all six measurements in the phantom were within the middle 95% of the clinical distribution. Otherwise, a feature was considered unrealistic. More features were actually found to be realistic by this definition in the CIRS phantom (305 out of 341 features or 89.44%) than in the phantom derived from a specific patient's mammogram (261 out of 341 features or 76.54%). We conclude that the texture is realistic overall in both phantoms.

Keywords: Radiomics, digital mammography, anthropomorphic phantom, x-ray imaging, image acquisition.

1. INTRODUCTION

Breast density has consistently been shown to be an independent predictor of breast cancer risk.[1,2] Recent studies have demonstrated that combining radiomic texture features with mammographic density results in an even better assessment of breast cancer risk.[3,4] This paper explores a different application for radiomic texture feature calculations; namely, evaluating how closely the breast parenchymal patterns in an anthropomorphic phantom match a clinical population.

In our previous work, we developed a computational model of the breast in which multiple compartments of dense tissue are grown from seed points in voxel phantoms.[5,6] The user can vary parameters controlling the size and shape of the phantom, as well as the percent density and spatial arrangement of dense tissue.[7] A key advantage of this model is that a population of virtual phantoms[8] can be simulated quickly on a graphics processing unit (GPU).

A physical phantom based off this model was 3D printed by CIRS (Computerized Imaging Reference Systems, Inc., Norfolk, VA) under license from the University of Pennsylvania. The CIRS phantom models a 50 mm thick breast under compression (450 mL by volume) with a volumetric density of 17%.[9] The phantom can be used in both 2D digital mammography (DM) and 3D digital breast tomosynthesis (DBT). The phantom was 3D printed in sections (slabs), allowing clusters of calcium oxalate to be inserted within the thickness of the phantom; these are surrogates for calcification clusters.[10]

15th International Workshop on Breast Imaging (IWBI2020), edited by Hilde Bosmans,
Nicholas Marshall, Chantal Van Ongeval, Proc. of SPIE Vol. 11513, 1151309
© 2020 SPIE · CCC code: 0277-786X/20/$21 · doi: 10.1117/12.2564363

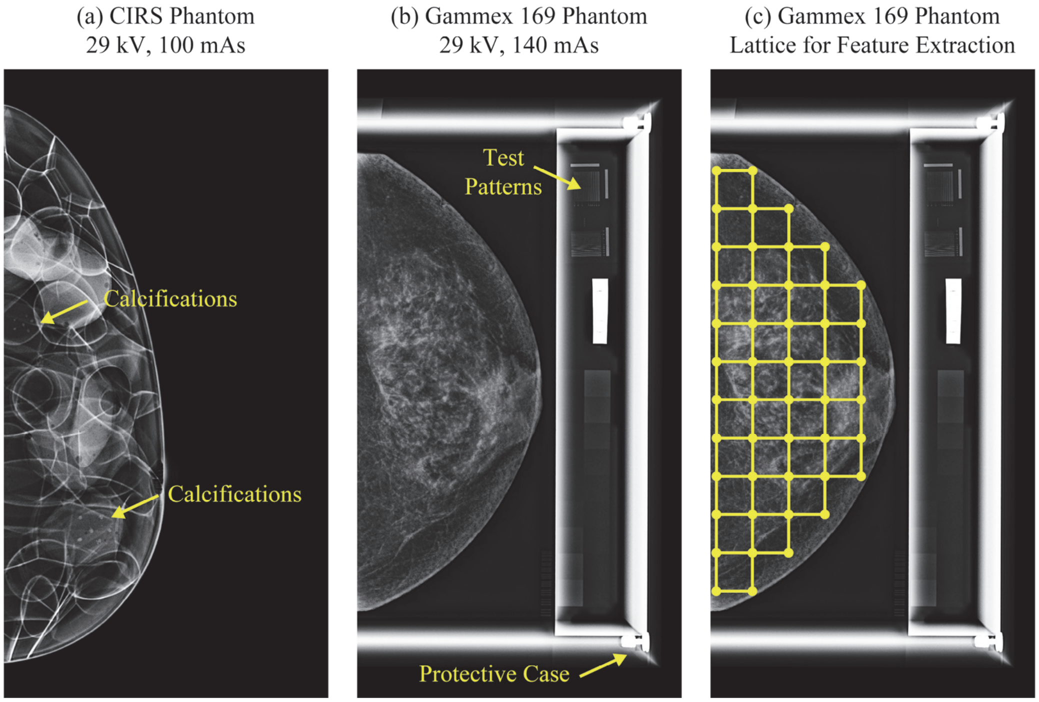

Figure 1. (a) The CIRS phantom was 3D printed from a computational breast model. (b) The Gammex 169 phantom was derived from an actual patient's mammogram. There are test patterns adjacent to the phantom; these were not analyzed for the purpose of this study. (c) The breast area was partitioned into a lattice of square windows (6.3 mm × 6.3 mm) for calculation of radiomic features. Although these calculations were done in raw DM images, processed DM images are shown.

In a previous study, Cockmartin *et al*. calculated power spectra in 2D and 3D images of the CIRS phantom, and showed that the power-law coefficients were in agreement with the values derived from a clinical population.[9] In radiomics, there are a multitude of additional features that can be used to validate the texture of a phantom. In this paper, 341 radiomic features are calculated in the CIRS phantom and compared against a clinical population. We also investigate how the texture of the CIRS phantom compares against a phantom derived from an actual patient's mammogram[11] ("Rachel, Gammex 169, Madison, WI), which by nature is expected to be highly realistic. For the purpose of this paper, all radiomics calculations are done exclusively for DM, since the Gammex 169 phantom was developed specifically for DM and not DBT.

2. METHODS

2.1 X-Ray Acquisitions of Phantoms

DM images of the two phantoms (CIRS and Gammex 169) were acquired with a Selenia Dimensions system (Hologic Inc., Bedford, MA) with a W/Rh target-filter combination (Figure 1). Images were acquired over a number of different kV and mAs combinations; the auto-timing curves illustrating the effect of kV are shown in Figure 2. A subset of these technique settings was chosen for the purpose of validating the texture of the phantoms. We based the choice of acquisition settings off of data tables for the automatic exposure control settings for a breast with comparable thickness (50 mm) to the phantoms; the appropriate kV is 29 kV for a W/Rh target-filter combination. Additional kV settings in ± 1 kV increments relative to 29 kV were also analyzed. These images were acquired in "Manual" mode at mAs settings designed to match the auto-timing curves. Since the system supports a discrete set of mAs values in "Manual" mode, the closest mAs settings were chosen (Table 1). Two cranial-caudal (CC) images were acquired at each technique setting; these were used for reproducibility analysis. Hence there were six acquisitions per phantom.

Table 1. DM technique settings for each phantom are summarized below. The target-filter combination was W/Rh.

	mAs Setting (28 kV)	**mAs Setting (29 kV)**	**mAs Setting (30 kV)**
CIRS Phantom	120 mAs	100 mAs	95 mAs
Gammex 169 Phantom	160 mAs	140 mAs	120 mAs

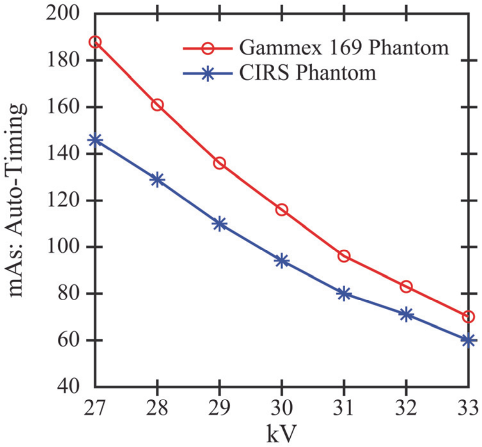

Figure 2. DM images of the two phantoms were acquired at auto-timed technique settings. As the kV increases, there is greater x-ray penetration and hence the mAs (relative number of x-ray photons) is reduced.

2.2 Overview of Clinical Data Set

DM images (CC views) were also analyzed from 1,000 women with negative screening exams at the University of Pennsylvania (Table 2). The images were acquired with Selenia Dimensions systems between 9/1/2014 and 12/31/2014. This research was approved by the Institutional Review Board at the University of Pennsylvania and was compliant with the Health Insurance Portability and Accountability Act. Since previous work demonstrated that radiomic features are dependent on breast thickness under compression[12], we compared the phantom data against the subset of clinical data with comparable thickness (±10 mm relative to a 50 mm thick phantom).

2.3 Calculation of Radiomic Texture Features

Radiomic features were calculated in raw ("FOR PROCESSING") DM images. As the first step in these calculations, the breast outline was segmented with LIBRA (Laboratory for Individualized Breast Radiodensity Assessment), a software tool.[13] Next, the breast area was partitioned into a regular lattice of square windows [Figure 1(c)]. Each feature was calculated separately in each window. These values were in turn averaged across all windows, resulting in a single image-wise value for each feature. A total of 341 features were calculated; *i.e.*, 12 gray-level histogram, 7 co-occurrence, 7 run length, 2 fractal dimension, 32 Gabor Wavelet, 36 local binary pattern, 125 Laws, and 120 co-occurrence Laws features.[14-18]

The window size used in the lattice for these feature calculations was 6.3 mm. A previous work by Zheng *et al.* considered the effect of varying the window size between 6.3 mm and 25.5 mm.[3] They found that the smallest window size (6.3 mm) yields the highest area under the receiver-operating-characteristic curve in case-control classification calculations.

Table 2. Demographic information derived from the data set of 1,000 women with negative screening exams is summarized below.

Age	< 40 y	29 (2.9 %)
	40-49 y	255 (25.5%)
	50-59 y	292 (29.2%)
	60-69 y	279 (27.9 %)
	≥ 70 y	145 (14.5%)
BI-RADS® Density	Type a	114 (11.4%)
	Type b	553 (55.3%)
	Type c	311 (31.1%)
	Type d	22 (2.2%)
Ethnicity	African American	463 (46.3%)
	Caucasian	441 (44.1%)
	Other/Unknown	96 (9.6%)

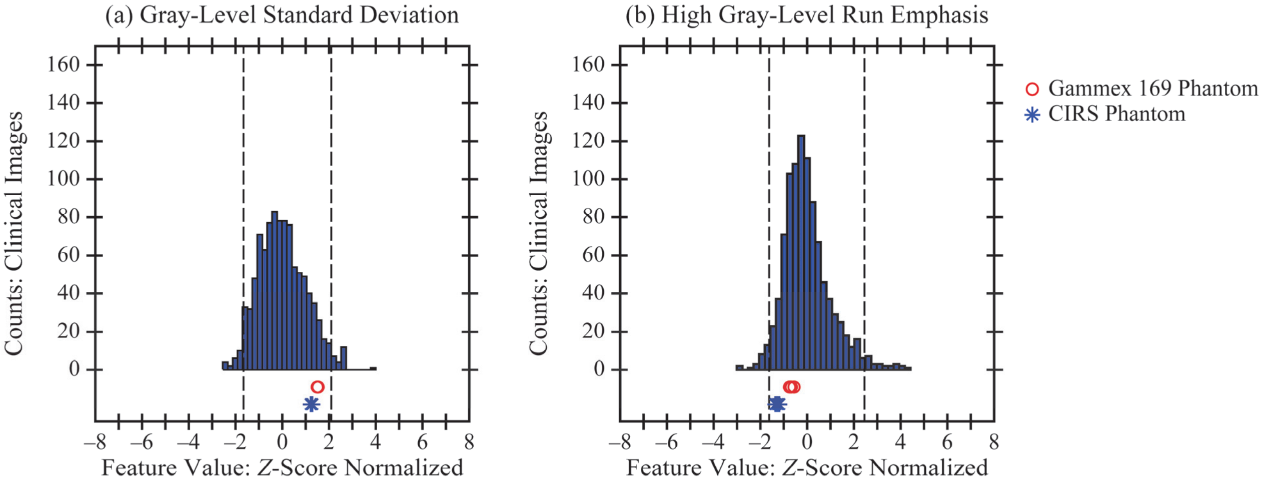

Figure 3. Each phantom was found to have realistic texture in terms of these two features. The phantom data points derived from six images are all within the middle 95% of the clinical distribution. Dashed lines denote the 2.5th and 97.5th percentiles of the clinical distribution.

2.4 Analysis of Textural Realism of Phantoms

For the two phantoms, the textural realism of each feature was defined based on the middle 95% of the clinical distribution; this was considered to be a realistic range of values for a feature. More specifically, a feature was considered realistic if all six data points derived from phantom images were between the 2.5th and 97.5th percentiles of the clinical distribution. By contrast, a feature was considered unrealistic if the percentile ranks of at least one of the six phantom data points was below 2.5% or above 97.5% (dashed vertical lines in Figures 3-5). Note that other definitions of realism exist, and that different conclusions may result from the use of alternate definitions of realism. For example, in Figure 3, both phantoms are deemed realistic by our metric, but if we defined textural realism in terms of closeness to the 50th percentile of the clinical distribution, then the CIRS phantom is more realistic in terms of the gray-level standard deviation and the Gammex 169 phantom is more realistic in terms of high gray-level run emphasis.

3. RESULTS

3.1 Calculations of Textural Realism

For each feature, the distribution of values in the clinical data set was *Z*-score normalized and plotted as a histogram (Figures 3-5). This normalization was also applied to the six phantom data points. To illustrate examples of realistic texture in both phantoms, standard deviation (a gray-level feature) and high gray-level run emphasis (a run length feature) are shown in Figure 3. In these examples, the six data points derived from the phantom acquisitions are clustered over a narrow range of values within the middle 95% of the clinical distribution.

Table 3. Summary statistics for each phantom were calculated separately by feature family.

Feature Family (Number of Features)	Realistic Features in CIRS Phantom	Realistic Features in Gammex 169 Phantom
Co-occurrence (7)	7 (100%)	3 (42.86%)
Co-occurrence Laws (120)	106 (88.33%)	87 (72.50%)
Fractal Dimension (2)	1 (50%)	0 (0%)
Gabor Wavelet (32)	32 (100%)	32 (100%)
Gray Level (12)	12 (100%)	12 (100%)
Laws (125)	111 (88.80%)	93 (74.40%)
LBP (36)	29 (80.56%)	29 (80.56%)
Run Length (7)	7 (100%)	5 (71.43%)

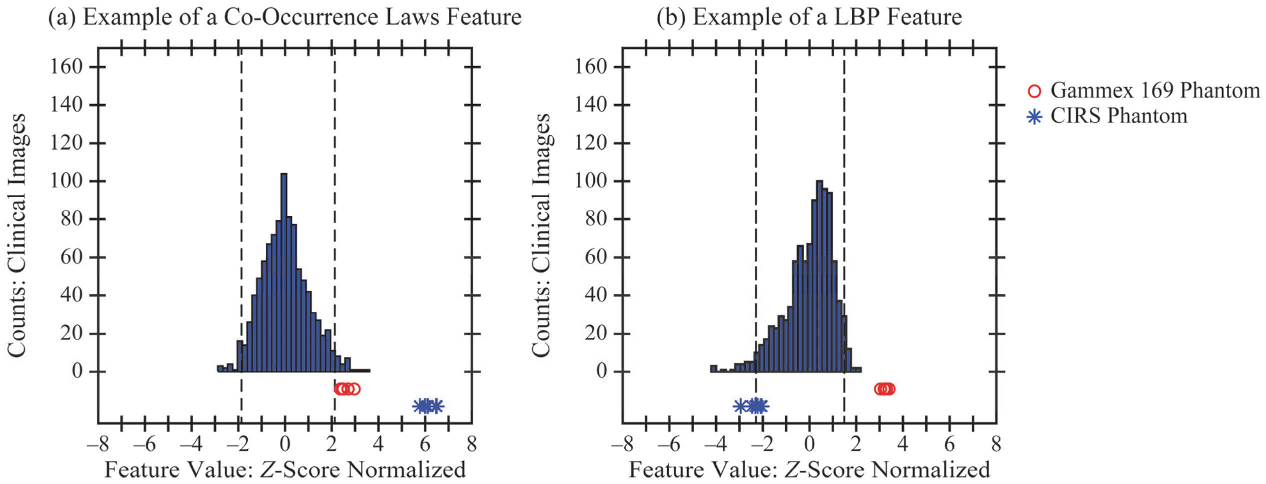

Figure 4. The phantoms were found to have unrealistic texture in terms of these two features. At least one of the six phantom data points is outside the middle 95% of the clinical distribution.

To illustrate the opposite result (unrealistic texture in both phantoms), two additional examples are shown in Figure 4. In some features, all six phantom data points were outside the middle 95% of the clinical distribution, as can be seen in one of the co-occurrence Laws features [Figure 4(a)]. The texture was also considered unrealistic if any subset of phantom data points was outside the middle 95% of the clinical distribution [Figure 4(b)].

3.2 Summary Statistics

The CIRS phantom was found to have realistic texture in terms of 305 features out of 341 (89.44%). By contrast, the Gammex 169 phantom was found to have realistic texture in terms of 261 features out of 341 (76.54%). These results can be analyzed in more detail on the basis of individual feature families (Table 3). The phantoms showed realistic texture in terms of all the gray-level and Gabor Wavelet features. The phantoms showed unrealistic texture in terms of some measures of fine structural detail.

It is also useful to create a confusion matrix (a 2 × 2 table) summarizing the results for each phantom (Table 4). Both phantoms were shown to have realistic texture in terms of 239 features (70.09%) and unrealistic texture in terms of 14 features (4.11%). In addition, there are 88 features (25.81%) for which the texture is realistic in one phantom but not the other; Figure 5 shows examples of these features.

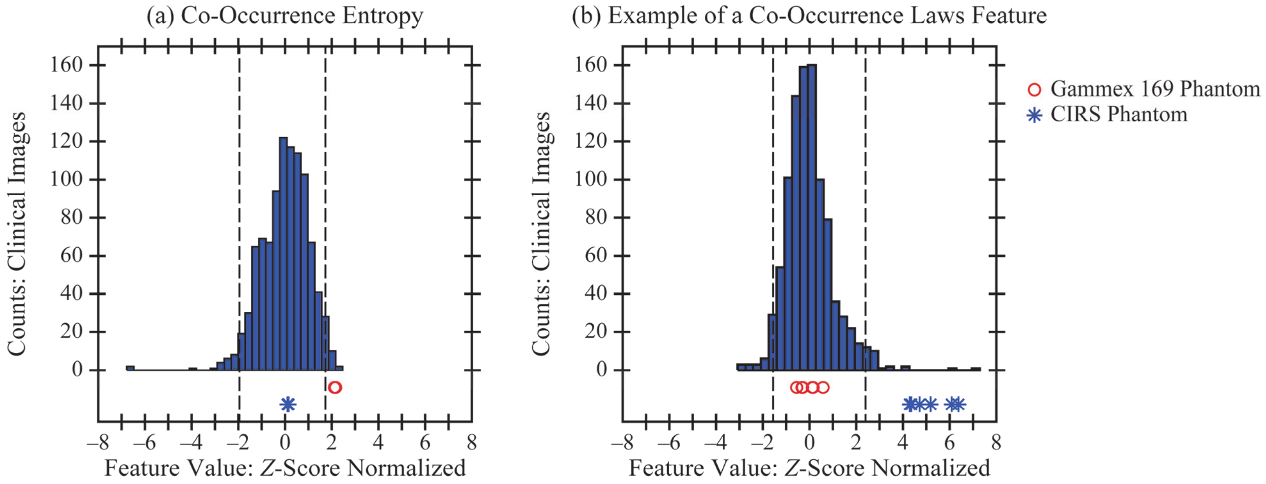

Figure 5. In some features, only one of the two phantoms was shown to have realistic texture; for example, the CIRS phantom in terms of co-occurrence entropy and the Gammex 169 phantom in terms of a Co-Occurrence Laws features.

Table 4. Summary statistics for each phantom can be analyzed with a confusion matrix.

		Gammex 169 Phantom		
		Realistic	Unrealistic	
CIRS Phantom	Realistic	239 (70.09%)	66 (19.35%)	305 (89.44%)
	Unrealistic	22 (6.45%)	14 (4.11%)	36 (10.56%)
		261 (76.54%)	80 (23.46%)	341 (100%)

4. DISCUSSION AND CONCLUSION

This paper evaluates the textural realism of two phantoms for DM. One would expect the Gammex 169 phantom to have realistic texture by its very nature, since it was created from an actual patient's mammogram. In this paper, we offer a validation of the textural realism of this phantom, and show that the CIRS phantom also has realistic texture. We conclude that phantoms based off a computational model can indeed have realistic texture.

In the years since the CIRS phantom was 3D printed, there have been advancements in the voxel phantom. The phantom now includes a model of tissue microstructure, which is simulated with the use of subcompartments of breast tissue designed to match the appearance of histological images.[19] Future work should investigate how the texture of the phantom changes based on the addition of these finer details.

5. ACKNOWLEDGEMENT

Support was provided by the following grants: R01CA207084 and U54CA163313 from the National Institute of Health, W81XWH-18-1-0082 from the Department of Defense Breast Cancer Research Program, and PDF17479714 from Susan G. Komen®. The content is solely the responsibility of the authors and does not necessarily represent the official views of the funding agencies.

ADAM receives research support from Hologic Inc., Barco NV, and Analogic Corporation. Also, ADAM is a shareholder and member of the scientific advisory board of Real Time Tomography, LLC. EFC receives grant support and is part of the advisory panel of Hologic Inc. EFC also receives grant support and is part of the advisory panel of iCAD Inc.

6. REFERENCES

1. Boyd NF, Rommens JM, Vogt K, et al. Mammographic breast density as an intermediate phenotype for breast cancer. *The Lancet Oncology.* 2005;6(10):798-808.
2. Boyd NF, Guo H, Martin LJ, et al. Mammographic Density and the Risk and Detection of Breast Cancer. *The New England Journal of Medicine.* 2007;356(3):227-236.
3. Zheng Y, Keller BM, Ray S, et al. Parenchymal texture analysis in digital mammography: A fully automated pipeline for breast cancer risk assessment. *Medical Physics.* 2015;42(7):4149-4160.
4. Gastounioti A, Conant EF, Kontos D. Beyond breast density: a review on the advancing role of parenchymal texture analysis in breast cancer risk assessment. *Breast Cancer Research.* 2016;18:91.
5. Chui JH, Pokrajac DD, Maidment ADA, Bakic PR. Towards Breast Anatomy Simulation Using GPUs. *Lecture Notes in Computer Science.* 2012;7361:506-513.
6. Pokrajac DD, Maidment ADA, Bakic PR. Optimized generation of high resolution breast anthropomorphic software phantoms. *Medical Physics.* 2012;39(4):2290-2302.

7. Chui JH, Zeng R, Pokrajac DD, et al. Two Methods for Simulation of Dense Tissue Distribution in Software Breast Phantoms. Paper presented at: SPIE Medical Imaging2013; Orlando, FL.
8. Barufaldi B, Bakic PR, Pokrajac DD, Lago MA, Maidment ADA. Developing Populations of Software Breast Phantoms for Virtual Clinical Trials. Paper presented at: 14th International Workshop on Breast Imaging (IWBI 2018)2018; Atlanta, GA.
9. Cockmartin L, Bakic PR, Bosmans H, et al. Power Spectrum Analysis of an Anthropomorphic Breast Phantom Compared to Patient Data in 2D Digital Mammography and Breast Tomosynthesis. *Lecture Notes in Computer Science.* 2014;8539:423-429.
10. Vieira MAC, Oliveira HCRd, Nunes PF, et al. Feasibility Study of Dose Reduction in Digital Breast Tomosynthesis Using Non-Local Denoising Algorithms. Paper presented at: SPIE Medical Imaging2015; Orlando, FL.
11. Yaffe MJ, Johns PC, Nishikawa RM, Mawdsley GE, Caldwell CB. Anthropomorphic radiologic phantoms. *Radiology.* 1986;158(2):550-552.
12. Acciavatti RJ, Hsieh M-K, Gastounioti A, et al. Validation of the Textural Realism of a 3D Anthropomorphic Phantom for Digital Breast Tomosynthesis. Paper presented at: 14th International Workshop on Breast Imaging (IWBI 2018)2018; Atlanta, GA.
13. Keller BM, Nathan DL, Wang Y, et al. Estimation of breast percent density in raw and processed full field digital mammography images via adaptive fuzzy c-means clustering and support vector machine segmentation. *Medical Physics.* 2012;39(8):4903-4917.
14. Haralick RM, Shanmugam K, Dinstein IH. Textural Features for Image Classification. *IEEE Transactions on Systems, Man, and Cybernetics.* 1973;SMC-3(6):610-621.
15. Galloway MM. Texture analysis using gray level run lengths. *Computer Graphics and Image Processing.* 1975;4(2):172-179.
16. Chu A, Sehgal CM, Greenleaf JF. Use of gray value distribution of run lengths for texture analysis. *Pattern Recognition Letters.* 1990;11(6):415-419.
17. Ojala T, Pietikäinen M, Mäenpää T. Multiresolution Gray-Scale and Rotation Invariant Texture Classification with Local Binary Patterns. *IEEE Transactions on Pattern Analysis and Machine Intelligence.* 2002;24(7):971-987.
18. Manduca A, Carston MJ, Heine JJ, et al. Texture Features from Mammographic Images and Risk of Breast Cancer. *Cancer Epidemiology, Biomarkers & Prevention.* 2009;18(3):837-845.
19. Bakic PR, Pokrajac DD, Caro RD, Maidment ADA. Realistic Simulation of Breast Tissue Microstructure in Software Anthropomorphic Phantoms. *Lecture Notes in Computer Science.* 2014;8539:348-355.

MRMC ROC Analysis of Calcification Detection in Tomosynthesis Using Computed Super Resolution and Virtual Clinical Trials

Bruno Barufaldi*, Trevor L. Vent, Raymond J. Acciavatti, Predrag R. Bakic, Peter B. Noël and Andrew D. A. Maidment

Department of Radiology, University of Pennsylvania, Philadelphia, United States.
*Bruno.Barufaldi@pennmedicine.upenn.edu

ABSTRACT

Digital breast tomosynthesis (DBT) reduces breast tissue overlap, which is a major limitation of digital mammography. However, DBT does not show significant improvement in calcification detection, because of the limited angle and small number of projections used to reconstruct the 3D breast volume. Virtual clinical trials (VCTs) were used to evaluate the benefits of computed super resolution (SR) and the optimal combination of the acquisition parameters to improve calcification detection in DBT. We simulated calcifications that were embedded into software breast phantoms. DBT projections of the breast phantoms with and without calcifications were synthesized. We simulated detector elements of 0.085 mm and reconstructed DBT images using 0.0425 mm and 0.085 mm voxels. Channelized Hotelling observers (CHOs) were trained and tested to simulate five virtual readers. Differences in area under the curve (AUC) between SR images and images synthesized with 0.085 mm voxels were calculated using the one-shot multiple-reader multiple-case receiver operator curve (MRMC ROC) methods. Our results show that the differences in AUC is approximately 0.10, 0.03 and 0.03 for DBT images simulated using calcifications sizes 0.001 mm^3, 0.002 mm^3, and 0.003 mm^3, respectively. SR shows a substantial improvement for calcification detection in DBT. The impact of SR on calcification detection is more prominent for small calcifications.

Keywords: virtual clinical trial; multiple-reader, multiple-case; digital breast tomosynthesis; super resolution.

1. INTRODUCTION

Digital breast tomosynthesis (DBT) has been shown to reduce recall rates by resolving overlapped breast structures seen on digital mammography.[1] However, there is some concern that DBT may not depict small breast structures such as calcifications,[2,3] due to the limited angle and small number of tomographic projections. Alternative imaging methods are required to improve calcification detection and to maximize the benefits of mammography screening with DBT.

Computed super-resolution (SR) is a reconstruction method with pixels that are smaller than the detector element size; superior spatial resolution is achieved through the elimination of aliasing and alteration of the sampling function imposed by the reconstructed pixel aperture.[4] However, this reconstruction method is not well explored by others because it can increase the image size and time to reconstruct tomographic projections.

We have developed an open-source Virtual Clinical Trial (Open VCT) framework that allows the projection and reconstruction of DBT images in real-time. Our VCT framework has been used to evaluate and to optimize imaging systems by performing simulations of the human breast anatomy, DBT image acquisition, and image interpretation.[5–7]

We have shown in a previous study that calcification detection in DBT is substantially affected by reconstructed voxel size, detector element size, and tube motion.[8] However, the optimal combination of acquisition parameters in DBT is still under investigation.[9] VCTs can be used to investigate the limit of calcification detection and to evaluate promising imaging designs, avoiding the pursuit of inefficient DBT acquisition parameters.[8,10]

In this work, we present a VCT method for determining the most suitable reconstructed voxel size for calcification detection in DBT. Voxelized single calcifications 0.001 mm^3, 0.002 mm^3, and 0.003 mm^3 were inserted into software breast phantoms. Fifteen DBT projections of the breast phantoms with and without lesions were synthesized simulating the imaging geometry of the next generation of tomosynthesis (NGT) system. We simulated and varied the reconstructed voxel size using 0.0425 mm and 0.085 mm, with 0.085 mm detector elements (del). We also simulate five virtual readers to evaluate the calcification detection using multiple-reader, multiple-case (MRMC) receiver operator curve (ROC) analyses.[11]

15th International Workshop on Breast Imaging (IWBI2020), edited by Hilde Bosmans,
Nicholas Marshall, Chantal Van Ongeval, Proc. of SPIE Vol. 11513, 1151313
· doi: 10.1117/12.2564118

2. MATERIALS & METHODS

2.1 DBT Image Simulations

Virtual anthropomorphic breast phantoms were developed to simulate healthy breast anatomy using an efficient recursive partitioning method.[12,13] The recursive partitioning method supports a large number of breast simulations in terms of simulations per GPU-hour.[5] In this work, we simulated 80 breast phantoms with 700mL and uncompressed breast thickness of 126.6 mm. We combined coarse- and fine-breast phantoms,[13] with volumetric breast densities that varied from 5% to 60% to improve the realism of the anthropomorphic breast phantoms.

The simulation of medio-lateral (ML) breast compression uses a GPU accelerated 3D mesh software.[14] The breast tissue compression was simulated using neo-Hookean models, with Poisson ratio of 0.49 and Young's modulus of 12.75 kPa, to reduce the phantom thickness by 50% (thickness=63.3 mm).[6]

Single calcifications were simulated using one-, two- and three- voxel polycubes,[13] with individual cubic voxels of size 0.1 mm. The calcification composition was varied by a weighting factor, which controls the calcification attenuation in the synthesized x-ray image. This factor represents the fraction of hydroxyapatite in the calcifications (Figure 1). The weighting factor was varied as a fraction of 0.30, 0.40, and 0.50 hydroxyapatite. The specific range of weighting factors was selected based upon results presented in a previous study. We inserted a dense array of 42 calcifications, arranged 20 mm apart, into each compressed breast phantoms. The array was positioned in the central plane parallel to detector at the level of the nipple (ML phantom view). The method used for inserting calcifications into the breast phantoms was described in previous studies.[8,15]

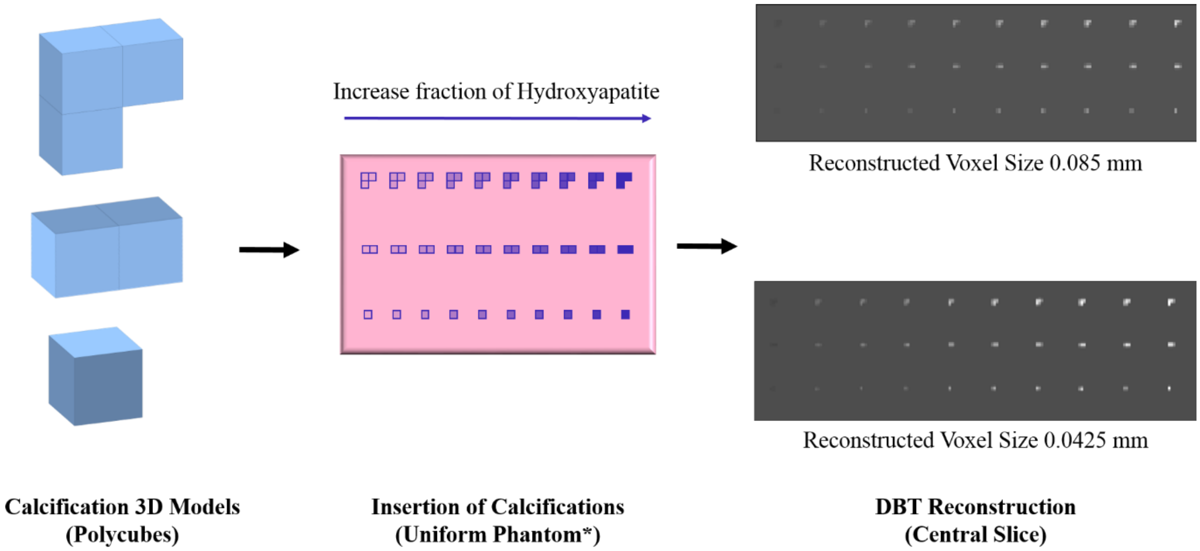

Figure 1. Method used to insert calcifications into the anthropomorphic breast phantoms. *Illustrative phantom used to visualize differences in fraction of hydroxyapatite in the DBT reconstructions.

In this study, we simulated the NGT acquisition geometry to synthesize DBT projections of the breast phantoms with and without calcifications. The image acquisition was simulated using step-and-shoot tube motion, and the angular range of the x-ray source was simulated using ±7.5°. In total, 15 equally-spaced DBT projections were simulated using the Siddon algorithm for x-ray tracing.[16] The DBT projections were generated using 0.085 mm^2 del, with a detector contained a total of 3584×2816 dels. The DBT images were reconstructed using 0.085 mm and 0.0425 mm reconstructed voxel sizes. DBT images reconstructed with 0.0425 mm voxel size represent the SR images. The images were reconstructed only at the central ML phantom view to accelerate the image simulations. The reconstructed DBT images were synthesized using the Briona software (Real-Time Tomography, Villanova, PA).[17]

We cropped regions of interest (ROIs) with and without calcifications, with sizes of 175×175 and 350×350 pixels for each image reconstructed using 0.085 mm and 0.0425 mm reconstructed voxel size, respectively. The ROIs with lesions were selected with the calcifications centered at the ROI.

2.2 Virtual Readers and ROC analyses

Channelized Hotelling observers (CHOs) were trained and tested to simulate five virtual readers.[18,19] The CHOs were simulated using 15 Laguerre-Gauss (LG) channels. We used LG spread sizes of 26 and 52, for each image reconstructed with reconstructed voxel size of 0.085 mm and 0.0425 mm, respectively. For each reader, independent training and testing image sets included 252 ROIs with simulated calcifications and 252 calcification-free ROIs. The readers were tested with a common image set that also included 252 ROIs. The ROIs used for training and testing were selected randomly.

We measured the readers' performance in calcification detection using MRMC ROC analyses provided by the MeVIC software (Barco NV, Kortrijk, Belgium).[20] The MeVIC software provides a module that estimates one-shot MRMC statistics.[11,21] We calculated the ROCs of each individual reader using the readers' scores. We analyzed the difference in area under the curve (AUC) and SE AUC between readers. We also evaluated differences in AUC between SR images and images reconstructed with 0.085 mm voxel size. Finally, we calculated the one-shot MRMC, which summarizes the ROC statistics of five readers.

3. RESULTS & DISCUSSION

The following parameters were varied and evaluated in our DBT simulations: number of calcification voxels (1, 2, and 3), weighting factor (0.30, 0.40, and 0.50), and reconstructed voxel size (0.0425 mm and 0.085 mm). The detector element did not vary (0.085 mm), so we can evaluate the performance of each individual reader in calcification detection using smaller reconstructed voxel sizes (i.e., SR images). The pooled ROC curves of mixed calcifications using the three weighting factors are shown in Figure 2. Note that there is a small variation between readers for each analyzed condition because of the large number of ROIs used for training and testing. There is a significant improvement in the calcification detection using smaller reconstructed voxels; this is more prominent for 1-voxel calcifications.

The AUC results of each reader are summarized in Table 1. Note that SR images (Table 1B, Table 1D, and Table 1F) have an AUC improvement in calcification detection. The improvement in detection of SR images results in a difference in AUC of approximately 0.10, 0.03, and 0.03 for 1-, 2-, and 3- voxel calcifications. For DBT projections simulated using 0.085 mm del, the calcification detection is substantially affected using SR images. Again, the SR impact is more prominent for images synthesized using 1- voxel calcification.

For calcification detection, the difference in AUC between SR images and images synthesized with 0.085 mm reconstructed voxel size were calculated using the one-shot MRMC ROC analysis (Figure 3). For 1-voxel calcifications, the difference in AUC of SR and images reconstructed using 0.085 mm del was 0.11, 0.08 and 0.11 for DBT images simulated using weighting factors 0.3, 0.4, and 0.5, respectively. For 2-voxel calcifications, the difference in AUC of SR and images reconstructed using 0.085 mm del was 0.02, 0.03 and 0.03 for DBT images simulated using weighting factors 0.3, 0.4, and 0.5, respectively. Finally, for 3-voxel calcifications, the difference in AUC of SR and images reconstructed using 0.085 mm del was 0.06, 0.02 and 0.01 for DBT images simulated using weighting factors 0.3, 0.4, and 0.5, respectively. Although the AUC difference is higher for 1-voxel calcifications, the standard deviation is also higher.

To predict readers' performance in calcification detection, synthetic calcifications should be calibrated based upon the size and composition of calcifications found in breast carcinomas. In this study, we simulated single calcifications as polycubes (i.e., cubic calcifications) of sizes 0.001 mm^3, 0.002 mm^3, and 0.003 mm^3 to predict and to evaluate the *limit in calcification detection* of DBT. Previous stereoscopic studies have shown clusters of punctuated calcifications of variable sizes from 0.1 to 0.3 mm, [23,24] which represent spherical calcifications of diameters 0.124, 0.156, and 0.180 mm in the DBT image. In addition, calcifications should be simulated using admixtures of different material compositions [e.g., $Ca_3(PO_4)_2$, $CaCo_3$, $Mg_3(PO_4)_2 \cdot H_2O$, Protein, etc.].[23,24] Thus, we varied the weighting factors of hydroxyapatite to simulate more realistic calcifications.

Ultimately, we will evaluate calcification detection in DBT using SR images synthesized with larger detector element sizes, and a range of weighting factors. We will also calculate the *d'* statistics and validate results acquired using the one-shot MRMC ROC analyses. The *d'* represents the *effective signal-to-noise ratio perceived by the observer*, while the AUC represents values that vary non-linearly from 0.5 (i.e., random guessing) to 1.0 (i.e., relationship between disease and normal found with 100% certainty). Based upon results in previous studies,[8,15] we can better discriminate improvement in the performance of calcification detection in DBT by calculating the ratio of *d'* between the new and the predicate DBT acquisition geometry instead of difference in AUCs.

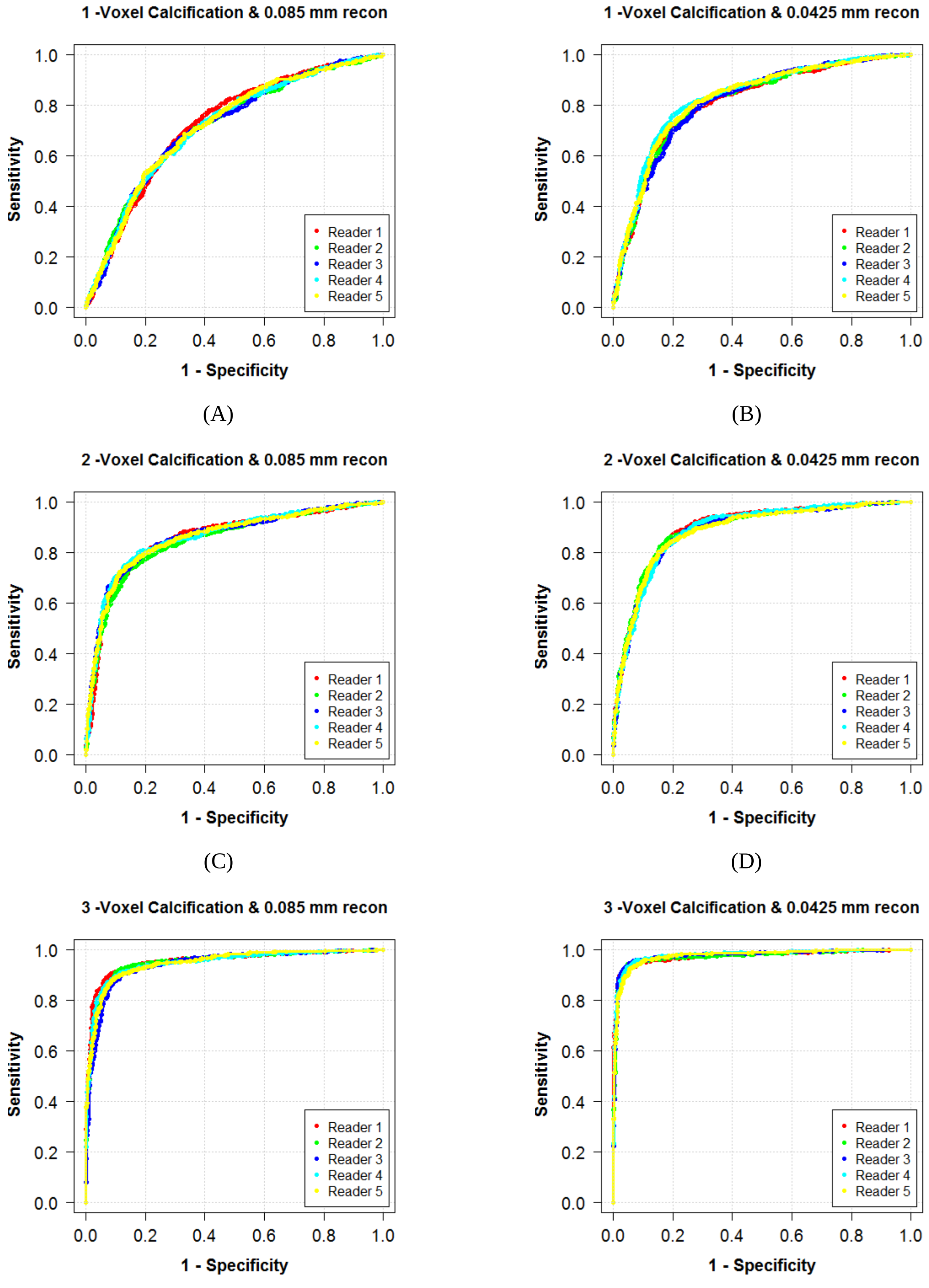

(A) (B)

(C) (D)

(E) (F)

Figure 2. ROC curves of each individual reader using the image set: (left) 0.085 mm reconstructed voxel size and (right) 0.0425 mm reconstructed voxel size.

Table 1. Summary of the AUCs of each individual reader: (left) 0.085 mm reconstructed voxel size and (right) 0.0425 mm reconstructed voxel size. Standard error (SE) AUC, and 95% CI upper and lower are also shown.

	(A) 1-Voxel Calcification & 0.085 mm recon					**(B) 1-Voxel Calcification & 0.0425 mm recon**				
	Reader 1	**Reader 2**	**Reader 3**	**Reader 4**	**Reader 5**	**Reader 1**	**Reader 2**	**Reader 3**	**Reader 4**	**Reader 5**
AUC	0.724	0.716	0.715	0.717	0.719	0.812	0.814	0.814	0.830	0.824
SE AUC	0.013	0.013	0.013	0.013	0.013	0.011	0.011	0.011	0.011	0.011
95% CI upper	0.749	0.742	0.741	0.742	0.744	0.834	0.835	0.836	0.850	0.845
95% CI lower	0.698	0.690	0.689	0.691	0.693	0.790	0.792	0.793	0.809	0.803
	(C) 2-Voxel Calcification & 0.085 mm recon					**(D) 2-Voxel Calcification & 0.0425 mm recon**				
	Reader 1	**Reader 2**	**Reader 3**	**Reader 4**	**Reader 5**	**Reader 1**	**Reader 2**	**Reader 3**	**Reader 4**	**Reader 5**
AUC	0.858	0.849	0.863	0.863	0.861	0.895	0.891	0.885	0.890	0.885
SE AUC	0.010	0.010	0.010	0.010	0.010	0.008	0.008	0.009	0.008	0.009
95% CI upper	0.878	0.869	0.882	0.882	0.880	0.911	0.907	0.902	0.906	0.902
95% CI lower	0.839	0.829	0.844	0.844	0.842	0.878	0.874	0.868	0.873	0.868
	(E) 3-Voxel Calcification & 0.085 mm recon					**(F) 3-Voxel Calcification & 0.0425 mm recon**				
	Reader 1	**Reader 2**	**Reader 3**	**Reader 4**	**Reader 5**	**Reader 1**	**Reader 2**	**Reader 3**	**Reader 4**	**Reader 5**
AUC	0.956	0.951	0.944	0.950	0.950	0.975	0.973	0.978	0.981	0.977
SE AUC	0.005	0.006	0.006	0.006	0.005	0.004	0.004	0.004	0.003	0.004
95% CI upper	0.967	0.962	0.955	0.961	0.961	0.983	0.982	0.986	0.987	0.984
95% CI lower	0.946	0.941	0.932	0.939	0.940	0.968	0.965	0.971	0.975	0.971

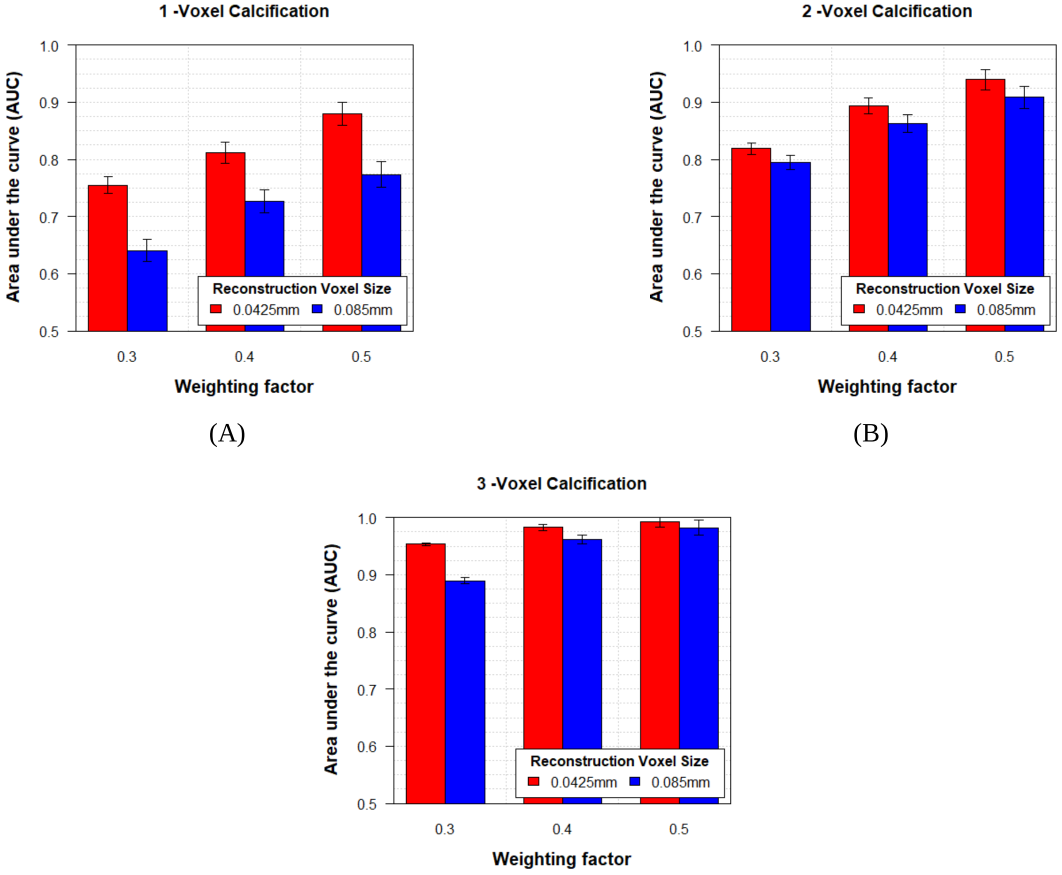

(A) (B)

(C)

Figure 3. Summary of the AUCs of one-shot MRMC ROC analyses, categorized by weighing factor. Standard deviations between five virtual readers are shown.

4. CONCLUSION

In this study, we sought to determine the most suitable reconstructed voxel size for calcification detection in DBT, as well as to analyze the impact of computed-SR in calcification detection. Computed-SR is superior to conventional reconstruction methods for calcification detection in DBT. In this study, the impact of SR on calcification detection is more prominent for small calcifications. These results are still preliminary; however, we believe they provide guidance on how to improve the detectability of calcifications, which is an ongoing problem in tomosynthesis. Analysis of how additional conditions may affect calcification detection are forthcoming.

ACKNOWLEDGEMENTS

Funding for the research is supported by the following grants: NIH R01 CA154444, NIH R01 EB018958, Komen IIR-13262248, BWF IRSA 1016451, and DoD W81XWH-18-1-0082.

REFERENCES

[1] Gur, D., Abrams, G. S., Chough, D. M., Ganott, M. a., Hakim, C. M., Perrin, R. L., Rathfon, G. Y., Sumkin, J. H., Zuley, M. L. and Bandos, A. I., "Digital breast tomosynthesis: Observer performance study," Am. J. Roentgenol. **193**(2), 586–591 (2009).

[2] Poplack, S. P., Tosteson, T. D., Kogel, C. A. and Nagy, H. M., "Digital breast tomosynthesis: Initial experience in 98 women with abnormal digital screening mammography," Am. J. Roentgenol. **189**(3), 616–623 (2007).

[3] Rafferty, E. A., Park, J. M., Philpotts, L. E., Poplack, S. P., Sumkin, J. H., Halpern, E. F. and Niklason, L. T., "Diagnostic accuracy and recall rates for digital mammography and digital mammography combined with one-view and two-view tomosynthesis: Results of an enriched reader study," Am. J. Roentgenol. **202**(2), 273–281 (2014).

[4] Maidment, T. D., Vent, T. L., Ferris, W. S., Wurtele, D. E., Acciavatti, R. J. and Maidment, A. D. A., "Comparing the imaging performance of computed super resolution and magnification tomosynthesis," Med. Imaging 2017 Phys. Med. Imaging **10132**, 1013222 (2017).

[5] Barufaldi, B., Bakic, P. R., Higginbotham, D. and Maidment, A. D. A., "OpenVCT: a GPU-accelerated virtual clinical trial pipeline for mammography and digital breast tomosynthesis," SPIE Med. Imaging 2018 **1057358**(March), 1–8, Houston, TX (2018).

[6] Barufaldi, B., Bakic, P. R., Pokrajac, D. D., Lago, M. A. and Maidment, A. D. A., "Developing populations of software breast phantoms for virtual clinical trials," 14th Int. Work. Breast Imaging (IWBI 2018)(July), 73 (2018).

[7] Badano, A., Graff, C. G., Badal, A., Sharma, D., Zeng, R., Samuelson, F. W., Glick, S. J. and Myers, K. J., "Evaluation of Digital Breast Tomosynthesis as Replacement of Full-Field Digital Mammography Using an In Silico Imaging Trial," JAMA Netw. Open **1**(7), 1–12 (2018).

[8] Barufaldi, B., Bakic, P. R. and Maidment, A. D. A., "Multiple-reader, multiple-case ROC analysis for determining the limit of calcification detection in tomosynthesis," SPIE Med. Imaging 2019 Phys. od Med. Imaging **10948**(March), 22 (2019).

[9] Elangovan, P., Mackenzie, A., Dance, D. R., Young, K. C., Cooke, V., Wilkinson, L., Given-Wilson, R. M., Wallis, M. G. and Wells, K., "Design and validation of realistic breast models for use in multiple alternative forced choice virtual clinical trials," Phys. Med. Biol. (2017).

[10] Vent, T. L., Barufaldi, B. and Maidment, A. D. A., "Simulation and experimental validation of high-resolution test objects for evaluating a next-generation digital breast tomosynthesis prototype," SPIE Med. Imaging 2019(March), 21 (2019).

[11] Gallas, B. D., "One-shot estimate of MRMC variance: AUC," Acad. Radiol. **13**(3), 353–362 (2006).

[12] Pokrajac, D. D., Maidment, A. D. A. and Bakic, P. R., "Optimized generation of high resolution breast anthropomorphic software phantoms," Med. Phys. **39**(4), 2290 (2012).

[13] Bakic, P. R., Barufaldi, B., Pokrajac, D., Weinstein, S. P. and Maidment, A. D., "Optimized simulation of breast anatomy for virtual clinical trials," 14th Int. Work. Breast Imaging (IWBI 2018)(July), 73 (2018).

[14] Lago, M. A., Maidment, A. D. A. and Bakic, P. R., “Modelling of mammographic compression of anthropomorphic software breast phantom using FEBio,” Int’l Symp. Comput. Methods Biomech. Biomed. Eng., Salt Lake City, UT (2013).

[15] Bakic, P. R., Barufaldi, B., Higginbotham, D., Weinstein, S. P., Avanaki, A., Espig, K., Xthona, A., Kimpe, T. and Maidment, A. D. A., “Virtual clinical trial of lesion detection in digital mammography and digital breast tomosynthesis,” SPIE Med. Imaging 2018 **1057306**(March), 1–13 (2018).

[16] Siddon, R. L., “Fast calculation of the exact radiological path for a three dimensional CT array,” Med. Phys. **12**(2), 252–255 (1985).

[17] Kuo, J., Ringer, P. A., Fallows, S. G., Bakic, P. R., Maidment, A. D. A. and Ng, S., “Dynamic reconstruction and rendering of 3D tomosynthesis images,” SPIE Med. Imaging **796116**(March 2011), 796116-796116–11, Orlando, FL (2011).

[18] Abbey, C. K. and Barrett, H. H., “Human- and model-observer performance in ramp-spectrum noise: effects of regularization and object variability,” J. Opt. Soc. Am. A (2001).

[19] Park, S., Zhang, G. and Myers, K. J., “Comparison of Channel Methods and Observer Models for the Task-Based Assessment of Multi-Projection Imaging in the Presence of Structured Anatomical Noise,” IEEE Trans. Med. Imaging **35**(6), 1431–1442 (2016).

[20] Marchessoux, C., Kimpe, T. and Bert, T., “A virtual image chain for perceived and clinical image quality of medical display,” IEEE/OSA J. Disp. Technol. **4**(4), 356–368 (2008).

[21] Gallas, B. D. and Barrett, H. H., “Validating the use of channels to estimate the ideal linear observer.,” J. Opt. Soc. Am. A. Opt. Image Sci. Vis. **20**(9), 1725–1738 (2003).

[22] Vedantham, S., Karellas, A., Vijayaraghavan, G. R. and Kopans, D. B., “Digital Breast Tomosynthesis: State of the Art,” Radiology **277**(3), 663–684 (2015).

[23] Lanyi, M. and Lanyi, M., “Clinically Occult, Mammographically Suspicious Microcalcification Clusters: Pre Intra-, and Postoperative Measures,” [Diagnosis and Differential Diagnosis of Breast Calcifications] (1986).

[24] Lanyi, M., [Diagnosis and Differential Diagnosis of Breast Calcifications] (1988).

Simulation of high-resolution test objects using non-isocentric acquisition geometries in next-generation digital tomosynthesis

Trevor L. Vent*, Bruno Barufaldi, Raymond J. Acciavatti, Andrew D.A. Maidment
Department of Radiology, University of Pennsylvania, Philadelphia, United States.
*Trevor.Vent@pennmedicine.upenn.edu

ABSTRACT

Digital breast tomosynthesis (DBT) systems utilize an isocentric acquisition geometry which introduces imaging artifacts that are deleterious to image reconstructions. The next-generation tomosynthesis (NGT) prototype was designed to incorporate various x-ray source and detector motions for the purpose of investigating alternative acquisition geometries for DBT. Non-isocentric acquisition geometries, acquisitions that vary the image magnification between projection images, are capable of ameliorating aliasing and other artifacts that are intrinsic to conventional DBT. We used virtual clinical trials (VCTs) to develop custom acquisition geometries for the NGT prototype. A high-resolution (5µm voxel size) star pattern test object was simulated to compare the high-frequency performance of isocentric with non-isocentric image reconstructions. A tilted bar pattern test object was also simulated to compare multiplanar reconstructions (MPR) of isocentric and non-isocentric acquisition geometries. Two source- and detector-motion paths were simulated to obtain super-sampled image reconstructions of the test objects. An aliasing-sensitive metric was used to evaluate spatial resolution performance for two orthogonal frequency orientations. Pairwise comparisons were made for the two frequency orientations between the isocentric and non-isocentric acquisition geometries. Non-isocentric acquisition geometries show an improvement over isocentric acquisition geometries. The greatest improvement was 75.2% for frequencies aligned perpendicular to x-ray source motion, which is the direction of frequencies for which DBT is prone to aliasing. Both frequency orientations exhibit super resolution for non-isocentric geometries. MPR of the tilted bar pattern show z-dependent degeneracies for the isocentric acquisition only, whereas MPR of the non-isocentric acquisition entirely exhibits super resolution.

Keywords: digital breast tomosynthesis, non-isocentric tomosynthesis, physics virtual clinical trial; ray tracing, radial fast Fourier transform, super-resolution, multiplanar reconstruction

1. INTRODUCTION

Digital breast tomosynthesis (DBT) acquires a three-dimensional (3D) image of a patient's breast by acquiring multiple, two-dimensional x-ray images from serial source positions. For a conventional DBT acquisition, the x-ray projections are acquired by translating the x-ray source along an arc in the mediolateral (ML) direction. The projections are spaced equidistantly in the chest-wall plane of the patient. This acquisition geometry is isocentric, because the arc rotates about a single fulcrum in space. Such DBT systems benefit the detection of masses and low-frequency objects in the breast. That said, the detection of high-frequency objects like microcalcifications, is not benefited by DBT when compared with full-field digital mammography (FFDM)[1].

Resolution for conventional DBT is anisotropic, favoring the frequencies that are aligned parallel to x-ray source motion ($\boldsymbol{\nu}_{\parallel}$) with super resolution. Using super-sampled image reconstructions, resolution for $\boldsymbol{\nu}_{\parallel}$ can be increased twofold, whereas the frequencies aligned perpendicular to source motion ($\boldsymbol{\nu}_{\perp}$) are limited to the alias frequency of the detector. Super resolution improves the resolution of periodic objects and the overall appearance and texture of breast tissue and lesions in image reconstructions.

The next-generation tomosynthesis (NGT) system is a DBT prototype that has been developed to improve the detection of microcalcifications in the breast. This prototype system investigates alternative acquisition geometries by introducing novel x-ray source and detector motions. The introduction of posteroanterior (PA) x-ray source motion has been shown to improve the spatial resolution[2–5] and volume estimation of anthropomorphic breast phantoms in image reconstructions[6,7]. Non-isocentric acquisition geometries, acquisitions that increment the detector **z**-position between each projection, can further improve spatial sampling. Non-isocentric acquisitions can also lessen the impact of imaging artifacts like masking[8,9], spatial resolution anisotropies[10–12], and aliasing[11,13] in image reconstructions.

15th International Workshop on Breast Imaging (IWBI2020), edited by Hilde Bosmans,
Nicholas Marshall, Chantal Van Ongeval, Proc. of SPIE Vol. 11513, 1151317
© 2020 SPIE · CCC code: 0277-786X/20/$21 · doi: 10.1117/12.2561098

The primary method for validating the performance of these prototypes is through clinical trials. Clinical trials of medical imaging systems require a large number of patients, who are imaged repeatedly to compare the performance of different systems. The associated cost, duration, and radiation risk represent a significant impediment to the efficient introduction of novel imaging technologies. Virtual clinical trials (VCTs) represent an approach, based upon computer simulation of human anatomy and imaging modalities, which can help develop, optimize, and validate new and existing medical imaging methods. Fast and detailed simulations of device performance are also instrumental in prototyping clinical trials and augmenting them with simulated data, and may also assist with regulatory approval[4,14,15].

Physics VCTs, in contrast to traditional VCTs, are intended to evaluate the implementation of the novel designs using simulated image acquisitions of virtual test objects and objective metrics to evaluate device performance. We have used physics VCTs to investigate novel acquisition geometries for the NGT prototype[4]. We have shown that physics VCTs can be used to investigate novel acquisition geometries for the NGT system without exhausting resources. In this work, we use physics VCTs and high-resolution test objects to compare the performance of isocentric with non-isocentric acquisition geometries for DBT using configurations of the NGT prototype.

2. MATERIALS & METHOD

Virtual Clinical Trial pipeline

Physics VCTs are implemented using the X-ray Physics Lab's (XPL) physics VCT pipeline. The physics VCT pipeline has been modified from the original VCT pipeline. Physics VCTs simulate the image acquisition of physical test objects and phantoms. However, rather than using a virtual reader phase of the original VCT pipeline, objective measures of physics are used to evaluate the performance of an imaging device. A tomosynthesis acquisition is simulated, in the same manner as the original pipeline, using ray-tracing methods with a dedicated graphics processing unit (GPU). The mechanical configuration of the NGT prototype is modeled using the physics VCT pipeline, where various acquisition geometries can be simulated.

Next-generation tomosynthesis prototype

Alternative acquisition geometries of the NGT prototype are achieved by creating custom x-ray source and detector motion paths for a series of x-ray projection images. The collection of projection images obtained from each custom acquisition geometry are used for tomographic reconstructions. Details of this prototype have been described in previous work[3,4,16,17]. The origin of the NGT system is defined at the center of the chest-wall edge of the breast support (Figure 1). The **x**-**y** plane of the NGT system serves as an address space for the x-ray focal spot to determine an acquisition geometry. The range of the source is ±150mm in **x** and +180mm in **y**. The NGT achieves non-isocentric acquisition geometries by translating the

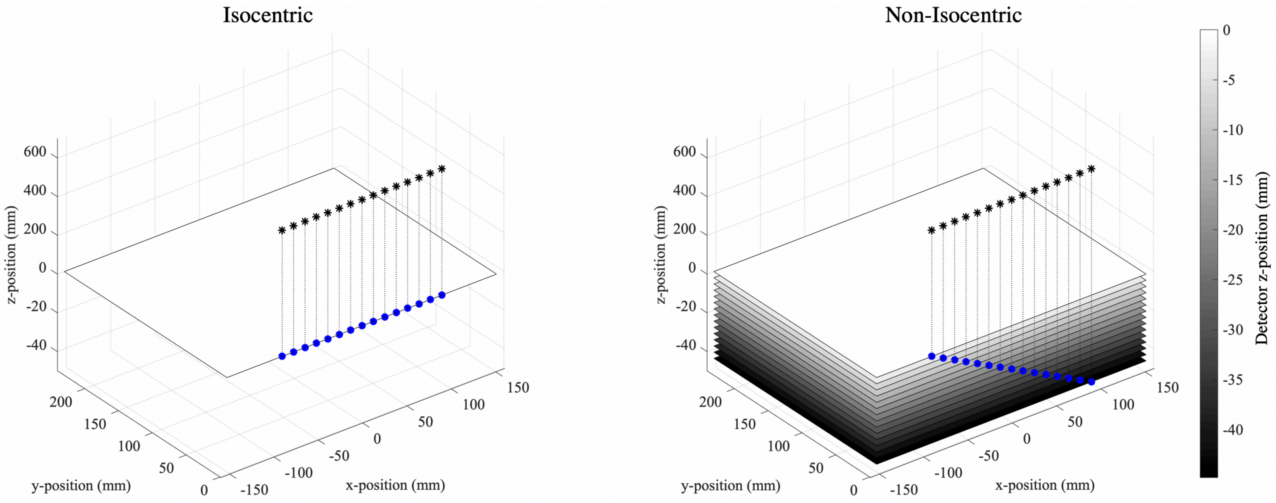

Figure 1: The two acquisition geometries that are used to simulate the NGT prototype. The black stars and blue dots indicate the position of the focal spot in the focal spot plane and the corresponding position of the focal spot relative to the detector position, respectively. **NB:** the positive and negative **z**-axes are scaled differently.

detector in **z** between x-ray projections with a 44.8mm range, translating 3.2 mm between projection over 15 projections. The configuration of the NGT prototype and the two acquisition geometries that are used for the physics VCT simulations in this study are shown in Figure 1. This study is constrained to the conventional x-ray source motion only and does not include acquisition geometries with PA source motion.

The geometric configuration and constraints of the NGT prototype dictate the image acquisition simulation of the physics VCTs. Physics VCTs simulate the radiographic technique for x-ray projection images that are used to render image reconstructions. Tomographic image reconstructions are created by filtered back-projection using commercial reconstruction software (Piccolo version 4.0.5, Real Time Tomography, Villanova, PA).

High-resolution test objects

A voxelized model of a star pattern test object (Model 07-542-1000, Supertech, Elkhart, IN) was created using Matlab (MathWorks, Natick, Massachusetts, version 2018a). This virtual star pattern (Figure 2) consists of 5µm isotropic voxels with three material indices: lead, acrylic, and air. The diameter of the star pattern is 45mm with a total thickness of 30µm. The range of resolution for this star pattern, from the outer edge to the innermost circle, is 1.3–20.0 line pairs per millimeter (lp/mm). The star pattern contains four quadrants, giving two possible frequency orientations for both **x** and **y** ($\boldsymbol{\nu}_{\parallel}$ and $\boldsymbol{\nu}_{\perp}$, respectively).

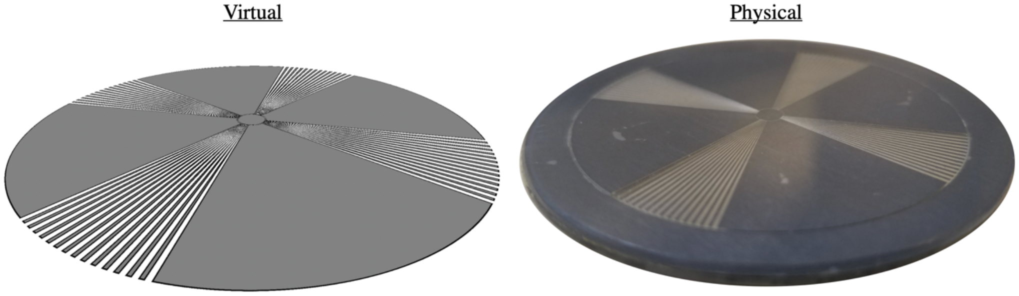

Figure 2: The virtual star pattern test object that was created to simulate the physical star pattern.

In addition to the star pattern, a bar pattern test object was created at a constant spatial resolution of 70 µm with a frequency orientation, $\boldsymbol{\nu}_{\parallel}$. The bar pattern is indexed with lead and air and was created at a 45° tilt relative to the breast support (Figure 3). The tilt of the bar pattern was used to compare the spatial resolution at various depths of the image reconstruction using multiplanar reconstructions (MPR). Using the commercial reconstruction software, MPR can be achieved at arbitrary angles[18]. This allowed us to visualize the plane of the bar pattern test object at a plane that is oriented 45° relative to the detector plane. Conventional DBT is anisotropic in the **z** dimension, which degenerate periodic signals like a bar pattern or punctate calcifications in the breast, at various intervals of **z**. Non-isocentric acquisition geometries can reduce these degeneracies.

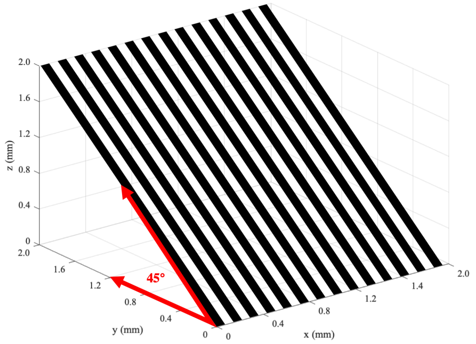

Figure 3: A diagram that illustrates a portion of the tilted bar pattern phantom. The spatial resolution of the phantom is 70µm (7.14 lp/mm).

Physics VCTs were used to simulate image acquisition of the virtual star pattern and tilted bar pattern using isocentric and non-isocentric configurations of the NGT prototype. The conventional x-ray source motion path (Figure 1) was simulated with and without **z**-direction detector motion (the **z**-detector position is 0 over all projections), to simulate non-isocentric and isocentric acquisition geometries, respectively. Repositioning and reproducibility of the image acquisition was simulated by perturbing the position of the phantom within 2 mm of the detector origin over 10 tomosynthesis acquisitions for each geometry. Poisson noise was also simulated for each projection image. Super-sampled image reconstructions of the star pattern test object were obtained using the simulated 2D projection images of each tomosynthesis acquisition simulation. The images were reconstructed at a 2.0x super-sampling rate (42.5 µm for the 85 µm detector element size).

The slice of the image reconstruction that contained the plane of the star pattern was used to evaluate the in-plane spatial resolution properties of the 20 image reconstructions. The radial fast Fourier transform (RFFT)[19] was used to evaluate the in-plane performance of both acquisition geometries. This metric used the star pattern image as an input to produce the contrast transfer function (CTF) and RFFT graphs (e.g. Figure 4), averaged over the 10 reconstruction slices for each geometry. The CTF is analogous to the modulation transfer function (MTF) but is not normalized to unity at zero spatial frequency. The RFFT graph shows modulation of all frequencies contained in a quadrant of a star pattern image reconstruction alongside the modulation of aliased signals. The CTF was used to determine the limit of spatial resolution (LSR). Conventional DBT is spatially anisotropic[11]; therefore, each image reconstruction is evaluated for $\boldsymbol{\nu}_{\parallel}$ and $\boldsymbol{\nu}_{\perp}$.

The same acquisition geometries were used to generate an MPR of the tilted bar pattern. Images of the tilted bar pattern were reconstructed at a 2x sampling rate. The reconstruction plane was oriented at the tilt of the bar pattern. Plot profiles of a degenerate region in the image reconstruction of the isocentric acquisition geometry was produced and compared with the plot profile of the same region for the non-isocentric acquisition geometry.

3. RESULTS AND DISCUSSION

Star pattern RFFT

An example of a Radial FFT and CTF calculation is shown for a single reconstruction slice in Figure 4. The RFFT and CTF graphs of the non-isocentric acquisition geometries show a reduction of spectral leakage compared with the isocentric acquisition geometries. The Radial FFT was computed for both frequency orientations, $\boldsymbol{\nu}_{\parallel}$ and $\boldsymbol{\nu}_{\perp}$, and averaged over the 10 reconstruction slices for each acquisition geometry.

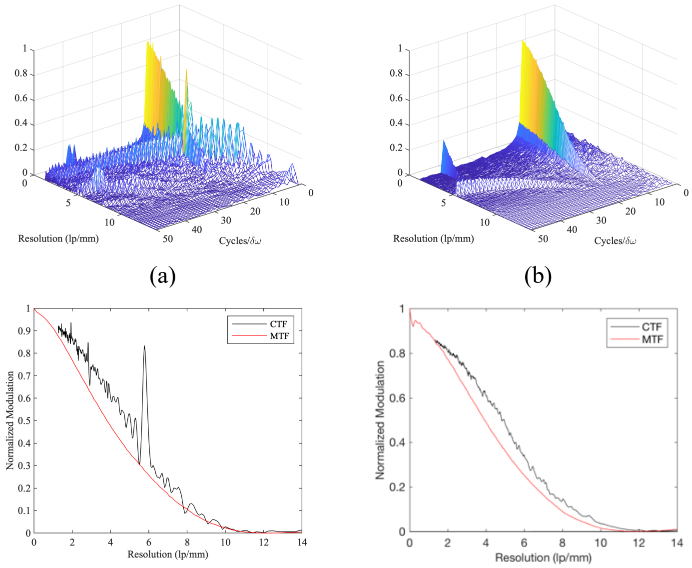

(a) (b)

(c) (d)

Figure 4: One sample of the Radial FFT for $\boldsymbol{\nu}_{\parallel}$ of the conventional, isocentric geometry (a), and $\boldsymbol{\nu}_{\parallel}$ of the conventional, non-isocentric geometry (b), and the corresponding MTF vs. CTF graphs (c-d).

The non-isocentric acquisition geometry exhibits isotropic super-resolution (Figure 5), achieving a limiting spatial resolution (LSR) above the alias frequency in both $\boldsymbol{\nu}_{\parallel}$ and $\boldsymbol{\nu}_{\perp}$, whereas the isocentric acquisition geometry achieves super resolution for $\boldsymbol{\nu}_{\parallel}$; however, resolution is limited to the alias frequency for $\boldsymbol{\nu}_{\perp}$. The isocentric acquisition geometry shows more significant aliasing in the form of Moiré patterns compared with the non-isocentric acquisition geometry. The modulation contrast is higher for the isocentric acquisition geometries at the lowest spatial frequencies of the star pattern, regardless of frequency orientation.

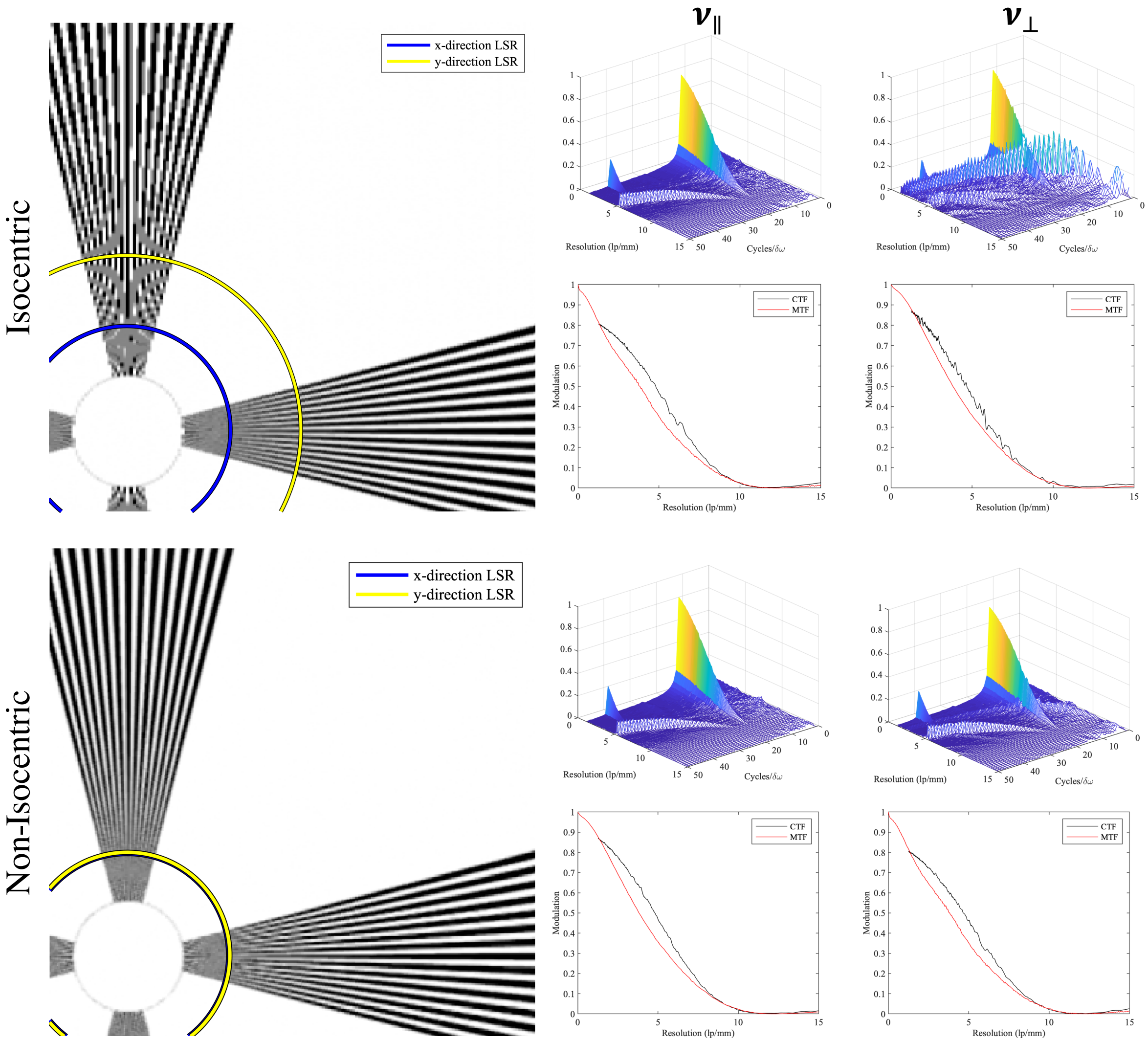

Figure 5: Simulated image reconstruction slices of the isocentric and non-isocentric acquisition geometry (left) and the results of the RFFT metric (right).

The LSR of the four conditions was measured using images of the star pattern and the CTF. All isocentric image reconstructions exhibited significant aliasing for $\boldsymbol{\nu}_{\perp}$, and the LSR was limited to near the alias frequency of the detector (5.88 lp/mm). For reconstruction slices where super resolution was achieved, the LSR was measured at a 5% modulation of the CTF. The improvement of the LSR for the non-isocentric over the isocentric geometry was 75.2% for $\boldsymbol{\nu}_{\perp}$. Both the image of the star pattern and the RFFT graph for the non-isocentric case exhibit residual aliasing artifact, but this artifact does not overcome the modulation of the input frequency.

Tilted bar pattern MPR

The tilted bar pattern was reconstructed with a roll of 45° about the **x**-axis for each acquisition geometry. The MPR of the isocentric acquisition geometry shows four distinct degenerate regions (e.g. the region bounded by the red box in Figure

6). Super resolution cannot be achieved at the corresponding **z**-locations in the image reconstruction. The MPR of the non-isocentric acquisition geometry shows multiple regions of decreased modulation, but no fully degenerate regions of the bar-pattern are seen. Super resolution is observed over the entire MPR.

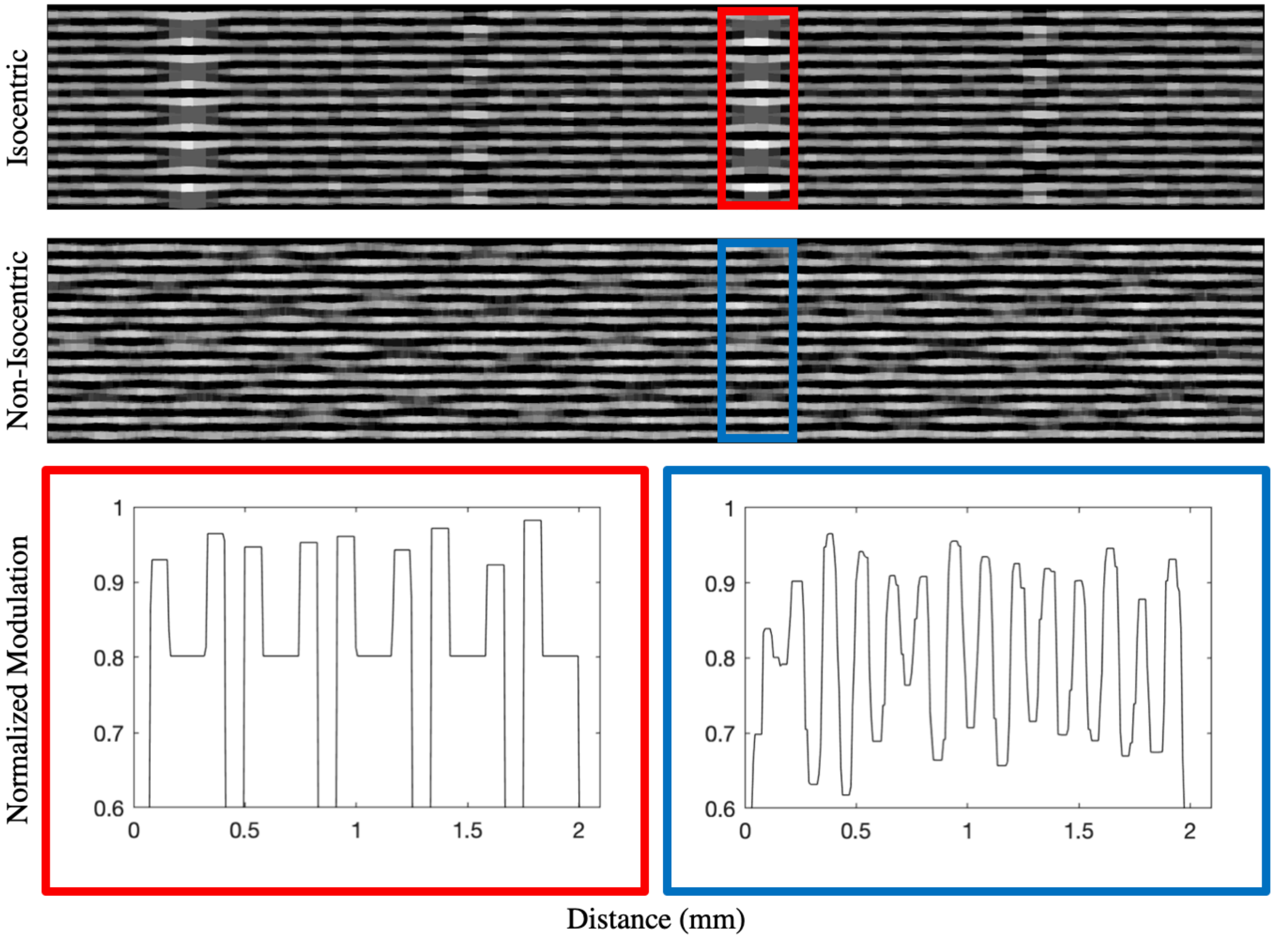

Figure 6: MPR of the tilted bar pattern for the isocentric and non-isocentric acquisition geometries with corresponding plot profiles.

4. CONCLUSION

We have shown that non-isocentric acquisition geometries can be simulated with high accuracy using physics VCTs. With 10 simulated tomosynthesis image reconstructions, we were able to measure the RFFT and LSR accurately and achieve results that are commensurate with physical experiments[4]. The LSR improved for every frequency orientation with the introduction of **z**-detector motion. The highest overall improvement in LSR for the non-isocentric over isocentric acquisition geometry is 75.2% for $\boldsymbol{\nu}_{\perp}$. All frequency orientations of the non-isocentric reconstructions exhibit super resolution, whereas the isocentric geometry was prone to aliasing. These results suggest that non-isocentric acquisition geometries can improve the detection of high-frequency objects like microcalcifications for DBT. In the future, we will simulate additional non-isocentric acquisition geometries that include PA source motion to optimize super resolution further.

5. ACKNOWLEDGEMENTS

The authors would like to thank Johnny Kuo, Susan Ng, and Peter Ringer of Real Time Tomography for technical assistance with Piccolo. Andrew D. A. Maidment is a shareholder of Real Time Tomography and is a member of the scientific advisory board.

Support was provided by the following grants: W81XWH-18-1-0082 from the Department of Defense Breast Cancer Research Program, IRSA 1016451 from the Burroughs Welcome Fund, 1R01CA196528 from the National Institute of Health, and IIR13264610 from Susan G. Komen. In addition, equipment support was provided by Analogic Inc., Barco NV, and Real Time Tomography. The content is solely the responsibility of the authors and does not necessarily represent the official views of the funding agencies.

REFERENCES

[1] Rafferty, E. a, Park, J. M., Philpotts, L. E., Poplack, S. P. and Sumkin, J. H., "Digital Mammography and Breast Tomosynthesis Compared with Digital Mammography Alone : Results of a Multicenter, multireader trial," Radiology **266**(1), 104–113 (2013).

[2] Eben, J. E., Vent, T. L., Choi, C. J., Yarrabothula, S., Chai, L., Nolan, M., Kobe, E., Acciavatti, R. J. and Maidment, A. D. A., "Development of a next generation tomosynthesis system," Prog. Biomed. Opt. Imaging - Proc. SPIE **10573** (2018).

[3] Maidment, T. D., Vent, T. L., Ferris, W. S., Wurtele, D. E., Acciavatti, R. J. and Maidment, A. D. A., "Comparing the imaging performance of computed super resolution and magnification tomosynthesis," Med. Imaging 2017 Phys. Med. Imaging **10132**, 1013222 (2017).

[4] Vent, T. L., Barufaldi, B. and Maidment, A. D. A., "Simulation and experimental validation of high-resolution test objects for evaluating a next-generation digital breast tomosynthesis prototype," 21 (2019).

[5] Vent, T. L., Lepore, B. L. and Maidment, A. D. A., "Evaluating the imaging performance of a next-generation digital breast tomosynthesis prototype," Med. Imaging 2019 Phys. Med. Imaging(March), 19 (2019).

[6] Acciavatti, Raymond; Rodriguez-Ruiz, Alejandro; Vent, Trevor L.; Bakic, Predrag R.; Reiser, Ingrid; Sechopoulos, Ioannis; Maidment, A. D. A., "Analysis of volume overestimation artifacts in the breast outline segmentation in tomosynthesis," Med. Imaging 2018 Phys. Med. Imaging, 10573 (2018).

[7] Acciavatti, R. J., Barufaldi, B., Vent, T. L., Wileyto, E. P. and Maidment, A. D. A., "Personalization of x-ray tube motion in digital breast tomosynthesis using virtual Defrise phantoms," Med. Imaging 2019 Phys. Med. Imaging(March), 10 (2019).

[8] Friedewald, S. M., Rafferty, E. A., Rose, S. L., Durand, M. A., Plecha, D. M., Greenberg, J. S., Hayes, M. K., Copit, D. S., Carlson, K. L., Cink, T. M., Barke, L. D., Greer, L. N., Miller, D. P. and Conant, E. F., "Breast cancer screening using tomosynthesis in combination with digital mammography," JAMA - J. Am. Med. Assoc. **311**(24), 2499–2507 (2014).

[9] Roth, R. G., Maidment, A. D. A., Weinstein, S. P., Roth, S. O. and Conant, E. F., "Digital Breast Tomosynthesis: Lessons Learned from Early Clinical Implementation," RadioGraphics **34**(4), E89–E102 (2014).

[10] Hu, Y.-H., Zhao, B. and Zhao, W., "Image artifacts in digital breast tomosynthesis: Investigation of the effects of system geometry and reconstruction parameters using a linear system approach," Med. Phys. **35**(12), 5242–5252 (2008).

[11] Acciavatti, R. J. and Maidment, A. D. A., "Observation of super-resolution in digital breast tomosynthesis," Med. Phys. **39**(12), 7518–7539 (2012).

[12] Hatt, C. R., Tomkowiak, M. T., Dunkerley, D. A. P., Slagowski, J. M., Funk, T., Raval, A. N. and Speidel, M. A., "Depth-resolved registration of transesophageal echo to x-ray fluoroscopy using an inverse geometry fluoroscopy system," Med. Phys. **42**(12), 7022–7033 (2015).

[13] Vent, T. L., Acciavatti, R. J., Kwon, Y. J. and Maidment, A. D. A., "Quantification of resolution in multiplanar reconstructions for digital breast tomosynthesis," Med. Imaging 2016 Phys. Med. Imaging **9783**(March 2016), 978303 (2016).

[14] Bakic, P. R., Barufaldi, B., Pokrajac, D., Lago, M. A. and Maidment, A. D., "Developing populations of software breast phantoms for virtual clinical trials," 14th Int. Work. Breast Imaging (IWBI 2018)(July 2018), 73 (2018).

[15] Barufaldi, B., Bakic, P. R., Higginbotham, D. and Maidment, A. D. A., "OpenVCT: a GPU-accelerated virtual clinical trial pipeline for mammography and digital breast tomosynthesis," Med. Imaging 2018 Phys. Med. Imaging **1057358**(March), 194 (2018).

[16] Eben, J. E., Vent, T. L., Choi, C. J., Yarrabothula, S., Chai, L., Nolan, M., Kobe, E., Acciavatti, R. J. and Maidment, A. D. A., "Development of a Next Generation Tomosynthesis System," Med. Imaging 2018 Phys. Med. Imaging, 10573 (2018).

[17] Maidment, Andrew D. A.; Acciavatti, Raymond J.; Vent, Trevor L.; Conant, Emily F.; Kwon, Young Joon; NG, Susan; Kuo, Jhonny; Ringer, Peter A.; Maidment, Tristan; Wurtele, David; Licata, Joseph; Narayan, Tejas; Zhang, David; Higginbotham, D., "Construction of a Prototype Digital Breast Tomosynthesis System with Superior Spatial Resolution," RSNA Phys. Basic Sci., RSNA (2016).

[18] Vent, T. L., Acciavatti, R. J., Kwon, Y. J. and Maidment, A. D. A., "Quantification of resolution in multiplanar reconstructions for digital breast tomosynthesis," Med. Imaging 2016 Phys. Med. Imaging **9783**, 978303 (2016).

[19] Vent, T., Acciavatti, R. and Maidment, A., "Development and Evaluation of a Spatial Resolution Metric for Tomosynthesis: we-g-601-02," Med. Phys. **44**(6), 3261 (2017).

DETECTOR MOTION DESIGN FOR NEXT-GENERATION DIGITAL BREAST TOMOSYNTHESIS

ABSTRACT

Our previous work showed that digital breast tomosynthesis (DBT) systems are capable of super-resolution (*i.e.*, subpixel resolution). Super-resolution can be demonstrated with a bar pattern phantom. Unlike a single projection image, the reconstruction can resolve frequencies above the alias frequency of the detector. DBT systems are not currently designed to optimize super-resolution; there are anisotropies (aliasing artifacts) depending on the position and orientation of the bar pattern phantom. This paper shows that the anisotropies can be eliminated by introducing detector motion in the direction perpendicular to the breast support; *e.g.*, superior-to-inferior in a cranial-caudal view. To demonstrate the advantage of this design, the reconstruction of a high-frequency sinusoidal test object was calculated from first principles, and the Fourier transform was analyzed. The largest Fourier peak less than the alias frequency was compared against the peak at the input frequency. The ratio of these two respective amplitudes was termed the *r*-factor; this ratio should be minimized (approaching zero) to achieve super-resolution with high quality. The *r*-factor was calculated at randomly-sampled points in a volume-of-interest (VOI). We analyzed the histogram of *r*-factor values in the VOI. The use of detector motion minimizes the *r*-factor in such a way that super-resolution is achievable at every point in the VOI. In the new design, the *r*-factor also shows less dependence on the orientation of the input frequency, allowing for isotropic resolution. In conclusion, the next generation of DBT systems should be designed with detector motion to optimize high-frequency imaging tasks, such as calcification imaging.

Key words: Digital Breast Tomosynthesis, Super-Resolution, Image Reconstruction, Fourier Transform, Anisotropy.

1. INTRODUCTION

Many medical centers now incorporate digital breast tomosynthesis (DBT) or "3D mammography" into their breast cancer screening practices.[1, 2] In DBT, a 3D image is created from multiple x-ray projection views of the breast acquired over a narrow range of angles. With the implementation of DBT, there has been a modest increase in sensitivity and a reduction in the recall rate in screening mammography.[3, 4]

Current systems represent just the first generation of DBT. In this paper, we argue that the design of DBT systems needs to evolve, just as computed tomography (CT) systems evolved over many generations. A lesson from the many evolutions of CT is that, to suppress aliasing, careful thought needs to be given to the detector positioning. In a third-generation CT scanner, each detector element (del) is offset by one-quarter of the del size relative to the iso-center.[5] This effectively doubles the sampling rate for the two projection views that are acquired 180° apart. This paper expands on the idea of using detector positioning as an anti-aliasing strategy. We propose the next evolution of DBT that incorporates detector motion as an anti-aliasing strategy.

To achieve the highest spatial resolution, it is necessary to perform a DBT reconstruction with smaller pixelation than the detector. Our previous work demonstrated that this reconstruction offers super-resolution and improves the visibility of calcifications.[6, 7] In the same work, we also performed theoretical modeling to show that, while super-resolution is achievable in DBT, it is not supported everywhere in the image. We illustrate this effect here with a bar pattern phantom, which was canted at an angle (Fig. 1) to visualize the spatial resolution over a range of positions in the z direction (the source-to-image direction). The phantom was imaged using a Selenia Dimensions system (Hologic Inc., Marlborough, MA) with 0.14 mm detector pixelation and hence an alias frequency of 3.6 mm^{-1}. The reconstruction was prepared with Piccolo$^{\text{TM}}$ (Real Time Tomography LLC, Villanova, PA) in an oblique plane[8] matched to the plane of the phantom. The frequency 5.0 mm^{-1} can clearly be resolved at most positions in the image (Fig. 2). However, there are distinct bands of aliasing, shown by the arrows, at which there are fewer line pairs than expected. This reconstruction illustrates the need for a new design that more reliably suppresses aliasing at every position in the image.

To understand why there are aliasing artifacts at some positions in the image, a thought experiment can be performed with multiple projection views of a point-like object (Fig. 3). In current DBT systems, the x-ray tube moves laterally (left-to-right) in the chest-wall plane. In the x direction, the shift in the image of the object is effectively constant from one projection view to the next. This translational shift is depicted as a subpixel fraction of the del size, resulting in super-resolution. As the elevation of the object changes, the translational shift changes in proportion with the magnification. At some z-coordinates, it is possible for the increment to be an integer multiple of the del size; we use the term "degeneracy" to refer to such a z-coordinate. The aliasing bands (arrows) in the bar pattern reconstruction (Fig. 2) can be used to identify the degenerate z-coordinates.

In this paper, we calculate a closed-form solution for the degenerate z-coordinates, and design a detector motion to suppress the degeneracies. The detector is translated in the z direction during the scan; for example, superior-to-inferior in a cranial-caudal (CC) view. This detector motion ensures that the translational shift from one projection view to the next is not a constant (Fig. 3); this is explored as a strategy to yield super-resolution everywhere in the image. The advantage of theoretical modeling is that it allows us to simulate many different ranges of detector motion and identify the optimum range of motion. This model is being used to optimize the design of a prototype next-generation tomosynthesis (NGT) system that we are constructing.[9] We simulate the reconstruction of a high-frequency test object, and demonstrate that the NGT design supports super-resolution everywhere in the image.

2. METHODS

A. Acquisition Geometry

We now use theoretical modeling to derive a closed-form solution for the degenerate z-coordinates in DBT. The system is modeled with the origin (O) defined to be the midpoint of the breast support at the chest-wall side of the image (Fig. 4). We assume that the detector is parallel with the breast support in all projection views. The focal spot (FS) follows a circular arc over the angular range Θ, with the projection angle ψ_n for the n^{th} projection view determined by

$$\psi_n = \frac{\Theta\left[n-1-\left(\frac{N-1}{2}\right)\right]}{N-1} \tag{1}$$

where n varies from 1 to N (the total number of projections). The FS coordinates are thus

$$x_{\text{FS}} = \left(z_{\text{DM}} - z_{\text{COR}}\right)\sin\psi_n \tag{2}$$

$$y_{\text{FS}} = 0 \tag{3}$$

$$z_{\text{FS}} = z_{\text{COR}} + \left(z_{\text{DM}} - z_{\text{COR}}\right)\cos\psi_n \tag{4}$$

where z_{DM} is the z-coordinate of the FS in the central projection, corresponding to the projection view of 2D digital mammography (DM). The center-of-rotation (COR) of the FS motion is defined to be the point $(0, 0, z_{\text{COR}})$. The radius of the source motion is $z_{\text{DM}} - z_{\text{COR}}$. We are building a NGT prototype system that supports this motion under the parameters shown in Table 1.

Now, to trace a ray from the FS to the detector, a primed origin (O′) needs to be defined in the detector plane. Similar to point O, point O′ is defined to be the midpoint (of the detector) in the chest-wall side of the image. An arbitrary detector position (point B) has the coordinate (u, v) relative to O′ (Fig. 5). With the shift from point O to point O′ defined by the coordinates b_x, b_y, and b_z in the three respective directions, it follows that a ray from the FS at point A to the detector at point B can be described by the parametric equations

$$\begin{pmatrix} x \\ y \\ z \end{pmatrix} = w \begin{pmatrix} b_x + u - x_{\mathrm{FS}} \\ b_y + v - y_{\mathrm{FS}} \\ b_z - z_{\mathrm{FS}} \end{pmatrix} + \begin{pmatrix} x_{\mathrm{FS}} \\ y_{\mathrm{FS}} \\ z_{\mathrm{FS}} \end{pmatrix} \tag{5}$$

where w is a parameter ranging from zero at point A to unity at point B. Using a computer algebra system (Maple 15, Maplesoft, Waterloo, Ontario) to solve this system of equations for u

$$u = \frac{x\left(z_{\mathrm{FS}} - b_z\right) + z\left(b_x - x_{\mathrm{FS}}\right) + b_z x_{\mathrm{FS}} - b_x z_{\mathrm{FS}}}{z_{\mathrm{FS}} - z} \tag{6}$$

we can now derive a formula for the degenerate z-coordinates by considering two cases for the acquisition geometry; first, a conventional acquisition geometry with a stationary detector; and second, the NGT geometry with detector motion in the z direction.

Case 1: Stationary Detector. To model a stationary detector, the following substitutions can be made in Eq. (6): $b_x = 0$, $b_y = 0$, and $b_z = b_{z,1}$ where $b_{z,1}$ is defined to be the z-coordinate of the detector plane in projection view $n = 1$. Making these assumptions in Eq. (6) in conjunction with Eqs. (2)-(4) yields

$$u_n \approx \frac{x\left(z_{\mathrm{DM}} - b_{z,1}\right)}{z_{\mathrm{DM}} - z} + \left(b_{z,1} - z\right) M_{\mathrm{COR}} \psi_n , \tag{7}$$

where the subscript n in the left-hand side of the equation is introduced to emphasize the dependency on projection number. To derive this result, we used the small angle approximation; that is $\cos\psi_n \approx 1$ and $\sin\psi_n \approx \psi_n$. The quantity M_{COR} is introduced to simplify intermediate calculations.

$$M_{\mathrm{COR}} = \frac{z_{\mathrm{DM}} - z_{\mathrm{COR}}}{z_{\mathrm{DM}} - z} \tag{8}$$

Returning to the thought experiment involving the point-like object (Fig. 3), Eq. (7) can be used to derive the shift Δ_x in the image of this object from one projection view to the next

$$\Delta_x = \frac{M_{\mathrm{COR}} \Theta\left(b_{z,1} - z\right)}{N-1} \tag{9}$$

where

$$\Delta_x \equiv u_{n+1} - u_n, \quad n \in \left[1, N-1\right]. \tag{10}$$

According to Eq. (9), the shift Δ_x is a constant (independent of n); it is the same for any two adjacent projection views. For this reason, a degenerate z-coordinate ($z = z_{\mathrm{d}}$) can arise if Δ_x is equal to an integer multiple of the del size, a

$$\Delta_x\big|_{z=z_{\mathrm{d}}} = ja, \quad j \in \mathbb{Z} \tag{11}$$

giving

$$z_{\mathrm{d}} = \frac{b_{z,1}\Theta\left(z_{\mathrm{DM}} - z_{\mathrm{COR}}\right) - jaz_{\mathrm{DM}}\left(N-1\right)}{\Theta\left(z_{\mathrm{DM}} - z_{\mathrm{COR}}\right) - ja\left(N-1\right)}. \tag{12}$$

When we apply this formula in Section 3A, we presume that the FS is moving in the +x direction, so the shift Δ_x is negative and hence j is negative.

Case 2: Moving Detector. We are designing the NGT system with detector motion in the z direction ($b_x = b_y = 0$). The detector is translated by a constant increment between projection views

$$b_z = b_{z,1} + \frac{h_z\left(n-1\right)}{N-1}, \tag{13}$$

where h_z is the total range of detector motion in the z direction (the source-to-image direction). With steps similar to those described previously, it can be shown that the shift Δ_x in the image of a point-like object from one projection view to the next is

$$\Delta_x = \Omega_1 + \Omega_2 \tag{14}$$

where

$$\Omega_1 = \frac{h_z}{p_z}\left(n - \frac{N+1}{4}\right)a \tag{15}$$

$$\Omega_2 = \frac{\Theta\left(b_{z,1} - z\right)\left(z_{\mathrm{DM}} - z_{\mathrm{COR}}\right) - h_z x}{\left(N-1\right)\left(z_{\mathrm{DM}} - z\right)} \tag{16}$$

and where

$$p_z = \frac{\left(N-1\right)^2 a}{2\Theta M_{\mathrm{COR}}}. \tag{17}$$

Eqs. (14)-(17) prove that the shift from one projection view to the next is not a constant, which is the intention of this new design. This arises because Ω_1 is dependent on n. Eqs. (14)-(17) need to be analyzed carefully to optimize the range of detector motion, h_z. It is important to understand the conditions under which Δ_x can be an integer multiple of the del size (a); this results in a "degenerate" detector motion that does not effectively suppress aliasing at all positions.

We now calculate the degenerate detector motion in a system for which $N = 15$ (consistent with Table 1), so that $N + 1$ is divisible by 4 [Eq. (15)]. The most general value of N is considered in the Supplementary Document. In Eq. (15), Ω_1 degenerates to an integer multiple of the del size, a, if $h_z = -p_z$ (we assume a *descending* detector motion, so the sign of h_z is negative). The term p_z is z-dependent through the term M_{COR} [Eq. (8)]; the value of M_{COR} varies minimally over the range of z-coordinates in a compressed breast. For example, in a 50.0 mm thick breast under compression,

M_{COR} varies between 1.0 ($z = 0$) and 1.07 ($z = 50.0$ mm). We approximate p_z based on the mid-thickness of the breast ($z = z_{\mathrm{mid}} = 25.0$ mm), and define this approximation as the quantity q_z.

$$q_z = p_z\big|_{z=z_{\mathrm{mid}}} \tag{18}$$

In this example, $q_z = 24.0$ mm and hence $h_z/p_z \approx -1$, yielding the degeneracy criterion

$$\Omega_2\big|_{z=z_d} = ja \tag{19}$$

giving

$$z_{\mathrm{d}} = \frac{b_{z,1}\Theta\left(z_{\mathrm{DM}} - z_{\mathrm{COR}}\right) - jaz_{\mathrm{DM}}\left(N-1\right) - h_z x}{\Theta\left(z_{\mathrm{DM}} - z_{\mathrm{COR}}\right) - ja\left(N-1\right)}. \tag{20}$$

In summary, this derivation offers insight into a detector motion ($h_z = -24.0$ mm) that does not effectively suppress aliasing at every position, and thus should be avoided in designing the system.

B. Model of High-Frequency Test Object

We now simulate a high-frequency test object to quantify image quality under various ranges of detector motion, and use these calculations to identify the optimum range of motion. The object is a thin rectangular prism (thickness ε) with mid-thickness at $z = z_0$ (Fig. 4). The attenuation coefficient, μ, varies sinusoidally (frequency f_0). The model that we propose is more general than our previous work[6]; we allow the input frequency to vary along any angle α (relative to the x direction) and we allow for arbitrary FS and detector trajectories (Fig. 5), assuming that the detector remains parallel with the breast support in all projection views. The simple backprojection (SBP) reconstruction of this object (μ_{SBP}) can be calculated in closed form. This solution is detailed in the Supplemental File.

To determine whether the object is resolved in the reconstruction, the Fourier transform of μ_{SBP} is calculated over the interval $\left[x'_{\min}, x'_{\max}\right]$

$$\mathcal{F}\mu_{\text{SBP}} = \int_{x'_{\min}}^{x'_{\max}} \mu_{\text{SBP}} e^{-2\pi i f' x'} dx' \tag{21}$$

$$\approx \left(\frac{x'_{\max} - x'_{\min}}{K} \right) \sum_{k=1}^{K} \mu_{\text{SBP}} e^{-2\pi i f' x'} \Big|_{x' = x'_{\min} + (x'_{\max} - x'_{\min})\left(\frac{k-1/2}{K}\right)}, \tag{22}$$

where x' is the direction of the input frequency (along angle α), f' is frequency along this direction, and K is the number of samples in the summation.

We now illustrate this calculation in the conventional geometry ($h_z = 0$), assuming $\alpha = 0°$. The frequency 8.0 mm^{-1} is chosen to investigate super-resolution, since it exceeds the alias frequency (5.9 mm^{-1}) of the detector[9] (AXS-2430, Analogic Canada Corporation, Montreal, Quebec) being proposed in the design of the NGT system. At a position where the object is resolved (*e.g.*, $z_0 = 5.0$ mm), the Fourier transform has a major peak at the input frequency, 8.0 mm^{-1} [Fig. 6(b)]. By contrast, at a degenerate z-coordinate ($z_0 = 0.6$ mm), the major peak is at a lower frequency, 3.9 mm^{-1} [Fig. 6(d)]. These two examples motivate the r-factor, a summary metric that was introduced in our previous work.[6] The r-factor is the ratio of the amplitude of the highest peak less than the alias frequency to the amplitude at the input frequency (8.0 mm^{-1}); *i.e.*, the ratio of the amplitudes A_1 to A_2 (Fig. 6).

$$r\text{-Factor} = \frac{A_1}{A_2} \tag{23}$$

Super-resolution is achieved if r-factor < 1. In these two examples, the r-factor is 0.14 at the position demonstrating super-resolution [Fig. 6(b)], and is 1.91 at the position exhibiting aliasing [Fig. 6(d)].

C. Statistical Analysis

Two orientations of the input frequency ($\alpha = 0°, 90°$) were simulated. We are designing the NGT system to achieve isotropic image quality (independent of orientation, α). To measure how image quality varies throughout a volume-of-interest (VOI), we calculated the *r*-factor at 1,000 random points in the VOI. Figure 7(a) illustrates the *r*-factor histogram, which was derived from the conventional geometry described previously (assuming $\alpha = 0°$). The VOI is a rectangular prism with dimensions 200.0 × 100.0 × 50.0 (in mm) and 0.020 mm spacing between points in each direction.

To ensure that the interval $\left[x'_{\min}, x'_{\max}\right]$ in Eq. (21) is included fully within the detector field-of-view for the orientation $\alpha = 90°$ (Fig. 5), it was necessary to displace the VOI slightly anterior to the chest wall (the plane $y = 0$). We chose to displace the VOI by +4.0 mm from the plane $y = 0$. Thus the geometric centroid of the VOI was the coordinate (0, 54.0, 25.0) (in mm).

Using the conventional acquisition geometry as an example, we now illustrate summary metrics that can be derived from the *r*-factor histogram generated from 1,000 random points in the VOI [Fig. 7(a)].

Upper Percentiles: If super-resolution is not achievable everywhere in the VOI, the *r*-factor histogram is expected to have a long tail exceeding 1.0. For this reason, we can use the upper percentiles of the histogram (*e.g.*, the 85th, 90th, and 95th percentiles) to determine if there are points in the VOI at which super-resolution is not achieved. Each of these percentiles was analyzed with bootstrapping (200 re-samplings of 1,000 random points). Figure 7(b) illustrates this calculation for the 90th percentile; the histogram shown in this figure represents 200 bootstrappings of the 90th percentile. From the middle 95% of this histogram, we calculated a 95% confidence interval (CI_{95}). In this example, CI_{95} ranges between 0.77 and 0.89.

Threshold Selection: To achieve high image quality, the *r*-factor should be as close to zero as possible. One can set a threshold for the *r*-factor (for example, *r*-factor < 1/3), and calculate the proportion of points in the VOI that meet this threshold (again, with bootstrapping). To illustrate this calculation, the histogram shown in Figure 7(c) represents 200 bootstrapped re-samplings of the proportion of points that meet the threshold *r*-factor < 1/3. In this example, CI_{95} ranges between 0.59 and 0.65.

The choice of threshold is somewhat arbitrary. The threshold of 1/3 considered in Figure 7(c) is just one example. For this reason, the CI_{95} calculations are performed over a continuous range of thresholds between zero and unity.

3. RESULTS

A. Identifying the Coordinates of the Degeneracies

First, in the conventional acquisition geometry ($h_z = 0$), we analyzed the *r*-factor in the range between $z_0 = 0$ and $z_0 = 50.0$ mm [Fig. 8(a)]. The plot was created with 0.020 mm spacing between points. For the purpose of the plot, the test object was centered on the coordinate $(x, y) = (0, 40.0)$ (in mm), and frequency was oriented in the direction of x-ray tube motion ($\alpha = 0°$). There are 16 peaks in this plot. From Eq. (12), one would expect the peaks to be present at the coordinates marked by asterisks. We found that Eq. (12) does indeed predict the coordinates of the peaks very well. To validate this, we manually identified the coordinates of the local maxima, and plotted these results as a function of the coordinates given by Eq. (12). The resultant curve is effectively the function $y = x$; linear fitting yields a slope of 0.997, a *y*-intercept of −0.117, and a R^2 of 0.9999 [Fig. 8(b)].

Similar plots were generated for the geometry with the "degenerate" detector motion; *i.e.*, $h_z = -q_z = -24.0$ mm [Figs. 8(c)-(d)]. There continues to be 16 peaks in the *r*-factor. The coordinates of these peaks are predicted very well [Eq. (20)]. The plot shown in Figure 8(d) is effectively the function $y = x$; linear fitting yields a slope of 0.982, a y-intercept of 0.379, and a R^2 of 1.0000.

B. Optimization of the Detector Motion Range

Next, detector motion was analyzed up to a range of $-3.5 \cdot q_z = -84.0$ mm (Fig. 9) in increments of $0.1 \cdot q_z$ (2.4 mm). We model a *descending* detector motion. In a CC view, this motion is superior-to-inferior. For this reason, the sign of h_z is negative.

Upper Percentiles: The three r-factor percentiles described in Section 2C (85th, 90th, and 95th) demonstrate an overall trend downward (Fig. 9). From this trend, we conclude that aliasing artifacts are being suppressed effectively by the use of detector motion. Results derived for the 0° angle, α, offer proof that the detector motion range $-1.0 \cdot q_z$ (-24.0 mm) should be avoided, as one would expect. There is a local maximum at this range of motion. There are subtler local maxima at the motion ranges $-2.0 \cdot q_z$ (-48.0 mm) and $-3.0 \cdot q_z$ (-72.0 mm). These ranges of motion (*i.e.*, integer multiples of q_z) cause the term Ω_1 [Eq. (15)] to degenerate to an integer multiple of the del size, a, just like the motion range $-1.0 \cdot q_z$.

The three curves in Figure 9 demonstrate a long tail at detector motion ranges between $-3.5 \cdot q_z$ (-84.0 mm) and $-2.4 \cdot q_z$ (-57.6 mm). We consider the motion range $-2.4 \cdot q_z$ (-57.6 mm) to be the optimum for the NGT system. Increasing the magnitude of the motion range beyond 57.6 mm does not improve the r-factor substantially, and it could actually degrade image quality if one considers the effect of FS blurring at high magnification. In this paper, we treat the FS as point-like; previous work has shown that the modulation transfer function (MTF) of the FS is degraded with increasing magnification.[10] The improvement in the r-factor going from a motion range of $-2.4 \cdot q_z$ to $-3.5 \cdot q_z$ is so minimal that it would not justify the MTF trade-off that arises with increased magnification.

We are designing the NGT system to achieve isotropic image quality (independent of angle, α). The two subplots in Figure 9 illustrate the effect of varying this angle. In the conventional design of the system ($h_z = 0$), there is clearly a difference between the two orientations; the confidence intervals are all higher in subplot (b) than in subplot (a). From this result, we conclude that image quality is not isotropic in the conventional design.

Results along the 90° angle [Fig. 9(b)] can be understood in more detail by returning to the thought experiment with the point-like object (Fig. 3). In the conventional design, the shift from one projection view to the next is minimal (effectively zero) in the y direction. With the use of detector motion, the shifts become more pronounced, allowing for subpixel sampling differences between the projections and hence super-resolution. At broad motion ranges ($-3.5 \cdot q_z$ to $-2.4 \cdot q_z$), the confidence intervals in Figure 9 all tend toward an asymptote that is effectively independent of the angle, α, resulting in isotropic super-resolution.

Threshold Selection: As an alternate metric of image quality, we calculated the proportion of points in the VOI that meet a threshold for the r-factor (Fig. 10). As can be seen from the horizontal axis of these plots, we varied the threshold between zero and unity. The shaded area represents the 95% confidence interval for the proportion of points that meet the threshold. Results for the conventional design ($h_z = 0$) show a clear dependency on the angle, α, of the test frequency. There is inherently poorer image quality along the 90° angle, since this direction is perpendicular to the x-ray tube motion. If frequency is aligned along a 90° angle [Fig. 10(b)], a relatively small proportion of points (under 50%) meet any threshold up to 1.0.

In the NGT design (modeled with a motion range of $-2.4 \cdot q_z = -57.6$ mm), the curves in Figure 10 rise much more quickly to a plateau. From the shape of these curves, we conclude that there is much less variability in image quality compared against the conventional system. We are designing the NGT system to ensure that image quality is effectively uniform everywhere in the reconstruction.

4. DISCUSSION

In DBT, the motion of the x-ray tube is directed laterally (*x* direction, Fig. 4). This motion gives rises to shifts in the image of the object in this direction. We calculated these shifts for a point-like object (Fig. 3). There are "degenerate" *z*-coordinates at which the shift (Δ_x) between projection views is an integer multiple of the del size. Super-resolution is not achievable at these *z*-coordinates. This paper proposes a closed-form solution for the degenerate *z*-coordinates in DBT, and validates this solution based on the simulated reconstruction of a high-frequency sinusoidal test object.

We also calculated the *r*-factor as a metric of image quality based on the Fourier transform of the sinusoidal test object. The *r*-factor is the ratio of the amplitude at the low-frequency Fourier peak relative to the amplitude at the input frequency. Super-resolution is achieved with high quality if the *r*-factor is as close to zero as possible. We measured the distribution of *r*-factor values throughout a VOI in terms of a histogram. To demonstrate the advantage of designing the system with detector motion, we analyzed how the upper tail of the histogram (*i.e.*, the upper percentiles of the *r*-factor) was affected by different ranges of motion, and concluded that super-resolution can be achieved with higher quality by broadening the range of motion.

Although image quality is improved with the use of detector motion, the range of motion should not be chosen arbitrarily. We demonstrate that there is a "degenerate" range of motion

($h_z = -q_z$) that should be avoided. With this motion, the r-factor is characterized by peaks in the z direction, similar to the conventional design (Fig. 8). One can draw an analogy to a third-generation CT scanner. If each del were offset from the iso-center by one half of the del size (as opposed to one quarter of the del size[5]), there would be no subpixel sampling differences between projection views that are 180° apart. The offset of one half of the del size can be interpreted as a "degenerate" detector positioning in CT; it is perfectly analogous to the range of motion given by $-q_z$ in that it would not effectively suppress aliasing artifacts at every position in the image.

We modeled the sinusoidal test object along different orientations ($\alpha = 0°, 90°$) to demonstrate that the NGT design allows for isotropic image quality, unlike the conventional design. Since the x-ray tube motion is limited to one direction (x), there are effectively no shifts in the image of the object in the perpendicular direction (y); *i.e.*, the posteroanterior (PA) direction (Fig. 3). With the use of detector motion, the shifts in the y direction become more pronounced, allowing for subpixel sampling gain in this direction. In the NGT design, the r-factor results show much less orientation dependence (Figs. 9-10).

In this paper, we presume that the FS is point-like. Increasing the source-to-image distance does introduce FS blurring, which was not modeled in this paper. For example, if $h_z = -2.4 \cdot q_z$ (corresponding to −57.6 mm of motion), the magnification at the mid-thickness of the VOI ($z_{\text{mid}} = 25.0$ mm) varies from 1.05 to 1.13.

We can minimize FS blurring by minimizing the gap between the breast support and detector. In the model of detector motion proposed in this paper, the gap is smallest (10.0 mm) in the first projection view of the scan. If the gap could be made even smaller than 10.0 mm, it would minimize FS blurring. As the NGT system is constructed, future work will explore how small this gap can be.

In this paper, the resolution at each point in the 3D image is determined using SBP reconstruction. One of the limitations of this paper is that there was no analysis of how filtering impacts super-resolution. Since filtering places a different relative weight on each frequency in Fourier space, future work should determine whether the filter can be optimized to minimize the *r*-factor.

One assumption made in the theoretical model is that there are no sources of blurring in the x-ray converter, and hence the point spread function (PSF) is a delta function. Previous work demonstrated that this assumption is valid at normal incidence for amorphous-selenium (*a*-Se) detectors.[11] The AXS-2430 detector modeled in the simulations is an example of an *a*-Se detector. In an *a*-Se detector, the PSF is blurred at positions for which there is increasing obliquity in the incidence angle; for example, near the edge of the detector opposite the chest wall.[12-16] To model the blurring due to non-normal incidence in future work, the signal in the x-ray converter should be convolved with the PSF.

5. CONCLUSION

Although super-resolution is achievable in DBT, anisotropies are unavoidable in the current design of the system. The anisotropies can be suppressed with the use of detector motion in the *z* direction (the direction perpendicular to the breast support). We are designing a prototype physical system based on the theoretical model proposed in this paper.

ACKNOWLEDGEMENTS

We are grateful to David Higginbotham for his valuable feedback. In addition, we thank Johnny Kuo, Susan Ng, and Peter Ringer of Real Time Tomography (RTT) for providing technical assistance with Piccolo™.

Support was provided by grants PDF14302589 and IIR13264610 from Susan G. Komen®; grant W81XWH-18-1-0082 from the Department of Defense Breast Cancer Research Program; and grant 1R01CA196528 from the National Institute of Health. In addition, equipment support was provided by Analogic Inc., Barco NV, and RTT. The content is solely the responsibility of the authors and does not necessarily represent the official views of the funding agencies.

DISCLOSURE OF CONFLICTS OF INTEREST

Andrew D. A. Maidment has received research support from Hologic Inc., Barco NV, and Analogic Corporation; is a spouse to an employee and stockholder of Real Time Tomography (RTT), LLC; is a member of the scientific advisory board of RTT; and is an owner of Daimroc Imaging, LLC.

Author to whom correspondence should be addressed. Electronic mail:
racci@pennmedicine.upenn.edu;
Telephone: +1-215-746-8759; Fax: +1-215-746-8764

REFERENCES

[1] Sechopoulos I. A review of breast tomosynthesis. Part I. The image acquisition process. Medical Physics. 2013;40(1):014301-1 to -12.
[2] Sechopoulos I. A review of breast tomosynthesis. Part II. Image reconstruction, processing and analysis, and advanced applications. Medical Physics. 2013;40(1):014302-1 to -17.
[3] Friedewald SM, Rafferty EA, Rose SL, Durand MA, Plecha DM, Greenberg JS, et al. Breast Cancer Screening Using Tomosynthesis in Combination With Digital Mammography. Journal of the American Medical Association. 2014;311(24):2499-507.
[4] Conant EF, Zuckerman SP, McDonald ES, Weinstein SP, Korhonen KE, Birnbaum JA, et al. Five Consecutive Years of Screening with Digital Breast Tomosynthesis: Outcomes by Screening Year and Round. Radiology. 2020;295(2):285-93.
[5] Hsieh J. Chapter 7: Image Artifacts: Appearances, Causes, and Corrections. Computed Tomography: Principles, Design, Artifacts, and Recent Advances. Bellingham, WA: SPIE Press; 2015. p. 245-347.

[6] Acciavatti RJ, Maidment ADA. Observation of super-resolution in digital breast tomosynthesis. Medical Physics. 2012;39(12):7518-39.
[7] Acciavatti RJ, Maidment ADA. Oblique reconstructions in tomosynthesis: II. Super-resolution. Medical Physics. 2013;40(11):111912-1 to -19.
[8] Kuo J, Ringer PA, Fallows SG, Bakic PR, Maidment ADA, Ng S, editors. Dynamic Reconstruction and Rendering of 3D Tomosynthesis Images. SPIE Medical Imaging; 2011; Lake Buena Vista, FL: SPIE.
[9] Eben JE, Vent TL, Choi CJ, Yarrabothula S, Chai L, Nolan M, et al., editors. Development of a Next Generation Tomosynthesis System. SPIE Medical Imaging; 2018; Houston, TX: SPIE.
[10] Johns HE, Cunningham JR. Chapter 16: Diagnostic Radiology. The Physics of Radiology. 4th ed. Springfield, IL: Charles C Thomas; 1983. p. 557-669.
[11] Lee DL, Cheung LK, Rodricks B, Powell GF, editors. Improved imaging performance of a 14 x 17-inch Direct Radiography (TM) System using Se/TFT detector. SPIE Conference on Physics of Medical Imaging; 1998; San Diego, CA: SPIE.
[12] Que W, Rowlands JA. X-ray imaging using amorphous selenium: Inherent spatial resolution. Medical Physics. 1995;22(4):365-74.
[13] Hajdok G, Cunningham IA, editors. Penalty on the detective quantum efficiency from off-axis incident x rays. Medical Imaging 2004: Physics of Medical Imaging; 2004; San Diego, CA: SPIE.
[14] Badano A, Freed M, Fang Y. Oblique incidence effects in direct x-ray detectors: A first-order approximation using a physics-based analytical model. Medical Physics. 2011;38(4):2095-8.
[15] Acciavatti RJ, Maidment ADA. Non-stationary model of oblique x-ray incidence in amorphous selenium detectors: I. Point spread function. Medical Physics. 2019;46(2):494-504.
[16] Acciavatti RJ, Maidment ADA. Nonstationary model of oblique x-ray incidence in amorphous selenium detectors: II. Transfer functions. Medical Physics. 2019;46(2):505-16.

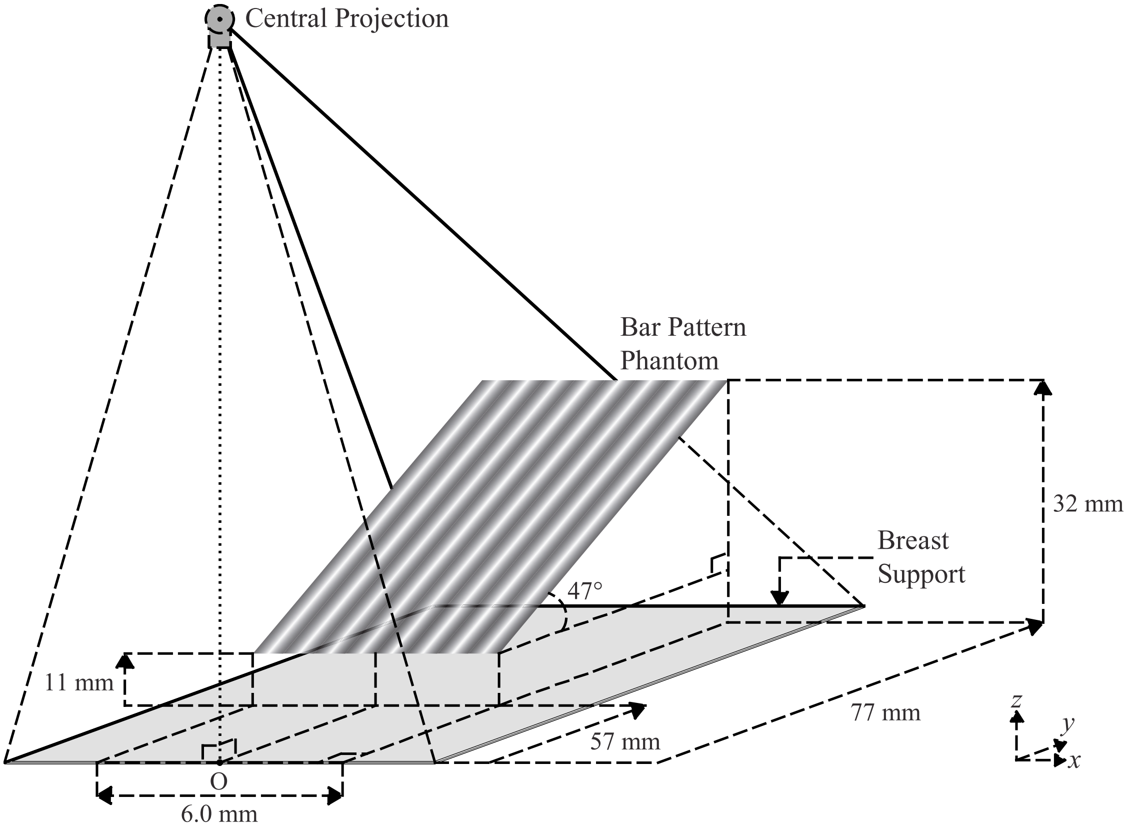

Figure 1. Diagram of bar pattern phantom in oblique plane. This setup was used to demonstrate the anisotropies in super-resolution in the *z* direction.

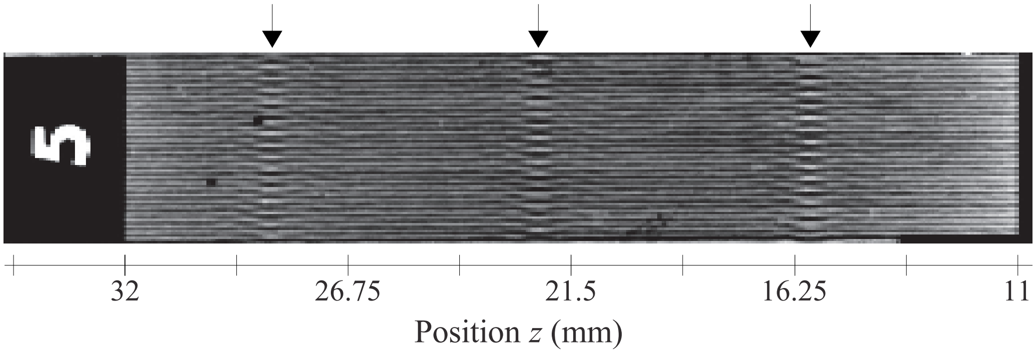

Figure 2. Aliasing artifacts (arrows) corresponding to positions at which super-resolution cannot be achieved. The reconstruction plane is matched to the oblique plane of the phantom in Fig. 1.

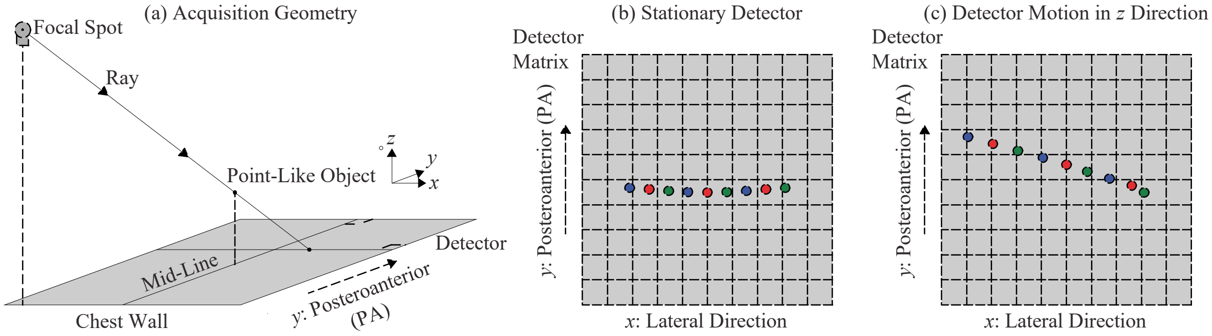

Figure 3. Thought experiment with point-like object. (a) The system is modeled with source motion in the *x* direction. (b) In a conventional system, the shifts between projections effectively vary by a constant increment in the *x* direction. (c) In a system with detector motion, the shifts in the *x* direction do not vary by the same increment. Also, there are more pronounced shifts in the *y* direction. Isotropic super-resolution can be achieved with this new design.

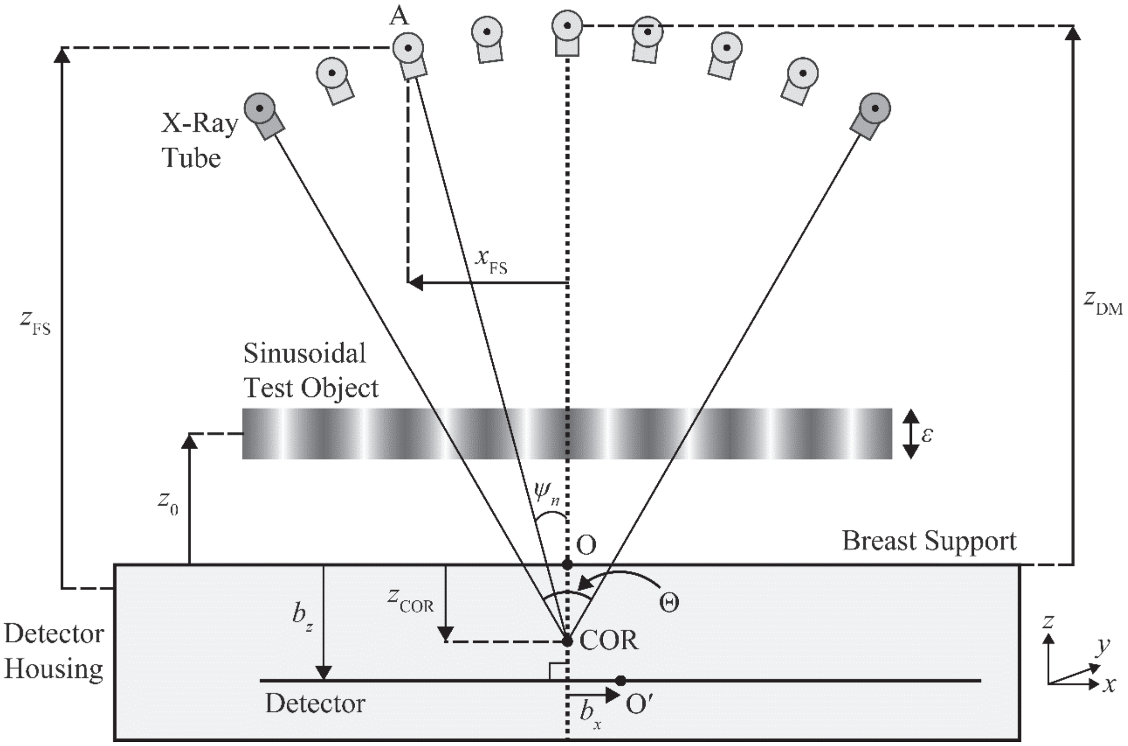

Figure 4. Diagram of source motion in a circular arc. The origin (O) is the midpoint of the chest-wall side of the breast support. The primed origin (O′) is the corresponding midpoint of the detector. The test object is a thin rectangular strip with a sinusoidal attenuation coefficient.

Table 1. Summary of parameters in the simulation, including acquisition geometry and sinusoidal test object.

Symbol	**Description**	**Value**
N	Number of projections	15
Θ	Range of source motion	19.2°
z_{DM}	Source-to-support distance	734.82 mm
z_{COR}	COR positioning	0 mm
$(b_x, b_y, b_{z,1})$	Point O′ for projection $n = 1$	(0, 0, −10.0) (in mm)
ε	Thickness	0.03 mm
a	Del size	0.085 mm
f_0	Frequency	8.0 mm^{-1}
x'_{min}	Lower Limit [Eq. (21)]	−3.125 mm
x'_{max}	Upper Limit [Eq. (21)]	3.125 mm
K	Number of samples [Eq. (22)]	1,000

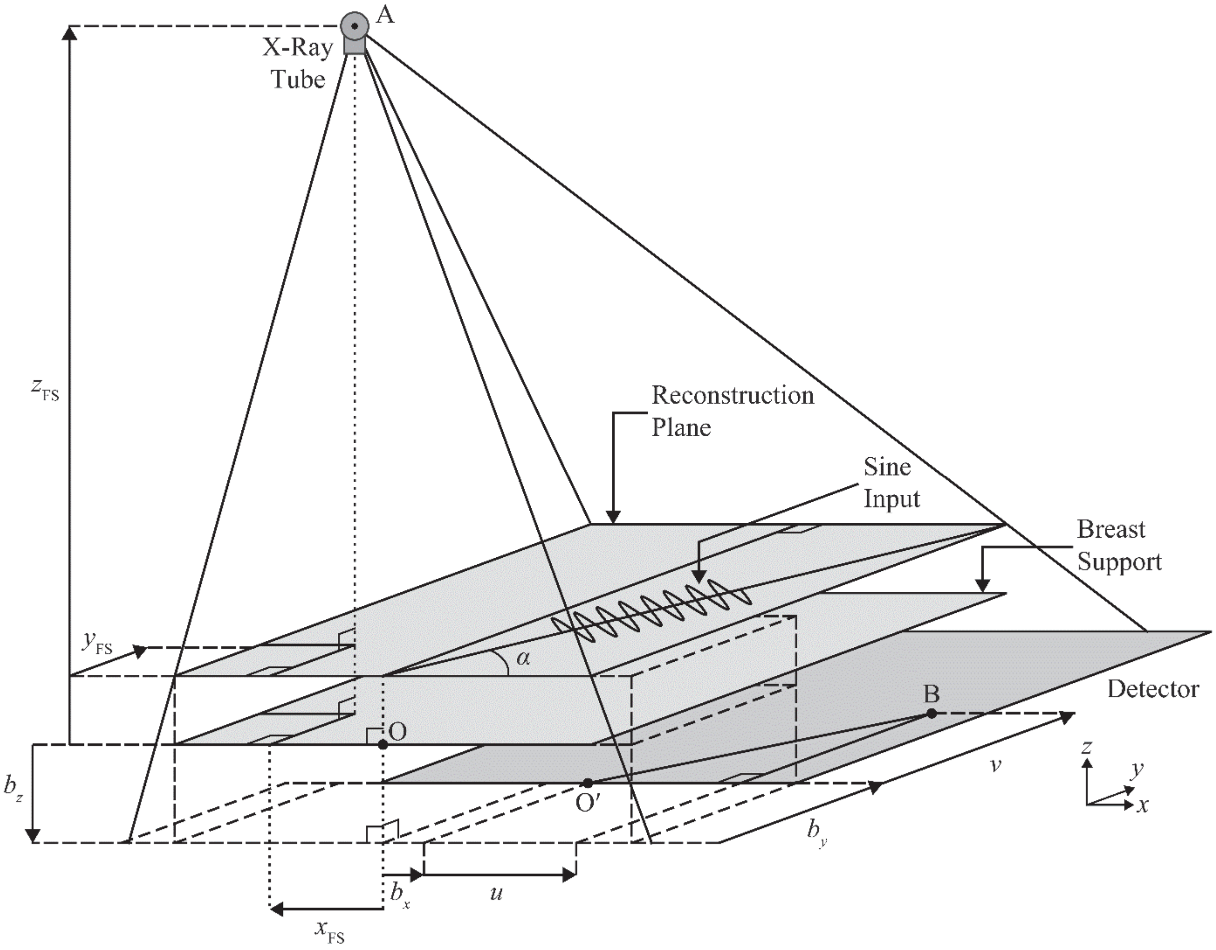

Figure 5. Diagram of acquisition geometry showing 3D coordinates for the x-ray source and detector. The detector is assumed to be parallel with the breast support in all projection views.

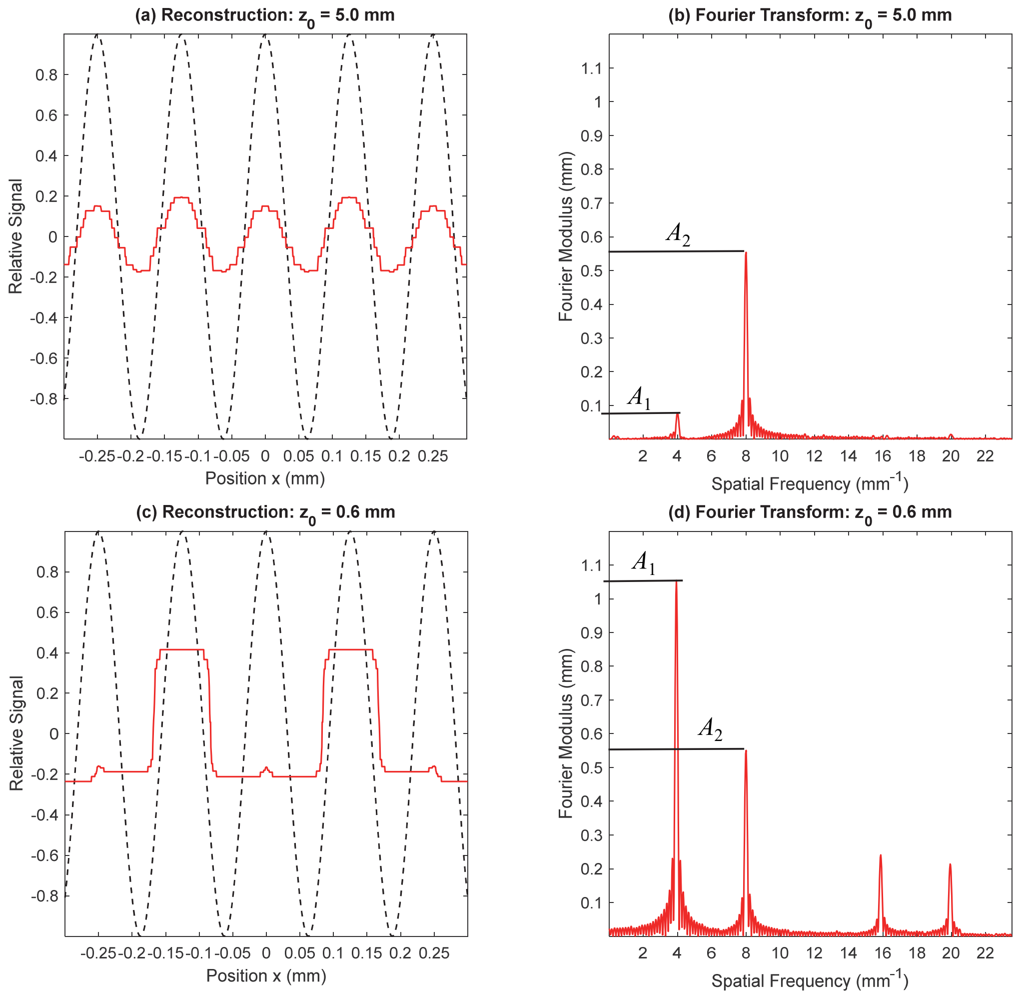

Figure 6. Reconstruction of sinusoidal test object to illustrate the calculation of *r*-factor. In Fourier space, the *r*-factor is the ratio of amplitudes A_1 to A_2. Super-resolution is achieved if *r*-factor < 1. At the coordinate $z_0 = 5.0$ mm, the *r*-factor is 0.14 and hence super-resolution is achieved. By contrast, at the coordinate $z_0 = 0.6$ mm, the *r*-factor is 1.91 and hence the signal is aliased.

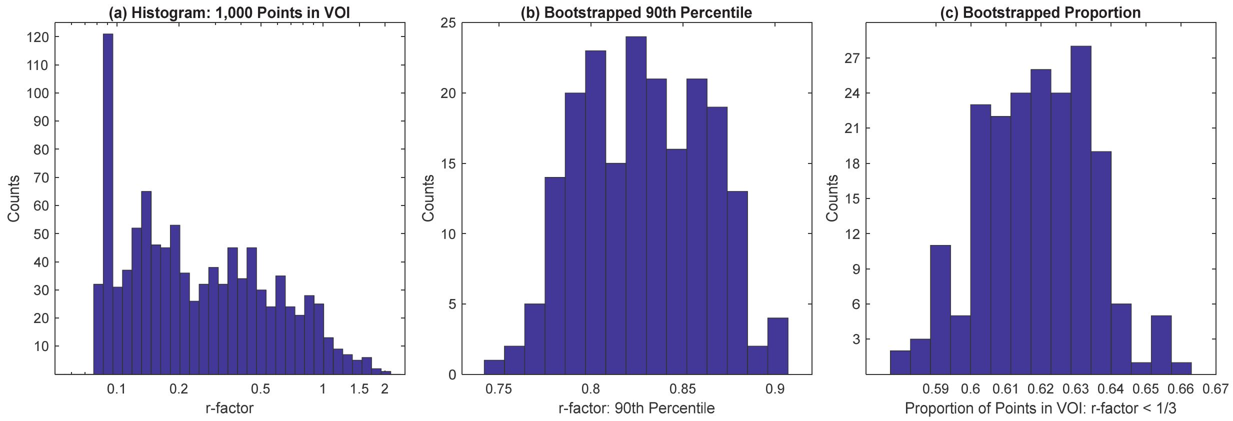

Figure 7. Random sampling of *r*-factor at 1,000 points in a VOI (bootstrapped 200 times). (a) First, the *r*-factor histogram was calculated from 1,000 points. (b) We determined the 90th percentile of the histogram in (a). The bootstrapped 95% confidence interval for this percentile ranges from 0.77 to 0.89. (c) Alternatively, using the histogram in (a), one can calculate the proportion of points in the VOI that meet a threshold (*e.g.*, *r*-factor < 1/3). The bootstrapped 95% confidence interval for this proportion ranges from 0.59 to 0.65.

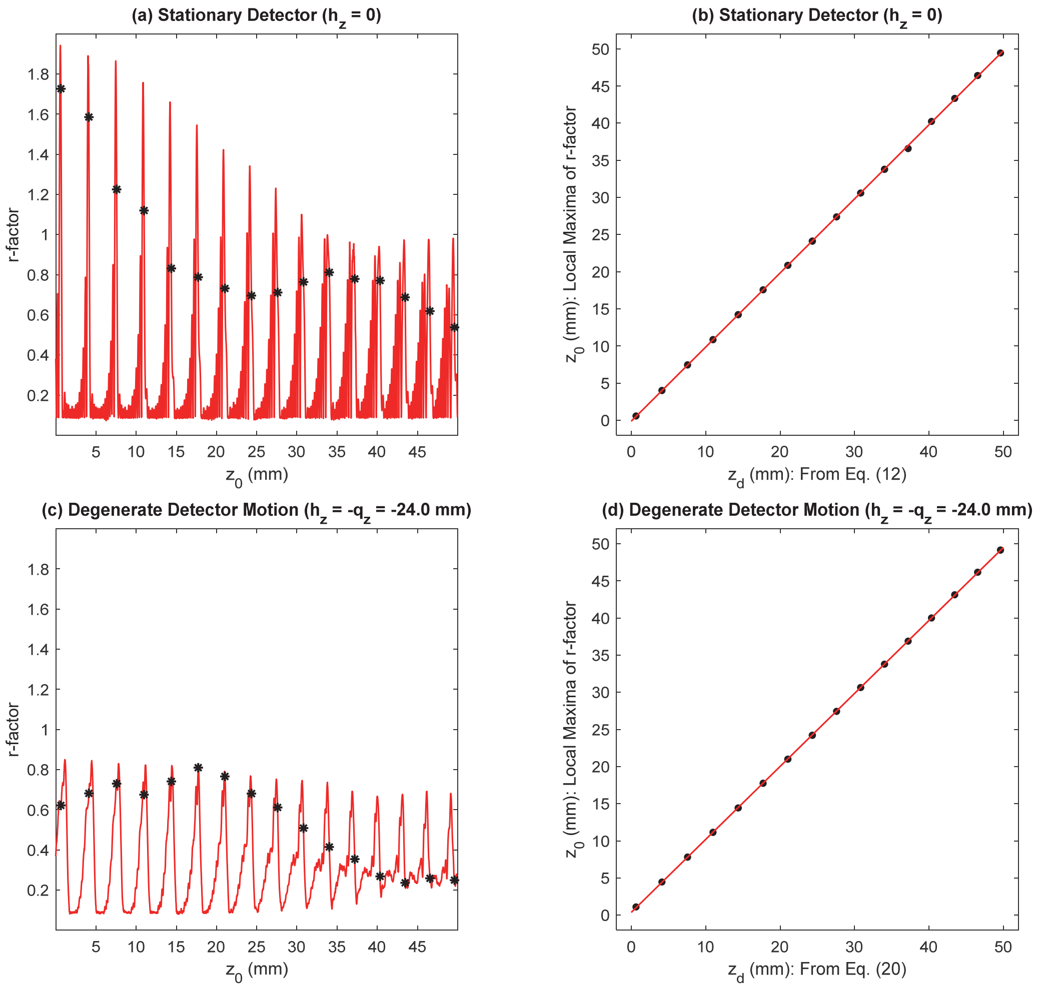

Figure 8. Illustration of degenerate z-coordinates. (a) In the conventional design ($h_z = 0$), there are 16 degeneracies in the range between $z_0 = 0$ and $z_0 = 50.0$ mm. (b) The peaks in the r-factor in subplot (a) are predicted very well by Eq. (12). (c) The detector motion range considered here ($h_z = -q_z = -24.0$ mm) is an example of a degenerate motion. There continues to be 16 peaks in the r-factor. (d) The peaks in the r-factor in subplot (c) are predicted very well by Eq. (20).

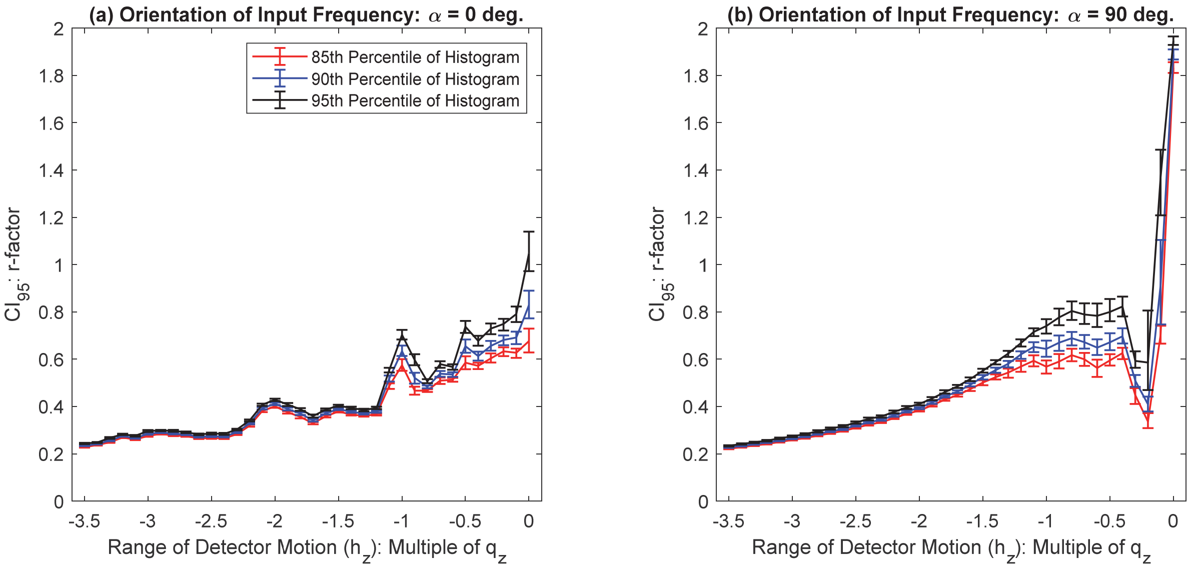

Figure 9. Effect of detector motion range on *r*-factor summary statistics. The *r*-factor was calculated at 1,000 random points in a VOI. The upper tail of this distribution was analyzed in terms of three percentiles (85th, 90th, and 95th). To achieve super-resolution with high quality, these summary statistics should be minimized (approaching zero). Error bars denote the bootstrapped 95% confidence interval.

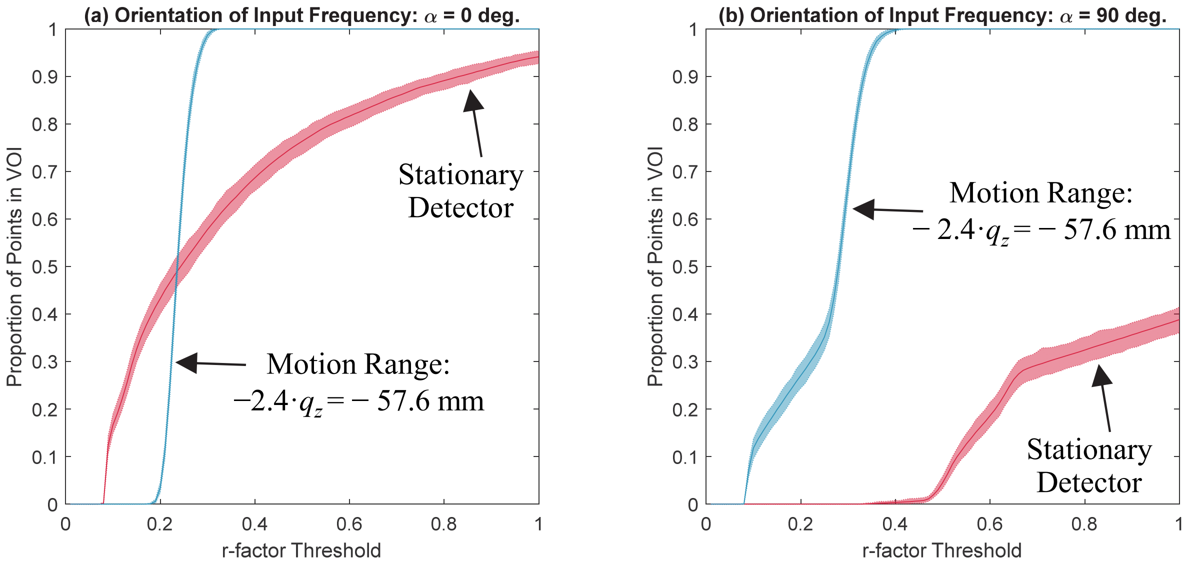

Figure 10. Effect of varying the *r*-factor threshold. We calculated the proportion of points in the VOI that meet a threshold. In a system with a stationary detector, less than 100% of points meet any threshold between zero and unity. By contrast, in the NGT design with detector motion, the curves rise more sharply to a plateau, indicating that the image quality is more uniform throughout the VOI. Shaded areas represent bootstrapped 95% confidence intervals.

Development of Magnification Tomosynthesis for Superior Resolution in Diagnostic Mammography

Raymond J. Acciavatti, Trevor L. Vent, Chloe J. Choi, E. Paul Wileyto,
Peter B. Noël, Andrew D. A. Maidment
University of Pennsylvania, Department of Radiology, 3400 Spruce Street, Philadelphia PA 19104
E-mail: {Raymond.Acciavatti | Trevor.Vent | Jeongin.Choi | epw | Peter.Noel |
Andrew.Maidment}@pennmedicine.upenn.edu

ABSTRACT

Our previous work showed that digital breast tomosynthesis (DBT) supports super-resolution (SR). Clinical systems are not yet designed to optimize SR; this can be demonstrated with a high-frequency line-resolution pattern. SR is achieved if frequencies are oriented laterally, but not if frequencies are oriented in the perpendicular direction; *i.e.*, the posteroanterior (PA) direction. We are developing a next-generation tomosynthesis (NGT) prototype with new trajectories for the x-ray source. This system is being designed to optimize SR not just for screening, but also for diagnostic mammography; specifically, for magnification DBT (M-DBT). SR is not achieved clinically in magnification mammography, since the acquisition is 2D. The aim of this study is to investigate SR in M-DBT, and analyze how anisotropies differ from screening DBT (S-DBT). We have a theoretical model of a high-frequency sinusoidal test object. First, a conventional scanning motion (directed laterally) was simulated. In the PA direction, SR was not achieved in either S-DBT or M-DBT. Next, the scanning motion was angled relative to the lateral direction. This motion introduces submillimeter offsets in source positions in the PA direction. Theoretical modeling demonstrated that SR was achieved in M-DBT, but not in S-DBT, in the PA direction. This work shows that, with the use of magnification, anisotropies in SR are more sensitive to small offsets in the source motion, leading to insights into how to design M-DBT systems.

Keywords: Digital breast tomosynthesis, magnification mammography, super-resolution, aliasing, Fourier transform, digital imaging, image quality, image reconstruction.

1. INTRODUCTION

Magnification mammography is a diagnostic study that uses the principle of geometric magnification to increase the spatial resolution.[1-2] The breast is elevated closer to the x-ray source, allowing subtle structures to appear larger. Current clinical systems support only 2D magnification mammography for diagnostic exams, even though screening exams are increasingly being performed with digital breast tomosynthesis (DBT) or "3D mammography".[3-6]

We have built a prototype next-generation tomosynthesis (NGT) system that supports new acquisition geometries for DBT.[7] Unlike clinical systems, the use of magnification DBT (M-DBT) is unique to the NGT system.[8] The NGT system also supports reconstructions with super-resolution (SR)[9]; the reconstruction grid is prepared with smaller pixelation than the detector. With a high-frequency star-pattern phantom, our previous work showed that the spatial resolution in both screening DBT (S-DBT) and M-DBT is improved with the use of SR. Additionally, a M-DBT image prepared with SR supports even higher resolution than a S-DBT image prepared with SR; hence the use of geometric magnification allows for a gain in resolution that cannot be achieved with SR alone.[8]

Our previous work showed that, in contact mode (S-DBT), there are anisotropies in SR if the input frequency is oriented perpendicular to the direction of the x-ray source motion; *i.e.*, the posteroanterior (PA) direction.[9] While clinical systems are not designed to include x-ray source motion in the PA direction, this paper demonstrates the potential benefit of introducing a secondary component of motion in this direction (Figure 1). The advantage of this design can be understood from the projection images of a point-like object (Figure 2). Angling the x-ray source positions gives rise to subpixel shifts in the image in the PA direction. These shifts are more pronounced in magnification mode (M-DBT), allowing for subpixel sampling gain in the PA direction and hence SR in this direction. In this paper, this design is investigated as a strategy to optimize SR in M-DBT.

Medical Imaging 2021: Physics of Medical Imaging, edited by Hilde Bosmans, Wei Zhao,
Lifeng Yu, Proceedings of SPIE Vol. 11595, 115951J · © 2021 SPIE
CCC code: 1605-7422/21/$21 · doi: 10.1117/12.2580280

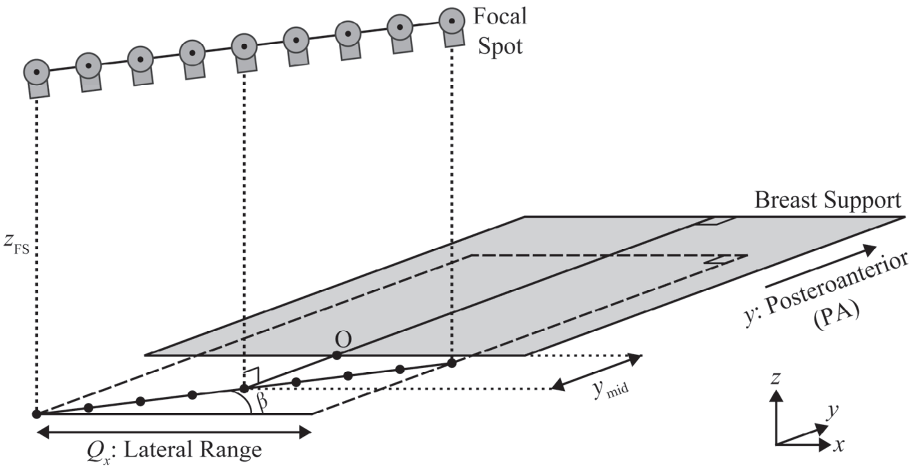

Figure 1. In this acquisition geometry, the focal spot (FS) motion is directed along the angle β. Angling the FS positions in this manner introduces a small secondary component of motion in the PA direction.

Our previous work analyzed SR in contact mode (S-DBT) using a theoretical model of a high-frequency sinusoidal test object.[10] This paper extends the theoretical model to magnification mode (M-DBT). We model the acquisition geometry with a secondary component of scanning motion in the PA direction; specifically, by simulating a range of different angles (β) in this direction. This paper identifies a range of angles, β, that support SR in the PA direction in M-DBT.

2. METHODS

2.1 Acquisition Geometry

We model an acquisition geometry with a small secondary component of motion in the PA direction (Figure 1). In this geometry, the focal spot (FS) positions lie along a line at the angle β relative to the primary direction of motion (lateral or x direction). The FS coordinates x_{FS} and y_{FS} for the n^{th} projection image are thus

$$x_{\mathrm{FS}} = \frac{(2n - N - 1)Q_x}{2(N-1)} \tag{1}$$

$$y_{\mathrm{FS}} = y_{\mathrm{mid}} + x_{\mathrm{FS}} \tan\beta \tag{2}$$

where n varies from 1 to N and Q_x is the range of source motion in the x direction (the primary direction of motion). These coordinates are measured relative to point O (the origin in Figure 1); *i.e.*, the midpoint of the chest-wall side of the breast support. The distance y_{mid} is the PA coordinate of the central source position relative to point O.

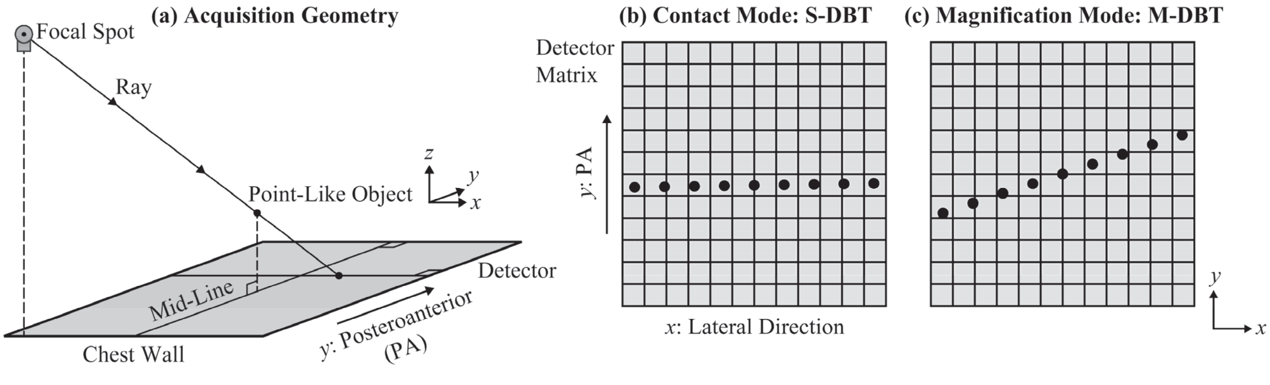

Figure 2. Projection images of a point-like object are shown for the acquisition geometry in Figure 1. In contact mode (S-DBT), the shifts in the image of the object are minimal in the PA direction. In magnification mode (M-DBT), the shifts are more pronounced, allowing for subpixel sampling gain in the PA direction.

Table 1. The simulation parameters for this study are summarized below.

Parameter	Value
Q_x: Lateral Range of X-Ray Source Motion	182.0 mm
y_{mid}: PA Displacement of Central Source Position	–2.0 mm
Distance z_{FS}: Breast Support to Source	685.0 mm
Distance b_z: Breast Support to Detector	–25.0 mm
N: Number of Projections	15
Thickness (ε) of Test Object	0.030 mm
Frequency of Test Object	9.5 mm^{-1}
Fourier Sampling: J_{FT}	1,000
x''_{min}: Lower Endpoint of Fourier Transform	–2.63 mm
x''_{max}: Upper Endpoint of Fourier Transform	2.63 mm

In the NGT system, the z-coordinate of the FS (z_{FS}) is constant in all projection images. The detector is stationary (displaced 25.0 mm below the breast support). The NGT detector (AXS-2430, Analogic Canada Corporation, Montreal, Quebec) has 0.085 mm pixelation and hence an alias frequency of 5.9 mm^{-1}. All other acquisition parameters are shown in Table 1.

2.2 Quantifying the Spatial Resolution

Our previous work developed a theoretical model of a high-frequency test object in DBT.[10] This object is a thin rectangular prism (thickness ε) with a sinusoidal attenuation coefficient (Figure 3). The mid-thickness of the object was modeled at an arbitrary position ($z = z_0$) in our previous work; therefore, magnification mode (M-DBT) can be simulated by varying z_0.

Our previous work calculated the simple backprojection (SBP) reconstruction of this object from first principles.[10] The Fourier transform of the reconstruction (μ_{SBP}) is analyzed to determine if the input frequency (9.5 mm^{-1}, Table 1) is resolved. This transform can be calculated with the midpoint formula for integration

$$\mathcal{F}\mu_{\mathrm{SBP}} \approx \left(\frac{x''_{\mathrm{max}} - x''_{\mathrm{min}}}{J_{\mathrm{FT}}}\right) \sum_{j_{\mathrm{FT}}=1}^{J_{\mathrm{FT}}} \mu_{\mathrm{SBP}} e^{-2\pi i f_x'' x''} \Big|_{x'' = x''_{\mathrm{min}} + (x''_{\mathrm{max}} - x''_{\mathrm{min}})\left(\frac{j_{\mathrm{FT}} - 1/2}{J_{\mathrm{FT}}}\right)}, \tag{3}$$

where x'' is position in the direction of the input frequency measured relative to a point of interest, x''_{min} and x''_{max} are the endpoints of the interval over which the reconstruction is calculated, and J_{FT} is the number of samples. From this transform, we calculate the r-factor, a metric introduced in our previous work on SR.[9,10] This metric is now illustrated for a conventional acquisition geometry (β = 0°), assuming z_0 = 50.0 mm (Figure 4), under two orientations for the input frequency: lateral (parallel with the direction of source motion) and PA (perpendicular to the direction of source motion).

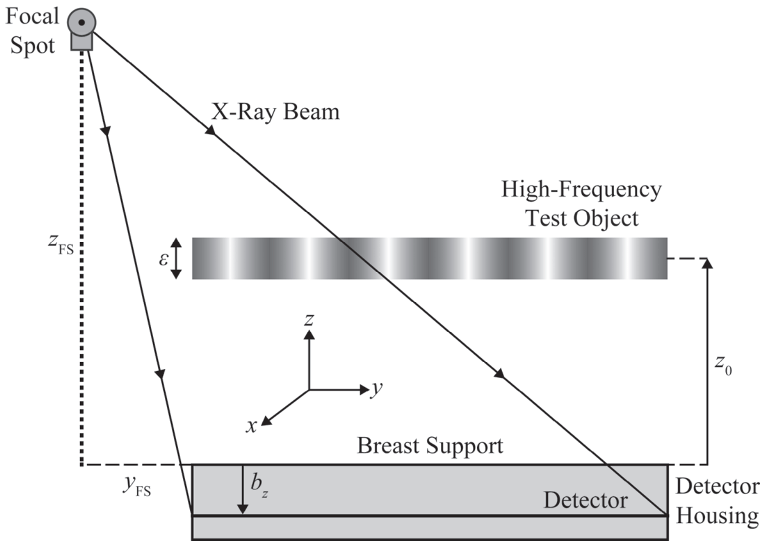

Figure 3. To investigate whether super-resolution is achievable in the PA direction in both contact mode (S-DBT) and magnification mode (M-DBT), the z_0-coordinate can be varied. This coordinate controls the height of the test object above the breast support.

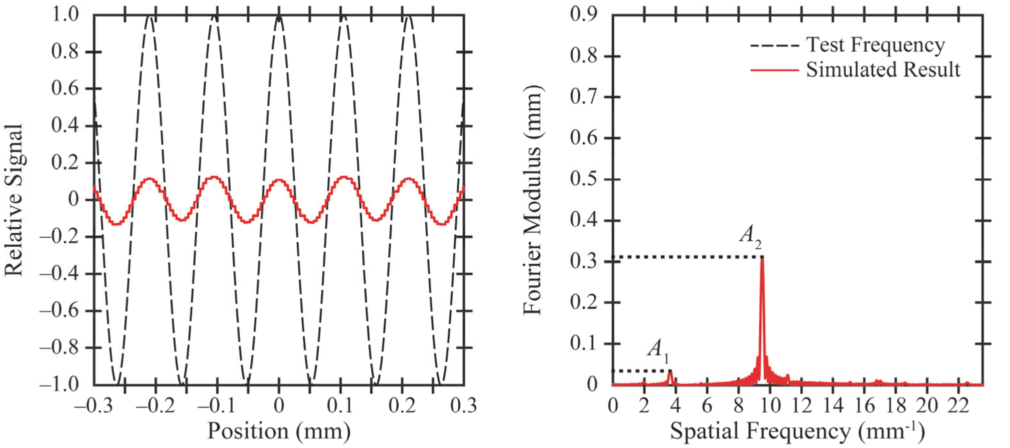

(a) Reconstruction: Lateral Orientation

(b) Fourier Transform: Lateral Orientation

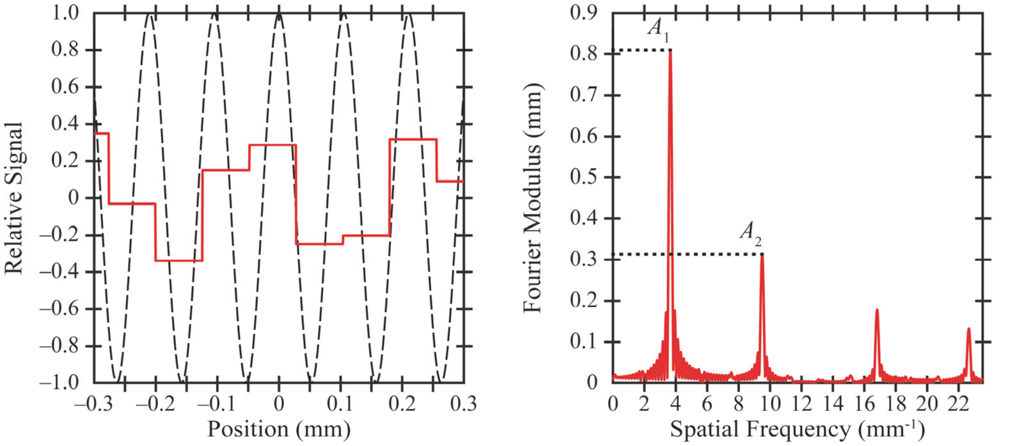

(c) Reconstruction: PA Orientation

(d) Fourier Transform: PA Orientation

Figure 4. (a) A conventional acquisition geometry, for which $\beta = 0°$, is simulated. The sinusoidal test object is resolved perfectly if frequency is oriented parallel with the direction of x-ray source motion. (b) The Fourier transform has a major peak at the input frequency, 9.5 mm^{-1}, under this orientation. (c) If the input frequency is rotated to the direction perpendicular to the source motion, the same object is not resolved properly. (d) The Fourier transform has a major peak at 3.7 mm^{-1} under this orientation.

Reconstructions of the object clearly differ based on the orientation of the input frequency. For the lateral orientation [Figure 4(b)], the Fourier transform has a major peak at the input frequency (9.5 mm^{-1}). By contrast, for the PA orientation [Figure 4(d)], the Fourier transform has a major peak at a lower frequency (3.7 mm^{-1}). The *r*-factor is defined to be the ratio of the amplitude at the low-frequency peak (A_1) to the amplitude at the input frequency (A_2).

$$r\text{-Factor} = \frac{A_1}{A_2} \tag{4}$$

SR is achieved if *r*-factor ≤ 1. The *r*-factor should be as close to zero as possible to achieve SR with high quality. In the example shown in Figure 4, the *r*-factor is 0.11 for the lateral orientation [Figure 4(b)] and is 2.6 for the PA orientation [Figure 4(d)].

2.3 Statistical Analysis

We used the *r*-factor to measure variation in image quality throughout the breast volume. For the purpose of these simulations, the volume-of-interest (VOI) was a rectangular prism with dimensions 200.0 × 100.0 × 50.0 (in mm) and 0.020 mm spacing between points in each direction. The *r*-factor was calculated at 1,000 random points in the VOI. These simulations focused on the PA orientation of the input frequency (the orientation corresponding to the anisotropy in SR in the conventional geometry). The VOI was displaced anterior to the chest-wall plane by +4.0 mm; this was done to ensure that the interval over which the Fourier transform is calculated [Eq. (3)] is included fully within the detector field-of-view.

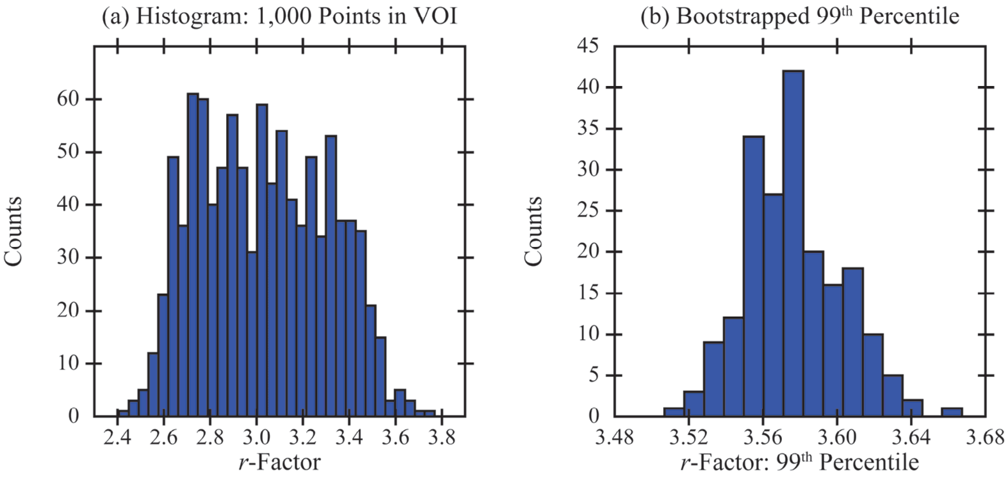

Figure 5. (a) First, the *r*-factor was calculated at 1,000 random points, yielding a histogram of values modeling the variation in image quality throughout the VOI. (b) The 99th percentile of the histogram in (a) was calculated 200 times with bootstrapping, resulting in the histogram shown. The bootstrapped 95% confidence interval (CI_{95}) for the 99th percentile ranges between 3.5 and 3.6.

We calculated the histogram of *r*-factor values at 1,000 random points; an example is shown in Figure 5(a) for the conventional acquisition geometry ($\beta = 0°$) in contact mode (S-DBT). To identify acquisition geometries that eliminate the anisotropy in SR in the PA direction, it is necessary for the upper tail of this histogram (*e.g.*, the 99th percentile) to be minimized below 1.0; this ensures that SR is achieved in at least 99% of points in the VOI. Figure 5(b) is a histogram representing 200 bootstrappings of the 99th percentile; from this histogram, a 95% confidence interval (CI_{95}) can be calculated for the 99th percentile. The middle 95% of the histogram yields CI_{95}. In this example, CI_{95} ranges between 3.5 and 3.6.

2.4 Comparing Contact Mode and Magnification Mode

In addition to contact mode, the same calculations were performed in magnification mode by elevating the VOI by 150.0 mm above the breast support. The z_0-coordinates in the VOI thus ranged between 150.0 and 200.0 mm. These coordinates correspond to magnifications of 1.3 and 1.5, respectively, where magnification (M) is given by

$$M = \frac{z_{\mathrm{FS}} - b_z}{z_{\mathrm{FS}} - z_0} \tag{5}$$

where b_z is the distance between the breast support and detector (Table 1). The alias frequency, which scales proportionate with the magnification, varies between 7.8 and 8.6 mm^{-1} in the VOI. For the purpose of the simulations, the frequency of the test object was fixed (specifically, at 9.5 mm^{-1}). We chose to hold the input frequency constant since the visualization task was specified relative to the patient anatomy, and hence independent of the positioning of the patient.

For both S-DBT and M-DBT, we simulated 16 acquisition geometries, differing in terms of the angle β (the angle of the secondary scanning motion in Figure 1). The angle β varied between 0° and 0.3° in 0.02° steps. The purpose of these simulations was to investigate whether increasing the angle β allows for SR in the PA direction, as determined by minimizing CI_{95} below 1.0.

3. RESULTS

3.1 Dependency of Super-Resolution on Magnification

First, a single (x, y) coordinate was analyzed; specifically, the coordinate (0, 25.0) (in mm). At this coordinate, the *r*-factor was calculated as a function of z_0, corresponding to an increase in the magnification, M [Figure 6(a)]. In the conventional acquisition geometry for which $\beta = 0°$ (solid red curve), the *r*-factor shows a downward trend as a function of magnification, indicating that there is an improvement in image quality. However, the *r*-factor does not fall below 1.0. Therefore, according to this model, SR is not achievable in the PA direction in either S-DBT or M-DBT.

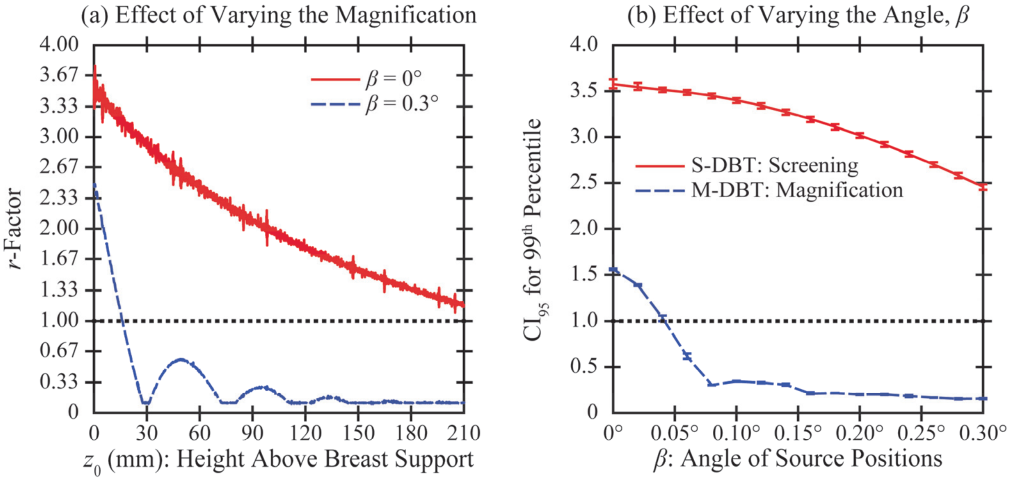

Figure 6. (a) Two acquisition geometries are analyzed in terms of the effect of increasing z_0 (increasing magnification). Higher image quality is achieved in the acquisition geometry with a small secondary component of source motion in the PA direction ($\beta = 0.3°$). (b) The upper tail of the *r*-factor distribution was analyzed in terms of the 99th percentile. In contact mode (S-DBT), the 95% confidence interval (CI_{95}) for this percentile is higher than 1.0, irrespective of the angle β. However, in magnification mode (M-DBT), CI_{95} does fall below 1.0 as the angle β increases.

Next, we simulated a scanning motion oriented at an angle relative to the direction of primary motion; specifically, at a 0.3° angle (dashed blue curve). This geometry is characterized by a secondary component of motion in the PA direction. With theoretical modeling, it can be seen that the *r*-factor exceeds 1.0 in contact mode ($z_0 = 0$, magnification of 1.04), and hence SR is not achieved in the PA direction. However, at magnifications exceeding 1.06 ($z_0 \geq 16.2$ mm), the *r*-factor does fall below 1.0. At magnifications that would be characteristic of M-DBT, the *r*-factor is well below 1.0, which indicates that there is high image quality. For example, at a z_0 coordinate of 200.0 mm (corresponding to a magnification of 1.5), the *r*-factor is 0.12. This indicates that, by angling the source motion in the manner shown by Figure 1, it is possible to achieve SR in the PA direction in M-DBT.

3.2 Statistical Analysis

The next focus of this study was on quantifying image quality as a function of the angle (β) of the source motion [Figure 6(b)]; specifically, through the analysis of CI_{95} as described in Sections 2.3 and 2.4. It can be seen that SR is not achievable in contact mode (S-DBT) at any of the angles considered (ranging between 0° and 0.3°). However, in magnification mode (M-DBT), it is possible to angle the source positions in such a way that CI_{95} does fall below 1.0; specifically, at angles of 0.06° or greater. At the highest angle considered ($\beta = 0.3°$), CI_{95} ranges between 0.15 and 0.16. Since this confidence interval is well below 1.0, SR is achieved with high image quality.

4. DISCUSSION AND CONCLUSION

In our previous work on magnification tomosynthesis, we showed that SR is achievable in experimental images of a star-pattern phantom.[8] This paper expands that work by demonstrating that there are anisotropies in SR in M-DBT depending on the orientation of the input frequency. Specifically, in a conventional acquisition geometry with source motion directed laterally ($\beta = 0°$), SR is not achievable in the PA direction; *i.e.*, the direction perpendicular to the scanning motion.

To achieve SR in the PA direction, it is necessary to re-design the acquisition geometry to include source motion in this direction. We model source motion with submillimeter offsets in the PA direction along the angle β (Figure 1). For example, if $\beta = 0.3°$, the source is translated in 0.068 mm steps in the PA direction per projection (corresponding to a total motion of 0.95 mm in the PA direction over 15 projection views). To validate this design as a strategy for suppressing the anisotropy in M-DBT, a scanning motion similar to the one described in this paper will be the subject of future experiments with the NGT prototype system and a star-pattern phantom.

Although scanning along the angle β is beneficial for magnification mode, the same motion does not suppress the anisotropy in screening mode (S-DBT); the *r*-factor continues to exceed 1.0 over the range of angles considered in this paper (0° to 0.3°). Our previous work proposed the use of detector motion in the PA direction to optimize SR in S-DBT.[11] The detector motion presented in our previous work is perfectly analogous to the source motion described in this paper in that the offsets are in submillimeter increments in the PA direction.

5. ACKNOWLEDGEMENT

ADAM has received research support from Hologic Inc., Barco NV, and Analogic Corporation; is a spouse to an employee and stockholder of Real Time Tomography (RTT), LLC; is a member of the scientific advisory board of RTT; and is an owner of Daimroc Imaging, LLC. PBN is a consultant to Stryker, and is a member of the computed tomography advisory board of Philips Healthcare. PBN also receives research support, travel award, speaker fees, and paid honorarium from Philips Healthcare.

Support was provided by the following grants: W81XWH-18-1-0082 from the Department of Defense Breast Cancer Research Program, IRSA 1016451 from the Burroughs Wellcome Fund, 1R01CA196528 from the National Institute of Health, and IIR13264610 from Susan G. Komen®. In addition, equipment support was provided by Analogic Inc., Barco NV, and RTT. The content is solely the responsibility of the authors and does not necessarily represent the official views of the funding agencies.

6. REFERENCES

[1] Muntz EP. On the comparison of actual and calculated improvements in the imaging of calcifications using magnification mammography. Medical Physics. 1981;8(4):496-501.
[2] Boyce SJ, Samei E. Imaging properties of digital magnification radiography. Medical Physics. 2006;33(4):984-996.
[3] Sechopoulos I. A review of breast tomosynthesis. Part I. The image acquisition process. Medical Physics. 2013;40(1):014301.
[4] Sechopoulos I. A review of breast tomosynthesis. Part II. Image reconstruction, processing and analysis, and advanced applications. Medical Physics. 2013:40(1):014302.
[5] Friedewald SM, Rafferty EA, Rose SL, Durand MA, Plecha DM, Greenberg JS, et al. Breast cancer screening using tomosynthesis in combination with digital mammography. Journal of the American Medical Association. 2014;311(24):2499-2507.
[6] Conant EF, Zuckerman SP, McDonald ES, Weinstein SP, Korhonen KE, Birnbaum JA, et al. Five consecutive years of screening with digital breast tomosynthesis: outcomes by screening year and round. Radiology. 2020;295(2):285-293.
[7] Eben JE, Vent TL, Choi CJ, Yarrabothula S, Chai L, Nolan M, Kobe E, Acciavatti RJ, Maidment ADA. Development of a Next Generation Tomosynthesis System. In: Lo JY, Schmidt TG, Chen G-H, editors; Physics of Medical Imaging; 2018; Houston, TX: SPIE; 2018. p. 105735Q-1 – 105735Q-8.
[8] Maidment TD, Vent TL, Ferris WS, Wurtele DE, Acciavatti RJ, Maidment ADA. Comparing the Imaging Performance of Computed Super Resolution and Magnification Tomosynthesis. In: Flohr TG, Lo JY, Schmidt TG, editors; Physics of Medical Imaging; 2017; Orlando, FL: SPIE; 2017. p. 1013222-1 – 1013222-10.
[9] Acciavatti RJ, Maidment ADA. Observation of super-resolution in digital breast tomosynthesis. Medical Physics. 2012;39(12):7518-39.
[10] Acciavatti RJ, Wileyto EP, Maidment ADA. Modeling acquisition geometries with improved super-resolution in digital breast tomosynthesis. In: Kontos D, Flohr TG, Lo JY, editors; Physics of Medical Imaging; 2016; San Diego, CA: SPIE; 2016. p. 978363-1 – 978363-12.
[11] Acciavatti RJ, Maidment ADA. Proposing an Acquisition Geometry That Optimizes Super-Resolution in Digital Breast Tomosynthesis. Lecture Notes in Computer Science. 2012;7361:386-93.

Next generation tomosynthesis image acquisition optimization for dedicated PET-DBT attenuation corrections

Trevor L. Vent*, Bruno Barufaldi, Raymond J. Acciavatti, Srilalan Krishnamoorthy, Suleman Surti, Andrew D.A. Maidment
Department of Radiology, University of Pennsylvania, Philadelphia, United States.
*Trevor.Vent@pennmedicine.upenn.edu

ABSTRACT

A next generation tomosynthesis (NGT) prototype is under development to investigate alternative acquisition geometries for digital breast tomosynthesis (DBT). A positron emission tomography (PET) device will be integrated into the NGT prototype to facilitate DBT acquisition followed immediately by PET acquisition (PET-DBT). The aim of this study was to identify custom acquisition geometries that (1) improve dense/adipose tissue classification and (2) improve breast outline segmentation. Our lab's virtual clinical trial framework (OpenVCT) was used to simulate various NGT acquisitions of anthropomorphic breast phantoms. Five custom acquisition geometries of the NGT prototype, with posteroanterior (PA) x-ray source motion ranging from 40-200 mm in 40 mm steps, were simulated for five phantoms. These acquisition geometries were compared against the simulation of a conventional DBT acquisition geometry. Signal in the reconstruction was compared against the ground truth on a voxel-by-voxel basis. The segmentation of breast from air is performed during reconstruction. Within the breast, we use a threshold-based classification of glandular tissue. The threshold was varied to produce a receiver operating characteristic (ROC) curve, representing the proportion of true fibroglandular classification as a function of the proportion of false fibroglandular classification at each threshold. The area under the ROC curve (AUC) was the figure-of-merit used to quantify adipose-glandular classification performance. Reconstructed breast volume estimation and sensitivity index (*d'*) were calculated for all image reconstructions. Volume overestimation is highest for conventional DBT and decreases with increasing PA source motion. AUC and *d'* increase with increasing PA source motion. These results suggest that NGT can improve PET-DBT attenuation corrections over conventional DBT.

Keywords: multi-modality imaging, digital breast tomosynthesis, positron emission tomography, attenuation correction, virtual clinical trial; ray tracing, binary classification, sensitivity index

1. INTRODUCTION

Digital breast tomosynthesis (DBT) has been shown to improve breast cancer detection and reduce patient callbacks,[1] indicating an increase in sensitivity and specificity.[2] Despite these advantages over full-field digital mammography, conventional DBT does not favor the detection and characterization of calcifications; and lacks prognostic capability.[2] Next generation tomosynthesis (NGT) is under development to investigate potential advances in breast cancer diagnostics and prognostics.

The first stage of development for the NGT prototype was the incorporation of novel x-ray acquisition geometries, including two-dimensional (2D) x-ray source motion in the mediolateral (ML) and posteroanterior (PA) directions and craniocaudal (CC) detector motion. We have evaluated the imaging capabilities of the preliminary NGT prototype using tests of physics and image quality.[3] NGT has been shown to support isotropic and high-quality super resolution,[4,5] improved breast volume estimation,[6,7] and reduced image reconstruction artifacts.[6,8]

Two planar positron emission tomography (PET) detectors will be integrated with the NGT prototype to provide functional imaging as a dedicated PET-DBT device (Figure 1). As an emission imaging modality, the 511 keV annihilation photons that form a PET signal are susceptible to Compton scatter and photoelectric absorption within the breast prior to detection leading to image nonuniformities. In order to achieve quantitative PET images, accurate attenuation correction of the PET data is necessary. In commercial whole-body PET/CT, the CT image is routinely used for PET attenuation correction. In a similar fashion, we anticipate using the DBT images for accurate attenuation correction of the PET data.

Adipose and fibroglandular tissue are the primary breast tissues in the female breast.[9] The task of determining the 3D volumetric outline (breast segmentation and breast volume estimation) and the task of classifying the adipose and fibroglandular tissue using DBT image reconstructions are two of the primary concerns for attenuation correction of the PET-DBT device.[10] DBT is an under-sampled tomographic technique and is thus prone to cone-beam artifacts and out-of-

Medical Imaging 2021: Physics of Medical Imaging, edited by Hilde Bosmans, Wei Zhao,
Lifeng Yu, Proceedings of SPIE Vol. 11595, 115954V · © 2021 SPIE
CCC code: 1605-7422/21/$21 · doi: 10.1117/12.2581097

plane reconstruction artifacts in the depth dimension due to overlapping structures. Cone-beam artifacts overestimate the breast volume and out-of-plane artifacts introduce difficulties for distinguishing fibroglandular tissue from adipose tissue. For these reasons, it is especially difficult to determine the true percent density of patient breasts without known ground truth.[11] The 2D x-ray source motion of the NGT prototype can be optimized using a virtual clinical trial (VCT) framework for these tasks with known ground truth. We hypothesize introducing PA source motion will improve breast volume segmentation and adipose-fibroglandular tissue classification.

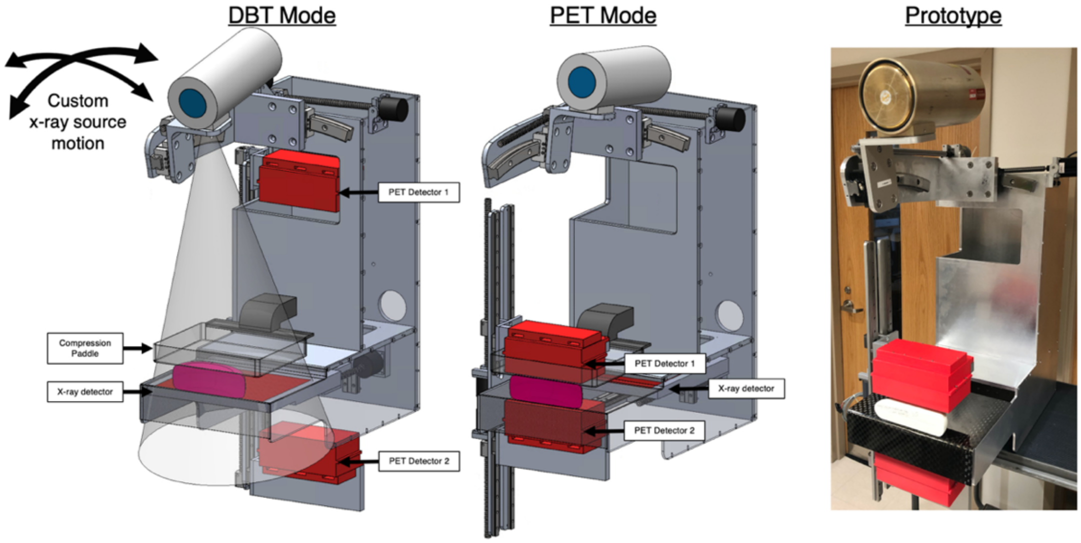

Figure 1: Design and photograph of the PET-DBT prototype. During **DBT Mode**, x-ray images are acquired while PET detectors are retracted into a homing position. Immediately following a tomosynthesis acquisition, PET detectors are positioned above and under the compressed breast and a PET scan is acquired (**PET mode**).

2. MATERIALS & METHOD

Image Acquisition

We used our open-source virtual clinical trial framework (OpenVCT)[12] to evaluate breast segmentation (breast volume estimation), and adipose-glandular classification for custom NGT acquisition geometries compared with conventional DBT. Five phantoms were generated and simulated using mediolateral (ML) compression (Figure 3). Each phantom consisted of a random distribution of adipose and glandular tissue compartments with skin surrounding these tissues. Phantoms were created using an isotropic voxel resolution of 0.1 mm. Each phantom has a volume of 700 mL and measures 7.8 cm × 6.3 cm × 20.5 cm after compression.

Five bowtie acquisition geometries that incorporate increasing distances of x-ray source motion in the PA direction, forming a V (Figure 2), were simulated for each phantom. In addition, a conventional acquisition geometry with the same number of projections and no PA source motion, was used to acquire projection images for all 5 phantoms. Each acquisition geometry consisted of 15 x-ray projections. The source to detector distance was constant at 652 mm. Images were acquired using 35 kVp, 70 mAs (4.67 mAs/projection), and aluminum filtration per projection.

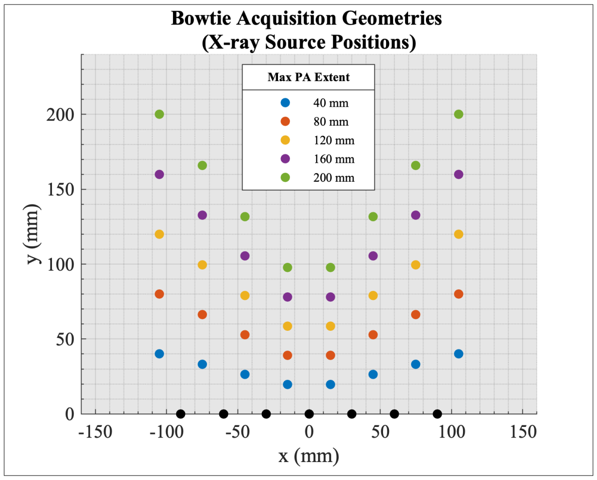

Figure 2: The bowtie acquisition geometries that were used for this study. The black dots represent the common projection locations amongst the 5 geometries. The maximum extent of PA-source motion (y) is indicated in the legend for each geometry. The coordinate (0,0) represents the origin of the NGT prototype at the center of the chest wall.

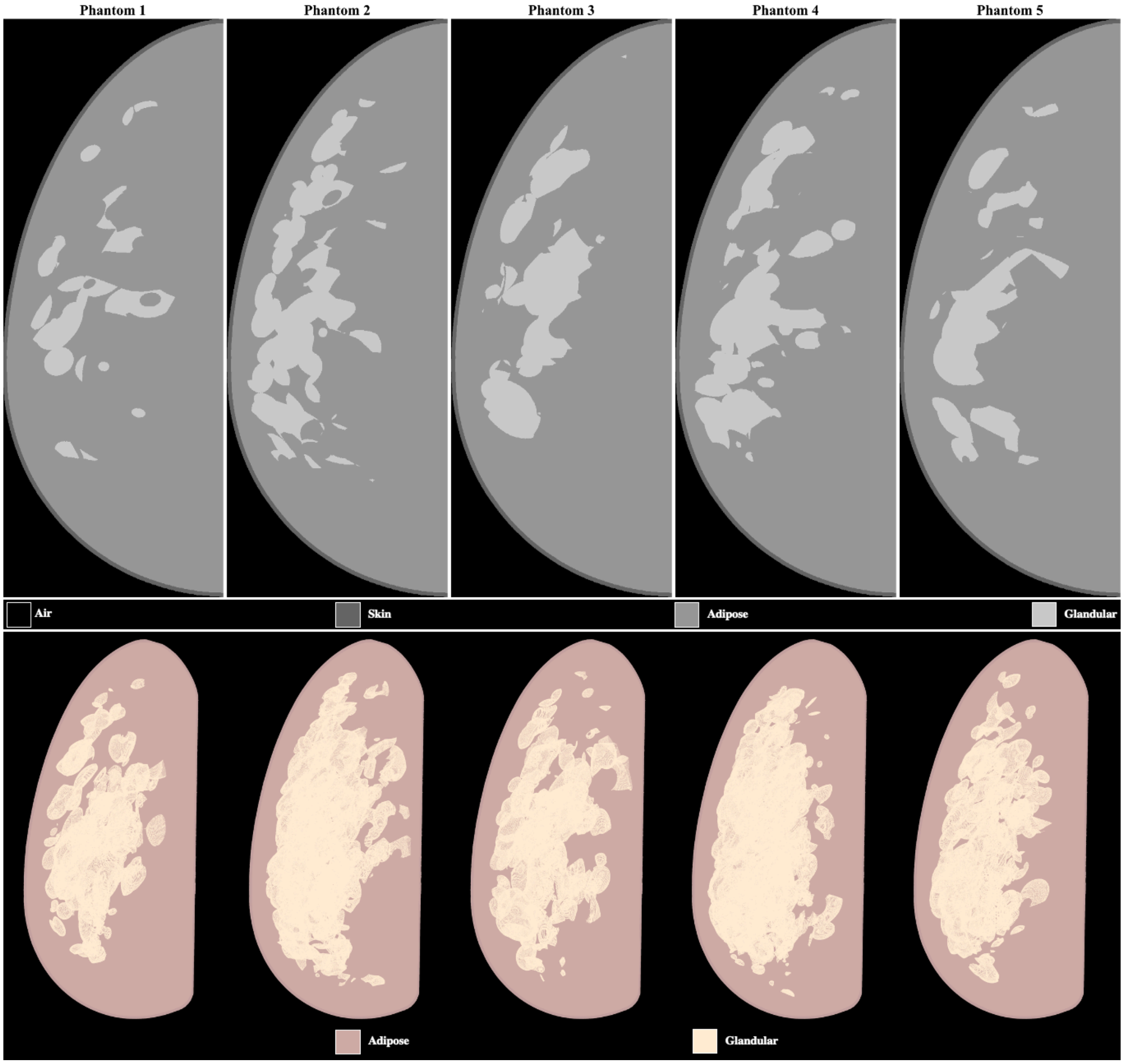

Figure 3: The central slice and maximum intensity projection render of each of the five phantoms are shown. Adipose, skin, and glandular breast tissue are the only materials that were simulated for the phantoms used in this study.

Simulated projection images were used to create image reconstructions of each acquisition using commercial reconstruction software. The outline of the breast was segmented from the background for each image reconstruction. Reconstructions were produced with a voxel resolution of $0.1 \times 0.1 \times 0.5$ mm^3 and processed with contrast enhancement filtering isotropically and bilaterally on each projection image (Piccolo version 4.0.5, Real Time Tomography, Villanova, PA).

Quantitative assessment

The reconstructed breast volume was estimated using the full-resolution image reconstructions. The reconstruction mask of each simulated acquisition was determined by the total volume of voxels with a signal greater than zero. Then, the reconstruction mask was normalized to the phantom mask of non-air voxels for each respective phantom (ground truth).

The reconstruction of the adipose-fibroglandular structures was assessed using a binary classification metric akin to ROC methods previously developed in our lab.[6] This analysis is computationally burdensome for full-resolution phantoms and reconstructions, so both the phantom and image reconstructions were down sampled to an isotropic resolution of 0.5 mm. The phantoms were down-sampled using nearest-neighbor interpolation (mode), and image reconstructions were down sampled using bilinear interpolation. The down-sampled image reconstructions were compared against the phantom ground truth.

ROC curves were produced by using the signal intensity of the image reconstruction as a threshold for a binary classification task. Signals above the threshold were classified as glandular tissue (including voxels containing skin) and signals below were classified as adipose. The true positive rate (TPR) was graphed against the false positive rate (FPR) for each image reconstruction as a function of the threshold value. Area under the curve (AUC) was calculated for each ROC. Colormap images, showing voxel-by-voxel representations of the binary classifications, were created to visualize the differences in image reconstructions of the various acquisition geometries.

In binary classification tasks, the sensitivity index (d') quantifies the effective signal-to-noise ratio of a two-alternative forced choice classification.[13] We use d' to determine differences between different geometries. d' is obtained using an inverse error function and AUC:

$$d' = 2 \cdot \operatorname{erf}^{-1}(2 \cdot \mathrm{AUC} - 1) \tag{1}$$

We then calculated the difference in d' ($\Delta_{d'}$) between bowtie acquisition geometries (b) and the conventional acquisition geometry (c) to quantify performance:

$$\Delta_{d'} = \frac{d'_b - d'_c}{d'_c} \tag{2}$$

3. RESULTS AND DISCUSSION

The central slice of the bowtie acquisition geometry with 80 mm of PA source motion is shown as an example for all five phantoms in Figure 4. Image reconstructions for the conventional and remaining bowtie acquisition geometries have a similar overall appearance. It is difficult to discern any differences qualitatively between the reconstructions of the various acquisition geometries in the conventionally reconstructed sagittal slices. Therefore, coronal and transverse reconstruction slices near respective midplanes of Phantom 2 are shown for the six geometries alongside the ground truth in Figure 5.

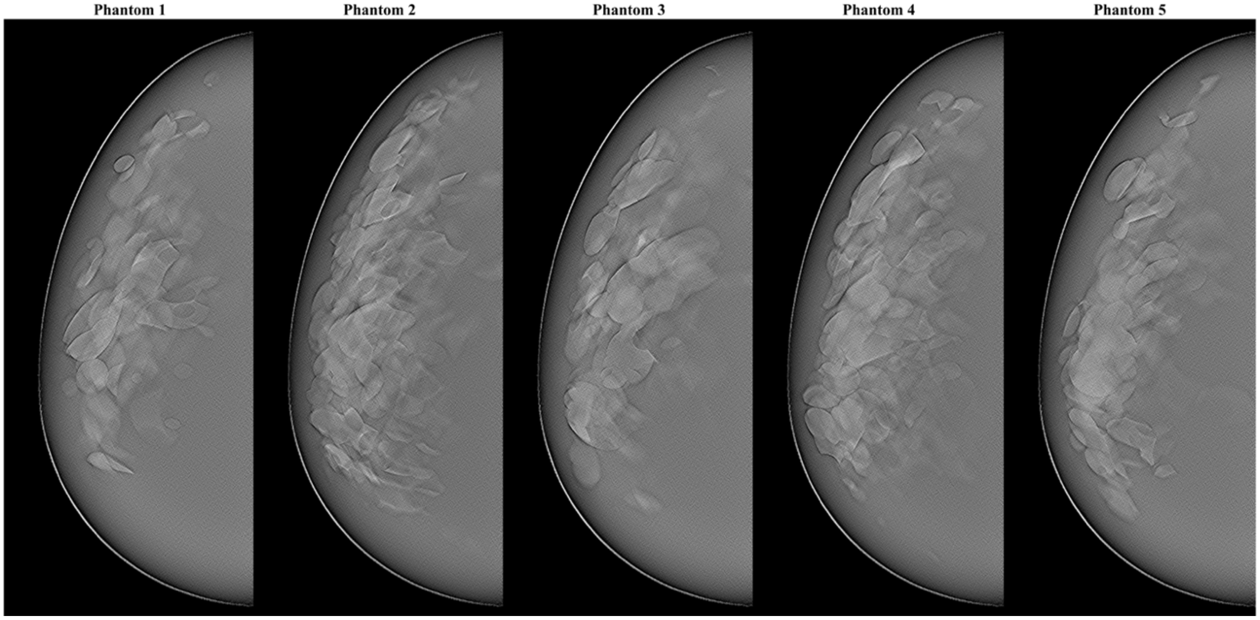

Figure 4: Examples of the central slice of image reconstructions for each of the five phantoms in the conventionally reconstructed sagittal slices (bowtie acquisition with 80 mm PA source motion).

Coronal and sagittal reconstruction slices show trends of improved breast outline delineation and signal contrast of overlapping tissue that scale with PA source motion. Coronal slices Additionally, the effect of cone-beam artifacts is observed in the transverse slices. The artifacts are most prominent in the conventional acquisition geometry (0 mm) and are reduced for acquisition geometries with PA source motion greater than 80 mm.

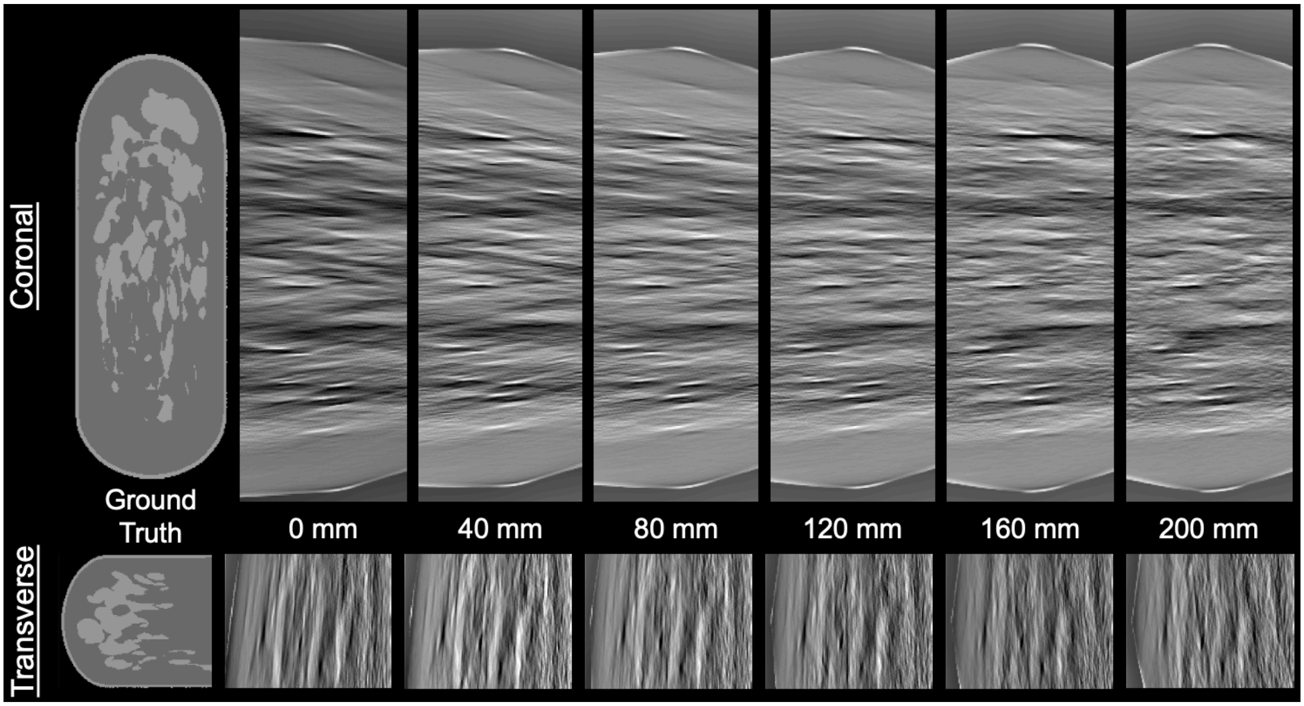

Figure 5: Coronal and transverse reconstruction slices of the conventional acquisition geometry (0 mm) and the five NGT acquisition geometries with increasing PA source motion (40 – 200 mm).

An example of the binary classification is shown for the central slice of a conventional acquisition geometry and an NGT acquisition geometry with 200 mm of PA source motion as a colormap in Figure 6 (sagittal plane) and Figure 7 (transverse plane). This example is shown with a signal threshold at the optimal operating cut-point and was determined by the minimum Euclidean distance from the top left corner (0,1) of the ROC curve. The colormap images of the NGT geometry show fewer out-of-plane reconstruction artifacts compared with the conventional geometry.

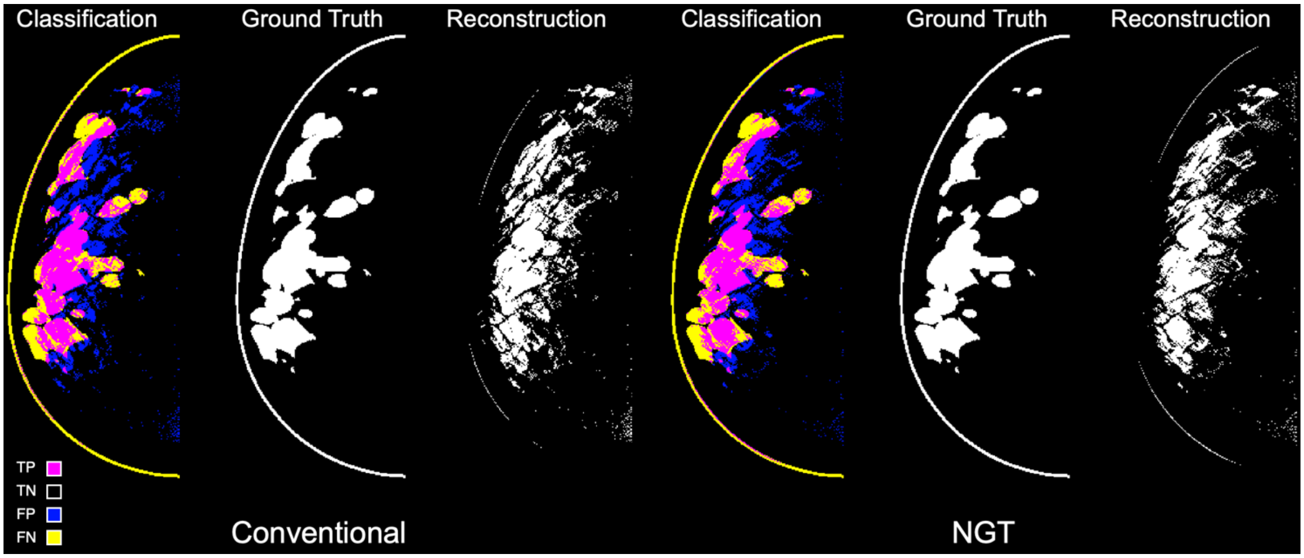

Figure 6: Binary classification colormap of a conventional reconstruction and NGT acquisition with 200 mm of PA source motion. The classification image shows true positives (TP), true negatives (TN), false positives (FP), and false negatives (FN). For the Ground Truth and Reconstruction images, white represents fibroglandular tissue.

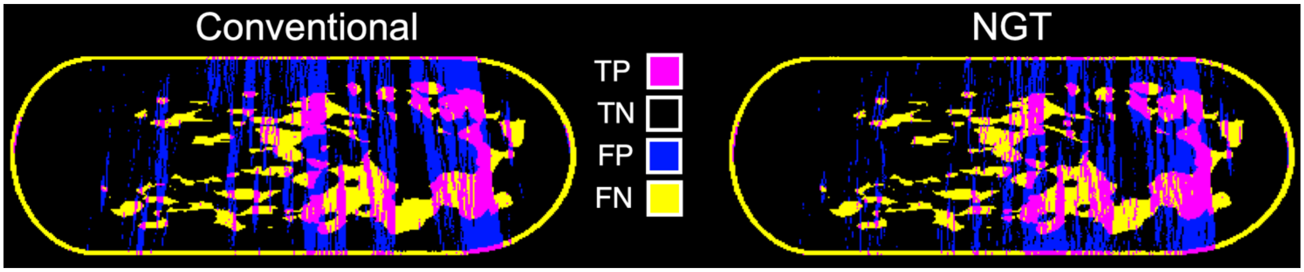

Figure 7: Coronal slice examples of the colormap images. The NGT acquisition geometry shows fewer out-of-plane artifacts (false positives) compared with the conventional geometry.

The mean volume overestimation of the five phantoms is graphed against PA source motion in Figure 8 (left). The conventional DBT acquisition geometry shows the highest overall volume estimation at 112.4% of the ground truth. Volume estimation decreases with increasing PA source motion to a low of 108.0% with 200 mm of PA source motion. This result is consistent with previous results[6,7] and indicates that PA source motion in DBT decreases artifacts in image reconstructions.

Average improvement in *d'* is graphed against PA source motion in Figure 8 (right). Positive values indicate that all bowtie acquisition geometries show improvement in *d'* over conventional DBT. The greatest overall improvement is 8% for two of the five phantoms. These results are preliminary and need to be evaluated further. Phantoms of different volumes and various percent density will be analyzed to evaluate additional factors that can affect volume overestimation and the sensitivity index. The impact of image processing has not been evaluated. For the sake of this study, image processing was the same across all acquisition geometries. Acquisition-geometry specific image processing could provide improved filtering of out-of-plane artifacts for novel geometries. We chose the simplest method of segmentation – threshold segmentation – to test the physics of the NGT system and optimize image acquisition geometries. This approach will improve input data for the ultimate segmentation task.

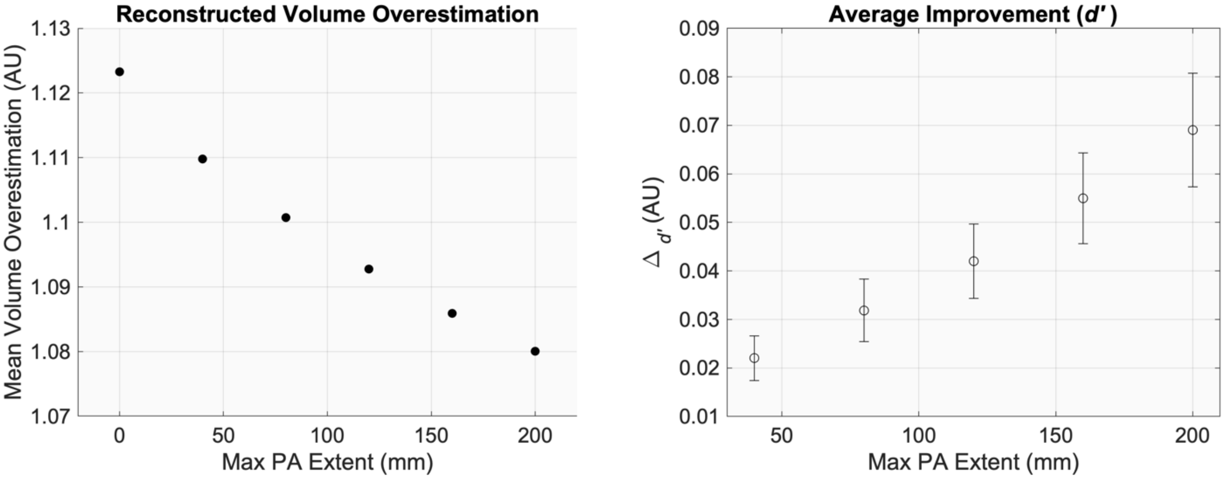

Figure 8: Mean volume overestimation as a function of PA source motion (left). Improvement in *d'* for bowtie acquisition geometries with PA-source motion ranging from 40 mm to 200 mm (right).

4. CONCLUSION

The PA source motion of the custom NGT acquisition geometries has been shown to improve volume estimation and adipose-glandular classification for DBT using a simple threshold-based method. Results suggest that the NGT acquisition geometries can improve the accuracy of PET-DBT attenuation corrections. This method will be used to evaluate additional phantom parameters and acquisition geometries. These results can also be used to help determine a superior classification or tissue segmentation method for DBT.

5. ACKNOWLEDGEMENTS

The authors would like to thank Johnny Kuo, Susan Ng, and Peter Ringer of Real Time Tomography for technical assistance with Piccolo. Andrew D. A. Maidment is a shareholder of Real Time Tomography and is a member of the scientific advisory board.

Support was provided by the following grants: W81XWH-18-1-0082 from the Department of Defense Breast Cancer Research Program, IRSA 1016451 from the Burroughs Welcome Fund, 1R01CA196528 from the National Institute of Health, IIR13264610 from Susan G. Komen, and 2020 Research Seed Grant from American Association of Physicists in Medicine. In addition, equipment support was provided by Analogic Inc., Barco NV, and Real Time Tomography. The content is solely the responsibility of the authors and does not necessarily represent the official views of the funding agencies.

REFERENCES

[1] Rafferty, E. a, Park, J. M., Philpotts, L. E., Poplack, S. P. and Sumkin, J. H., “Digital Mammography and Breast Tomosynthesis Compared with Digital Mammography Alone : Results of a Multicenter, multireader trial,” Radiology **266**(1), 104–113 (2013).

[2] Conant, E. F., “Clinical Implementation of Digital Breast Tomosynthesis,” Radiol. Clin. North Am. **52**(3), 499–518 (2014).

[3] Vent, T. L., Acciavatti, R. J. and Maidment, A. D. A., “Development and Evaluation of the Fourier Spectral Distortion Metric,” IEEE Trans. Med. Imaging, 1 (2020).

[4] Vent, T. L., Barufaldi, B. and Maidment, A. D. A., “Simulation and experimental validation of high-resolution test objects for evaluating a next-generation digital breast tomosynthesis prototype,” 21 (2019).

[5] Vent, T. L., Lepore, B. L. and Maidment, A. D. A., “Evaluating the imaging performance of a next-generation digital breast tomosynthesis prototype,” SPIE Med. Imaging(March), 19 (2019).

[6] Acciavatti, R. J., Barufaldi, B., Vent, T. L., Wileyto, E. P. and Maidment, A. D. A., “Personalization of x-ray tube motion in digital breast tomosynthesis using virtual Defrise phantoms,” SPIE Med. Imaging(March), 10 (2019).

[7] Acciavatti, R. J., Rodriguez-Ruiz, A., Vent, T. L., Bakic, P. R., Reiser, I., Sechopoulos, I. and Maidment, A. D. A., “Analysis of volume overestimation artifacts in the breast outline segmentation in tomosynthesis,” SPIE Med. Imaging, 10573 (2018).

[8] Vent, T. L., Barufaldi, B., Acciavatti, R. J. and Maidment, A., “Simulation of high-resolution test objects using non-isocentric acquisition geometries in next-generation digital tomosynthesis,” 15th Int. Work. Breast Imaging **11513**, C. Van Ongeval, N. Marshall, and H. Bosmans, Eds., 23, SPIE (2020).

[9] McCarthy, A. M., Kontos, D., Synnestvedt, M., Tan, K. S., Heitjan, D. F., Schnall, M. and Conant, E. F., “Screening outcomes following implementation of digital breast tomosynthesis in a general-population screening program,” J. Natl. Cancer Inst. **106**(11) (2014).

[10] Krishnamoorthy, S., Vent, T., Barufaldi, B., Maidment, A. D. A., Karp, J. S. and Surti, S., “Evaluating attenuation correction strategies in a dedicated, single-gantry breast PET-tomosynthesis scanner,” Phys. Med. Biol. (2020).

[11] Pertuz, S., McDonald, E. S., Weinstein, S. P., Conant, E. F. and Kontos, D., “Fully automated quantitative estimation of volumetric breast density from digital breast tomosynthesis images: Preliminary results and comparison with digital mammography and MR imaging,” Radiology (2016).

[12] Barufaldi, B., Bakic, P. R., Higginbotham, D. and Maidment, A. D. A., “OpenVCT: a GPU-accelerated virtual clinical trial pipeline for mammography and digital breast tomosynthesis,” Med. Imaging 2018 Phys. Med. Imaging **1057358**(March), 194 (2018).

Analysis of Digital Breast Tomosynthesis Acquisition Geometries in Sampling Fourier space

Chloe J. Choi, Trevor L. Vent, Raymond J. Acciavatti, Andrew D. A. Maidment
University of Pennsylvania, Department of Radiology, 3400 Spruce Street, Philadelphia, PA 19104
Email: {Jeongin.Choi, Trevor.Vent, Raymond.Acciavatti,
Andrew.Maidment}@pennmedicine.upenn.edu

ABSTRACT

Tomosynthesis acquires projections over a limited angular range and thus samples an incomplete projection set of the object. For a given acquisition geometry, the extent of tomosynthesis sampling can be measured in the frequency domain based on the Fourier Slice Theorem (FST). In this paper we propose a term, "sampling comprehensiveness", to describe how comprehensively an acquisition geometry samples the Fourier domain, and we propose two measurements to assess the sampling comprehensiveness: the volume of the null space and the nearest sampled plane. Four acquisition geometries, conventional (linear), T-shape, bowtie, and circular geometries, were compared on their comprehensiveness. The volume of the null space was estimated as the percentage of voxels subtended by zero slices in the sampled Fourier space. For each voxel in the frequency space, the nearest sampled plane and the distance to that plane were recorded. Among the four, the circular geometry was determined to be the most comprehensive based on the two measurements. We review tomosynthesis sampling with a finite number of projections and discuss how the sampling comprehensiveness should be interpreted. We further suggest that the decision on a system geometry should consider multiple factors including the sampling comprehensiveness, the task to be performed, the thickness of the imaged object, system specifications, and reconstruction algorithm.

Keywords: Fourier space, tomosynthesis sampling, Fourier slice theorem

1. INTRODUCTION

In tomography, the extent to which an object is tomographically sampled can be estimated through analysis of the projections in the Fourier domain. Tomosynthesis acquires projections over a limited angular range, sampling only a subset of the Fourier domain. Due to incomplete sampling, tomosynthesis suffers from more extensive artifacts and poorer in-depth resolution compared to computed tomography.[1-3] To overcome this inevitable limitation of tomosynthesis, researchers have investigated the effects of various acquisition geometries on image quality and hence data sampling.

Multiple acquisition geometries have been investigated since the introduction of tomosynthesis. The conventional geometry is the linear, or arced, geometry, in which the source and the detector move linearly around the patient. [3,5]Although this geometry is well-studied in clinical settings and easy to implement mechanically, out-of-plane objects are blurred into lines and their appearance is highly dependent on orientation[4]. In addition, super-resolution (i.e., subpixel resolution) is absent or poor in the perpendicular direction to the system motion[5]. More advanced geometries including two-dimensional linear source motion, circular source motion, and others have been studied, many of which were shown to have distinct benefits over the linear geometry, although at the expense of other qualities.[4,6-11,13].

A next generation tomosynthesis (NGT) system has been constructed at the University of Pennsylvania to investigate various acquisition geometries.[12] Multiple geometries have been proposed for different tasks and tested with the NGT system including a T-shape source trajectory, a bowtie source trajectory, and a circular source trajectory, with and without detector motion[10,11,13,15,16]. They have been analyzed quantitatively in terms of the modulation transfer function (MTF), noise power spectra (NPS), reconstructed breast volume estimation, and feasibility of super-resolution (SR) in our previous works[10,11,15,22]. However, we have not previously assessed how comprehensively these acquisition geometries sample the imaged object.

The extent of tomosynthesis sampling in the frequency domain can be approximated based on the Fourier Slice Theorem (FST). The Fourier Slice Theorem, also known as the Central Projection Theorem or the Projection Slice Theorem, relates the two-dimensional Fourier transform (2D-FT) of the projection of a three-dimensional object to the three-dimensional Fourier transform (3D-FT) of the same object. Specifically, it states[14] that the 2D-FT of the projection at an angle θ is equal to a slice of the 3D-FT of the object at the same angle θ. One can apply the FST to visualize how various acquisition geometries sample data in the frequency domain as shown in Figure 1.

Medical Imaging 2021: Physics of Medical Imaging, edited by Hilde Bosmans, Wei Zhao,
Lifeng Yu, Proceedings of SPIE Vol. 11595, 115954W · © 2021 SPIE
CCC code: 1605-7422/21/$21 · doi: 10.1117/12.2582229

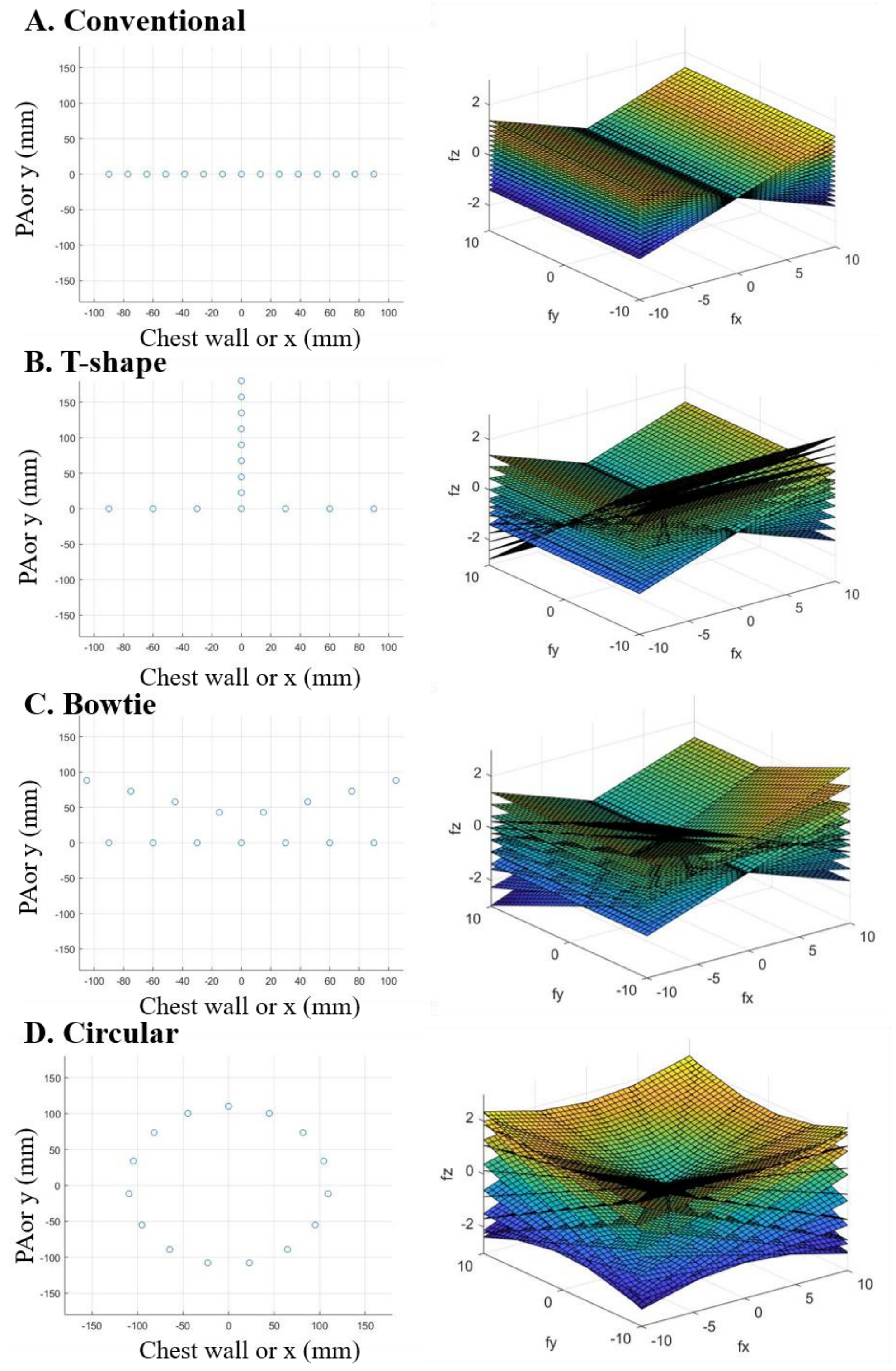

Figure 1. X-ray source acquisition geometries (left) and how each geometry samples the reconstructed images in Fourier space based on the Fourier slice theorem (right). One x-ray projection samples a slice through the origin in Fourier space. f_x, f_y, and f_z are in cycles per millimeters (mm^{-1}).

Each acquisition geometry shown in Figure 1 includes 15 x-ray projections. The axes in the Fourier space figures (Figure 1, right) are frequency domains in x, y, and z (f_x, f_y, f_z) as noted and they are in scale with one another and across all figures. The figures are shown with $f_x, f_y \in [-10,10]$ and $f_z \in [-3,3]$ in mm^{-1}.

Note, the figures are created under the following assumptions:

(1) The object being imaged is located at the origin (0,0,0) of the spatial domain.
(2) A parallel x-ray beam projects onto the detector, which moves isocentrically with the x-ray source.
(3) No imaging parameters (e.g., detector element size, shape and orientation) are considered. This means that the limits of sampling frequency (i.e., Nyquist frequency) in any direction are not illustrated.

In this paper, we propose a term "sampling comprehensiveness" to describe the extent of Fourier data sampling by a particular tomosynthesis scan geometry. An acquisition geometry which spans the greatest volume in Fourier space will be said to have the highest sampling comprehensiveness. The concept of sampling comprehensiveness will be further expanded throughout the paper as we suggest two measurements to assess it. The four acquisition geometries shown in Figure 1 will be compared. We review frequency sampling in tomosynthesis with a finite number of projections and discuss how to interpret the sampling comprehensiveness. We further suggest that the decision on choosing an acquisition geometry for an imaging system should consider multiple factors including the sampling comprehensiveness, the task to be performed, the thickness of the imaged object, system specifications, and reconstruction algorithm.

2. METHODS

Two measurements will be introduced to assess the sampling comprehensiveness of each geometry. Both measurements will be computed in the sampled Fourier space illustrated in Figure 1 (right).

2.1 Volume of the null space

Based on the FST, each slice in the sampled Fourier space (Figure 1) is infinitesimally thin, hence the volume of the sampled space is zero for all acquisition geometries. This assumption is not true for most imaging tasks, as we will discuss below. However, to estimate the volume of the null space, Fourier space was divided into $n \times n \times n$ voxels with n ranging from 2 to 20. For each voxel, the number of slices going through the voxel was measured. This number indicates the number of x-ray projections which sampled the particular voxel in Fourier space. The volume of the null space is then defined as the percentage of the voxels that were not subtended by any projection.

Because this measurement is dependent on the value of n, it would not be used to evaluate one specific geometry; rather, it will be used to compare two or more geometries as a function of n. For the analysis, the domain of the space was $f_x, f_y \in [-4,4]$ and $f_z \in [-1.2,1.2]$ in mm^{-1}.

As alluded to above, the projection plane is not infinitesimally thin for any real object, because all x-rayed objects have limited thickness (measured in the direction of the projection). As a result, modulation outside the plane arises; the smaller the object the greater the modulation. Knowledge of the imaging task would allow us to calculate the Fourier transform more precisely; however, this is beyond the scope of the current work.

2.2 Distance to the nearest sampled plane

Stevens *et al* has shown that the sampling density in Fourier space can be directly calculated as the inverse of the distance from a sampled point in one view to the nearest sampled point from another view given a large number of projections.[6] As we have attempted to assess and compare the sampling comprehensiveness of acquisition geometries with only a small number of projections, we computed the distance from every point in the space to its nearest sampled plane, rather than its inverse.

For each geometry, the sampled Fourier space within $f_x, f_y, f_z \in [-4,4]$ mm^{-1} was divided into 200 x 200 x 200 cubic voxels. For every voxel, the nearest plane was recorded in terms of its projection number (1 to 15) and the minimum distance to that plane was computed. The distribution of voxels in terms of their nearest projection was then compared.

3. RESULTS

3.1 Volume of the null space

In Figure 2, the percentage of frequency voxels (20 x 20 x 20) subtended by various numbers of projections is shown for each acquisition geometry. In this figure, the percentage of voxels at zero projections represents the percentage of the volume that is never sampled by any x-ray projections in the described acquisition geometry. In this analysis, we define the volume of the null space as this percentage for a given *n* as summarized in Table 1.

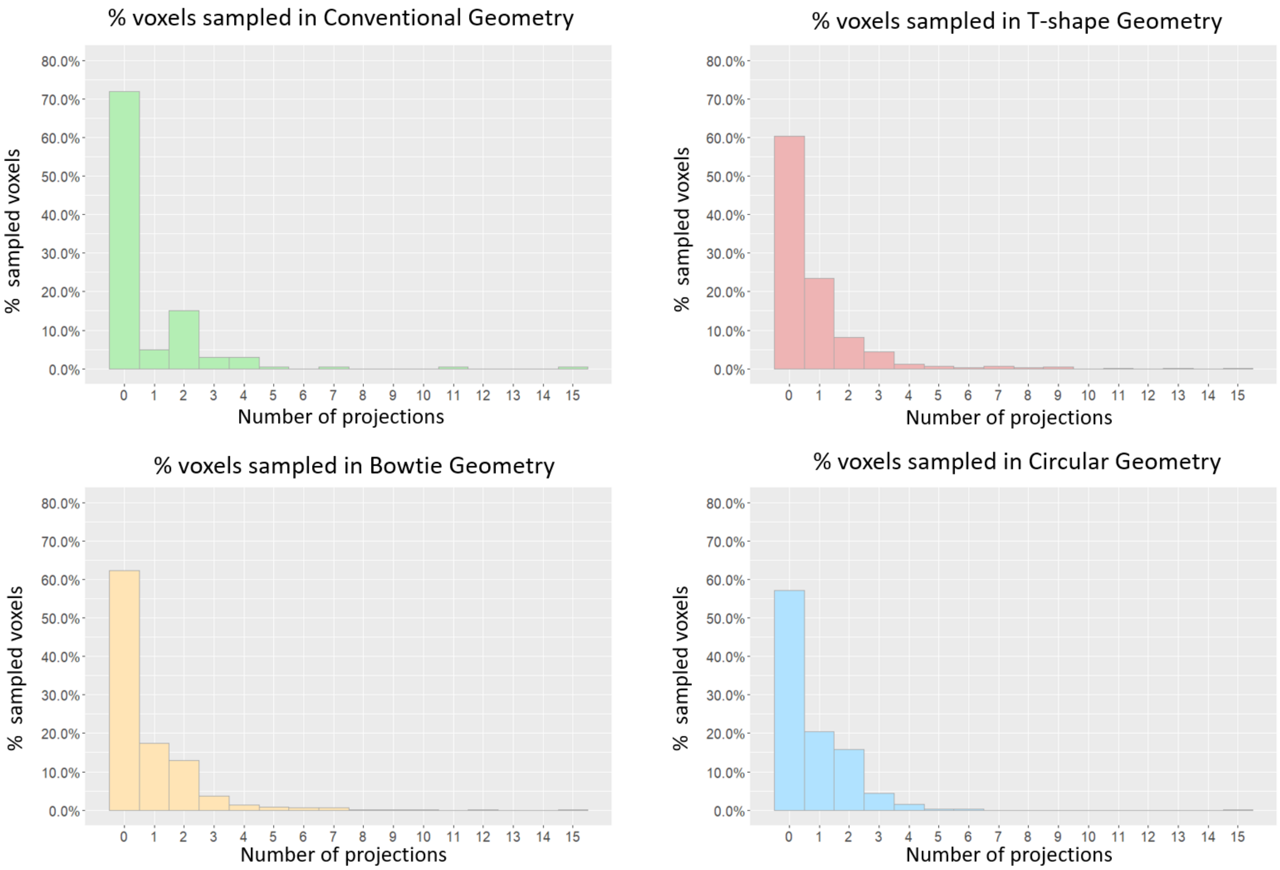

% voxels sampled in Conventional Geometry

% voxels sampled in T-shape Geometry

% voxels sampled in Bowtie Geometry

% voxels sampled in Circular Geometry

Figure 2. Percentage of voxels sampled by projections in each acquisition geometry. The space is voxelized into 20x20x20 cuboids.

Table 1. The volume of the null space measured for each acquisition geometry. The percentage of voxels sampled by zero projections is defined as the volume of the null space. For each measurement, the space was voxelized into *n* x *n* x *n* cuboids.

n	**Conventional**	**T-shape**	**Bowtie**	**Circular**
2	50.00 %	50.00 %	50.00 %	50.00 %
4	50.00 %	43.75 %	43.75 %	37.50 %
8	62.50 %	52.34 %	51.56 %	46.88 %
16	70.31 %	57.61 %	58.98 %	53.61 %
20	72.00 %	60.40 %	62.35 %	57.25 %

The distribution of the histograms in Figure 2 varies with acquisition geometries. These differences may portray and compare the sampling comprehensiveness of the listed acquisition geometries. For example, if more voxels are sampled by exactly one projection, the reconstructed space becomes more comprehensively sampled. By the same logic, as more voxels are repeatedly sampled by more than one projection, space becomes less and less comprehensively sampled.

As the volume of the null space is dependent on the total number of voxels (*n* x *n* x *n*), it was computed as a function of *n* as shown in Table 1. Although the exact values vary with *n*, the comparison between acquisition geometries mostly holds across the value of *n*; the volume of null space decreases in the order of Conventional, Bowtie, T-shape, and Circular acquisition geometry.

3.2 Distance to the nearest sampled plane

The distribution of frequency voxels in terms of their nearest projection in the reconstructed Fourier space is illustrated in Figure 3. Most voxels are nearest to either two, three or four specific projection slices in conventional, T-shaped, and bowtie geometries, respectively. On the other hand, the histogram of the circular geometry shows that the voxels are evenly distributed throughout the projections, all with percentages between 5.5% and 8.5%. This indicates that the circular acquisition geometry more comprehensively samples the space and the sampling density within the space does not vary significantly, compared to the others.

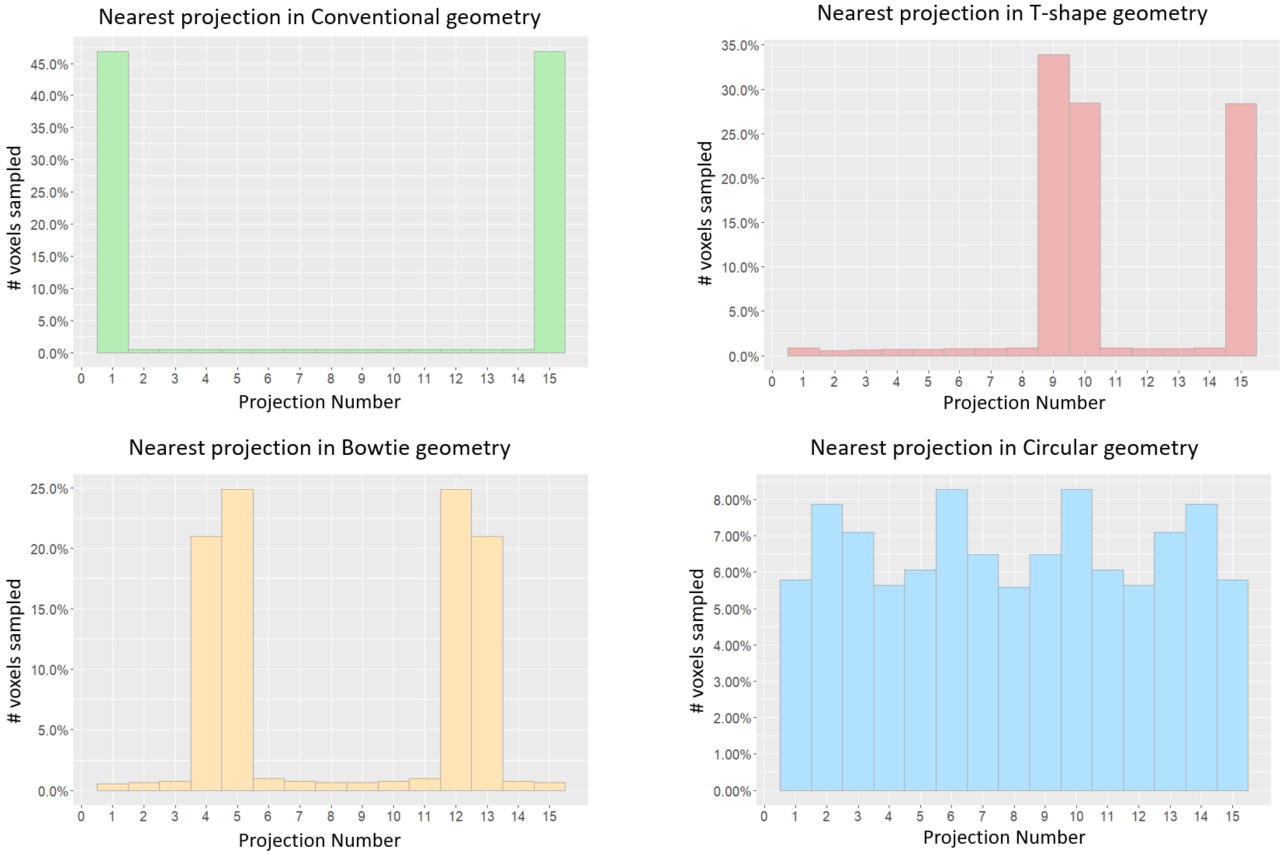

Figure 3. For each voxel (200 x 200 x 200) in the sampled Fourier space (f_x, f_y, $f_z \in [-4,4]$) for each acquisition geometry, its nearest slice was recorded as projection number from projection 1 to projection 15. Note that the scale of the y-axis differs between the subplots.

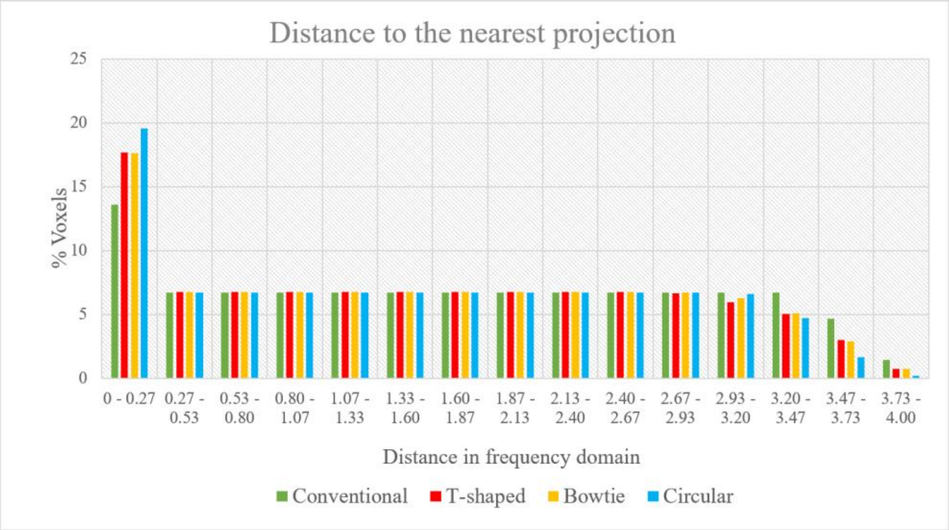

Figure 4. For each voxel (200 x 200 x 200) in the sampled Fourier space for each acquisition geometry, the distance to its nearest projection was measured.

The distance from each voxel to its nearest projection is plotted for each acquisition geometry in Figure 4. As expected from Figure 3 and Table 1, the circular geometry has the highest value in the shortest distance bin and its tail decreases rapidly. This suggests that for a given voxel in the Fourier domain, there is a higher probability that it is adjacent to a measurement point in the circular geometry than in other geometries; that is, the circular geometry is more comprehensive. The conventional, T-shaped, and bowtie acquisition geometries have distinct shapes in the figure as well.

4. DISCUSSION

4.1 Tomosynthesis sampling with a finite number of projections

Assuming an infinite number of projections along the source motion path, the acquisition geometry filling the greatest volume in Fourier space will produce the most comprehensive image reconstruction. In practice, the number of projections in tomosynthesis scans is finite. Assuming a parallel beam, as we did to visualize the Fourier space sampling, projections produce infinitesimally thin planes, comprising zero volume, in the Fourier domain.

Here, we revisit and extend the work by Acciavatti and Maidment to interpret the sampling comprehensiveness for acquisition geometries with a finite number of projections.[17] In their work, they mathematically prove that the Fourier transform of a pitched sine plate with a finite thickness is modulated by a sinc function (equation (22)). This is illustrated in Figure 5.

The shaded FDC (Fourier double cone) region refers to the sampled region of an infinite number of projections for a tomosynthesis scan with angular range Θ. Note the pitched angle of the sine plate object is outside the sampled region in the above figure. Yet, because the Fourier transform of a pitched sine plate is modulated by a sinc function, the reconstruction is expected to retain some information about the object. We make a simple modification to illustrate the data sampling with a finite number of projections in Figure 5. This is equivalent to an orthogonal slice of Figure 2a (right).

As we decrease the number of projections, sampling within the shaded region becomes less dense. Therefore, the sinc-modulated signal may only be sampled at certain points (i.e., the intersection of blue lines and black lines upon which the red sinc functions are plotted in figure 5) and the information retained in the reconstruction for the function is reduced.

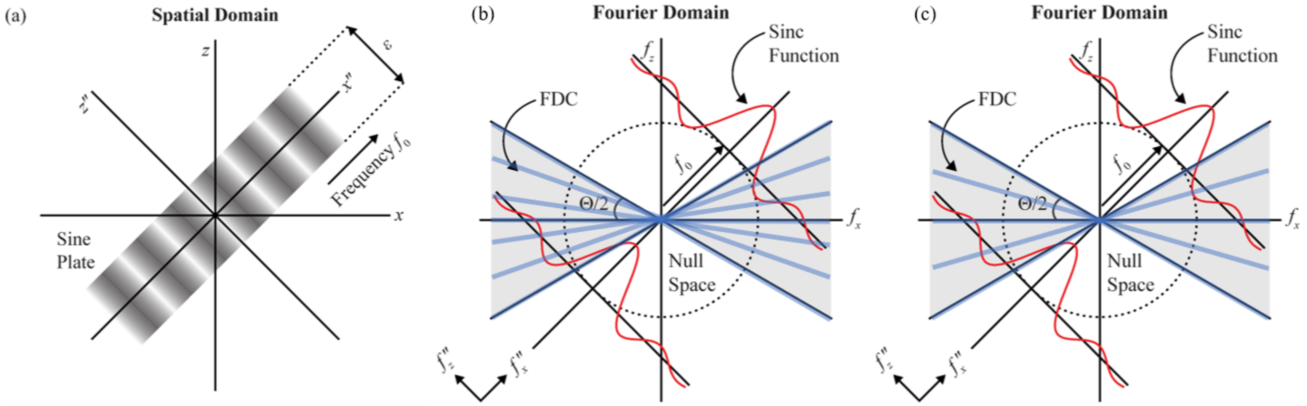

Figure 5. The angled sine plate (Figure 5a) is imaged with only seven (Figure 5b) and five (Figure 5c) projections. Each blue solid line in the figures represents the plane sampled by one x-ray projection. (Figure adapted from Acciavatti *et al*[17])

4.2 The null space and the nearest sampled plane

A close examination of the distributions of the histograms in Figure 2 reveals that the acquisition geometry that most comprehensively samples Fourier space will meet the following criteria:

1) The percentage of voxels sampled by zero projections (i.e., volume of the null space) is minimized.
2) The percentage of voxels sampled by one projection is maximized.
3) The percentage of voxels sampled by more than one projection decreases rapidly with increasing number of projections.

Furthermore, as seen in Figure 5, the amplitude of the sinc-modulated Fourier transforms decreases as we move away from the plane. Hence, the nearest sampled plane from a point (f_x, f_y, f_z) carries the greatest amount of information about that frequency. Note that while this assertion will generally hold true, it is possible that the sampled frequencies will occur at the zeros of the sinc; however, the likelihood of sampling such an object strictly at the zeros of its Fourier representation is small.

The distributions of the nearest projections (Figure 3) present distinct patterns for each acquisition geometry. In the conventional geometry, more than 90% of the space is adjacent to the two most angled projections. This indicates that the distances between the sampled planes are small. In other words, the imaged object would not be comprehensively sampled but would be densely sampled in certain regions in Fourier space; and sparsely sampled elsewhere. The T-shape and the bowtie trajectories add additional directionalities; as a result, the frequency space is more uniformly and comprehensively sampled than it would be with the conventional geometry. The histogram of the circular geometry is quite distinctive from others; voxels are evenly distributed between all 15 projections. Fourier space would be most comprehensively sampled compared to other geometries described above.

This observation adds two more criteria to the above list:

4) The nearest planes are distributed as uniformly as possible.
5) The distance from each voxel to its nearest plane is minimized.

According to these criteria, the acquisition geometry that most comprehensively samples the space is the circular geometry, whereas the acquisition geometry that least comprehensively samples the space is the conventional (linear) geometry.

4.3 Interpretation of comprehensiveness

The ultimate question for tomosynthesis system designers comes down to "how do we acquire the most information of the object within the dose and time constraints of the imaging task?". We will not discuss the scan time constraint in this paper as it may be managed with advanced hardware such as a multisource array[18]. Assuming taking any one projection contributes to 1/nth of the total dose limit, the question becomes: "how do we efficiently select n projections for the best image quality?".

In Figure 5, two imaging modes are illustrated: Figure 5b with seven projections, and 5c with only five projections. Figure 5c effectively has more dose budget left than figure 5b in which it can use to fill the FDC more densely or fill outside the FDC. If one chooses to fill the FDC more densely, it will result in a less comprehensive sampling but input frequencies within the region will be better sampled. If one chooses to spend the budget to fill outside the FDC, it will result in a more comprehensive sampling but input frequencies within the FDC will not be as well-sampled.

Each geometry uses this budget differently. The conventional (linear) geometry fills the FDC more densely and input frequencies within or close to the FDC are well sampled. Some geometries, such as the T-shape and bowtie geometries, use a portion of the budget to fill the space in other directions. More complex geometries, such as the circular geometry, spend the budget for the most uniform and comprehensive sampling.

4.4 Theoretical strategies for choosing an acquisition geometry

The decision on an acquisition geometry must consider the fact that the geometry directly affects how the object will be sampled, and hence, the quality of its reconstruction. Although we proposed "sampling comprehensiveness" as a factor to assess system geometries, an acquisition geometry with high comprehensiveness is not necessarily superior to acquisition geometries with relatively low comprehensiveness. We propose that this decision should consider other factors including: (1) the task to be performed, (2) the thickness of the object being imaged, (3) system specification, and (4) reconstruction algorithm. We will briefly discuss the effect of each factor.

First, the decision on tomosynthesis acquisition geometry should be task dependent. As discussed in previous sections, unique geometries use the dose budget for filling the Fourier space differently. If the presence of a lesion is unknown and the probability is equal throughout the imaged object, a uniform distribution of dose might be more appropriate. One of the geometries that could be used for this purpose is the circular geometry. The circular geometry may remove out-of-plane artifacts more effectively with the complicated system motion and appropriate reconstruction filters[4,6]. Furthermore, it would allow super-resolution in both directions and oblique reconstructions over a broad range of pitches[5,10,11,12,13,17], all of which would be beneficial for a thorough inspection of the lesion. On the other hand, if the presence and more importantly the location and orientation of the lesion is known, a selective distribution of dose should be considered.

Moreover, specific requirements related to the performed task may help to determine which acquisition geometry would be used. For example, real-time tomosynthesis guided biopsy proposed by Singh *et al.* requires a repeated scan at the same source positions[15,16]. This is only feasible with an acquisition geometry which has a cyclical behavior. In his work, Singh simulates the scan with a circular geometry.

The thickness of the object being imaged should impact the decision as well. We refer back to the work of Acciavatti *et al.* where they prove that the Fourier transform of a pitched sine plate is modulated by a sinc function.[17] This sinc function, in fact, is dependent on the thickness of the pitched plate (eq. (22)). The amplitude of the sinc function that intersects the sampled planes increases and broadens as the thickness of the object decreases. If the object is sufficiently thin, dense sampling might be unnecessary for a certain range of input frequencies.

The specifications of the tomosynthesis system should also be considered to investigate various acquisition geometries thoroughly. We have noted that Figure 2 does not consider any parameters of the imaging system, such as the detector element size, shape and orientation. Therefore, the Nyquist frequency in any direction, including the depth (z) direction, is not illustrated in the figure. Incorporation of the effects of the Nyquist frequencies will essentially truncate the figure in all three directions as illustrated in Figure 6[19]. Sampling of the object outside the truncated region does not have to be considered when inspecting an acquisition geometry, as it would be null.

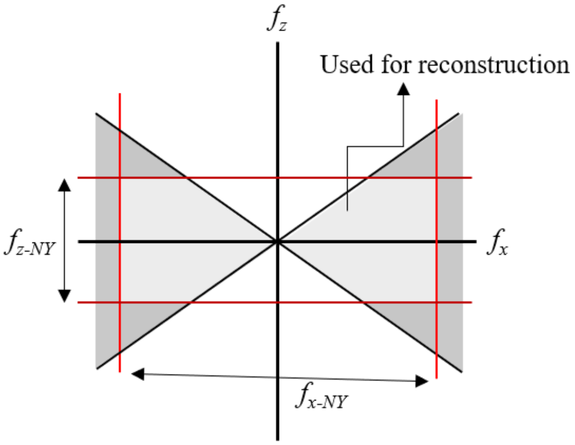

Figure 6. Incorporation of the effects of the Nyquist frequencies ($f_{x\text{-}NY}$, $f_{y\text{-}NY}$, $f_{z\text{-}NY}$) will essentially truncate the sampled region in all three directions, f_x, f_y, and f_z. Only f_x and f_z directions are shown in the figure for simplicity.

Although they are not examined in this paper, reconstruction algorithms are often specific to acquisition geometries. One advantage of acquisition-specific reconstruction filters is more effective removal of out-of-plane artifacts in tomosynthesis. Researchers have investigated to optimize filter design and assess filter performance for various geometries[4,6,17,18]. Availability of appropriate filters and of different reconstruction algorithms should be recognized.

5. CONCLUSION

This study introduces the concept of the sampling comprehensiveness and propose two measurements to assess it for each acquisition geometry. It further discusses tomosynthesis data sampling in the Fourier domain with a finite number of projections and how it relates to the proposed measurements. It further provides how to interpret sampling comprehensiveness in terms of the dose budget and image quality. Theoretical strategies for deciding an acquisition geometry suggested based on five factors: (1) sampling comprehensiveness, (2) task to be performed, (3) thickness of the imaged object, (4) system specifications, and (5) reconstruction algorithm.

6. ACKNOWLEDGEMENT

ADAM has received research support from Hologic Inc., Barco NV, and Analogic Corporation; is a spouse to an employee and stockholder of Real Time Tomography (RTT), LLC; is a member of the scientific advisory board of RTT; and is an owner of Daimroc Imaging, LLC.

Support was provided by the following grants: W81XWH-18-1-0082 from the Department of Defense Breast Cancer Research Program, IRSA 1016451 from the Burroughs Wellcome Fund, 1R01CA196528 from the National Institute of Health, and IIR13264610 from Susan G. Komen®. In addition, equipment support was provided by Analogic Inc., Barco NV, and RTT. The content is solely the responsibility of the authors and does not necessarily represent the official views of the funding agencies.

7. REFERENCES

[1] Dobbins III, J. T., "Tomosynthesis imaging: at a translational crossroads," Med. Phys. 36 (6), 1956-1967 (2009).

[2] Dobbins III, J. T. and Godfrey, D. J., "Digital X-ray tomosynthesis: current state of the art and clinical potential," Phys. Med. Biol. 48 (19), 65-106 (2003).

[3] Dance, D. R., Christofides, S., Maidment, A. D. A., McLean, I.D., and Ng, K.H., [Diagnostic Radiology Physics: A Handbook for Teachers and Students], IAEA, Austria, 231-232 (2014).

[4] Reiser, I. and Glick, S. Chapter 5: Cicular Tomosynthesis. [Tomosynthesis Imaging], Taylor & Francis, New York, 65-79 (2014).

[5] Acciavatti, R. J. and Maidment, A. D. A., “Observation of super-resolution in digital breast tomosynthesis”, Med. Phys., 39 (12), 7518-7539 (2012).

[6] Stevens, G. M., Fahrig, R., and Pelc, N. J., “Filtered backprojection for modifying the impulse response of circular tomosynthesis, Med. Phys. 28 (3), 372-380 (2001).

[7] Curry, T. S., Dowdey, J. E., and Murray Jr, R. C. [Christensen’s physics of diagnostic radiology], Wolter, 242-256 (1990).

[8] Levakhina, Y. M., Duschka, R. L., Vogt, F. M., Barkhausen, J., and Buzug, T. M., “A dual-axis tilt acquisition geometry for digital musculoskeletal tomosynthesis”, Phys. Med. Biol. 58, 4827-4848 (2013).

[9] Maidment, T. D., Vent, T. L., Ferris, W. S., Wurtele, D. E., Acciavatti, R. J. and Maidment, A. D. A., “Comparing the imaging performance of computed super resolution and magnification tomosynthesis,” Med. Imaging 2017 Phys. Med. Imaging 10132, 1013222 (2017).

[10] Vent, T. L., Lepore, B., and Maidment, A. D. A., “Evaluating the imaging performance of a next-generation digital breast tomosynthesis prototype”, Proc. SPIE 10948, Medical Imaging 2019: Physics of Medical Imaging, 109480K (1 March 2019)

[11] Vent, T. L., Barufaldi, B. and Maidment, A. D. A., "Simulation and experimental validation of high-resolution test objects for evaluating a next-generation digital breast tomosynthesis prototype", Proc. SPIE 10948, Medical Imaging 2019: Physics of Medical Imaging, 109480M (1 March 2019);

[12] Eben, J. E., Vent, T. L., Choi, C. J., Yarrabothula, S., Chai, L., Nolan, M., Kobe, E., Acciavatti, R. J. and Maidment, A. D. A., “Development of a Next Generation Tomosynthesis System,” Med. Imaging 2018 Phys. Med. Imaging, 10573 (2018).

[13] Acciavatti, R. J. and Maidment, A. D. A., “Proposing an Acquisition Geometry that Optimizes Super-Resolution in Digital Breast Tomosynthesis”, IWDM 2012: Breast Imaging, 386-396 (2012).

[14] Kak, A. C. and Slaney, M., [Principles of Computerized Tomographic Imaging], IEEE Press, 49-112 (1988).

[15] Singh, P., Choi, C. J., Vent, T. L., and Maidment, A. D. A, “Novel Reconstruction Algorithms that Facilitate Real Time 4D Tomosynthesis”, Med. Imaging 2021 Phys. Med. Imaging (2020).

[16] Singh, P., Choi, C., Vent, T. L., Maidment, A. D. A., “Real Time Image Reconstruction Technique for Digital Breast Tomosynthesis-Guided Needle Biopsy,” PO-GeP-I-185, Med. Phys. 2020: 47 (6). E551

[17] Acciavatti, R. J. and Maidment, A. D. A., “Oblique reconstructions in tomosynthesis. I. Linear systems theory”, Med. Phys. 40 (11), 111911-1-111911-21 (2013).

[18] Neculaes, V. B., Edic, P. M., Frontera, M., Caiafa, A., Wang, G. and Man, B. D., “Multisource X-Ray and CT: Lessons Learned and Future Outlook”, IEEE, 1568-1585 (2014).

[19] Zhao, B. and Zhao, W., “Three-dimensional linear system analysis for breast tomosynthesis”, Med. Phys. 35 (12), 5219-5232 (2008).

[20] Mertelmeier, T., Orman, J., Haerer, W. and Dudam, M. K., "Optimizing filtered backprojection reconstruction for a breast tomosynthesis prototype device," Proc. SPIE 6142, Medical Imaging 2006: Physics of Medical Imaging, 61420F (2006).

[21] Lauritsch, G. and Haerer, W. H., “A theoretical framework for filtered backrprojection in tomosynthesis”, Proc. SPIE 3338, 1127-1137 (1998).

[22] Vent, T. L., Barufaldi, B., Acciavatti, R. J., Krishnamoorthy, S., Surti, Suleman, and Maidment, A. D. A., “Next Generation Tomosynthesis Image Acquisition Optimization for Dedicated PET-DBT Attenuation Corrections”, Proc. SPIE 11595, Medical Imaging 2021 Phys. Med. Imaging (2021).

Signal-to-Noise Ratio and Contrast-to-Noise Ratio Measurements for Next Generation Tomosynthesis

David A. Martin, Trevor L. Vent, Chloe J. Choi, Bruno Barufaldi,
Raymond J. Acciavatti, Andrew D. A. Maidment
University of Pennsylvania, Department of Radiology, 3400 Spruce Street, Philadelphia PA 19104
Email: {Dave.Martin, Trevor.Vent, Bruno.Barufaldi, Jeongin.Choi,
Raymond.Acciavatti, Andrew.Maidment}@pennmedicine.upenn.edu

ABSTRACT

It is standard for the x-ray source in conventional digital breast tomosynthesis (DBT) acquisitions to move strictly along the chest wall of the patient. A prototype, next-generation tomosynthesis (NGT) system has been developed that is capable of acquiring customized geometries with source motion parallel and perpendicular to the chest wall. One well-known consequence of acquiring projections with the x-ray source anterior to the chest wall is that a small volume of tissue adjacent to the chest wall is missed. Here we evaluate strategies in DBT to avoid missing tissue while improving overall image quality. Acquisition geometries tested in this study include the conventional (control), "T-shape," and "bowtie" geometries. To evaluate the impact of moving the x-ray source away from the chest wall, the signal-to-noise ratio (SNR) and contrast-to-noise ratio (CNR) were measured as a function of location within the reconstructed volume. Using simulations and physical experiments, the SNR and CNR were compared with conventional DBT. Simulations of two different phantoms were performed: a "tube" phantom and a "lattice" phantom. Experiments with uniform and textured phantoms were also conducted. While the image quality was slightly reduced immediately adjacent to the chest wall, there was no missed tissue and both the T-shape and Bowtie geometries exhibited SNR and CNR improvement over the vast majority of the reconstruction volume; the overall result being an improvement in image quality with both the T-shape and bowtie geometries.

INTRODUCTION

Digital breast tomosynthesis (DBT) has been shown to improve cancer detection and reduce false positive recalls in screening when compared to traditional 2D mammography[1,2]. DBT acquires x-ray projections over a limited angular range to create a three-dimensional (3D) or volumetric image of the breast. Conventional DBT systems acquire x-ray projections strictly along the chest wall. Customized DBT acquisition geometries have been proposed as an alternative to improve the visualization of breast tissue[3–6]. It has been shown previously that acquisition geometries with a two-dimensional source trajectory can improve image quality by better estimating breast shape (i.e., outline and volume), reducing artifacts and out-of-plane blurring, and improving in-plane spatial resolution and super-resolution[4–9].

Designing a new acquisition geometry for breast imaging must consider certain criteria, including: (i) the acquisition geometry should be designed to avoid missing tissue at the chest wall[10,11], and (ii) overall image quality throughout the entire breast must be maximized. The conventional DBT geometry satisfies (i) by acquiring x-ray projections directly over the chest wall. With regard to criterion (ii), we will define the conventional geometry as the control case. In designing our NGT system, it has been our hypothesis that by varying the source location in both the lateral and posteroanterior (PA) directions, the image quality could be improved (ii) while ensuring that the breast is sampled by including a sufficient number of projections along the chest wall to avoid missed tissue (i).

In this work, we evaluate the overall image quality of DBT reconstructions resulting from two custom acquisition geometries, T-shape and bowtie. As shall be made clear in this work, we have intentionally located half of the source locations in the plane of the chest wall. This will ensure that all of the breast will be exposed to at least half of the full radiation dose budget; the remainder of the dose budget can be used to acquire projections outside of the chest wall plane. Note, here we are assuming an equal distribution of dose between projections.

We assess the image quality of the reconstructions for each geometry in terms of spatially-dependent signal-to-noise ratio (SNR) and contrast-to-noise ratio (CNR). Based on Poisson statistics, one can assert that when using half the dose, the reduction in SNR and CNR at the chest wall is proportional to $1/\sqrt{2}$, thus neither SNR or CNR should be reduced by more

Medical Imaging 2021: Physics of Medical Imaging, edited by Hilde Bosmans, Wei Zhao,
Lifeng Yu, Proceedings of SPIE Vol. 11595, 115951L · © 2021 SPIE
CCC code: 1605-7422/21/$21 · doi: 10.1117/12.2582279

than 30%. By contrast, one would expect that SNR and CNR will increase anteriorly if x-ray source locations are positioned anterior to the chest wall plane due to the inverse square law and the reduced obliquity of the incident rays.

We posit that acquisition geometries with PA source motion, such as the T-shape and bowtie geometries, may be designed to improve SNR and CNR over the bulk of the reconstructed volume, and thus improve lesion conspicuity, while minimizing the impact on lesions immediately adjacent to the chest wall. The ultimate goal of this study is to develop a method for optimizing customized DBT acquisitions using objective metrics commonly used for image quality, such as SNR and CNR.

MATERIALS

The NGT Prototype

The configuration of the NGT prototype was used to simulate image acquisition of three typical acquisition geometries (conventional, T-shape, and bowtie)[7,8,12] using the OpenVCT simulation framework[13] and physical experiments. The conventional acquisition geometry does not incorporate PA source motion, while the T-shape and bowtie geometries both incorporate PA source motion.

Virtual Phantoms

Two virtual phantoms were created to evaluate SNR and CNR for the three acquisition geometries. The tube phantom (Figure 1, left) is 306 mm x 240 mm x 40 mm (in x, y, and z, respectively) and comprises 29 equidistant tubes of glandular tissue placed in the center (z dimension) of a volume of adipose tissue. Tubes are spaced equidistantly in the mediolateral direction (ML, x). The lattice phantom (Figure 1, right) is the same shape and comprises the same materials as the tube phantom, with 23 additional tubes of glandular tissue spaced equidistantly in the PA direction.

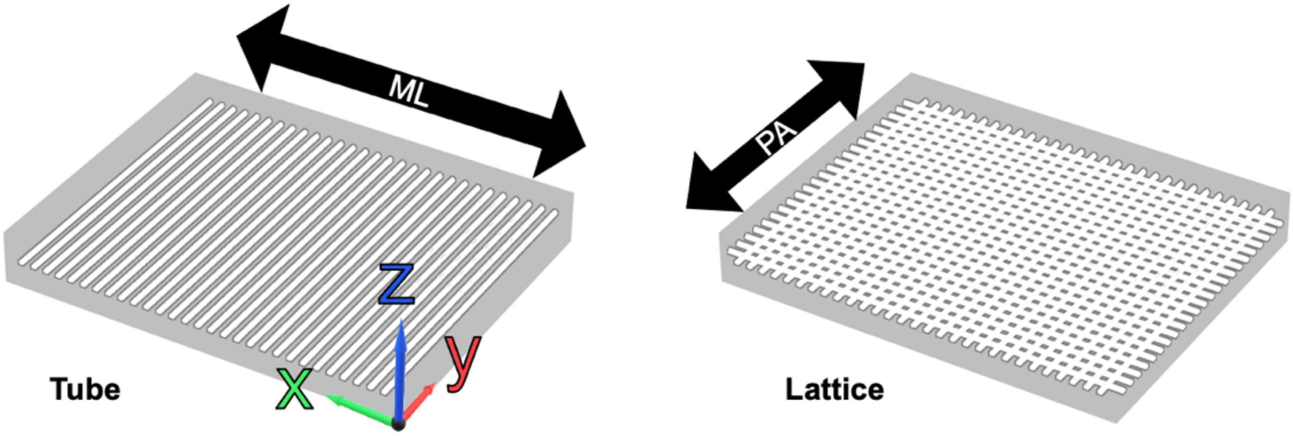

Figure 1: Volume renderings of the tube (left) and lattice (right) phantoms and the coordinate axis.

Physical Phantoms

A uniform Lucite phantom (FF) was used to measure SNR of the acquisition geometries with the NGT prototype. Similarly, a low-frequency contrast phantom (LFC) was used to measure CNR. The LFC was created by placing a 3.18 mm thick perforated polypropylene sheet with 3.18 mm diameter holes between the flat field phantom and the detector. The LFC and FF phantoms both cover the entire detector field of view (Figure 2).

Figure 2: Experimental design for the physical CNR measurements using the LFC phantom. SNR measurements were performed without the LFC in place.

METHODS

Simulated SNR and CNR Measurements

X-ray projection images of the lattice and tube phantoms were acquired using the OpenVCT simulation framework. Fifteen projection images were simulated for each geometry at 32kVp, 5mAs, and 0.5mm Al filtration per projection. Central slices of the phantoms were reconstructed using commercial reconstruction software (Briona version 7.12, Real Time Tomography, Villanova, PA). Acquisitions were repeated 10 times with random noise, and the central slices of each reconstruction were used to measure SNR and CNR.

For the tube phantom, 15x15 pixel regions of interest (ROIs) were centered on the tubes and background regions. Starting at y = 0 mm ROIs were incremented by one pixel to y = 238.7 mm (Figure 3, left). The lattice phantom has tubes intersecting in both directions. ROIs were defined to measure SNR and CNR in the PA direction only (Figure 3, right).

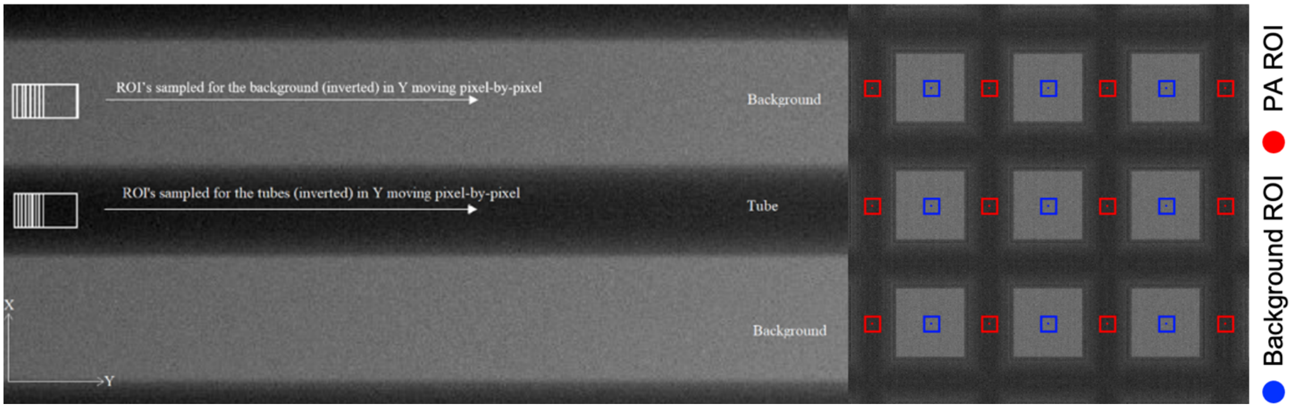

Figure 3: ROIs for the tube phantom (left). ROIs for the Lattice phantom (Right).

The SNR was measured for each ROI of the tube and lattice phantoms using eq. (1). $\sigma[R(x,y)]$ is the standard deviation and $\bar{R}(x,y)$ is the mean value of each ROI at each respective location (x, y). The CNR was measured for each ROI using eq. (2). Where $\bar{R}(x,y)_{tube}$ and $\bar{R}(x,y)_{bgd}$ are the mean values of each ROI for the glandular and adipose tissue regions, respectively. σ_{tube} and σ_{bgd} are the standard deviations. SNR and CNR was repeated for ten central reconstruction slices of each geometry.

$$SNR(x,y) = \frac{(|\bar{R}(x,y)|_{tube})}{\sigma[R(x,y)_{tube}]} \tag{1}$$

$$CNR(x,y) = \frac{\overline{R}(x,y)_{tube} - \overline{R}(x,y)_{bgd}}{\sqrt{\frac{(\sigma_{tube}^2 + \sigma_{bgd}^2)}{2}}} \tag{2}$$

Physical SNR and CNR Measurements

The NGT prototype was used to acquire experimental images of the physical FF and LFC phantoms. Acquisitions were acquired for each geometry at 31 kVp, 4.5 mAs, and 0.5 mm Al filtration per projection. Acquisitions were repeated ten times for FF and twice for LFC phantoms. Central slices were reconstructed using the method described above. Central slices of FF and LFC reconstructions were used to measure SNR and CNR across the detector, respectively.

For FF SNR measurements, 15x15 pixel ROIs were incremented by 4 pixels in x and y across the image. For the LFC CNR measurements, the contrast was measured using line profiles of LFC reconstructions. Noise was measured using noise only images created by subtracting one reconstruction slice from another. Five line profiles were created in the PA direction, at equidistant positions mediolaterally, from one edge of the image to the other for contrast and noise measurements (Figure 9, below). Contrast was measured by the difference between peaks and valleys of the profile. Differences in SNR and CNR for all measurements were evaluated using a two-sample T-test.

RESULTS

Areal Analysis of Mammograms

We analyzed the PA extent of 1091 craniocaudal (CC) and 1311 mediolateral-oblique (MLO) mammograms from a previous study.[14] The maximum PA extent of tissue was measured using the binary masks of the mammograms. The average values are 120.83 mm and 131.32 mm with standard deviations of 39.54 mm and 38.73 mm for CC and MLO views, respectively. The results are summarized as histograms for each laterality in Figure 4. In addition, 54 images had breasts which extended off the anterior edge of the detector. These images are excluded from the calculate of the mean and standard deviation.

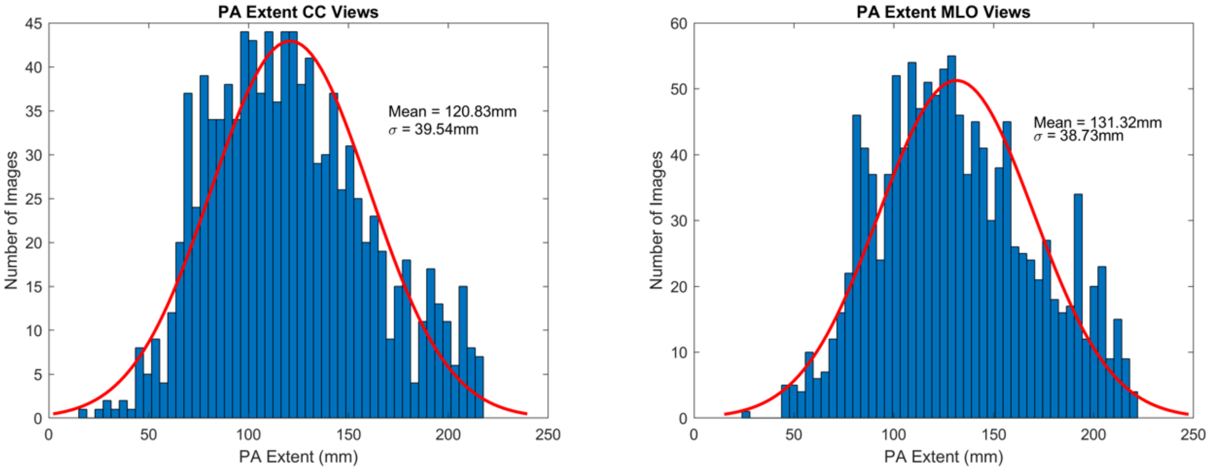

Figure 4: Areal analysis of the maximum PA extent for 1091 CC and 1311 MLO mammograms.

Simulated SNR and CNR Measurements

Figures 5 and 6 show central reconstruction slices, SNR, and CNR for the tube (ML evaluation) and lattice phantoms (PA evaluation), respectively. For ML tubes, the conventional geometry has higher SNR at the chest wall, whereas bowtie and T-shape have higher SNR away from the chest wall. The T-shape has higher SNR medially, and the bowtie has higher SNR laterally. SNR for conventional is lower overall (Figure 5). For PA tubes (Figure 6), the trends are very similar, and again the bowtie geometry had the highest SNR overall. The T-shape and bowtie geometries have higher overall SNR and CNR for the PA tube orientation. The CNR of PA tube measurements decreases with increasing PA distance.

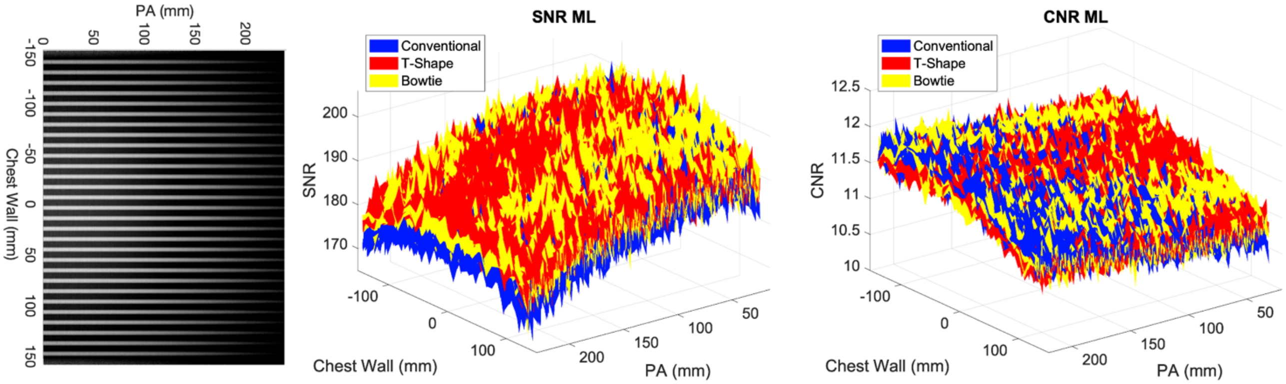

Figure 5: Central reconstruction slice, SNR, and CNR for ML measurements.

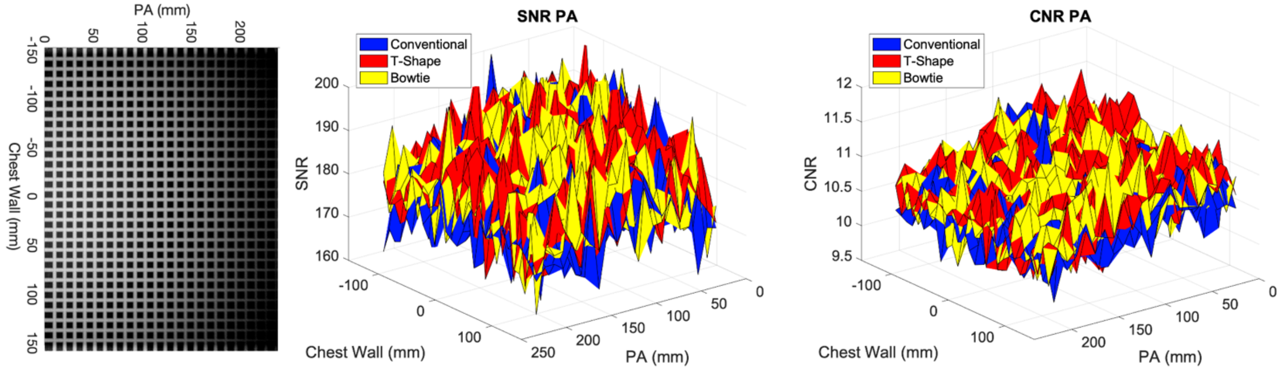

Figure 6: Central reconstruction slice, SNR, and CNR for PA measurements.

SNR and CNR Physical Phantoms

SNR FF measurements are higher for bowtie and T-shape geometries away from the chest wall. Only the central profile of the SNR is shown for FF (Figure 7). The zoomed window of the SNR shows the impact of missed tissue in the reconstruction for the T-shape geometry (Figure 7, right). Little difference is seen between the conventional and bowtie performance near the chest wall. The T-shape motion which has a larger motion in the PA (y) direction has a lower signal at the chestwall. This signal deficit extends for about 3 mm in the reconstructed plane. The CNR for the LFC is consistent with simulation results (Figure 8).

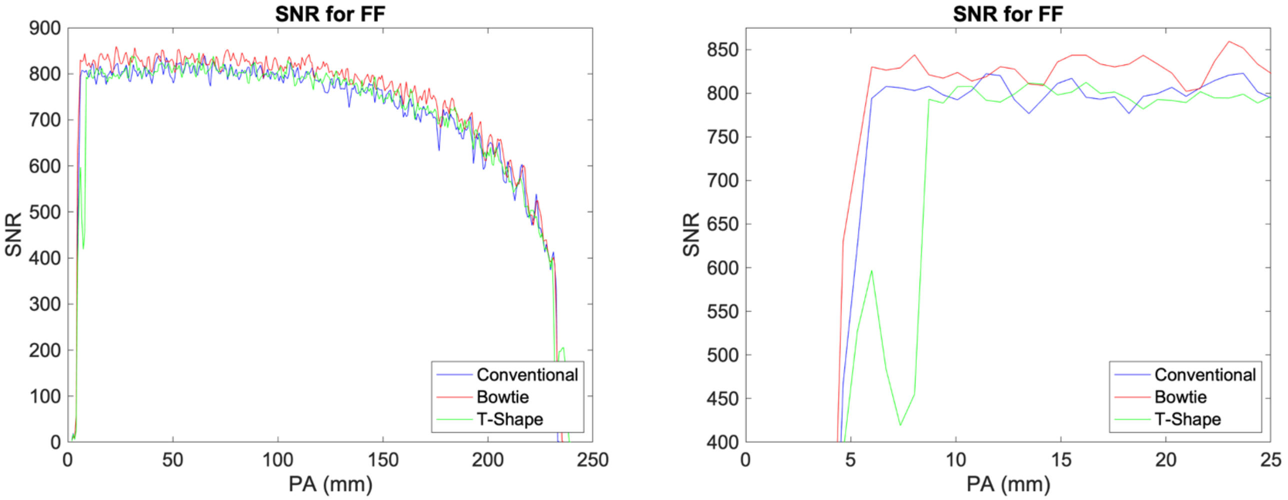

Figure 7: SNR of FF. Note the lag in SNR for T-Shape geometry before it reaches its maximum. This represents the lower exposure for the tissue near the chest wall compared with the other geometries.

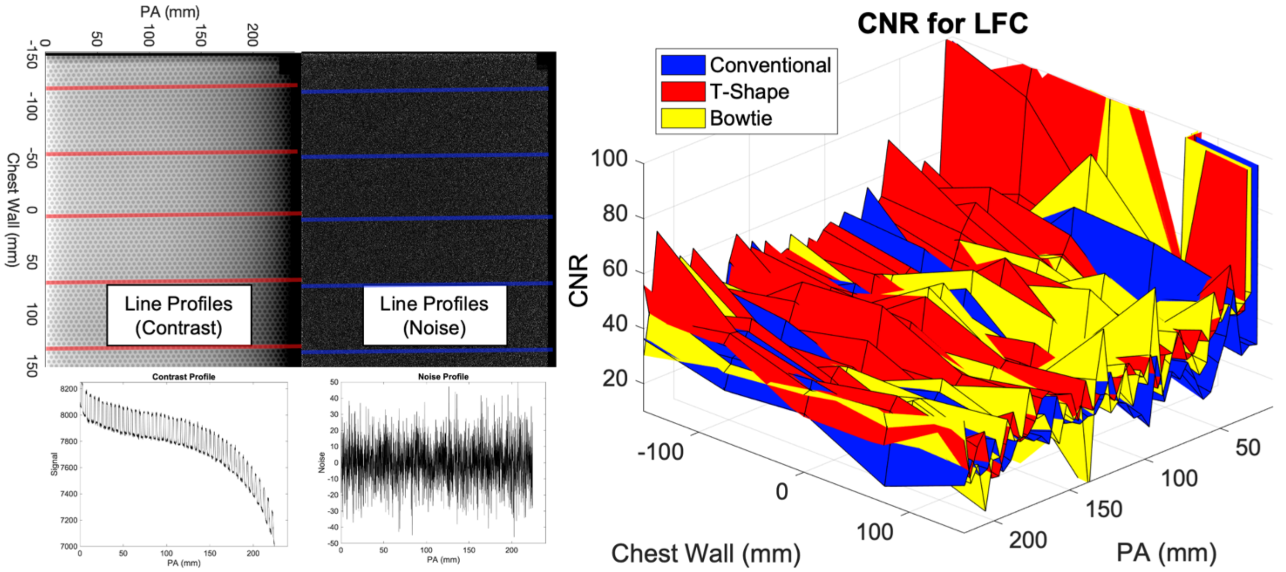

Figure 8: An example of line profiles across the LFC central reconstruction slice and noise image for CNR measurements and the LFC CNR results.

Table 1: Comparison of mean SNR and CNR for NGT acquisition geometries vs. conventional. All p-values are referenced to the conventional geometry. Note that even small differences in means were statistically significant due to the fact that the data were averaged over the entire reconstructed plane.

Phantom	**SNR**			**CNR**		
	Conventional	**T-Shape**	**Bowtie**	**Conventional**	**T-Shape**	**Bowtie**
Tube	187.5	190.1 p<<0.05	190.3 p<<0.05	11.30	11.30 p<<0.05	11.33 p<<0.05
Lattice (PA)	179.9	183.8 p<<0.05	182.8 p<<0.05	10.55	10.75 p<<0.05	10.72 p<<0.05
FF	650.2	645.5 p<<0.05	667.13 p<<0.05			

DISCUSSION

As shown in Figure 4, within the studied population, the majority of women had breasts that covered at least half of the PA dimension of the detector, and more than 50 had breasts that extended beyond the anterior limits of the detector. These results are specific to the population studied. The exact numbers will vary by geographic location and population; however, the fact remains that most breasts have substantial PA extent. As evidenced by Figures 5-8, there is a strong spatial dependence on the SNR and CNR of the reconstructed image. Thus, consideration of the breast size and spatial dependence of image quality are both important.

The simulations and measurements of SNR and CNR for the NGT acquisition geometries do show an overall higher performance compared with conventional DBT, both for ML and PA measurements. In fact, the vast majority of the reconstructed volume is benefited by x-ray projections made with motion in the PA direction. In addition, through careful allocation of source locations and projection dose, it is possible to have only minimal impact on the SNR and CNR adjacent to the chest wall with the NGT geometries. These results suggest that the benefit of the NGT geometries exceeds any possible detriment. As detailed by Caulkin *et al*[15], the vast majority of breast tumors are more proximal to the nipple than the chest wall, so that the vast majority of breast lesions would benefit in terms of SNR and CNR from the NGT geometries.

The results further suggest that individuals with larger breasts could benefit more from acquisition geometries that incorporate PA source motion. Approximately 2% of the reconstruction volume will be adversely affected by the experimental geometries in terms of SNR and CNR. The maximum SNR reduction is about 30%. By comparison, the other 98% of the reconstructed volume shows a benefit in terms of SNR and CNR. The average SNR improvement is about 3%. Thus, the larger the breast the more benefit derived.

These data also support the concept of customized scanning. We have previously shown[6] that acquisition geometries customized to the shape and size of a woman's breast are superior to generic acquisition geometries. In this study, customized scanning geometries scaled to the size of the breast would serve to minimize the impact of PA source motion immediately adjacent to the chest wall. Women with small breasts would require less PA motion and hence the region of reduced SNR would be minimized.

Given that we have already shown numerous benefits to the NGT system, one of the goals of this research was to address concerns expressed by some attendees at previous SPIE Medical Imaging conferences that the NGT system would "miss tissue". To be clear, from our first NGT design meeting, we were cognizant that PA source motion could miss tissue adjacent to the chest wall. For that reason, we have always ensured that the dose was appropriately budgeted between source locations within and without the plane of the chest wall.

In this work, we have shown that this strategy is sound. This work also provides support for the methods used. As such, we will continue in future work to explore additional strategies to improve image quality with the NGT system, including acquisition geometries customized to each breast, by assessing the spatial distribution of SNR and CNR. We also plan to incorporate anthropomorphic models that test for lesion detectability adjacent to the chest wall using virtual clinical trials. We also plan to evaluate different corrective image processing, image reconstruction, and noise stabilization[16] techniques to ameliorate the loss of radiation dose in the area immediately adjacent to the chest wall. Such techniques would also have value at the far lateral extent of the reconstructed volume where source locations opposite to the reconstructed location are collimated to avoid being projected off the detector.

CONCLUSION

In conclusion, we have shown that adding PA source motion does improve the image quality, as measured by SNR and CNR, for the vast majority of the reconstructed breast volume. We have also shown that these geometries do not result in "missed tissue". Future studies need to examine the impact on specific breast sizes, explore the option to customize acquisition geometry to specific breast sizes, and measure the impact on lesion detectability.

ACKNOWLEDGEMENT

ADAM has received research support from Hologic Inc., Barco NV, and Analogic Corporation; is a spouse to an employee and stockholder of Real Time Tomography (RTT), LLC; is a member of the scientific advisory board of RTT; and is an owner of Daimroc Imaging, LLC.

We thank Johnny Kuo, Susan Ng, and Peter Ringer of RTT for technical assistance with the reconstruction software. Support was provided by the following grants: W81XWH-18-1-0082 from the Department of Defense Breast Cancer Research Program, IRSA 1016451 from the Burroughs Welcome Fund, 1R01CA196528 from the National Institute of Health, IIR13264610 from Susan G. Komen®, and 2020 Research Seed Grant from American Association of Physicists in Medicine. In addition, equipment support was provided by Analogic Inc., Barco NV, and RTT. The content is solely the responsibility of the authors and does not necessarily represent the official views of the funding agencies.

REFERENCES

[1] Aujero, M. P., Gavenonis, S. C., Benjamin, R., Zhang, Z. and Holt, J. S., "Clinical performance of synthesized two-dimensional mammography combined with tomosynthesis in a large screening population," Radiology (2017).

[2] Michell, M. J., Iqbal, A., Wasan, R. K., Evans, D. R., Peacock, C., Lawinski, C. P., Douiri, A., Wilson, R. and Whelehan, P., "A comparison of the accuracy of film-screen mammography, full-field digital mammography, and digital breast tomosynthesis," Clin. Radiol. (2012).

[3] Acciavatti, R. J. and Maidment, A. D. A., "Proposing an acquisition geometry that optimizes super-resolution in digital breast tomosynthesis," Lect. Notes Comput. Sci. (including Subser. Lect. Notes Artif. Intell. Lect. Notes Bioinformatics) (2012).

[4] Acciavatti, R. J., Vent, T. L., Barufaldi, B., Wileyto, E. P., Noël, P. B. and Maidment, A. D., "Super-resolution in digital breast tomosynthesis: limitations of the conventional system design and strategies for optimization," 2020.

[5] Barufaldi, B., Vent, T. L., Acciavatti, R. J., Bakic, P. R., Noel, P. B., Conant, E. F. and Maidment, A. D. A., "Determining the optimal angular range of the X-ray source motion in tomosynthesis using virtual clinical trials," 18 (2020).

[6] Acciavatti, R. J., Barufaldi, B., Vent, T. L., Wileyto, E. P. and Maidment, A. D. A., "Personalization of x-ray tube motion in digital breast tomosynthesis using virtual Defrise phantoms," SPIE Med. Imaging(March), 10 (2019).

[7] Vent, T. L., Lepore, B. L. and Maidment, A. D. A., "Evaluating the imaging performance of a next-generation digital breast tomosynthesis prototype," SPIE Med. Imaging(March), 19 (2019).

[8] Vent, T. L., Barufaldi, B. and Maidment, A. D. A., "Simulation and experimental validation of high-resolution test objects for evaluating a next-generation digital breast tomosynthesis prototype," 21 (2019).

[9] Acciavatti, R. J., Rodriguez-Ruiz, A., Vent, T. L., Bakic, P. R., Reiser, I., Sechopoulos, I. and Maidment, A. D. A., "Analysis of volume overestimation artifacts in the breast outline segmentation in tomosynthesis," SPIE Med. Imaging, 10573 (2018).

[10] Bloomquist, A. K., Yaffe, M. J., Pisano, E. D., Hendrick, R. E., Mawdsley, G. E., Bright, S., Shen, S. Z., Mahesh, M., Nickoloff, E. L., Fleischman, R. C., Williams, M. B., Maidment, A. D. A., Beideck, D. J., Och, J. and Seibert, J. A., "Quality control for digital mammography in the ACRIN DMIST trial: Part I," Med. Phys. (2006).

[11] Yaffe, M. J., Bloomquist, A. K., Mawdsley, G. E., Pisano, E. D., Hendrick, R. E., Fajardo, L. L., Boone, J. M., Kanal, K., Mahesh, M., Fleischman, R. C., Och, J., Williams, M. B., Beideck, D. J. and Maidment, A. D. A., "Quality control for digital mammography: Part II recommendations from the ACRIN DMIST trial," Med. Phys. (2006).

[12] Eben, J. E., Vent, T. L., Choi, C. J., Yarrabothula, S., Chai, L., Nolan, M., Kobe, E., Acciavatti, R. J. and Maidment, A. D. A., "Development of a Next Generation Tomosynthesis System," Med. Imaging 2018 Phys. Med. Imaging, 10573 (2018).

[13] Barufaldi, B., Bakic, P. R., Higginbotham, D. and Maidment, A. D. A., "OpenVCT: a GPU-accelerated virtual clinical trial pipeline for mammography and digital breast tomosynthesis," Med. Imaging 2018 Phys. Med.

Imaging **1057358**(March), 194 (2018).

[14] Barufaldi, B., Borges, L. R., Bakic, P. R., Vieira, M. A. C., Schiabel, H. and Maidment, A. D. A., "Assessment of automatic exposure control performance in digital mammography using a no-reference anisotropic quality index," Med. Imaging 2017 Image Perception, Obs. Performance, Technol. Assess. **10136**, 101360U (2017).

[15] Caulkin, S., Astley, S., Asquith, J. and Boggis, C., "Sites of Occurrence of Malignancies in Mammograms" (1998).

[16] Brandão, R., Borges, L. R., Barufaldi, B., Vent, T. L., Caron, R. F., Oliveira, B. B., Maidment, A. D. A. and Vieira, M. A. C., "Iterative method to achieve noise variance stabilization in single raw digital breast tomosynthesis," Med. Imaging 2021 Phys. Med. Imaging **11595-93**.

W81XWH-18-1-0082 (BC170226): Design of a 3D Mammography System in the Age of Personalized Medicine

PI: Raymond J. Acciavatti, University of Pennsylvania

Budget: $603,749.00 **Topic Area:** Breast Cancer Research Program **Mechanism:** Breakthrough Award-Level 1

Research Area: X-Ray Imaging (708) Digital Imaging (704) **Award Status: Open** March 15, 2018 to March 14, 2022 (NCE)

Study Goals:

Even with the latest "3D" digital breast tomosynthesis systems, most women that are recalled for follow-up testing after a suspicious mammogram are ultimately found to be cancer-free. To improve the sensitivity and specificity of breast imaging for cancer detection, we are proposing to re-design mammography systems around the principle of "personalized medicine", so that the orbits of the detector and x-ray tube are customized to the size, shape, and composition of each breast. The new designs for both screening and diagnostic mammography will be validated with a virtual clinical trial using realistic simulations of breast anatomy and a highly-validated observer model.

Specific Aims:

SA1: Design a personalized image acquisition technique for screening mammography. SA2: Design a 3D magnification mammography call-back exam. SA3: Evaluate the new designs for screening and call-back imaging with a virtual clinical trial.

Key Accomplishments:

Publications:

1. Acciavatti et al. Personalization of x-ray tube motion in digital breast tomosynthesis using virtual Defrise phantoms. In: Schmidt TG, Chen G-H, Bosmans H, editors; Physics of Medical Imaging; 2019; San Diego, CA: SPIE; 2019. p. 109480B.
2. Acciavatti et al. Non-stationary model of oblique x-ray incidence in amorphous selenium detectors: I. Point spread function. Med. Phys. 2019; 46(2):494-504.
3. Acciavatti et al. Nonstationary model of oblique x-ray incidence in amorphous selenium detectors: II. Transfer Functions. Med. Phys. 2019; 46(2); 505-16.
4. Acciavatti et al. Proposing Rapid Source Pulsing for Improved Super-Resolution in Digital Breast Tomosynthesis. In: Chen G-H, Bosmans H, editors; Physics of Medical Imaging; 2020; Houston, TX: SPIE; 2020. p. 113125G.
5. Acciavatti et al. Robust Radiomic Feature Selection in Digital Mammography: Understanding the Effect of Imaging Acquisition Physics Using Phantom and Clinical Data Analysis. In: Hahn HK, Mazurowski MA, editors; Computer-Aided Diagnosis; 2020; Houston, TX: SPIE; 2020. p. 113140W.
6. Barufaldi et al. Determining the Optimal Angular Range of the X-Ray Source Motion in Tomosynthesis Using Virtual Clinical Trials. In: Chen G-H, Bosmans H, editors; Physics of Medical Imaging; 2020; Houston, TX: SPIE; 2020. p. 113120I.
7. Acciavatti et al. Super-Resolution in Digital Breast Tomosynthesis: Limitations of the Conventional System Design and Strategies for Optimization. In: Bosmans H, Marshall N, Van Ongeval C, editors; 15th International Workshop on Breast Imaging; 2020; Virtual Conference (held during COVID-19 Pandemic): SPIE; 2020. p. 115130V.
8. Acciavatti et al. Calculation of Radiomic Features to Validate the Textural Realism of Physical Anthropomorphic Phantoms for Digital Mammography. In: Bosmans H, Marshall N, Van Ongeval C, editors; 15th International Workshop on Breast Imaging; 2020; Virtual Conference (held during COVID-19 Pandemic): SPIE; 2020. p. 1151309.
9. Vent et al. Simulation of high-resolution test objects using non isocentric acquisition geometries in next-generation digital tomosynthesis. In: Bosmans H, Marshall N, Van Ongeval C, editors; 15th International Workshop on Breast Imaging; 2020; Virtual Conference (held during COVID-19 Pandemic): SPIE; 2020. p. 1151317.
10. Barufaldi et al. MRMC ROC Analysis of Calcification Detection in Tomosynthesis Using Computed Super Resolution and Virtual Clinical Trials. In: Bosmans H, Marshall N, Van Ongeval C, editors; 15th International Workshop on Breast Imaging; 2020; Virtual Conference (held during COVID-19 Pandemic): SPIE; 2020. p. 1151313.
11. Martin et al. Signal-to-Noise Ratio and Contrast-to-Noise Ratio Measurements for Next Generation Tomosynthesis. In: Bosmans H, Zhao W, Yu L, editors; Physics of Medical Imaging; 2021 (virtual conference held during COVID-19 Pandemic): SPIE; 2021. p. 115951L.
12. Choi et al. Analysis of Digital Breast Tomosynthesis Acquisition Geometries in Sampling Fourier Space. In: Bosmans H, Zhao W, Yu L, editors; Physics of Medical Imaging; 2021 (virtual conference held during COVID-19 Pandemic): SPIE; 2021. p. 115954W.
13. Vent et al. Next generation tomosynthesis image acquisition optimization for dedicated PET-DBT attenuation corrections. In: Bosmans H, Zhao W, Yu L, editors; Physics of Medical Imaging; 2021 (virtual conference held during COVID-19 Pandemic): SPIE; 2021. p. 115954V.
14. Acciavatti et al. Development of Magnification Tomosynthesis for Superior Resolution in Diagnostic Mammography. In: Bosmans H, Zhao W, Yu L, editors; Physics of Medical Imaging; 2021 (virtual conference held during COVID-19 Pandemic): SPIE; 2021. p. 115951J.
15. Vent et al. Development and Evaluation of the Fourier Spectral Distortion Metric. IEEE Transactions on Medical Imaging 2021; 40(3):1055-64.

Patents: None as of the end of Year 3 of this grant.

Funding Obtained: The PI (Raymond Acciavatti) was a mentor for the 2019 summer undergraduate fellowship program through the American Association of Physicists in Medicine (AAPM). Stipend funding was provided directly to the undergraduate student, who performed research in virtual clinical trials.